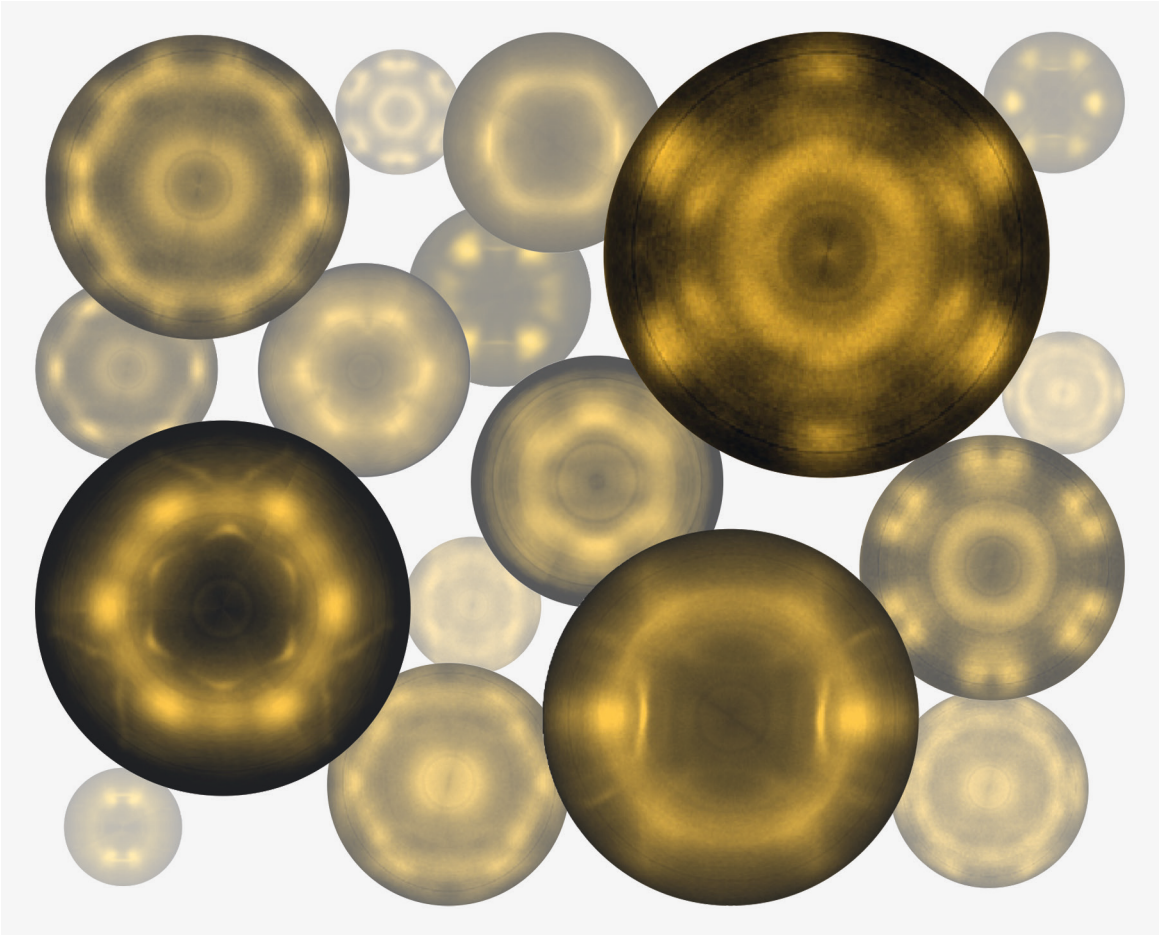

Advances in Photoemission Orbital Tomography

Anja Haags

Information
Band / Volume 104
ISBN 978-3-95806-766-0

Mitglied der Helmholtz-Gemeinschaft

JÜLICH
Forschungszentrum

Schriften des Forschungszentrums Jülich
Reihe Information / Information Band / Volume 104

Forschungszentrum Jülich GmbH
Peter Grünberg Institut (PGI)
Quantum Nanoscience (PGI-3)

Advances in Photoemission Orbital Tomography

Anja Haags

Schriften des Forschungszentrums Jülich
Reihe Information / Information Band / Volume 104

ISSN 1866-1777 ISBN 978-3-95806-766-0

Bibliografische Information der Deutschen Nationalbibliothek.
Die Deutsche Nationalbibliothek verzeichnet diese Publikation in der
Deutschen Nationalbibliografie; detaillierte Bibliografische Daten
sind im Internet über http://dnb.d-nb.de abrufbar.

Herausgeber und Vertrieb:	Forschungszentrum Jülich GmbH Zentralbibliothek, Verlag 52425 Jülich Tel.: +49 2461 61-5368 Fax: +49 2461 61-6103 zb-publikation@fz-juelich.de www.fz-juelich.de/zb
Umschlaggestaltung:	Grafische Medien, Forschungszentrum Jülich GmbH
Druck:	Grafische Medien, Forschungszentrum Jülich GmbH
Copyright:	Forschungszentrum Jülich 2024

Schriften des Forschungszentrums Jülich
Reihe Information / Information, Band / Volume 104

D 82 (Diss. RWTH Aachen University, 2024)

ISSN 1866-1777
ISBN 978-3-95806-766-0

Vollständig frei verfügbar über das Publikationsportal des Forschungszentrums Jülich (JuSER)
unter www.fz-juelich.de/zb/openaccess.

This is an Open Access publication distributed under the terms of the Creative Commons Attribution License 4.0,
which permits unrestricted use, distribution, and reproduction in any medium, provided the original work is properly cited.

"In Wirklichkeit aber hatte man eben etwas Neues gelernt,
an das man vorher nicht gedacht hatte."

W. Heisenberg
in "Kausalgesetz und Quantenmechanik" (1931)

Abstract

Photoemission orbital tomography (POT) is an established technique to investigate the electronic properties of organic adsorbates on surfaces. In POT, a combined experimental and theoretical approach, angle-resolved photoelectron spectroscopy data are measured in a large angular range at a constant kinetic energy and compared to calculated wave functions of organic molecules. To simulate the photoemission process, the final state of the photoelectrons is approximated by a plane wave (PW). Then, the experimentally-obtained photoemission intensity distribution can be correlated directly to theoretical density of states to identify individual orbitals. Due to the used PW approximation (PWA), POT is commonly restricted to π orbitals of large, planar molecules, and a particular experimental geometry. Yet, some reports in literature suggest that POT is not fixed to these conditions. In this work, we verify the limits of POT and thus extend its potential.

To this end, we demonstrate that POT is applicable to σ orbitals allowing to extract orbital energies of both, π and σ orbitals, in a large binding energy range. Using an example of bisanthene on Cu(110), we show that POT of σ orbitals can be successfully used to reveal the exact chemical state of on-surface synthesized reaction products. Moreover, POT of frontier π orbitals allows to shed light on the nature of π stabilization in organic molecules. In particular, the aromatic state of kekulene, which was long disputed to be of either Clar or superaromatic type, is investigated with POT. To this end, specially designed precursor molecules were used in an on-surface synthesis to produce kekulene/Cu(111). If Cu(110) is used instead of Cu(111), we observe the formation of planar kekulene and an isomeric nonplanar derivative of kekulene, iso-kekulene. Hence, opposed to the preconditions of the technique mentioned earlier, POT is capable of differentiating between planar and nonplanar isomers of kekulene.

The application of a simple PW as final state in POT is inspected in this work in two ways. First, we exploit the fact that the PWA is equivalent to the more correct independent atomic center approximation, if the photoemission experiment is recorded in a specific way. To this end, we conducted incidence-angle-dependent measurements on three organic systems to obtain POT data fulfilling the *ideal* so-called $\boldsymbol{\epsilon} \parallel \boldsymbol{k}_f$ condition. Second, photon-energy-dependent POT data of graphene were compared to the results of three calculations using different levels of theory and final-state descriptions. We found clear deviations between the simple PWA and the experimental data. Yet using higher level theory allowed us to extract experimental photoemission cross sections and understand the findings in a comprehensive physical picture.

List of Acronyms

AFM	Atomic force microscopy
ARPES	Angle-resolved photoemission spectroscopy
ARUPS	Angle resolved ultraviolet photoelectron spectroscopy
BG	Background
BWD	Backward direction
BZ	Brillouin zone
CT	Charge transfer
CCD	Charge-coupled device
D3BIA	Density, degeneracy, delocalization-based index of aromaticity
DBBA	10, 10'-dibromo-9,9'bianthracene
DFT	Density functional theory
$\boldsymbol{E_{\mathrm{ad}}}$	Adsorption energy
$\mathbf{E_b}$	Binding energy
$\mathbf{E_D}$	Dirac energy
EDC	Energy distribution curve
$\mathbf{E_F}$	Fermi energy
$\mathbf{E_{kin}}$	Kinetic energy
EMLG	Epitaxial monolayer graphene
$\mathbf{E_{pass}}$	Pass energy
$\mathbf{E_{vac}}$	Vacuum level
fcc	face centered cubic
FT	Fourier transform
FWD	Forward direction

GGA	Generalized gradient approximation
GI	Grazing incidence
GNR	Graphene nanoribbons
H	Hollow
HAXPES	Hard X ray Photoelectron Spectroscopy
$\mathbf{h_C}$	Average adsorption heights of carbon atoms
hcp	hexagonal closed packed
HF	Hartree-Fock
^{1}**H-NMR**	proton nuclear magnetic resonance
HOMA	Harmonic oscillator model of aromaticity
HOMO	Highest occupied molecular orbital
HSE	Heyd, Scuseria and Ernzerhof
IAC	Independent atomic center
LB	Long bridge
LEED	Low-energy electron diffraction
LUMO	Lowest unoccupied molecular orbital
MAE	Mean absolute error
MCP	Multichannel plate
ME	Mean error
MLS	Metrology Light Source
MO	Molecular orbital
MOPDOS	Molecular orbital projected density of states
NI	Normal incidence
NIXSW	Normal-incidence X ray standing wave
NN	Nearest neighbor
ODMR	Optically detected magnetic resonance
OI	Oblique incidence

$\mathbf{\Phi_a}$	Work function of the analyzer
$\mathbf{\Phi_s}$	Work function of the sample
PAH	Polycyclic aromatic hydrocarbons
PBE	Perdew, Burke and Ernzerhof
PDI	Para-delocalization index
pDOS	Projected density of states
PE	Photoemission
PEEM	Photoemission electron microscopy
PES	Photoelectron spectroscopy
POT	Photoemission orbital tomography
PTB	Physikalisch-Technische Bundesanstalt
PTCDA	3,4,9,10-Perylene tetracarboxylic dianhydride
PW	Plane wave
PWA	Plane wave approximation
QFMLG	Quasifreestanding monolayer graphene
QFtBLG	Quasifreestanding twisted bilayer graphene
RT	Room temperature
ROI	Region of interest
SB	Short bridge
SI	Supplementary information
SiC	Silicon carbide
SIESTA	Spanish initiative for electronic simulations with thousands of atoms
SS	Single-scattering
STM	Scanning tunneling microscopy
SWA	Scattered-wave approximation
TDDFT	time dependent density functional theory
TEA	Toroidal electron analyzer

TS	Tkatschenko Scheffler
UHV	Ultrahigh vacuum
UPS	Ultraviolet photoemission spectroscopy
VASP	Vienna *ab initio* simulation package
vdW	van der Waals
XPS	X ray photoelectron spectroscopy
XRD	X-ray diffraction
ZLG	Zero-layer graphene

Contents

1 Introduction

The wave function Ψ is the central mathematical entity in quantum mechanics and is related to the chance to find a quantum system at a particular point in space. This probability distribution is, for instance, used to describe the spatial distribution of electrons in atoms and molecules, the so-called atomic and molecular orbitals, respectively.

The mathematical foundations of Ψ were established by Schrödinger [1], Dirac [2], and Bohr [3] among others in the late 1920's. About 50 years later, it was realized in the surface science community that the "photoemission AD [angular distribution] contains detailed information on the chemisorption bond geometry and the angular variations of the atomic orbitals involved in the bond" [4] and expressed "the hope that the photoemission technique can be used to identify not only the bond orbitals of chemisorbed atoms but also the symmetry of adsorption site." [5]. This proves the awareness in the community of the opportunity to image orbital patterns experimentally in photoelectron spectroscopy (PES).

Yet, it was clear that such angle-resolved ultraviolet photoelectron spectroscopy (ARUPS) measurements need to be rationalized by simulations calling for reasonable models of the photoemission process which "must properly treat both the initial and final states" [4]. Therein, the focus is on the final state as it contains information about the actual photoemission process [5]. Although N.V. Smith and J. W. Davenport saw the unique potential of this combined experimental and theoretical approach "to determine possible both the plane wave decomposition of the final state and the shapes of the atomic orbitals" [6], "to identify the levels" [7] and "to find the orientation of the molecule relative to the surface" [7], Smith also stated that "the plane-wave final state at UPS energies is too crude to expect detailed quantitative agreement" [8]. Not only would the outgoing photoelectrons be described better using spherical waves, but also interaction processes, interference effects, and scattering events within the molecule and by the environment (e.g., the substrate or neighboring molecules) would not be accounted for if the plane wave approximation (PWA) was used. Although electron analyzers providing angular resolution of photoemission intensity were already in use [8, 9], "the amount of data available [...] is already far too overwhelming!" [8]. Due to the theoretical and experimental challenges, the technique's further development was thus not pursued after the 1980's, despite of experimental studies in favor of the PWA [10].

Nevertheless, the combination of experimental angle-resolved photoemission spectroscopy (ARPES) data and simulations based on the PWA was reconsidered in 2009 by Puschnig et al. who presented the "Reconstruction of Molecular Orbital Densities from Photoemission Data" [11]. This photoemission (orbital) tomography (PT or POT) technique has been developed further using varying theoretical advancements and was applied to many molecular systems focusing on different aspects of the individual electronic properties.

POT combines experimental and theoretical views on the photoemission results, namely the photoelectron distribution in reciprocal- (momentum-) space, the so-called k maps. In the experiment, k maps are generated by collecting photoelectrons in a large range of emission angles at a constant kinetic energy and recalculating the photoelectron distribution into reciprocal-space coordinates k_x and k_y. On the theoretical side, the photoemission process has to be simulated first, starting from the electron in its initial state to its final state as an emitted photoelectron traveling freely in vacuum with a particular velocity corresponding to the kinetic energy. If the final free state of the photoelectron is treated as a plane wave (PW), a simple mathematical correlation between the initial and final states can be achieved in theory. The simulated k maps are obtained by Fourier transforming the calculated initial state wave function of a particular orbital and correcting them by a geometrical factor [11]. Thereby, the simulated k maps serve as unique fingerprints for individual molecular orbitals. Comparing experimental and theoretical k maps finally allows to identify and image single molecular orbitals in the experimental data.

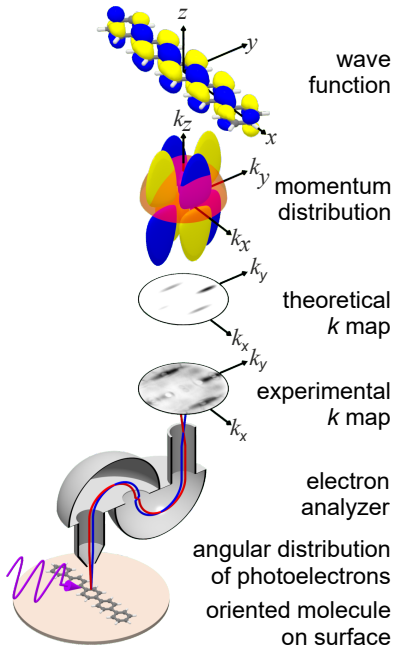

Figure 1.1: POT
Photoelectrons excited from an ordered molecular layer using photons (purple) and collected by the momentum microscope resulting in an experimental k map. The theoretical one is obtained by a hemispherical cut (red, Ewald sphere) through the three dimensional Fourier transform of the orbital's wave function. After Ref. [12] and shown with permission.

Since the PW final state approximation is the key element of POT, it is assumed [11] that the technique can only be applied in specific cases, namely (i) π orbitals from (ii) large, (iii) planar (iv) molecules, and (v) a particular experimental geometry. Moreover, the molecules should consist of many light atoms (H, C, N, O) expected to lead to rather weak and structureless angular patterns [11, 13, 14]. The success of POT following these guidelines has been proven by many publications in a variety of application fields within the last 13 years [AH3, AH4, AH5, AH6, AH8, AH9, AH10, AH12, 11, 12, 15–38]. Contradictory to previous assumptions, it was proven that POT can also be successfully applied to, e.g., small molecules such as CO, CN [39], and benzene [34], three-dimensional buckyball C_{60} molecules [40], strongly bent organic species [AH10], or metalated porphyrin molecules [AH5]. Therefore, it is crucial to test the original limits of POT based on the PW approximation and push these further through novel and unique applications.

Instead of the basic PWA, a more realistic model description of the photoelectron's final state is based on spherical waves as formulated in the independent atomic center (IAC) approximation introduced by W. D. Grobman [41]. Therein, the author analytically proved that the PW and IAC approximations become qualitatively similar if the investigated initial molecular orbital is composed of atomic orbitals of the "same chemical and orbital character" [41]. This condition is fulfilled for p_z-derived π states. However, a molecule naturally also consists of σ states built from s, p_x, and p_y orbitals. Therefore, the natural question arises, whether POT can be applied to molecular orbitals other than π orbitals such as σ orbitals or bent molecules which have nonplanar delocalized π states.

The predicted photoemission intensity resulting from the IAC and PW final state approximations can even emerge into exactly the same result if, in addition to the consistent orbital type, a particular experimental geometry of sample and photon beam is maintained. Namely, the polarization vector of the photon beam $\boldsymbol{\epsilon}$ and the direction of the emitted electron in its final state $\boldsymbol{k}_f$ should be parallel ($\boldsymbol{\epsilon} \parallel \boldsymbol{k}_f$ condition commonly referred to as $\mathbf{A}\|\mathbf{k}$ condition). Such a particular experimental validation of POT results is of great interest as it was already suggested in a critical report by A. M. Bradshaw and D. P. Woodruff in 2015 [42]. Estimating the agreement between photoemission results recorded at typically used experimental geometries and the mentioned idealized case remains to be clarified. Its outcome would serve as a general feasibility test of POT for π orbitals.

Another issue related to the simplicity of the PWA is observed in photon-energy-dependent POT of organic molecules. A deviation between experiment and theory was attributed to scattering at the substrate and correlated to the adsorption height of the molecules [22]. To understand the experimental results, verification using a specially selected system and higher level theory is required.

Summarizing the above mentioned aspects, five principal questions open up to justify the applications of POT and revisit its limitations: (1) Is POT applicable to a broader range of electronic states, particularly σ orbitals and bent π systems? (2) Using these extended possibilities, can POT shed light on details about the chemical state of molecules or (3) identify adsorbed molecules such as the reaction products of on-surface syntheses? (4) Is it possible to obtain experimental k maps fulfilling the ideal $\boldsymbol{\epsilon} \parallel \boldsymbol{k}_f$ condition and how strong is the deviation to typically-recorded ones? (5) Which theoretical model can appropriately reproduce experimental photon-energy-dependent POT and shed light on the nature of the observed resonances?

This thesis contains six main chapters. In the subsequent chapter 2, the experimental technique and the theoretical models are introduced. The subsequent chapters aim to answer the questions formulated above.

In Chapter 3, we expand the so-far experimentally accessible orbital range of POT from π to σ orbitals expected at much higher binding energies than π orbitals. This is investigated using the example of bisanthene/Cu(110). First and foremost, we will prove that σ orbitals can be successfully measured and identified with POT. Additionally, the study will deliver important insight into local chemical modifications of the adsorbed molecules by the substrate. In particular, POT of σ orbitals will allow to identify the chemical state of the adsorbate. Moreover, we extract actual experimental binding energies and spectral lineshapes for each identified orbital and we compare the results to predicted energies in order to benchmark four widely used functionals.

In Chapters 4 and 5, we will utilize POT to reveal information about the final products of thermally induced chemical reactions from a specifically designed precursor molecule on the Cu(111) and Cu(110) surfaces, respectively, focusing on different aspects of the systems.

In Chapter 4, the major reaction product on Cu(111) is a prototypical polycyclic aromatic hydrocarbon – kekulene – that provoked substantial dispute in the scientific community already in the 1970's. The discussion dealt with the ambiguously characterized concept of aromatic stabilization in kekulene, which can be described in two different manners. With our POT results, the molecule's aromatic state is identified from an electronic perspective in contrast to previous scanning tunneling microscopy (STM) studies focusing on geometrical properties [43].

In Chapter 5, we show that the on-surface synthesis of the same precursor molecules on Cu(110) results in three adsorption species - one is planar kekulene and the other two are the same isomeric derivative of kekulene (iso-kekulene) adsorbed in two different nonplanar configurations. Nevertheless, we find that POT is capable of

differentiating between these species on the metal surface and identify iso-kekulene as a major reaction product in agreement with STM results. Contrary to neutral kekulene on Cu(111), we determine charge transfer (CT) of more than two electrons from Cu(110) to the adsorbate.

In Chapter 6, we evaluate the deviation between typical k maps recorded at one incidence angle and k maps fulfilling the ideal $\boldsymbol{\epsilon} \parallel \boldsymbol{k}_f$ condition. This is performed using three systems, namely (i) a quasi zero-dimensional example of smallest delocalized π system benzene/Pd(110), (ii) a well-known organic molecule of typical size used in POT studies (bisanthene/Cu(110)), and (iii) an extended two-dimensional material epitaxial monolayer graphene (EMLG) on SiC(0001). After processing the incidence angle dependent data sets, synthetic $I_{\boldsymbol{\epsilon}\parallel\boldsymbol{k}_f}(k_x, k_y)$ maps are obtained in which the desired $\boldsymbol{\epsilon} \parallel \boldsymbol{k}_f$ condition is fulfilled in the complete k space. Thereby, we find with which experimental incidence angle conventionally recorded k maps and ideal $I_{\boldsymbol{\epsilon}\parallel\boldsymbol{k}_f}(k_x, k_y)$ maps become as similar as possible. This will head to the ideal incidence angle which should be used in the future and reveal if the recorded and investigated k maps in the literature were close to the IAC approximation.

In Chapter 7, we address the issue of reproducing photon-energy-dependent POT results with the PW approximation and show rich POT data sets of EMLG and quasifreestanding monolayer graphene (QFMLG) on $6H$-SiC(0001). In agreement with an earlier photon-energy-dependent POT study and the expectations of experts in the field of photoemission, both extracted photoemission intensity vs. photon energy distributions are genuinely more complex than the simple PW model [42, 44, 45]. To overcome this issue, we employ two theoretical models that give improved final state descriptions, namely time-dependent density functional theory (TDDFT) and a recently-developed simple but powerful model that we term the scattered-wave approximation (SWA). Finally, we are able to reproduce our experimentally-observed intensity modulation and even yield an intuitive physical picture of the photoemission process.

In this thesis, we prove that POT can be successfully applied to a broad range of electronic states including π and σ orbitals. The technique can be used to study a variety of surface materials from quasi zero-dimensional benzene to two-dimensional graphene and even permits to identify chemical states, reaction products of on-surface syntheses, and interactions at interfaces. Nevertheless, the utilized PWA in POT reaches its limits particularly in reproducing photon-energy-dependent POT data. To overcome this issue, higher level theory is consulted. Finally, we on the one hand significantly extend the applicability of POT beyond the limitations given by Puschnig et al. in 2009 [11]. On the other hand, we specify phenomena that cannot be properly explained using the theoretical key element

of POT, the PWA, which requires further theoretical development.

2 | Concepts of Photoemission Orbital Tomography

The viability and extended applicability of the POT technique is in the focus of this work. Therefore, this chapter introduces the basic principles behind the technique starting with PES and ARPES. Finally, the theoretical and experimental details of POT are discussed in more detail. Additionally, the electron analyzer and synchrotron beamline utilized to perform the POT experiments presented in this work are described including the procedure to normalize the experimental measurement data. Note that this chapter targets to inform about specific details of POT needed to understand the presented results of this work but cannot provide a full review of the method.

2.1 Photoelectron spectroscopy

Electronic properties of surfaces and crystals are nowadays routinely studied using PES. The fundamental principle of the method goes back to the 1880's, when Hertz [46] first discovered the photoelectric effect. That an electron is emitted from a solid material as a consequence of the absorption of a photon was explained later in 1905 by Einstein [47] and related to the quantum nature of light. In a typical photoemission experiment, a sample is illuminated by (monochromatic) light with energy $h\nu$, where h is the Planck's constant and ν the photon frequency. If this energy is large enough to overcome the binding energy E_b of the electronic state and the work function of the sample Φ_s (typically 4–5 eV for metals), the electrons can escape into the vacuum in some direction with a residual kinetic energy E_kin. Finally, the emitted electrons traveling through space are detected by an electron spectrometer (analyzer) providing their intensity (photocurrent) as a function of measured E_kin. Applying the principle of energy conservation, one can thus determine E_b of the emitted photoelectron by:

$$E_\mathrm{kin} = h\nu - \Phi_\mathrm{a} - |E_\mathrm{b}| \tag{2.1}$$

using the work function of the analyzer Φ_a (see Eq. 2.2).

In this work, we are interested in the electronic properties of organic molecule/-substrate systems, in particular weakly bound valence levels that participate in chemical bond formation. Using photon energies in the range of 10 eV to 110 eV as typically used in UPS holds several benefits, e.g., a relatively high cross section for excitation. Additionally, a good surface sensitivity is achieved in this energy range considering the mean free path λ of only a few Ångströms [48]. If larger photon energies in a range of 1 keV–10 keV are used, core-electron states are excited or one can look at valence levels with bulk sensitivity (HAXPES). The measurement and analysis of these photoelectrons is employed in x-ray photoelectron spectroscopy (XPS) to reveal the chemical composition of an adsorbate layer. Similar energies are used in the normal-incidence x-ray standing wave (NIXSW) technique to fulfill the condition of Bragg reflection from a crystalline substrate in order to analyze the vertical positions of atoms in molecules. As a result the molecules' adsorption height is revealed and can be directly related to the interaction strength between molecule and substrate. Details about XPS and NIXSW can be found in Refs. [49–52]. UPS and ARPES experiments performed in home laboratories typically utilize He discharge lamps that are restricted to certain photon energies ($h\nu_{\mathrm{He\,I}} = 21.22$ eV, $h\nu_{\mathrm{He\,II}} = 40.81$ eV). In synchrotron facilities, the photon energy can be tuned in a wide range depending on the beamline design. Experimental results presented in this work were acquired at the Metrology Light Source (MLS) insertion device beamline of the Physikalisch-Technische Bundesanstalt (PTB) in Berlin [53] using photon energies between 15 eV to 115 eV. Details about the employed photon flux calibration are described in Section 2.4.6.

In the conversion from E_{kin} to E_{b}, the analyzer work function Φ_{a} has to be considered in Eq. 2.1. The work function Φ is defined as the minimum energy required to remove an electron from a solid into the vacuum far away from the surface. More specifically in the definition by Wandelt [54], Φ is defined by the energetic difference of two states, namely the Fermi level, in which the electron is in the highest occupied level of the neutral ground state, and the electron at rest in infinity (at the absolute vacuum level $E_{\mathrm{vac}}(\infty)$) with the solid singly ionized. In reality, we, however, investigate finite surfaces, where the electron in the second state is localized just outside the solid at $E_{\mathrm{vac}}(\mathrm{s})$. In the measured UP spectrum, electrons stemming originally from the Fermi level can have kinetic energies of as much as $E_{\mathrm{kin}}^{\mathrm{max}}$, while minimum kinetic energy corresponds to either electrons which have just enough energy to escape from the solid or were previously higher energy electrons that have lost their energy via scattering on their way to the surface. Summing up the kinetic energy of the secondary low kinetic energy cut-off ($E_{\mathrm{kin}}^{\mathrm{min}}$) and the photon energy $h\nu$ represents the local vacuum level $E_{\mathrm{vac}}(\mathrm{s})$ of the sample as depicted in Fig. 2.1. Subtracting the energy of the electrons originating from the Fermi level of the sample $E_{\mathrm{kin}}^{\mathrm{max}}$ then results in Φ_{a}.

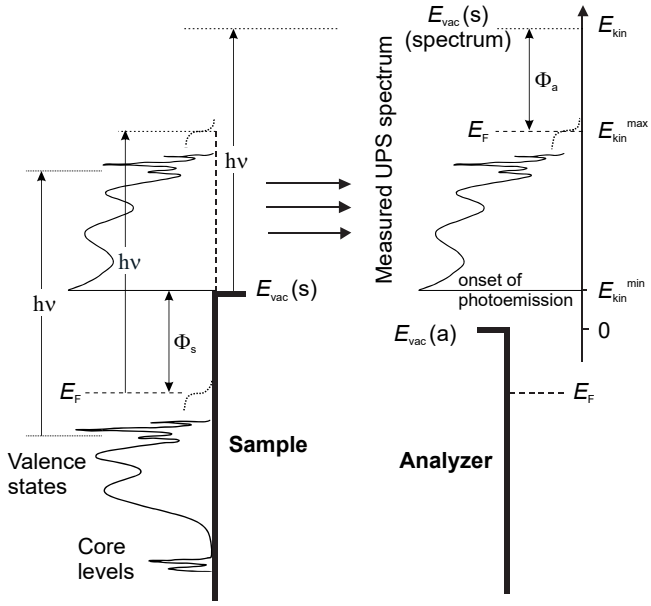

Figure 2.1: Photoemission process and UP spectrum
Left: Core levels and valence states of the sample with the Fermi level E_F. Electrons from the sample are excited by photons with energy $h\nu$ above the vacuum level E_{vac}. Right: Photoexcited electrons are detected by the analyzer with kinetic energy E_{kin}. The position of the vacuum level from the sample to the analyzer is translated by one $h\nu$. Emitted photoelectrons can have kinetic energies of minimum E_{kin}^{min} or maximum E_{kin}^{max}. Adapted from Ref. [55].

Since the work function of the analyzer Φ_a is typically smaller than that of the sample [55, 56], all photoelectrons with E_{kin}^{min} gain kinetic energy before they reach the entrance of the electron analyzer. The energy gain amounts to the difference in work functions of sample and analyzer. The measured E_{kin} at the analyzer therefore has to be corrected by that energy gain according to

$$E_{kin} = h\nu - E_b - \Phi_s + (\Phi_s - \Phi_a) = h\nu - E_b - \Phi_a \tag{2.2}$$

In this work, the energies of photoemitted electrons are either given by their binding energy E_b related to E_F ($E_b = E_F - E_{kin}$) or as $E - E_{vac} = h\nu - E_{kin}$ [1].

[1] $E - E_{vac} = h\nu - E_{kin}$ was used, if the calibration of E_F was ambiguous.

2.2 Photoemission differential cross section

That a photoelectron is emitted from its single-particle initial state i with wave vector $\boldsymbol{k}_f$ has a particular probability per unit time (or transition rate) $W_{i,\boldsymbol{k}_f}$ that is described in detail in Ref. [AH12]. Within the sudden approximation of the one-step model of photoemission, this probability is given by Fermi's golden rule:

$$\begin{aligned} W_{i,\boldsymbol{k}_f} &= \frac{2\pi}{\hbar}\left|\left\langle\psi_{\boldsymbol{k}_f}|\frac{e}{m}\boldsymbol{A}\cdot\hat{\boldsymbol{p}}|\psi_i\right\rangle\right|^2\delta\left(\varepsilon_i-\varepsilon_{\boldsymbol{k}_f}-\Phi+h\nu\right) \\ &= \frac{2\pi e^2\hbar|A_0|^2}{m^2}\left|\left\langle\psi_{\boldsymbol{k}_f}|\boldsymbol{\epsilon}\cdot\nabla|\psi_i\right\rangle\right|^2\delta\left(\varepsilon_i-\varepsilon_{\boldsymbol{k}_f}-\Phi+h\nu\right), \end{aligned} \tag{2.3}$$

Herein, $|\psi_i\rangle$ is the initial (bound) state vector with energy $\varepsilon_i < 0$, $|\psi_{\boldsymbol{k}_f}\rangle$ is the final (unbound) state vector with kinetic energy $E_{\mathrm{kin}} = \varepsilon_{\boldsymbol{k}_f}$, and $\Phi > 0$ is the work function. The photon field is characterized by the vector potential $\boldsymbol{A}$ and the polarization vector $\boldsymbol{\epsilon}$. $\hat{\boldsymbol{p}}$ is the momentum operator of the (photo)electron, and e and m are the electron's charge and mass, respectively. The perturbing operator $\boldsymbol{A}\cdot\hat{\boldsymbol{p}}$ arises from the minimal coupling principle by taking into account that the momentum operator commutes with the vector potential in the Coulomb gauge.

If photoelectrons with kinetic energy $E_{\mathrm{kin}} = \hbar^2k_f^2/2m$ emitted from initial state i into any direction $\Omega_{\boldsymbol{k}_f} = (\theta,\phi)$ are considered, the probability per unit time evolves into P_{i,k_f} which can be calculated as

$$P_{i,k_f} = \frac{1}{v_{\boldsymbol{k}_f}}\int_{|\boldsymbol{k}'_f|=k_f} d^3\boldsymbol{k}'_f W_{i,\boldsymbol{k}'_f}, \tag{2.4}$$

where $v_{\boldsymbol{k}_f} = (2\pi)^3/V$ is the $\boldsymbol{k}_f$-space volume per $\boldsymbol{k}_f$ vector. V is the (illuminated) real-space volume of the sample, in which $\int_V \psi^*_{\boldsymbol{k}_f}\psi_{\boldsymbol{k}_f}d^3\boldsymbol{r} = 1$. Note that for a given initial state ψ_i with energy ε_i and due to energy conservation enforced by the delta function in Eq. 2.3, the integration in Eq. 2.4 projects out the angular dependence at a fixed absolute value k_f, i.e., kinetic energy as described in Ref. [11]. Using Eq. 2.3, this becomes

$$\begin{aligned} P_{i,k_f} &= \frac{V}{(2\pi)^2}\frac{e^2\hbar|A_0|^2}{m^2}\int_{2\pi}d\Omega_{\boldsymbol{k}'_f}\int {k'_f}^2dk'_f\left|\left\langle\psi_{\boldsymbol{k}'_f}\left|\boldsymbol{\epsilon}\cdot\nabla\right|\psi_i\right\rangle\right|^2\times\delta(k'_f-k_f)\frac{1}{|s'(k_f)|} \\ &= \frac{V}{(2\pi)^2}\frac{e^2|A_0|^2k_f}{\hbar m}\int_{2\pi}d\Omega_{\boldsymbol{k}_f}\left|\left\langle\psi_{\boldsymbol{k}_f}\left|\boldsymbol{\epsilon}\cdot\nabla\right|\psi_i\right\rangle\right|^2 \end{aligned} \tag{2.5}$$

where $s(k_f') \equiv \varepsilon_i - \hbar {k_f'}^2/2m - \Phi + h\nu$.

The total cross section σ_{i,k_f} of the photoemission process from initial state i is related to P_{i,k_f} by

$$\frac{\sigma_{i,k_f}}{A_\square} \equiv n_{i,k_f} = P_{i,k_f}\Delta t, \tag{2.6}$$

where $A_\square$ is the illuminated area on the sample and n_{i,k_f} is the fraction of emitted photoelectrons per photon hitting the area $A_\square$ in the time interval Δt. $A_\square$ is given by $V_{\mathrm{ph}}/(c\Delta t)$, where V_{ph} is the volume, in which the energy of the photon field amounts to $h\nu$ and c the velocity of light.

The differential cross section is thus given by

$$\frac{d\sigma_{i,k_f}}{d\Omega} = \frac{V_{\mathrm{ph}}}{c}\frac{dP_{i,k_f}}{d\Omega} \tag{2.7}$$

after differentiation with respect to the solid angle Ω. It is important to note here that the differential cross section is a function of k_f, $\Omega = (\theta, \phi)$, the photon energy $h\nu$ (which selects possible initial states i according to their orbital energies ε_i, because of the delta function in Eq. 2.14), and light polarization $\boldsymbol{\epsilon}$. Therefore, we write $\frac{d\sigma}{d\Omega}(k_f, \Omega_{\boldsymbol{k}_f}; h\nu, \boldsymbol{\epsilon})$ from now on.

In a next step, we normalize the light field to the energy of one photon in the volume V_{ph}, which consequently fixes the amplitude A_0 of the vector field to

$$|A_0|^2 = \frac{\hbar}{\pi V_{\mathrm{ph}}\epsilon_0\nu}. \tag{2.8}$$

As a result, the differential cross section is converted by using Eqs. 2.5 and 2.7 to

$$\frac{d\sigma}{d\Omega}(k_f, \Omega_{\boldsymbol{k}_f}; h\nu, \boldsymbol{\epsilon}) = \frac{d\sigma_{i,k_f}}{d\Omega} = \frac{V}{4\pi^3}\frac{e^2 k_f}{cm\epsilon_0\nu}\left|\left\langle \psi_{\boldsymbol{k}_f} \left| \boldsymbol{\epsilon}\cdot\nabla \right| \psi_i \right\rangle\right|^2 \tag{2.9}$$

where we have also summed over all initial states i, taking into account a factor of 2 due to the spin degeneracy of the electron.

To correlate this differential cross section with our experimental data, we first figure out which intensities we actually measure at the analyzer. The photoelectron intensity $I(k_f, \Omega_{\boldsymbol{k}_f}; h\nu, \boldsymbol{\epsilon})$ measured at the analyzer originates from the photoemitted electrons from the area $A_\square$ on the sample which contains N photoemitters.

The calibrated beamline produces a known monochromatic photon flux $F_{\mathrm{ph}}(h\nu, \boldsymbol{\epsilon})$, yielding a photon intensity $I_{\mathrm{ph}}(h\nu, \boldsymbol{\epsilon}) = F(h\nu, \boldsymbol{\epsilon})A_\square$ on the area $A_\square$ from which

photoelectrons are detected with efficiency $\chi(k_f)$. If the photoemission data are obtained at a carefully calibrated beamline the photoelectron intensity is given by

$$I(k_f, \Omega_{\boldsymbol{k}_f}; h\nu, \boldsymbol{\epsilon}) = \chi(k_f)\, I_{\mathrm{ph}}(h\nu, \boldsymbol{\epsilon})\, N\, \frac{\frac{d\sigma}{d\Omega}(k_f, \Omega_{\boldsymbol{k}_f}; h\nu, \boldsymbol{\epsilon})}{A_{\square}}\, \Delta\Omega. \tag{2.10}$$

Thus, the intensity ratio $I(k_f, \Omega_{\boldsymbol{k}_f}; h\nu, \boldsymbol{\epsilon})/I_{\mathrm{ph}}(h\nu, \boldsymbol{\epsilon})$, if obtained at a carefully calibrated beamline with a carefully characterized linear response $\chi(k_f)$ of the analyzer, is a direct measure of the differential photoemission cross section. If we assume that the volume density of the photoemitters in the sample is ϱ, we can replace the ratio $N/A_{\square}$ in the above equation by ϱd, where d is the effective sampling depth. The relation in Eq. 2.10 in utilized in Chapter 7 to obtain photoemission cross sections from experimental POT data. The preliminary explanations and equation about the photoemission differential cross section are part of the respective journal article [AH12].

2.3 Angle-resolved photoemission spectroscopy

As a result of the photoelectric effect, electrons leave the sample and travel along different directions through vacuum with particular velocities, i.e., kinetic energies E_{kin}. If the directions of the photoelectrons are precisely detected, as in ARPES, it is possible to study the momentum-dependent electronic properties, e.g., the band structure of solids. In general, the wave vector or momentum $\boldsymbol{k_f} = \boldsymbol{p}/\hbar$ describes the wave vector of the photoelectron outside the crystal in the vacuum. Its modulus can be determined by $k_f = \sqrt{2m_{\mathrm{e}}E_{\mathrm{kin}}}/\hbar$, in which m_{e} is the mass of the electron. The vector $\boldsymbol{k_f}$ can be split into its parallel and perpendicular (to the surface) components $\boldsymbol{k}_{\parallel}$ and $\boldsymbol{k}_{\perp}$, respectively [57].

When an electron passes through an ordered surface, the component parallel to the surface is conserved due to translational symmetry and can be determined from the polar (θ) emission angle of the photoelectrons defined in the experimental geometry visualized in Fig. 2.2.

$$k_{\parallel} = \frac{\sqrt{2m_{\mathrm{e}}E_{\mathrm{kin}}}}{\hbar} \cdot sin(\theta) \tag{2.11}$$

The $k_{\parallel}$ range obtained in a measurement is, however, limited by the finite θ acceptance angle defined by the design of the particular measurement system. The

typical acceptance angle of common hemispherical analyzers is limited to up to ± 15° [58, 59]. A broader range has been demonstrated as well (EW 4000 Scienta [60] and ASTRAIOS 190 2D-CMOS (± 30°) [61]). Note that a popular instrument in the 1970's had an angular accpetance of ± 4° [8].

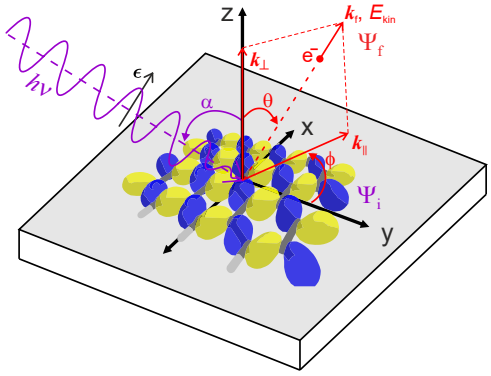

Figure 2.2: Experimental geometry of PE experiments
Excitation and emission of electrons from an initial molecular state ψ_i with incident p polarized photon beam with energy $h\nu$, incidence angle α (purple color), and polarization vector $\boldsymbol{\epsilon}$. Emitted photoelectrons in the final state ψ_f are characterized by their kinetic energy E_{kin} and the polar and azimuthal emission angles θ and ϕ, respectively. The consequential momentum vector $\boldsymbol{k}_f$ can be divided into two components parallel and perpendicular to the sample surface $\boldsymbol{k}_\parallel$ and $\boldsymbol{k}_\perp$, respectively.

The largest acceptance angle ranges are provided by the toroidal electron analyzer (TEA) (± 85°) [62] or photoemission electron microscopy (PEEM)-based systems [63–65] using specially designed electron lenses. The measurement of ARPES band maps with a large $k_\parallel$ range correspondingly may require to tilt the sample if the analyzer has an insufficiently large acceptance angle or to use higher excitation energies. The latter would, however, lead to stronger substrate contributions in the photoemission signal that may cover emission from the adsorbate under investigation.

In a cartesian coordinate system with the z-axis along the sample normal, $\boldsymbol{k_z} = \boldsymbol{k}_\perp$, while $\boldsymbol{k}_\parallel$ can be split into the two components $\boldsymbol{k_x}$ and $\boldsymbol{k_y}$, where x and y can be chosen to be, e.g., along high symmetry directions of the surface. Plotting the photoemission intensity against k_x and k_y at a constant E_{kin} results in so-called

k maps of photoemission. The interpretation of these experimental k maps is only adequately possible if theoretical simulations are consulted. The combination of those experimental photoemission data with sophisticated simulations lead to the development of POT which will be explained in the following.

2.4 Photoemission orbital tomography

The electronic properties of the investigated interfaces in this work are studied within the framework of POT – a combined experimental and theoretical approach introduced in 2009/2011 by P. Puschnig et al. to "characterize discrete orbitals of large π-conjugated molecules" [11, 16]. In POT, conventional ARPES data are presented and interpreted in a specific way, which allows to extract additional information. Namely, instead of band maps, where the photoemission intensity is presented as a function of energy and momentum parallel to the surface, so-called k maps are presented $I(k_x,\ k_y)$. These quantify the photoelectron momentum distributions that can be related to spatial distributions of initial state orbitals.

Technically, this is done by transforming the raw angle-resolved photoemission data $I(E_{\mathrm{kin}},\ \theta,\ \phi)$ into reciprocal-space coordinates resulting in a three-dimensional ARPES data cube $I(E_{\mathrm{kin}},\ k_x,\ k_y)$, where k_x and k_y are components of $\boldsymbol{k}_{\parallel}$. The experimental photoemission data recorded at one specific E_{kin} then give a two-dimensional intensity distribution – the k map.

To interpret experimental photoemission data, it is crucial to evaluate how and to which quantity accessible by simulations, they can and should be related to gain valuable information.

From Section 2.2, we know that the ratio of intensities I/I_{ph} is a direct measure of the differential cross section. Therein, I is the photoemission intensity measured at the analyzer originating from the photoemitted electrons from the area $A_{\square}$ on the sample and I_{ph} is the photoemission intensity produced by the beamline. The differential photoemission cross section $d\sigma/d\Omega(k_f, \Omega; h\nu, \boldsymbol{\epsilon})$ describes the probability to detect a photoelectron of kinetic energy E_{kin} and wave vector $\boldsymbol{k}_f$ at a solid angle $\Omega = (\theta, \phi)$ with the polar and azimuthal angles θ and ϕ, respectively, after illumination with photons of energy $h\nu$ and polarization vector $\boldsymbol{\epsilon}$.

The photo-excitation is treated as one single coherent event during which an electron is transferred from its initial state i with wave function ψ_{i} to a final state f with wave function ψ_{f}. This is commonly referred to as *one-step model of photoemission* (PE) [57, 66–69] which is the more realistic, yet also more complex approach in comparison to the three-step model [68, 70, 71]. Within the one-step model, the *sudden approximation* states that the system instantaneously responses

to the photoexcitation, i.e., the creation of the photohole. The remaining (N-1)-electron system thus does not interact with the emitted photoelectron [48].

In consequence of the sudden approximation within the one-step model, the probability per unit time (or transition rate) $W_{i,\boldsymbol{k}_f}$ that a photoelectron with wave vector $\boldsymbol{k}_f$ is emitted from the one particle initial state i is given by Fermi's golden rule

$$W_{i,\boldsymbol{k}_f} = \frac{2\pi}{\hbar}\left|\left\langle\psi_{\boldsymbol{k}_f}\left|H_{\mathrm{int}}\right|\psi_i\right\rangle\right|^2\delta\left(\varepsilon_i-\varepsilon_{\boldsymbol{k}_f}-\Phi+h\nu\right) \tag{2.12}$$

Therein, $|\psi_i\rangle$ is the initial (bound) state vector with energy $\varepsilon_i<0$ and $|\psi_{\boldsymbol{k}_f}\rangle$ is the final (unbound) state vector. The energy conservation during the photoemission process is preserved by the δ-function with kinetic energy $E_{\mathrm{kin}}=\varepsilon_{\boldsymbol{k}_f}$, and $\Phi>0$ as the work function. The interaction of the N-electron ground state with the photon is treated as a perturbation given by

$$H_{\mathrm{int}}=\frac{e}{2mc}(\boldsymbol{A}\hat{\boldsymbol{p}}+\hat{\boldsymbol{p}}\boldsymbol{A})+\frac{e^2}{2mc^2}\boldsymbol{A}\boldsymbol{A}\approx\frac{e}{mc}\boldsymbol{A}\hat{\boldsymbol{p}} \tag{2.13}$$

taking the electron momentum operator $\hat{\boldsymbol{p}}$ and the vector potential of the photon field $\boldsymbol{A}$ into account. e and m are the electron's charge and mass, respectively. The perturbation can be simplified by neglecting the quadratic term in $\boldsymbol{A}$ ($\boldsymbol{A}^2\approx 0$) as it describes two-photon processes. Additionally, we use the Coulomb gauge ($\nabla\cdot\boldsymbol{A}=0$) and set $\boldsymbol{A}$ as a constant $\boldsymbol{A}=\boldsymbol{A}_0$ (*dipole approximation*), because with the used photon energies the wavelength of the photon beam is considerably larger than interatomic distances [48, 49].

Fermi's rule (Eq. 2.12) can thus be rewritten as:

$$W_{i,\boldsymbol{k}_f} = \frac{2\pi}{\hbar}\left|\left\langle\psi_{\boldsymbol{k}_f}\left|\frac{e}{mc}\boldsymbol{A}_0\cdot\boldsymbol{p}\right|\psi_i\right\rangle\right|^2\delta\left(\varepsilon_i-\varepsilon_{\boldsymbol{k}_f}-\Phi+h\nu\right) \tag{2.14}$$

with $\boldsymbol{p}=\frac{\hbar}{i}\vec{\nabla}$. Using the polarization vector $\boldsymbol{\epsilon}$ (assumed to be constant in space) [30] instead of the vector potential of the photon field and that the normalization of the light field to the energy of one photon in the volume V_{ph} fixes the amplitude A_0 of the vector field, changes the probability per unit time for a photoelectron to be emitted to:

$$W_{i,\boldsymbol{k}_f} = \frac{2\pi e^2\hbar|A_0|^2}{m^2}\left|\left\langle\psi_{\boldsymbol{k}_f}\left|\boldsymbol{\epsilon}\cdot\nabla\right|\psi_i\right\rangle\right|^2\delta\left(\varepsilon_i-\varepsilon_{\boldsymbol{k}_f}-\Phi+h\nu\right) \tag{2.15}$$

with

$$|A_0|^2 = \frac{\hbar}{\pi V_{\mathrm{ph}} \epsilon_0 \nu}. \tag{2.16}$$

Bringing together the matrix element

$$M_{\boldsymbol{k}_f,i} = \left\langle \psi_{\boldsymbol{k}_f} | \boldsymbol{\epsilon} \cdot \boldsymbol{\nabla} | \psi_i \right\rangle. \tag{2.17}$$

and the relation of $d\sigma_{i,k_f}/d\Omega$ in Eq.2.9, we find that $d\sigma_{i,k_f}/d\Omega \propto |\boldsymbol{M}_{\boldsymbol{k}_f,i}|^2$.

Considering that the measured photoemission intensity is proportional to $d\sigma/d\Omega(k_f, \Omega; h\nu, \boldsymbol{\epsilon})$ (Eq. 2.10) as discussed in Section 2.2, we finally conclude that

$$I(k_f, \Omega; h\nu, \boldsymbol{\epsilon}) \propto |M_{\boldsymbol{k}_f,\boldsymbol{k}}|^2. \tag{2.18}$$

Since this matrix element is dependent on the one-particle initial (ψ_i) and final states ($\psi_{\boldsymbol{k}_f}$), as well as on the polarization of the incoming photon field, it strongly modulates the photoemission cross section beyond the spectral function and thus provides rich information regarding the initial-state wave functions [11, 30]. Therefore, we are particularly interested in the description of the matrix element $\boldsymbol{M}_{\boldsymbol{k}_f,i}$.

As soon as effects in the angular distribution of photoemitted electrons were noted theoretically [66, 72]and observed experimentally in the early 1970's [73–75], it was clear that "a complete theory must properly treat both the initial and final states on an equal footing" [4]. This, however, quickly developed into a pursuit of a correct description of the final state, since "the essential ingredient of our microscopic one-step model for the photoemission process lies in the description of the final state" [5]. To this end, the simple PWA was discussed [4–6, 8, 68, 76–78], which at first glance appears reasonable, because the superposition of multiple spherical wavelets results in a wave-front that can indeed be described as a PW according to the Huygens-Fresnel principle. Therefore, it was hoped to unravel the unique potential of the combined experimental and theoretical photoemission approach [7]. The results of the PWA [79] were, however, found to be "qualitatively wrong" [80] and finally it was pointed out that "the plane-wave final state at UPS energies is to crude to expect detailed quantitative agreement" [8]. The simulation of the photoemission process has been refined over the last 50 years improving the applicability of the PWA. How is it used in the modern POT technique, is described in the following section.

2.4.1 Plane wave final state approximation

If the final state of photoemission is approximated as a simple PW [11], the matrix element becomes proportional to the Fourier transform (FT) of the initial state times a momentum-dependent pre-factor:

$$M^2_{\boldsymbol{k}_f,\boldsymbol{k}} \propto \boldsymbol{\epsilon} \cdot \boldsymbol{k}_f \times \widetilde{\psi}_i(\boldsymbol{r})(\boldsymbol{k}_f). \tag{2.19}$$

This describes a direct relation between the photoemission intensity measured at a particular E_{kin} from a given initial state i and the FT of the initial state wave function ψ_{i} apart from a correction using the polarization factor $\boldsymbol{\epsilon} \cdot \boldsymbol{k}_f$:

$$I_i(\theta, \phi) \propto (\boldsymbol{\epsilon} \cdot \boldsymbol{k}_f)^2 |\widetilde{\psi}_i(\boldsymbol{r})(\boldsymbol{k}_f)|^2 \tag{2.20}$$

This allows a one-to-one correlation between individual molecular orbitals provided by, e.g., an appropriate level of theory in the simulation and the experimentally measured k maps.

The procedure to relate calculated real-space orbitals with experimentally measured k maps is depicted in Fig. 2.3 exemplary for a π orbital of bisanthene. First, the initial state WF $\psi_{\mathrm{i}}(x, y, z)$ of the respective orbital is calculated by density functional theory (DFT) calculations of the free molecule. Fig. 2.3**a** shows a real-space representation of a π orbital that is built out of p_{z} orbitals with electron density located above and below the molecular plane with a node in the plane of the molecule. The three-dimensional FT of $\psi_{\mathrm{i}}(x, y, z)$ leads to $\widetilde{\psi}_i(\boldsymbol{r})(\boldsymbol{k}_f)$ (Fig. 2.3**b**). To be able to compare the experimental k maps recorded at a constant E_{kin}, the FT of the orbital has to be evaluated on a hemispherical cut with constant radius $k_f = \sqrt{2m_e\ E_{\mathrm{kin}}/\hbar^2}$ indicated by the red dome (Ewald sphere) in Fig. 2.3 **b**. The $\widetilde{\psi}_i(\boldsymbol{r})$ distribution at the hemisphere is then projected onto the (k_x, k_y) plane, and modulus squared, resulting in the intensity distribution shown in Fig. 2.3 **c** as a function of momentum components k_x and k_y.

For atomic $2p_z$ orbitals with quantum numbers $\{nlm\} = \{210\}$, the analytic form of the FT in the PW final state prediction can be written as follows [22]:

$$\widetilde{\psi}_{p_z}(\mathbf{r})(k, \theta_k) = \widetilde{\psi}_{210}(k, \theta_k)] = \sqrt{8\pi i} \left(\frac{Z}{a_{\mathrm{B}}}\right)^{\frac{7}{2}} \frac{k}{\left(k^2 + \frac{Z^2}{4a_{\mathrm{B}}^2}\right)^3} \cos\theta_k \tag{2.21}$$

Here, k and θ_k are the length and the polar angle of the wave vector $\boldsymbol{k}$, Z the nuclear charge, and a_{B} the Bohr radius.

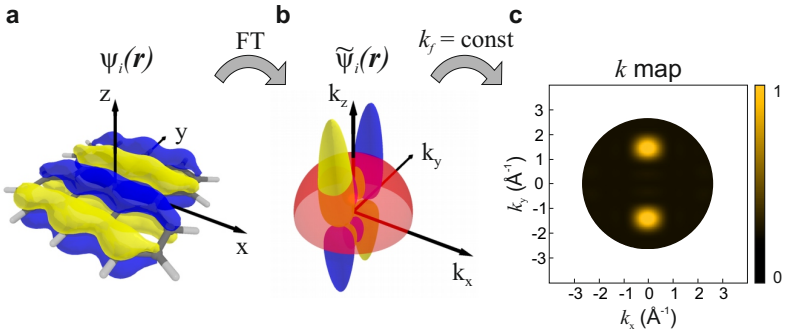

Figure 2.3: Theoretical k maps from real-space π orbitals distribution Exemplary procedure to produce k maps from real-space orbitals of bisanthene. **a** Real-space $\psi_{\mathrm{i}}(\boldsymbol{r})$ representation. The 3D FT of $\psi_{\mathrm{i}}(x, y, z)$ leads to **b** the k space representation of the orbital $\widetilde{\psi}_i(\boldsymbol{r})(\boldsymbol{k}_f)$. A hemispherical cut (red) at constant $E_{\mathrm{kin}} = 30$ eV, i.e., $k_f = \sqrt{2m_e E_{\mathrm{kin}}/\hbar^2}$ multiplied with the polarization factor leads to the **c** photoemission intensity I_{i} (k_x, k_y), the k map. Note the perspective projection in panels **a** and **b**.

Z is only dependent on the investigated atom type, while a_{B} is constant. Therefore one can abbreviate $k_0 = \frac{Z}{2a_{\mathrm{B}}}$. In combination with $\cos\theta_k = k_{\mathrm{z}}/k$ and a second fit parameter a_0, Eq. 2.21 can be reduced to:

$$\widetilde{\psi}_{p_{\mathrm{z}}}(\mathbf{r})(k_{\mathrm{z}}, \theta_k) = a_0^2 \frac{k_{\mathrm{z}}}{(k^2 + k_0^2)^3} \tag{2.22}$$

If normal emission ($\theta_k = 0$) is assumed, this function has a specific form. For $\mathrm{k_z} \to 0$, it rises as $\sim \frac{k_{\mathrm{z}}}{k_0^6}$, peaks at $k_{\mathrm{max}} = \frac{k_0}{\sqrt{5}}$, and decreases again for $\mathrm{k_z} \to \infty$ proportional to k_{z}^{-5}. The PW final state prediction of π states, correspondingly, forecasts one peak when plotting $\widetilde{\psi}_{p_{\mathrm{z}}}(\mathbf{r})(k_{\mathrm{z}})$ versus k_{z} [22].

This relation ($\widetilde{\psi}_{p_{\mathrm{z}}}(\mathbf{r})(k_{\mathrm{z}})$ *vs.* k_{z}) has been compared to experimental data for the highest occupied molecules orbital (HOMO) and lowest unoccupied molecular orbital (LUMO) of 3,4,9,10-perylene tetracarboxylic dianhydride (PTCDA) on Ag(110) by Weiss et al. [22]. To this end, Eq. 2.20 is employed, where $\boldsymbol{k}_f$ is replaced by k_{z} and the polarization factor is calculated by

$$|\boldsymbol{\epsilon} \cdot \boldsymbol{k}_f| = |\boldsymbol{\epsilon}||\boldsymbol{k}_f| \cos(\angle(\boldsymbol{\epsilon}, \boldsymbol{k}_f)) \propto \sqrt{E_{\mathrm{kin}}} \cdot \cos(\theta + \alpha - 90°). \tag{2.23}$$

The experimental E_{kin} are converted into k_{z} using $k = \frac{2m_e E_{\mathrm{kin}}}{\hbar^2}$ and Pythagorean $k_{\mathrm{z}} = \sqrt{k^2 - k_{\parallel}^2}$ [22], where $k_{\parallel}$ is defined by the position of the photoemission feature under investigation. Since the experimental intensities are divided by the polarization factor, which includes E_{kin}, the experimental intensities are diminished with increasing E_{kin}. Nevertheless, the experimentally-observed photoemission intensity distribution presented in Ref. [22] was not captured by the simple PW approximation.

The discrepancies of experimental photoemission data and the results of the calculations based on the PW final state can be tackled in different ways. We pursue two approaches in this work. First, we keep the PW final state but measure POT of different π systems in specially-designed experimental geometries in order to bring the experimental results mathematically closer to the PW prediction. The underlying ideas are explained in Section 2.4.2 and the results are shown in Chapter 6. In the second approach, we consult more sophisticated models for the final state. Namely, the scattered-wave approximation (SWA), which allows for interference of partial Coulomb waves with different orbital angular momenta emitted from each atom. Additionally, we consult time dependent density functional theory (TDDFT) which adequately describes the photoelectron excitation process. We use both methods and the PWA to describe the photoemission cross section of graphene [AH12]. Mathematical descriptions behind the SWA model that were developed further by S. Moser (Universität Würzburg) are presented in Section 2.4.3.The results are published in Ref. [AH12] and shown in Chapter 7.

2.4.2 Independent atomic center approximation

The discrepancies of experimental photoemission data and the results of the calculations based on the PW final state were observed about 50 years ago when angle-resolved photoemission intensities were first related to the PW final state description [4–6, 8, 68, 76–78]. Some authors realized that the PW based calculations did not correctly describe experimental results for large organic molecules on metal surfaces (lead-phthalocyanine/Cu(110)) [10]. Richardson [81] recalculated the observed angular ARPES distribution using spherical harmonics expansions for the final state and claimed to find a better agreement with the experimental data. His "point emitter model" was also used to approximate the angle resolved ultraviolet photoelectron spectroscopy (ARUPS) results of benzene/Pd(100) [82] and pyridine/Cu(110) [83]. However, it was soon recognized that approximating a molecule as a single-point emitter is too simplified for large, complex organic molecules.

Since that time, the critical discussion about the applicability of the PW final

state approximation continued in the photoemission and surface science communities [13, 84–88]. To achieve a physically more correct final state description, Grobman [41] developed the independent atomic center (IAC) approximation in 1978, which describes the photoemission amplitudes from individual atomic centers from oriented molecules. The IAC approximation was successfully combined with molecular orbital calculations (IAC/MO) and single-scattering (SS) approximations to analyze quantitative photoelectron angular distributions in the group of N. Ueno at the University of Chiba [13, 84, 85, 89–92].

Puschnig et al. [11] showed in 2009 that the PWA based calculation describes the photoemission from frontier π orbitals of organic molecules quantitatively adequate in a broad k space range. They also noted that the IAC and PW approximations become mathematically equivalent if particular conditions are fulfilled, namely if atomic orbitals of the same chemical and orbital character are investigated in an experimental geometry where the polarization vector of the incident photon beam $\boldsymbol{\epsilon}$ and the wave vector of the emitted photoelectron in the final state $\boldsymbol{k}_f$ are parallel. The photoelectron wave function A is then directly related to the measured photoemission intensity ($I \propto |A(\boldsymbol{R}, E_{\text{kin}})|^2$) as will be shown in the following.

In the early description of the IAC approximation by Grobman [41], the total photoemission amplitude $\mathrm{A}(\boldsymbol{R}, \epsilon)$ of final state energy $E_k = \frac{\hbar^2}{2m}k^2$ at a detector at the position $\boldsymbol{R}$ is calculated. With kinetic energy E_{kin}, the IAC expression for the photoelectron wave function $A(\boldsymbol{R}, E_{\text{kin}})$ can be written as follows:

$$A(\boldsymbol{R}, E_{\text{kin}}) = \sum_{\alpha} \sum_{nml} C_{\alpha,nml} e^{i\boldsymbol{k}\boldsymbol{R}_\alpha} \sum_{LM} M^{LM}_{\alpha,nml}(E_{\text{kin}}) Y^M_L(\hat{R}) \tag{2.24}$$

Here, the initial wave function is treated as an atomic orbital ϕ_α centered at the position $\boldsymbol{R}_\alpha$. If the photoemission from a molecular orbital is considered, a linear combination of atomic orbitals $\phi_{\alpha,nml}$ is used to describe its initial state $\psi_i(\boldsymbol{r})$, where nml represent the principal and angular-momentum quantum numbers of the atomic orbitals and α the atomic center on which $\psi_i(\boldsymbol{r})$ resides [11],

$$\psi_i(\boldsymbol{r}) = \sum_{\alpha} \sum_{nlm} C_{\alpha,nlm} \phi_{\alpha,nlm}(\boldsymbol{r} - \boldsymbol{R}_\alpha) \tag{2.25}$$

The sum over the final state angular-momentum quantum numbers LM represents the atomic factor, where the matrix elements are dipole matrix elements between the atomic wave functions $\phi_{\alpha,nml}$ and solutions of the Schrödinger equation in an atomic potential at the energy E_{kin} and angular momentum LM.

In the 1990's, the IAC approximation was applied to various systems in the group of N. Ueno at the University of Chiba. Extended by single scattering theory combined with molecular orbital (MO) calculations, the authors performed quantitative analyses of photoelectron angular distribution to reveal the molecular orientation of thin films of functional organic molecules. This included for example sexiphenyl on Ag/Cu films [90] and naphthacene on highly oriented pyrolytic graphite (HOPG) [89] with π states solely composed of C $2p_z$ orbitals. Importantly, successful simulations were also obtained for larger molecules such as bis(1,2,5-thiadiazolo)-*p*-quinobis(1,3)-dithiole (BTQBT) [85, 92] on MoS_2 with an extended π electron system composed of C, N, and S on HOPG. Additionally, Cu-phthalocyanine (CuPc, Cu-$C_{32}H_{16}N_8$) and H_2Pc with atomic C $2p_z$ and N $2p_z$ orbitals were investigated on cleaved MoS_2 [91].

It is crucial to note that the IAC simulations were successful for molecular orbitals composed of different chemical and orbital characters. Because already in 1978, Grobman [41] realized that Eq. 2.24 can be simplified if the initial molecular orbital consists of atomic orbitals of the same chemical and orbital character. This is, e.g., fulfilled for π orbitals of planar polyatomic molecules as studied in this work. In this case, the coefficients $C_{\alpha,nlm}$ in Eq. 2.24 only become non-zero for atomic p_z orbitals leading to

$$A(\boldsymbol{R}, E_{\mathrm{kin}}) = \sum_{\alpha} C_{\alpha,2p_z} e^{i\boldsymbol{k}\boldsymbol{R}_\alpha} \sum_{LM} M^{LM}_{2p_z}(E_{\mathrm{kin}}) Y^M_L(\hat{R}) \tag{2.26}$$

If only $2p_z$ orbitals are assumed for all contributing atoms, only the type of the atomic orbital is decisive. Additionally, one can omit the individual positions of the atoms α in the transition matrix elements. The atomic factor in Eq. 2.26 can thus be abbreviated as

$$N_{2p_z}(E_{\mathrm{kin}}, \hat{R}) = \sum_{LM} M^{LM}_{2p_z}(E_{\mathrm{kin}}) Y_{LM}(\hat{R}) \tag{2.27}$$

and put in front of the summation over α resulting in a simplified expression for the photoemission amplitude at the detector for explicitly π states:

$$A(\boldsymbol{R}, E_{\mathrm{kin}}) = N_{2p_z}(E_{\mathrm{kin}}, \hat{R}) \sum_{\alpha} C_{\alpha,2p_z} e^{i\boldsymbol{k}\boldsymbol{R}_\alpha} \tag{2.28}$$

Therein, the atomic factor $N_{2p_z}(E_{\mathrm{kin}}, \hat{R})$ only acts as a weakly varying envelope function as has been already noted by Grobman [41]. The last term, which is closely related to the FT of the initial molecular orbital, produces the main angular

dependence of the photoemission intensity. This can be easily recognized by taking the FT on both sides of Eq. 2.25

$$\widetilde{\phi}(\boldsymbol{k}) = \widetilde{\psi}_{2p_z}(\boldsymbol{k}) \sum_{\alpha} C_{\alpha,2p_z} e^{i\boldsymbol{k}\boldsymbol{R}_\alpha} \tag{2.29}$$

in which $\widetilde{\psi}_{2p_z}(\boldsymbol{k})$ is the FT of a p_z orbital with its angular part simply given by the spherical harmonic, $Y_{10}(\theta, \phi) \propto \cos\theta$ [4]. Combining Eqs. 2.28 and 2.28, we get

$$A(\boldsymbol{R}, E_{\text{kin}}) = \frac{N_{2p_z}(E_{\text{kin}}, \hat{R})}{\bar{\psi}_{2p_z}(\boldsymbol{k})} \times \widetilde{\phi}(\boldsymbol{k}) \tag{2.30}$$

which is very similar to the PW final state (Eq. 2.20), if the initial molecular orbital is composed of atomic orbitals of the same type, e.g., planar π conjugated molecules.

According to Grobman [41], a further simplification can be introduced if the geometry of molecule (sample), energy analyzer, and light polarization are chosen appropriately. Namely, the polarization vector of the photom beam $\boldsymbol{\epsilon}$ should be perpendicular to the molecular plane. Then, the prefactor $N_{2p_z}/\widetilde{\phi}_{2p_z}$ can be shown to become completely independent of the emission direction (θ, ϕ). This was likewise described by Goldberg et al. [78] who formulated that there are cases in which the exact photoemission cross sections from atoms are identical to calculations based on the PW if the polarization vector $\boldsymbol{\epsilon}$ is parallel to the wave vector $\boldsymbol{k}_f$ of the emitted photoelectrons. In this particular geometry, the photoemission intensity resulting from the IAC, which is the square of $A(\boldsymbol{R}; E_{\text{kin}})$, reduces exactly to the intensity emerging from the plane wave final state assumption. In 2015, Bradshaw and Woodruff [42] suggested to perform a control experiment, where the photoelectrons are always measured in the direction of the polarization vector of the incidence light. Using such experimental test measurements in the $\boldsymbol{\epsilon} \parallel \boldsymbol{k}_f$ geometry, it would be possible to evaluate the influence and importance of the spherical wave character of the initial outgoing photoelectron wavefield. Results of such experimental measurements are presented in Chapter 6.

2.4.3 Scattered-wave approximation

In the SWA, the PW final-state is replaced by a partial wave expansion of the unbound solutions of the Coulomb potential – the Coulomb waves. Scattering effects of this outgoing partial waves in the Coulomb potential of the ion core are, therefore, included via angular-momentum- and kinetic-energy-dependent phase shifts between partial waves of the outgoing Coulomb wave. There are two dipole-allowed $l\pm1$ partial wave channels in the final state. Their interference is dependent on the kinetic energy. This was already described in the photoemission of gas phase molecules [41, 84, 85, 93]. In our work [AH12], this approach is formally extended to the photoemission from C $2p_2$ in graphene as periodic system using the Bloch nature of the initial and final states. In a second step, nearest-neighbor (NN) Coulomb scattering of the outgoing photoelectrons is included. The supplementary information of our publication [AH12] includes a detailed description of the so-obtained photoemission final state in a general form based on the publication by Moser [94] and limited to C $2p_2$ orbitals either without or with nearest-neighbor scattering. The therein included formalism is summarized in this section using the most essential formula and approximations.

The simulated SWA photoemission intensity distributions and obtained photoemission cross sections of graphene at one specific binding energy in comparison the experimental data are presented in Chapter 7.

General framework

As mentioned earlier, the SWA is based on a partial wave expansion where the emitted photoelectrons are described as Coulomb waves. Its partial waves from the partial wave expansion [95–98] are characterized by angular momentum quantum numbers l and m, as well as the dimensionless Sommerfeld parameter $\eta = Z/(a_0 k_f)$ (a_0 is the Bohr radius), which describes the distortion of the outgoing photoelectron wave with spherical wave vector $\boldsymbol{k}_f$ in the Coulomb field of the ion that is left behind. Note that the Sommerfeld parameter takes the role of the principal quantum number n that characterizes bound solutions.

$$\chi_{\eta lm}(\boldsymbol{r}) = \langle \boldsymbol{r}|\chi_{\eta lm}\rangle = \boldsymbol{R}_{\eta l}(r)\langle \boldsymbol{r}|lm\rangle = \boldsymbol{R}_{\eta l}(r)Y_l^m(\Omega_r). \tag{2.31}$$

The Coulomb wave $|\boldsymbol{k}_f\rangle$ [99, 100] can be expanded in partial waves

$$|\boldsymbol{k}_f\rangle = 4\pi \sum_{l=0}^{\infty} \sum_{m=-l}^{l} i^l \; e^{i\sigma_l} \langle lm|\boldsymbol{k}_f\rangle |\chi_{nlm}\rangle \tag{2.32}$$

resulting in

$$\begin{aligned}\chi_{\boldsymbol{k}_f}(\boldsymbol{r}) &= \langle \boldsymbol{r}|\boldsymbol{k}_f\rangle \\ &= 4\pi \sum_{l=0}^{\infty}\sum_{m=-l}^{l} i^l\, e^{i\sigma_l} \boldsymbol{R}_{\eta l}(r,\boldsymbol{k}_f)\langle \boldsymbol{r}|lm\rangle\langle lm|\boldsymbol{k}_f\rangle \\ &= 4\pi \sum_{l=0}^{\infty}\sum_{m=-l}^{l} i^l\, e^{i\sigma_l} \boldsymbol{R}_{\eta l}(r,\boldsymbol{k}_f) Y_l^m(\Omega_r) Y_l^{m*}(\Omega_{\boldsymbol{k}_f})\end{aligned} \tag{2.33}$$

where $\sigma_l = \arg\Gamma(l+1+i\eta)$ is the Coulomb phase. This expression should be compared to the partial-wave expansion of the plane-wave final state

$$e^{i\boldsymbol{k}_f\cdot\boldsymbol{r}} = 4\pi \sum_{l=0}^{\infty}\sum_{m=-l}^{l} i^l j_l(k_f r) Y_l^{m*}(\Omega_r) Y_l^m(\Omega_{k_f}), \tag{2.34}$$

where j_l are spherical Bessel functions.

The final-state wave function of a photoelectron with wave vector $\boldsymbol{k}_f$ from a lattice of atoms is given by a coherent superposition of Coulomb waves $|\boldsymbol{k}_f\rangle$ emanating from all sites,

$$\Psi_{\boldsymbol{k}_f}(\boldsymbol{r}) = \frac{1}{\sqrt{V}} \sum_{\boldsymbol{R}} e^{i\boldsymbol{k}_f\cdot\boldsymbol{R}} \sum_{\boldsymbol{R}_j} e^{i\boldsymbol{k}_f\cdot\boldsymbol{R}_j} \chi_{\boldsymbol{k}_f}(\boldsymbol{r}-\boldsymbol{R}-\boldsymbol{R}_j), \tag{2.35}$$

in which the sums are carried out over all lattice vectors $\boldsymbol{R}$ and basis sites $\boldsymbol{R}_j$ within a unit cell of the lattice, respectively. The prefactor $\frac{1}{\sqrt{V}}$ with the normalization volume (= sample volume) V assures that $\langle\Psi_{\boldsymbol{k}_f}|\Psi_{\boldsymbol{k}_f}\rangle = 1$.

Since we need both, initial and final state wave functions, to describe the matrix element, we use the following initial Bloch state with band index κ:

$$|\Psi_{\boldsymbol{k}}^{\kappa}\rangle = \frac{1}{\sqrt{V}} \sum_{\boldsymbol{R}} e^{i\boldsymbol{k}\cdot\boldsymbol{R}} \sum_{\boldsymbol{R}_j}\sum_{nlm} c_{jnlm}^{\kappa}(\boldsymbol{k})|\boldsymbol{R}+\boldsymbol{R}_j, nlm\rangle. \tag{2.36}$$

This initial-state Bloch state is expanded in terms of atomic states given by bound atomic orbitals (negative energy)

$$\Phi_{nlm}(\boldsymbol{r}) = \langle \boldsymbol{r}|\boldsymbol{0}, nlm\rangle = R_{nl}(r) Y_l^m(\Omega_r) \tag{2.37}$$

with quantum numbers nlm centered at sites $\boldsymbol{R} + \boldsymbol{R}_j$.

To calculate the photoemission matrix element $M^{\kappa}_{\boldsymbol{k}_f \boldsymbol{k}}$ between the initial-state wave function $\Psi^{\kappa}_{\boldsymbol{k}}(\boldsymbol{r})$ (Eq. 2.36) and the final-state wave function $\Psi_{\boldsymbol{k}_f}(\boldsymbol{r})$ (Eq. 2.35), we use several conversion steps. Namely, we exclude inter-site final-state scattering, which is commonly referred to as IAC approximation, by assuming $\boldsymbol{R} = \boldsymbol{R}'$ and $\boldsymbol{R}_j = \boldsymbol{R}'_j$. $\boldsymbol{G}$ is the reciprocal lattice vector.

$$
\begin{aligned}
M^{\kappa}_{\boldsymbol{k}_f \boldsymbol{k}} &\propto \int d^3r\, \Psi^{*}_{\boldsymbol{k}_f}(\boldsymbol{r})\, \boldsymbol{\epsilon} \cdot \nabla \Psi^{\kappa}_{\boldsymbol{k}}(\boldsymbol{r}) \\
&= \frac{1}{V} \sum_{\boldsymbol{R}'} e^{-i\boldsymbol{k}_f \cdot \boldsymbol{R}'} \sum_{\boldsymbol{R}'_j} e^{-i\boldsymbol{k}_f \cdot \boldsymbol{R}'_j} \sum_{\boldsymbol{R}} e^{i\boldsymbol{k} \cdot \boldsymbol{R}} \sum_{\boldsymbol{R}_j} \sum_{nlm} c^{\kappa}_{jnlm}(\boldsymbol{k}) \\
&\times \int d^3r\, \chi^{*}_{\boldsymbol{k}_f}(\boldsymbol{r} - \boldsymbol{R}' - \boldsymbol{R}'_j + \boldsymbol{R} + \boldsymbol{R}_j)\, \boldsymbol{\epsilon} \cdot \nabla \Phi_{nlm}(\boldsymbol{r}) \\
&\approx \frac{1}{V} \sum_{\boldsymbol{R}} e^{i(\boldsymbol{k} - \boldsymbol{k}_f) \cdot \boldsymbol{R}} \sum_{\boldsymbol{R}_j} \sum_{nlm} c^{\kappa}_{jnlm}(\boldsymbol{k}) e^{-i\boldsymbol{k}_f \cdot \boldsymbol{R}_j} \\
&\times \int d^3r\, \chi^{*}_{\boldsymbol{k}_f}(\boldsymbol{r}) \epsilon \cdot \nabla \Phi_{nlm}(\boldsymbol{r}) \\
&= \frac{N}{V} \sum_{\boldsymbol{G}} \delta_{(\boldsymbol{k} - \boldsymbol{k}_f)_{\parallel}, \boldsymbol{G}} \sum_{\boldsymbol{R}_j} \sum_{nlm} c^{\kappa}_{jnlm}(\boldsymbol{k}) e^{-i\boldsymbol{k}_f \cdot \boldsymbol{R}_j}\, \boldsymbol{\epsilon} \cdot \boldsymbol{M}_{nlm}(\boldsymbol{k}_f)
\end{aligned}
\tag{2.38}
$$

Therein, $\boldsymbol{M}_{nlm}(\boldsymbol{k}_f)$ is defined as

$$
\boldsymbol{M}_{nlm}(\boldsymbol{k}_f) \equiv \int d^3r\, \chi^{*}_{\boldsymbol{k}_f}(\boldsymbol{r})\, \nabla \Phi_{nlm}(\boldsymbol{r}). \tag{2.39}
$$

The gradient of atomic orbitals $\nabla \Phi_{nlm}(\boldsymbol{r})$ taken from Ref. [101] is

$$
\begin{aligned}
\nabla \Phi_{nlm}(\boldsymbol{r}) &= \nabla [R_{nl}(r) Y^m_l(\Omega_r)] \\
&= -\sqrt{\frac{l+1}{2l+1}} \left[\frac{\partial}{\partial r} - \frac{l}{r} \right] R_{nl}(r) \boldsymbol{Y}_{l,l+1,m}(\Omega_r) \\
&+ \sqrt{\frac{l}{2l+1}} \left[\frac{\partial}{\partial r} + \frac{l+1}{r} \right] R_{nl}(r) \boldsymbol{Y}_{l,l-1,m}(\Omega_r) \\
&= -\sqrt{\frac{l+1}{2l+1}} f_{nl}(r)\, \boldsymbol{Y}_{l,l+1,m}(\Omega_r) + \sqrt{\frac{l}{2l+1}} g_{nl}(r)\, \boldsymbol{Y}_{l,l-1,m}(\Omega_r),
\end{aligned}
\tag{2.40}
$$

where we defined

$$\begin{aligned} f_{nl}(r) &\equiv \left(\frac{\partial}{\partial r} - \frac{l}{r}\right) R_{nl}(r), \\ g_{nl}(r) &\equiv \left(\frac{\partial}{\partial r} + \frac{l+1}{r}\right) R_{nl}(r). \end{aligned} \tag{2.41}$$

In Eq. 2.40, the vector spherical harmonics $\boldsymbol{Y}_{J,L,M}(\Omega_r)$ are constructed according to [101]

$$\boldsymbol{Y}_{J,L,M}(\Omega_r) = \sum_{m=-L}^{L} \sum_{m'=-1}^{1} \langle L, m; 1, m' | J, M \rangle Y_L^m(\Omega_r)\, \boldsymbol{\epsilon}_{m'}, \tag{2.42}$$

with Clebsch-Gordon coefficients $\langle j_1, m_1; j_2, m_2 | J, M \rangle$.

If the last form of $\nabla\Phi_{nlm}(\boldsymbol{r})$ in Eq. 2.40 is inserted in Eq. 2.39, we yield the final general form of the matrix element to be calculated for a specific initial state with quantum numbers nlm:

$$\begin{aligned} \boldsymbol{M}_{nlm}(\boldsymbol{k}_f) = &-\sqrt{\frac{l+1}{2l+1}} e^{-i\sigma_{l+1}} \widetilde{f}_{n,l,l+1}(k_f)\, \boldsymbol{Y}_{l,l+1,m}(\Omega_{\boldsymbol{k}_f}) \\ &+ \sqrt{\frac{l}{2l+1}} e^{-i\sigma_{l-1}} \widetilde{g}_{n,l,l-1}(k_f)\, \boldsymbol{Y}_{l,l-1,m}(\Omega_{\boldsymbol{k}_f}), \end{aligned} \tag{2.43}$$

with the Coulomb phases of the two emission channels σ_{l+1} and σ_{l-1}.

Therein, the spatial integrals on $\widetilde{f}_{nl}(r)$ and $\widetilde{g}_{nl}(r)$ are defined as

$$\begin{aligned} \widetilde{f}_{n,l,l+1}(k_f) &\equiv 4\pi(-i)^{l+1} \int dr\, r^2 R^*_{\eta l+1}(r) f_{nl}(r), \\ \widetilde{g}_{n,l,l-1}(k_f) &\equiv 4\pi(-i)^{l-1} \int dr\, r^2 R^*_{\eta l-1}(r) g_{nl}(r), \end{aligned} \tag{2.44}$$

and describe the kinetic(k_f)-energy-dependent amplitudes of the photoemission $l+1$ and $l-1$ channels, respectively, for photoemission from an initial state with quantum numbers nlm.

Photoemission from C $2p_z$ orbitals without NN scattering

In this work, the SWA is applied to the photoemission of graphene's π band. The atomic structure of graphene is illustrated in Fig. 2.4**a**. We therefore adapt the general form of the matrix element derived in Eq. 2.43 to the C $2p_z$ orbitals with quantum numbers $\{nlm\} = \{210\}$ resulting in

$$\begin{aligned} \boldsymbol{M}_{210}(\boldsymbol{k}_f) &= -\sqrt{\frac{2}{3}} e^{-i\sigma_2}\, \widetilde{f}_{2,1,2}(k_f)\; \boldsymbol{Y}_{1,2,0}(\boldsymbol{\Omega}_{k_f}) \\ &\quad + \sqrt{\frac{1}{3}} e^{-i\sigma_0}\, \widetilde{g}_{2,1,0}(k_f)\; \boldsymbol{Y}_{1,0,0}(\boldsymbol{\Omega}_{k_f}) \\ &= -\widetilde{f}(k)\; \boldsymbol{Y}_{1,2,0}(\boldsymbol{\Omega}_{k_f}) + \widetilde{g}(k)\; \boldsymbol{Y}_{1,0,0}(\boldsymbol{\Omega}_{k_f}), \end{aligned} \tag{2.45}$$

Note that the constants and phases ($e^{-i\sigma_2}$ and $e^{-i\sigma_0}$) in the first line of Eq. 2.45 are combined with the k_f-dependent amplitudes $\widetilde{g}_{2,1,0}$ and $\widetilde{f}_{2,1,2}$ in the second line.

The vector spherical harmonics are given according to Eq. 2.42 [101] by $\boldsymbol{Y}_{1,2,0}(\Omega_{k_f}) = \left(\sqrt{\frac{3}{10}} Y_2^{-1}(\Omega_{k_f}), -\sqrt{\frac{2}{5}} Y_2^0(\Omega_{k_f}), \sqrt{\frac{3}{10}} Y_2^1(\Omega_{k_f})\right)^\top$ and $\boldsymbol{Y}_{1,0,0}(\Omega_{k_f}) = (0, Y_0^0(\Omega_{k_f}), 0)^\top$. $\boldsymbol{Y}_{J,L,M}$ emerges from the angular-momentum coupling of the ordinary spherical harmonic Y_L^m with angular momentum quantum number L to the complex vector $\boldsymbol{u} = x\boldsymbol{e}_x + y\boldsymbol{e}_y + z\boldsymbol{e}_z$, $(x, y, z) \in \mathbb{C}^3$ with angular momentum quantum number 1 — the eigenstates of the $\hat{L}_z$ operator in the three-dimensional complex space of $\boldsymbol{u}$ are the $\boldsymbol{\epsilon}_{m'}$, given by $\boldsymbol{\epsilon}_{+1} = (-1/\sqrt{2}, -i/\sqrt{2}, 0)^\top$, $\boldsymbol{\epsilon}_0 = (0, 0, 1)^\top$, and $\boldsymbol{\epsilon}_{-1} = (1/\sqrt{2}, -i/\sqrt{2}, 0)^\top$. correspondingly, we can define the polarization vector $(\epsilon_+, \epsilon_0, \epsilon_-)$ if the experimental geometry is known.

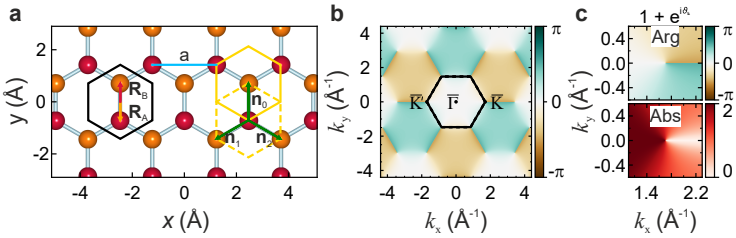

Figure 2.4: Atomic structure and phase of graphene
a Atomic structure of graphene, with sublattices A (red) and B (orange), primitive unit cell (black), non-primitive unit cell including all nearest neighbors of a sublattice (yellow), and vectors $\boldsymbol{n}_0$, $\boldsymbol{n}_1$ and $\boldsymbol{n}_2$ (green). **b** Relative geometric phase $\vartheta_{\boldsymbol{k}}$ **c** Amplitude (bottom) and phase (top) of the initial-state structure factor [AH12].

According to Eq. 2.38, $M^{\pm}_{\boldsymbol{k}_f\boldsymbol{k}}$ then becomes

$$
\begin{aligned}
M^{\pm}_{\boldsymbol{k}_f\boldsymbol{k}} &= \delta_{\boldsymbol{k},\boldsymbol{k}_{f\parallel}} \begin{pmatrix} \epsilon_+ & \epsilon_0 & \epsilon_- \end{pmatrix} \cdot \begin{pmatrix} \boldsymbol{M}_{210}(\boldsymbol{k}_f) & \boldsymbol{M}_{210}(\boldsymbol{k}_f) \end{pmatrix} \cdot \frac{1}{\sqrt{2}} \begin{pmatrix} 1 \\ \pm e^{i\vartheta_{\boldsymbol{k}_{f\parallel}}} \end{pmatrix} \\
&= \delta_{\boldsymbol{k},\boldsymbol{k}_{f\parallel}} \begin{pmatrix} \epsilon_+ & \epsilon_0 & \epsilon_- \end{pmatrix} \cdot \boldsymbol{M}_{210}(\boldsymbol{k}_f) \cdot \begin{pmatrix} 1 & 1 \end{pmatrix} \cdot \frac{1}{\sqrt{2}} \begin{pmatrix} 1 \\ \pm e^{i\vartheta_{\boldsymbol{k}_{f\parallel}}} \end{pmatrix} \\
&= \left(\underbrace{-\widetilde{f}(k_f) \left[\sqrt{\frac{3}{10}}\epsilon_- Y_2^1(\boldsymbol{\Omega}_{k_f}) - \sqrt{\frac{2}{5}}\epsilon_0 Y_2^0(\boldsymbol{\Omega}_{k_f}) + \sqrt{\frac{3}{10}}\epsilon_+ Y_2^{-1}(\boldsymbol{\Omega}_{k_f}) \right]}_{d\,\text{channel}} + \underbrace{\widetilde{g}(k_f)\,\epsilon_0 Y_0^0(\boldsymbol{\Omega}_{k_f})}_{s\,\text{channel}} \right) \\
&\times \frac{1}{\sqrt{2}}(1 \pm e^{i\vartheta_{\boldsymbol{k}_{f\parallel}}})
\end{aligned}
\tag{2.46}
$$

with the relative geometric phases $\vartheta_{\boldsymbol{k}}$ at graphene's lattice sites (see Fig. 2.4**b**).

This expression for the photoemission matrix elements can be simplified, if specific experimental geometries are considered. Following the two incidence settings in our work, where kinetic-energy-dependent POT data of graphene are recorded for $\alpha = 0°$ and $45°$, which we refer to as normal (NI) and oblique incidence (OI) geometries, we adapt Eq. 2.46 considering p polarized light as in our experiment.

For NI geometry, the vector potential is along $\boldsymbol{\epsilon}_x$, i.e., in the surface plane, leading to a polarization vector of $\boldsymbol{\epsilon}_{\text{NI}} = (\epsilon_+, \epsilon_0, \epsilon_-) = (-\frac{1}{\sqrt{2}}, 0, \frac{1}{\sqrt{2}})$. The spherical harmonics are expressed explicitly as $Y_2^1(\Omega_{k_f}) = -\sqrt{\frac{15}{8\pi}}\,\sin\theta\cos\theta\,e^{+i\phi}$, $Y_0^0(\Omega_{k_f}) = \frac{1}{2\sqrt{\pi}}$, $Y_2^0(\Omega_{k_f}) = \sqrt{\frac{5}{4\pi}}(\frac{3}{2}\cos^2\theta - \frac{1}{2})$, and $Y_l^{-m} = (-1)^m Y_l^{m*}$. The photoemission matrix element in NI geometry without NN scattering in the SWA model finally reads

$$
M^{\pm}_{\boldsymbol{k}_f\boldsymbol{k},\,\text{NI}} = \delta_{\boldsymbol{k},\boldsymbol{k}_{f\parallel}} \frac{3}{8\sqrt{\pi}}\,\widetilde{f}(k_f)\sin 2\theta\cos\phi(1 \pm e^{i\vartheta_{\boldsymbol{k}_{f\parallel}}}) \tag{2.47}
$$

leading to the following relation with the measured photoemission intensity after Eq. 2.18

$$
I^{\pm}(k_f,\theta,\phi;h\nu,\boldsymbol{\epsilon}_{\text{NI}}) \propto |M^{\pm}_{\boldsymbol{k}_f\boldsymbol{k},\,\text{NI}}|^2 = \delta_{\boldsymbol{k},\boldsymbol{k}_{f\parallel}} \frac{9}{64\pi}\,|\widetilde{f}(k_f)|^2 \sin^2 2\theta\cos^2\phi\,|1 \pm e^{i\vartheta_{\boldsymbol{k}_{f\parallel}}}|^2. \tag{2.48}
$$

Accordingly, we find that with $d_{\mathrm{NI}}(\phi,\theta) = \sin(2\theta)\cos\phi$

$$I_{\mathrm{NI}} \;\propto\; |\widetilde{f}(k_f)|^2\, d_{\mathrm{NI}}(\theta,\phi)^2 |1 + e^{i\vartheta_{\boldsymbol{k}_{f\parallel}}}|^2. \tag{2.49}$$

Comparing this expression with the photoemission matrix element in Eq. 2.46, we see that $\widetilde{g}(k_f)$ is absent, which means that photoemission in the s channel is suppressed. Photoemission data recorded in the NI geometry is therefore suitable to extract the (square) modulus of the complex, kinetic-energy-dependent photoemission amplitude in the d channel ($\widetilde{f}(k_f)$).

In OI geometry, the vector potential is in the $-x, z$ half plane leading to a polarization vector of $\boldsymbol{\epsilon}_{\mathrm{OI}} = (\epsilon_+,\, \epsilon_0,\, \epsilon_-) = (-\frac{1}{2}, \frac{1}{\sqrt{2}}, \frac{1}{2})$. Following Eq. 2.46, this leads to a photoemission matrix element of

$$M^{\pm}_{\boldsymbol{k}_f \boldsymbol{k},\,\mathrm{OI}} = \delta_{\boldsymbol{k},\boldsymbol{k}_{f\parallel}} \frac{1}{8\sqrt{2\pi}} \Big[\widetilde{f}(k_f)\;\; (3\sin 2\theta\cos\phi + 3\cos 2\theta + 1) + 2\sqrt{2}\,\widetilde{g}(k_f)\;\; \Big] \times (1 \pm e^{i\vartheta_{\boldsymbol{k}_{f\parallel}}}) \tag{2.50}$$

and

$$\begin{aligned} I^{\pm}(k_f,\theta,\phi;h\nu,\boldsymbol{\epsilon}_{\mathrm{OI}}) &\propto |M^{\pm}_{\boldsymbol{k}_f \boldsymbol{k},\,\mathrm{OI}}|^2 \\ &= \delta_{\boldsymbol{k},\boldsymbol{k}_{f\parallel}} \frac{1}{128\pi} \Big[|\widetilde{f}(k_f)|^2\;\; (3\sin 2\theta\cos\phi + 3\cos 2\theta + 1)^2 + 8\,|\widetilde{g}(k_f)|^2 \\ &+ 4\sqrt{2}|\widetilde{f}(k_f)||\widetilde{g}(k_f)|\,(3\sin 2\theta\cos\phi + 3\cos 2\theta + 1)\cos\Delta\sigma \Big] \times |1 \pm e^{i\vartheta_{\boldsymbol{k}_{f\parallel}}}|^2 \end{aligned} \tag{2.51}$$

which simplifies to

$$\begin{aligned} I_{\mathrm{OI}} \propto \big[&|\widetilde{f}(k_f)|^2 d_{\mathrm{OI}}(\theta,\phi)^2 + 8|\widetilde{g}(k_f)|^2 \\ &+ 4\sqrt{2}|\widetilde{f}(k_f)||\widetilde{g}(k_f)| d_{\mathrm{OI}}(\theta,\phi)\cos\Delta\sigma \big]\, |1 + e^{i\vartheta_{\boldsymbol{k}_{f\parallel}}}|^2, \end{aligned} \tag{2.52}$$

abbreviating $d_{\mathrm{OI}}(\theta,\phi) = 3\sin 2\theta\cos\phi + 3\cos 2\theta + 1$ and $\Delta\sigma(k_f) \equiv arg\, \frac{\widetilde{f}(k_f)}{\widetilde{g}(k_f)}$ as the energy-dependent relative phase between the s and d photoemission channels.

This expression and consequently the photoemission data recorded in OI geometry include interference from both, s and d channels. Using the results from Eq. 2.49 extracting the contribution from the s channel, we can also pinpoint the input of the d channel from Eq. 2.52.

Photoemission from C $2p_z$ orbitals including NN scattering

In the previous section, we evaluated the photoemission matrix element from C $2p_z$ orbitals in graphene prohibiting the on-site scattering in the final state, i.e., the scattering of photoelectrons emitted from sublattice A into the Coulomb wave centered at one of the neighboring B sites. This constraint was implemented by assuming that $\boldsymbol{R}' = \boldsymbol{R}$ and $\boldsymbol{R}'_j = \boldsymbol{R}_j$ saying that the initial-state orbital and final-state partial wave were required to be centered on the same carbon atom (independent-center approximation). The corresponding formula Eq. 2.38 is therefore replicated here:

$$\begin{aligned} M^{\kappa}_{\boldsymbol{k}_f\boldsymbol{k}} &\propto \int d^3r\, \Psi^*_{\boldsymbol{k}_f}(\boldsymbol{r})\, \boldsymbol{\epsilon}\cdot\nabla\Psi^{\kappa}_{\boldsymbol{k}}(\boldsymbol{r}) \\ &= \frac{1}{V}\sum_{\boldsymbol{R}'} e^{-i\boldsymbol{k}_f\cdot\boldsymbol{R}'}\sum_{\boldsymbol{R}'_j} e^{-i\boldsymbol{k}_f\cdot\boldsymbol{R}'_j}\sum_{\boldsymbol{R}} e^{i\boldsymbol{k}\cdot\boldsymbol{R}}\sum_{\boldsymbol{R}_j}\sum_{nlm} c^{\kappa}_{jnlm}(\boldsymbol{k}) \\ &\times \int d^3r\, \chi^*_{\boldsymbol{k}_f}(\boldsymbol{r}-\boldsymbol{R}'-\boldsymbol{R}'_j+\boldsymbol{R}+\boldsymbol{R}_j)\, \boldsymbol{\epsilon}\cdot\nabla\Phi_{nlm}(\boldsymbol{r}). \end{aligned} \tag{2.53}$$

In the next step, we want to loosen up the previous constraint by allowing an electron originating from a certain basis atom to be emitted in a partial wave centered on another basis atom ($\boldsymbol{R}'_j \neq \boldsymbol{R}_j$) in the same unit cell ($\boldsymbol{R}' = \boldsymbol{R}$) [AH12]. As a consequence, scattering between nearest neighbors within the unit cell is allowed during the photoemission process. Eq. 2.53 then becomes

$$\begin{aligned} M^{\kappa}_{\boldsymbol{k}_f\boldsymbol{k}} &\approx \frac{1}{V}\sum_{\boldsymbol{R}} e^{i(\boldsymbol{k}-\boldsymbol{k}_f)\cdot\boldsymbol{R}}\sum_{\boldsymbol{R}'_j} e^{-i\boldsymbol{k}_f\cdot\boldsymbol{R}'_j}\sum_{\boldsymbol{R}_j}\sum_{nlm} c^{\kappa}_{jnlm}(\boldsymbol{k})\int d^3r\, \chi^*_{\boldsymbol{k}_f}(\boldsymbol{r}-\boldsymbol{R}'_j+\boldsymbol{R}_j)\, \boldsymbol{\epsilon}\cdot\nabla\Phi_{nlm}(\boldsymbol{r}) \\ &= \frac{1}{V_0}\sum_{\boldsymbol{G}} \delta_{(\boldsymbol{k}-\boldsymbol{k}_f)_{\parallel},\boldsymbol{G}}\sum_{\boldsymbol{R}'_j} e^{-i\boldsymbol{k}_f\cdot\boldsymbol{R}'_j}\sum_{\boldsymbol{R}_j}\sum_{nlm} c^{\kappa}_{jnlm}(\boldsymbol{k})\int d^3r\, \chi^*_{\boldsymbol{k}_f}(\boldsymbol{r}-\boldsymbol{R}'_j+\boldsymbol{R}_j)\, \boldsymbol{\epsilon}\cdot\nabla\Phi_{nlm}(\boldsymbol{r}). \end{aligned} \tag{2.54}$$

In the previous case without nearest neighboring scattering, it was possible to simplify the integral or a single set of quantum numbers nlm using Eq. 2.39, i.e., by introducing $\boldsymbol{M}_{nlm}(\boldsymbol{k}_f)$. In the present case, this is not possible anymore. Instead, the shift $\Delta = \boldsymbol{R}_j - \boldsymbol{R}'_j$ between the centers of the $\chi_{\boldsymbol{k}_f}$ and Φ_{nlm} requires an expansion in terms of angular momentum eigenfunctions for all quantum numbers $\{n'l'm'\}$, with so-called Shibuya Wulfmann integrals [102, 103] $S^{\boldsymbol{R}'_j n'l'm'}_{\boldsymbol{R}_j nlm}$ as expansion coefficients.

Using

$$\int d^3r\, \chi^*_{\boldsymbol{k}_f}(\boldsymbol{r}-\boldsymbol{R}'_j+\boldsymbol{R}_j)\,\boldsymbol{\epsilon}\cdot\nabla\Phi_{nlm}(\boldsymbol{r}) = \sum_{n'l'm'} S^{\boldsymbol{R}'_j n'l'm'}_{\boldsymbol{R}_j nlm}\,\boldsymbol{\epsilon}\cdot\boldsymbol{M}_{n'l'm'}(\boldsymbol{k}_f) \tag{2.55}$$

and adjusting the nomenclature to the photoemission from π bands with band index $\kappa = \pm$ and quantum numbers $\{nlm\} = \{210\}$ of graphene with its two sublattices A and B, we get the following expression:

$$\begin{aligned} M^{\kappa}_{\boldsymbol{k}_f\boldsymbol{k}} &\approx \frac{1}{V_0}\sum_{\boldsymbol{G}}\delta_{(\boldsymbol{k}-\boldsymbol{k}_f)_\parallel,\boldsymbol{G}}\sum_{\boldsymbol{R}'_j} e^{-i\boldsymbol{k}_f\cdot\boldsymbol{R}'_j}\sum_{\boldsymbol{R}_j}\sum_{nlm} c^{\kappa}_{jnlm}(\boldsymbol{k})\sum_{n'l'm'} S^{\boldsymbol{R}'_j n'l'm'}_{\boldsymbol{R}_j nlm}\,\boldsymbol{\epsilon}\cdot\boldsymbol{M}_{n'l'm'}(\boldsymbol{k}_f) \\ &= \frac{1}{V_0}\sum_{\boldsymbol{G}}\delta_{(\boldsymbol{k}-\boldsymbol{k}_f)_\parallel,\boldsymbol{G}}\sum_{j\in\{\mathrm{A,B}\}} c^{\pm}_j(\boldsymbol{k})\sum_{j'\in\{\mathrm{A,B}\}}\sum_{\forall j'\neq j:i'=0}^{2} e^{-i\boldsymbol{k}_f\cdot\boldsymbol{n}_{ji'}}\sum_{n'l'm'} S^{j'n'l'm'}_{j210}(\boldsymbol{n}_{ji'})\boldsymbol{\epsilon}\cdot\boldsymbol{M}_{n'l'm'}(\boldsymbol{k}_f). \end{aligned} \tag{2.56}$$

The next changes in the description of $M^{\kappa}_{\boldsymbol{k}_f\boldsymbol{k}}$ are a result of the system under investigation: p_z orbitals in graphene. Namely, we identify that the vector pointing from an atom in sublattice j to a neighboring atom in sublattice i', $\boldsymbol{n}_{ji'}$, is equivalent for p_z orbitals with the same C_3 symmetry. As a result, $S^{Bn'l'm'}_{A210} = S^{An'l'm'}_{B210}$ and the sublattice indices j, j' in the Shibuya Wulfmann integrals can be omitted. According to Eq. (78) in Ref. [103], the Shibuya-Wulfmann integrals are the proportional to

$$S^{n'l'm'}_{210}(\boldsymbol{n}_{i'}) \propto \sum_{N,L}\sqrt{6n'N(2l'+1)}\langle l',-m';1,0|L,-m'\rangle f_{NL}(n_{i'})Y_L^{-m'}(\Omega_{n_{i'}}). \tag{2.57}$$

The Shibuya-Wulfmann integrals perform a basis change between C $2p_z$ orbitals centered at sublattice B to a linear combination of orbitals $n'l'm'$ centered at sublattice A and vice versa [102, 103]. The radial contributions f_{NL} decay exponentially with orbital distance, i.e., $f_{NL} \propto e^{-\frac{2Z}{a_0 n'}|\boldsymbol{n}_{i'}|/2}$with effective nuclear charge Z and Bohr radius a_0, where $|\boldsymbol{n}_{i'}|$ in our nearest-neighbor model is equivalent to the sublattice distance $n_{i'} = 1.421$ Å, which justifies our nearest-neighbor scattering approximation.

Since the angular components $Y_L^{-m'}$ included in $S_{210}^{n'l'm'}(\boldsymbol{n}_{i'}$ (Eq. 2.57) transform under ν-fold rotation C_ν as $C_\nu^{i'} Y_L^{-m'} = e^{-i2\pi/\nu i' m'} Y_L^{-m'}$, the Shibuya-Wulfmann integrals can be simplified to $S_{210}^{n'l'm'}(\boldsymbol{n}_{i'}) = C_3^{i'} S_{210}^{n'l'm'}(\boldsymbol{n}_0) = e^{-i\pi\frac{2i'}{3}m'} S_{210}^{n'l'm'}(\boldsymbol{n}_0)$.

In another simplification step, we evaluate which quantum numbers would in fact make sense in our case. To this end, we consider that there is centrifugal barrier that electrons need to overcome in order to effectively scatter into channels with angular momentum l' at another sublattice, Naturally, we set this barrier at $k_f^{\max} \geq 3$ Å^{-1} where we observe a considerable experimental scattering. Assuming that $k_f^2 \geq l'(l'+1)/a^2$, where a is the atomic radius ($a_{\text{carbon}} \sim 0.7$ Å), we find that only channels with $l' < 1.67$ significantly contribute to the scattering process. The lowest orbital order contributions thus originate from $l' = 1$ and $m' = 0$ leaving behind $S_{210}^{n'l'm'}(\boldsymbol{n}_{i'}) = e^{-i\pi\frac{2i'}{3}0} S_{210}^{n'10}(\boldsymbol{n}_0) = S_{210}^{n'10}(\boldsymbol{n}_0)$

Inserting Eq. 2.57 into Eq. 2.56 with the simplified Shibuya-Wulfmann integrals due to 3-fold rotational symmetry of the graphene and using $c_A^{\pm}(\boldsymbol{k}) = \frac{1}{\sqrt{2}}$ and $c_B^{\pm}(\boldsymbol{k}) = \pm\frac{1}{\sqrt{2}} e^{i\vartheta_k}$ leads to

$$M_{\boldsymbol{k}_f \boldsymbol{k}}^{\pm} \approx \frac{\delta_{\boldsymbol{k},\boldsymbol{k}_{f\parallel}}}{\sqrt{2}V_0} \boldsymbol{\epsilon} \cdot \left[(1 \pm e^{i\vartheta_k})\, \boldsymbol{M}_{210}(\boldsymbol{k}_f) + \sum_{n'} S_{210}^{n'10}(\boldsymbol{n}_0)\, \boldsymbol{M}_{n'10}(\boldsymbol{k}_f) \sum_{i'=0}^{2} (e^{-i\boldsymbol{k}_f \cdot \boldsymbol{n}_{i'}} \pm e^{i\vartheta_k} e^{i\boldsymbol{k}_f \cdot \boldsymbol{n}_{i'}}) \right]. \tag{2.58}$$

In the above equation, we simplify

$$\sum_{i'=0}^{2} (e^{-i\boldsymbol{k}_f \cdot \boldsymbol{n}_{i'}} \pm e^{i\vartheta_k} e^{i\boldsymbol{k}_f \cdot \boldsymbol{n}_{i'}}) = h^*(\boldsymbol{k}_{f\parallel}) \pm e^{i\vartheta_k} h(\boldsymbol{k}_{f\parallel}) = e^{-i\vartheta_{k_{f\parallel}}} \pm e^{i\vartheta_k} e^{-i\vartheta_{k_{f\parallel}}} \, |h^*(\boldsymbol{k}_{f\parallel})| \tag{2.59}$$

and introduce the complex function $u(\boldsymbol{k}_f)$ which essentially describes the overlap between initial-state $2p_z$ orbitals and scattered Coulomb waves on neighboring sites

$$u(\boldsymbol{k}_f) = \sum_{n'} S_{210}^{n'10}(\boldsymbol{n}_0)\, \boldsymbol{M}_{n'10}(\boldsymbol{k}_f) \tag{2.60}$$

In Eq. 2.58, the two sums are then simplified to

$$\begin{aligned} M^{\pm}_{\boldsymbol{k}_f\boldsymbol{k}} &= \frac{\delta_{\boldsymbol{k},\boldsymbol{k}_{f\parallel}}}{\sqrt{2}V_0}\boldsymbol{\epsilon}\cdot\Big[(1\pm e^{i\vartheta_k})\,\boldsymbol{M}_{210}(\boldsymbol{k}_f)+ \\ &\quad (e^{-i\vartheta_{k_{f\parallel}}}\pm e^{i\vartheta_k}e^{i\vartheta_{k_{f\parallel}}})|h^*(\boldsymbol{k}_{f\parallel})|\sum_{n'}S^{n'10}_{210}(\boldsymbol{n}_0)\,\boldsymbol{M}_{n'10}(\boldsymbol{k}_f)\Big] \\ &= \frac{\delta_{\boldsymbol{k},\boldsymbol{k}_{f\parallel}}}{\sqrt{2}V_0}\boldsymbol{\epsilon}\cdot\Big[(1\pm e^{i\vartheta_k})\boldsymbol{M}_{210}(\boldsymbol{k}_f)+(e^{-i\vartheta_{k_{f\parallel}}}\pm e^{i\vartheta_k}e^{i\vartheta_{k_{f\parallel}}})|h^*(\boldsymbol{k}_{f\parallel})|\,u(\boldsymbol{k}_f)\Big] \\ &= \frac{\delta_{\boldsymbol{k},\boldsymbol{k}_{f\parallel}}}{\sqrt{2}V_0}\boldsymbol{\epsilon}\cdot\boldsymbol{M}_{210}(\boldsymbol{k}_f)\Big[(1\pm e^{i\vartheta_k})+(e^{-i\vartheta_{k_{f\parallel}}}\pm e^{i\vartheta_k}e^{i\vartheta_{k_{f\parallel}}})\,u(\boldsymbol{k}_f)\Big] \\ &= \frac{1}{\sqrt{2}V_0}\underbrace{\boldsymbol{\epsilon}\cdot\boldsymbol{M}_{210}(\boldsymbol{k}_f)}_{\text{dipole selection}}\Big[\underbrace{(1\pm e^{i\vartheta_{k_{f\parallel}}})}_{\text{horseshoe}}+\underbrace{\left(e^{-i\vartheta_{k_{f\parallel}}}\pm e^{i2\vartheta_{k_{f\parallel}}}\right)\,u(\boldsymbol{k}_f)}_{\text{nearest-neighbor scattering}}\Big] \end{aligned} \tag{2.61}$$

Here, $(e^{-i\vartheta_{k_{f\parallel}}}\pm e^{i\vartheta_k}e^{i\vartheta_{k_{f\parallel}}})\,u(\boldsymbol{k}_f)$ collapses into $(e^{-i\vartheta_{k_{f\parallel}}}\pm e^{i2\vartheta_{k_{f\parallel}}})\,u(\boldsymbol{k}_f)$ due to momentum conservation.

The final expression in Eq. 2.61 is split in three parts. The first part denoted as "dipole selection" constrains the possible transitions of a system from one quantum state to another. The second term "horseshoe" represents the structure factor and therefore explains the intensity distribution that we will later refer to as *horseshoe* pattern in Chapter 7. This structure factor is proportional to $|\frac{1}{\sqrt{2}}(1\pm e^{i\vartheta_k})|^2 = 1\pm\cos\vartheta_k$ and results from the scattering of initial state Bloch waves at graphene's sublattices A and B. The last part in Eq. 2.61 represents the nearest-neighbor scattering in the final state. It is dominated by $(e^{-i\vartheta_{k_{f\parallel}}}\pm e^{i2\vartheta_{k_{f\parallel}}})$ which reflects the structural interference between initial *and* final state wave functions that are *both* scattered in *both* sublattices of graphene. $u(\boldsymbol{k}_f)$ varies only slowly on the photoemission hemisphere Ω_{k_f}. For a given photoelectron momentum defined by the used kinetic energy ($k_f=\sqrt{2mE_{\text{kin}}/\hbar^2}$): $u(\boldsymbol{k}_f)\sim|u(k_f)|e^{i\,arg\,u(k_f)}$, which means that $u(\boldsymbol{k}_f)$ is a merely kinetic-energy-dependent (but not momentum-vector-dependent) fit parameter that is constant across the horseshoe.

Adapting Eq. 2.18 which essentially says that the photoemission intensity is proportional to the squared matrix element, we find that

$$I(k_f,\Omega_{\boldsymbol{k}_f};h\nu,\boldsymbol{\epsilon})\propto|\boldsymbol{\epsilon}\cdot\boldsymbol{M}_{210}(\boldsymbol{k}_f)\times[1+e^{i\vartheta_k}+\left(e^{-i\vartheta_{k_{f\parallel}}}+e^{i2\vartheta_{k_{f\parallel}}}\right)u(\boldsymbol{k}_f)]|^2\delta_{\boldsymbol{k},\boldsymbol{k}_{f\parallel}} \tag{2.62}$$

which will finally allow to extract the kinetic-energy-dependent intensity distribution of $u(\boldsymbol{k}_f)$ from experimental data (Chapter 7).

2.4.4 Toroidal electron analyzer

To get a fingerprint k map of a particular orbital, its photoemission intensity needs to be measured in a wide k range. Therefore, we use the "second generation" toroidal electron analyzer (TEA) constructed by J. Riley and R. Leckey from the La Trobe University, Australia [104] in this work. The analyzer is owned and operated by Peter Grünberg Institut (PGI-3), Forschungszentrum Jülich and currently located at the U125 insertion device beamline at the MLS in Adlershof, Berlin [53]. Figure 2.5 shows a photo of the instrument at MLS consisting of a preparation chamber, an intermediate chamber called "transfer cube", and an analyzer chamber marked in light blue, red, and yellow, respectively. The ultrahigh vacuum (UHV) chamber has a base pressure in the range of 10^{-10} mbar.

To clean and prepare molecular layers on metal surfaces, the preparation chamber is equipped with a standard Ar^+ ion-sputter gun, a quarz-microbalance, and a mass spectrometer. For the deposition of layers, it has two slots for connecting two (typically molecular or metal) evaporators simultaneously. After preparing the sample, it is transferred through the "transfer cube" to the analyzer chamber onto a five-axes (x, y, z, polar θ, and in-plane azimuthal rotation ϕ) manipulator located on the symmetry axis of the analyzer.

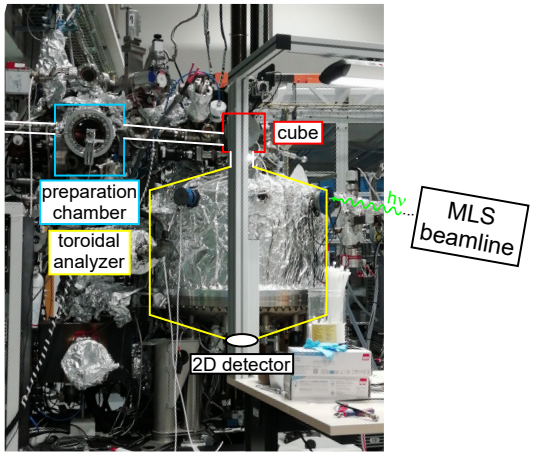

Figure 2.5: Photo of TEA
Photo of experimental setup at the beamline at MLS in Berlin.

The analyzer chamber is attached to the insertion beamline providing an absolutely calibrated photon flux (see Section 2.4.6). This analyzer itself was developed for angle-resolved photoemission experiments, in which photoelectrons are collected over the full hemisphere above the surface. In contrast to conventional hemispherical analyzers that typically enable the collection of photoelectrons in a polar angle range of $\pm$ 15 °, this angular acceptance is nearly 180 ° in the TEA.

Schematic drawings of the analyzer's internal structure are presented in Fig. 2.6**a**, **b**. The cross section in **b** shows that the sample is located in front of the input lens having two purposes. First, the emitted photoelectrons are

re-focused from the sample into the entrance of the toroidal sector given by the gap between the inner and outer energy dispersive elements (toroids). Only electrons with the selected pass energy E_{pass} are allowed to enter the toroidal sector. The input lens secondly reduces the kinetic energy of the photoelectrons to match E_{pass}. Electrons with kinetic energies in an energy window of $\Delta E_{\text{kin}} = \pm 4\% E_{\text{pass}}$ pass through the toroidal sector, reach the ring-shaped exit slit, pass through the output lens, and are imaged onto the two-dimensional detector.

The detector consists of a multichannel plate (MCP) and a phosphorous screen. The illumination on the latter is recorded by a charge-coupled device (CCD) camera and schematically looks like the sketch in Fig. 2.6**c**. The detected photoemission intensity forms an arc centered at the mid-point of the MCP, where the radial direction denotes the kinetic energies E_{kin} of the photoelectrons from the smallest ($E_{\text{pass}} - 4\% E_{\text{pass}}$) at the inner edge to the highest ($E_{\text{pass}} + 4\% E_{\text{pass}}$) at the outer edge, while the location around the arc is related to the polar emission angle θ. Thereby, the middle of the arc corresponds to normal emission.

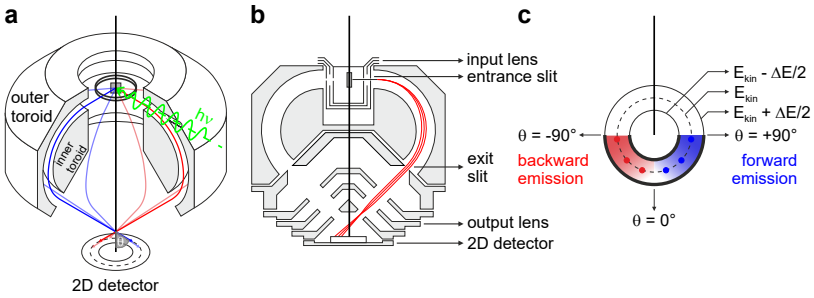

Figure 2.6: Schematic drawing of TEA
a Schematic drawing of the analyzer structure. Incident light beam (green) illuminating the sample (gray) that leads to the emission of photoelectrons in all directions. Those electrons in direction of the energy slit can either emit in forward (blue) or backward (red) emission for positive or negative θ. The trajectories of these electrons are bent between the inner and outer toroids and reach the 2D detector at the bottom of the analyzer. **b** Cross-section of the analyzer structure. **c** Photoemission "arc" as seen by 2D detector, a CCD camera. The electrons arrive between the two thick black lines that define the "arc". The radial distance to the center of the detector is indicative of E_{kin} with maximum (minimum) E_{kin} at outer (inner) border of the arc. The total width of the arc corresponds to $\Delta E_{\text{kin}} \approx 4\%\ E_{\text{pass}}$. The symmetry axis of the system is throughout indicated by a straight, black line. Adapted from X. Yang [105] after Refs. [62, 106] and shown with permission.

Backward and forward emission directions are defined depending on the sign of θ relative to normal emission in respect to the incidence beam. In Fig. 2.6, backward emission (negative θ) is indicated in red and forward emission (positive θ) is indicated in blue. The latter is exemplary drawn into Fig. 2.6**a** at the 2D detector. To obtain the intensity as a function of E_{kin} and polar angle, the LabVIEW-based measurement software requires the user to graphically define the outer and inner circular arcs (bolt black lines in Fig. 2.6**c**), as well as the energy and polar angle steps. Considering the chosen E_{pass}, the program calculates E_{kin} and θ, digitizes the image measured by the CCD camera in terms of its bit rate interpreted as the photoemission intensity which finally leads to the intensity distribution I(E_{kin}, θ). Rotating the sample around its normal and measuring I(E_{kin}, θ) for each ϕ angle, the three-dimensional data cube $I(E_{\mathrm{kin}}, \theta, \phi)$ is obtained. The data acquisition program, which controls the sample positioning via a LABVIEW hardware interface, is able to record the photoemission data in two different modes explained in the next section.

2.4.5 Measurement modes

In the experimental POT experiments, the TEA measures E_{kin} and the emission angle θ of the emitted photoelectrons. Additionally, the sample can be rotated around its normal (azimuthal rotation ϕ) during the measurement leading to a three-dimensional data cube $I(E_{\mathrm{kin}}, \theta, \phi)$. The angles can be recalculated into the reciprocal-space coordinates k_x and k_y considering E_{kin} (Eq. 2.11). Using E_{F} and the work function of the analyzer, E_{kin} is converted into the binding energy E_{b} (Eq. 2.1). Finally, the raw data cube $I(E_{\mathrm{kin}}, \theta, \phi)$ is converted into $I(E_{\mathrm{b}}, k_x, k_y)$ as illustrated in Fig. 2.7**a**. The photoemission intensity data included in this data cube is typically illustrated in two different modes, namely as k maps or band maps.

In one mode, the data cube is cut at a constant E_{b} as depicted in Fig. 2.7**a** resulting in a two-dimensional (k_x, k_y) intensity distribution, the k map. An example is shown for three different E_{b} of bisanthene on Cu(110). To record photoemission data for the k maps technically, the settings of the analyzer are fixed to collect electrons of a chosen E_{kin} and the sample is rotated azimuthally. Note that for each azimuthal orientation of the sample, a polar angle range of approximately $\pm 85°$ is collected. For the conversion of θ and ϕ into k_x and k_y, one can choose to use either positive (forward emission) or negative (backward emission) polar angles, i.e., either [0...+85°] or [0...−85°], relative to the incidence geometry. Note that in normal incidence geometry, these are supposed to be identical except for additional technical effects, e.g., related to an inhomogeneous sensitivity of the MCP. The used ϕ angle range is chosen depending on the sample, particularly dependent on

the rotation symmetry of the substrate. For example, for molecular layers adsorbed on $fcc(110)$ surfaces, it is sufficient to record the photoemission distribution in a ϕ range of slightly more than 90°. To avoid artifacts, typically a ϕ range of 180° is recorded in this case. This allows to reduce the total acquisition time, which is important to minimize beam damage. The incomplete map is completed by applying symmetry operations of the sample surface. Measuring full 360° ϕ range is thus usually not necessary. As already mentioned, the measured E_{kin} ranges in an energy window of $\Delta E_{\mathrm{kin}} = \pm 4\% E_{\mathrm{pass}}$. Dependent on the preformed settings of the digitization of the image recorded by the CCD camera by the measurement program, individual k map slices are recorded where the E_{kin} of two adjacently recorded slices differs by ΔE_{kin}/number of slices.

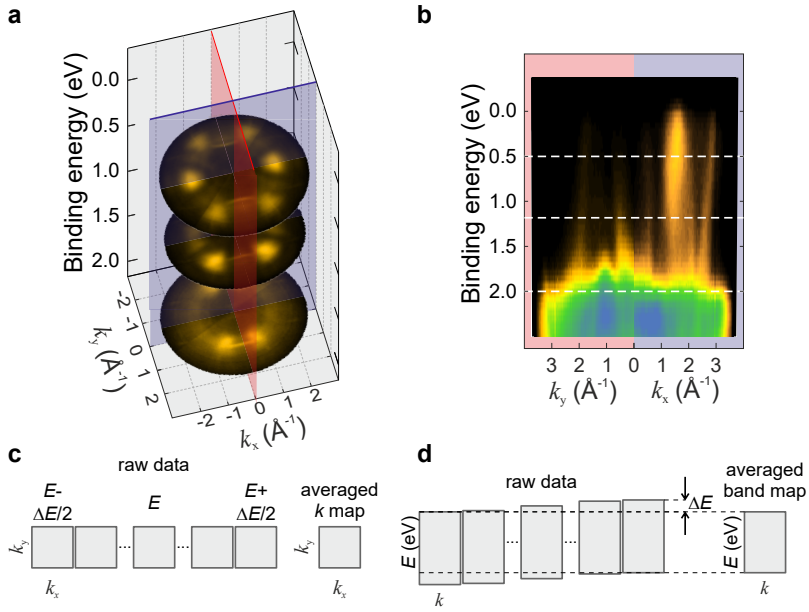

Figure 2.7: Illustration of POT data cube $I(E_{\mathrm{b}}, k_x, k_y)$
a Three dimensional data cube $I(E_{\mathrm{b}}, k_x, k_y)$ with three exemplary k maps of π orbitals of bisanthene/Cu(110) recorded at different E_{b}. The red and blue slice planes mark the cuts through the data cube for the creation of the two **b** band maps recorded along $k_x = 0$ Å^{-1} (red slice) and $k_y = 0$ Å^{-1} (blue slice) on the left and right sides (only shown for positive k values). The white dashed lines denote the E_{b} for the k maps shown in **a**. The sketches illustrating the two measurement modes for **c** k maps and **d** band maps are adapted from Ref. [105].

The upper and lower limits of E_{kin} then yield $E_{\mathrm{kin}} = E + (-)\ \Delta E_{\mathrm{kin}}/2$ with average energy E as displayed in Fig. 2.7**c**. The finally presented k maps are often averaged k maps taking into account several k map slices in the energy range of interest.

In the alternative data representation mode, the data cube is sliced vertically through its center ($(k_x, k_y) = (0,0)$) resulting in two-dimensional (E_{b}, k) intensity distributions – the band maps. In the example of bisanthene on Cu(110) presented in Fig. 2.7, the data cube schematically represented by three k maps in panel **a** is cut along $k_x = 0$ Å^{-1} (red slice) and $k_y = 0$ Å^{-1} (blue slice) resulting in the combined band maps presented in Fig. 2.7**b** (only shown for positive k values) on the left and right sides. Here, the x and y axes correspond to the [001] and [$\bar{1}$10] directions of Cu(110). Because of the specific orientation of molecules on a given surface and a strong anisotropy of emissions from particular π states only the band map along k_x contains emission intensity from the molecules. To be able to visualize the emission features present in the two other k maps of larger binding energies in band maps, the 3D data cube has to be cut in the directions of the desired emission features. This can be realized by rotating the sample to the desired azimuthal angle. During the acquisition of photoemission data for the band maps, the azimuthal rotation of the sample is fixed, while E_{kin} is scanned in a defined energy range. As defined by the electron analyzer and the set E_{pass}, an energy window of $\Delta E_{\mathrm{kin}} = \pm 4\% E_{\mathrm{pass}}$ is recorded in one shot with some mean E_{kin}. To record a band map in a defined E_{kin} range, the measurement is repeated with varying the mean E_{kin} in the desired E_{kin} range. Averaging multiple band maps then results in the final band map as depicted in Fig. 2.7**d**.

In the employed experimental setup, additional parameters can be changed, namely the incidence angle α by tilting the sample around the optical axis of the TEA (perpendicular to the symmetry axis of the system indicated by black, straight lines in Fig. 2.6, i.e., direction of the photon beam marked in green (Fig. 2.6)**a**), or the photon energy by employing different settings of the synchrotron beamline. Correspondingly, the parameter space of our experimental POT experiments can be significantly extended, finally having a multi-dimensional experimental dataset $I(E_{\mathrm{kin}}, k_x, k_y, h\nu, \alpha)$ which allows to study a broad range of effects related to the photoemission from molecules and metals.

A proper calibration and normalization of the so-obtained POT data is vital, if experimental measurement conditions such as the incidence angle (Chapter 6) or the photon energy (Chapter 7) are varied. In the latter, the total intensities of the k maps recorded at different photon energies need to be compared, which requires the normalization of the total k map intensity to the photon flux at varying photon energies. The analysis of POT data was performed with the analysis software `MOZI` written by X. Yang during his PhD thesis at Forschungszentrum Jülich.

2.4.6 Photon flux calibration

Typically, the photon flux of the synchrotron beamlines is strongly photon-energy-dependent, which means that the intensity of the beam changes drastically if the beam energy is varied. Therefore, a precise normalization of the data is needed in order to allow for reasonable comparison of the experimental data measured at different photon energies. Synchrotron beamlines commonly offer to monitor the photon flux using a drain current caused by beam-induced photoemission from some elements of the beamline, e.g., a mirror or specifically introduced meshes such as gold meshes [53]. Since the material of those elements has its own specific photoionization cross sections which is in turn dependent on the photon energy, an additional absolute calibration is required.

At the beamline at MLS in Berlin employed in this work, special care is taken to filter out parasitic contributions of the higher harmonics of the beam. This is done using a set of solid state filters (foils) introduced to the beam line during experiments for particular photon energy ranges [53]. The experiments presented in this work were performed in a photon energy range from 15 eV to 111 eV, which comprises the utilization of six different beamline configurations.The entire photon energy range is consequently split into six ranges realized by varying monochromator, undulator harmonics, and filter settings, namely 15 eV to 31 eV (NI, 3^{rd} harmonic, no filter), 25 eV to 45 eV (GI, 3^{rd} harmonic, Mg filter), 45 eV to 59 eV (GI, 6^{th} harmonic, Al filter), 59 eV to 71 eV (GI, 10^{th} harmonic, Al filter), 71 eV to 87 eV (GI, 10^{th} harmonic, Be filter), and 87 eV to 111 eV (GI, wiggler mode, Be filter) also summarized in Tab. 2.1.

Photon energy range	**undulator**	**filter**
14 eV – 31 eV	3^{rd} harmonic	–
25 eV – 45 eV	3^{rd} harmonic	Mg
45 eV – 59 eV	6^{th} harmonic	Al
59 eV – 71 eV	10^{th} harmonic	Al
71 eV – 87 eV	10^{th} harmonic	Be
87 eV – 115 eV	wiggler mode	Be

Table 2.1: Beamline settings
Undulator, monochromator and filter settings for different photon energy ranges at the beamline at MLS in Berlin.

The beamline at MLS in Berlin produces a known monochromatic photon flux $F_{\mathrm{ph}}(h\nu, \boldsymbol{\epsilon})$, yielding a photon intensity $I_{\mathrm{ph}}(h\nu, \boldsymbol{\epsilon}) = F(h\nu, \boldsymbol{\epsilon})A_{\square}$ on the area $A_{\square}$ from which photoelectrons are detected. The photon flux $F(h\nu, \boldsymbol{\epsilon})$ dependent on the photon energy and the light polarization $\boldsymbol{\epsilon}$ is due to the photon yield $\eta(h\nu)$ and the mirror current i_m.

The final photon flux $F(h\nu, \boldsymbol{\epsilon})$ used to calibrate experimental photon-energy-dependent POT data is then given by

$$F(h\nu, \boldsymbol{\epsilon}) = \eta(h\nu) i_m. \tag{2.63}$$

Therein, the drain current caused by photoemission at the beamline mirror $i_m(t)$ and used for calibration is effected by false light contributions. It is measured in nanoampere during each measurement, i.e., for every kinetic energy measured by the TEA, and is saved with each measurement (for k maps and band maps).

To measure the photon yield $\eta(h\nu)$, an absolutely calibrated semiconductor photodiode has to be inserted into the beam path and thus cannot be measured during the measurements. Instead, $\eta(h\nu)$ is obtained separately from the actual measurements and also saved in a separate file only including $h\nu, \eta$, and the mean error of η. The energy-dependent photon yield curve $\eta(h\nu)$ is measured in units of photons per seconds and nanoampere for each of the six beamline configurations.

In the present work, three sets of photon-energy-dependent POT data are analyzed, namely for three different graphene samples: epitaxial monolayer graphene (EMLG), quasifreestanding monolayer graphene (QFMLG), and quasifreestanding twisted bilayer graphene (QFtBLG) (Chapter 2). For normalization, separate $\eta(h\nu)$ measurements have been performed to enable precise photon flux normalization. Note that the first has been recorded in March 2019 and the other two in July 2019 directly after another. In general, the U125 insertion beamline at MLS guarantees at a metrological level of accuracy that the calibrated photon yield is stable and reproducible. Figure 2.8 shows the calibrated photon yield η measured in three different time intervals plotted against the photon energy. The overall shape of the curves is highly similar for each calibration series and the curves belonging to different settings of the beamline adjoin each other reasonably well except for the two settings before and after 87 eV. Note here that the 87 eV to 111 eV range is measured at a significantly different operation mode of the beamline, namely the wiggler mode.

However, one can distinguish that the curve recorded in March 2019 is shifted to higher values, which means that the photon yield was slightly increased at that time. Moreover, the gap in the photon yield at the transition from the purple to

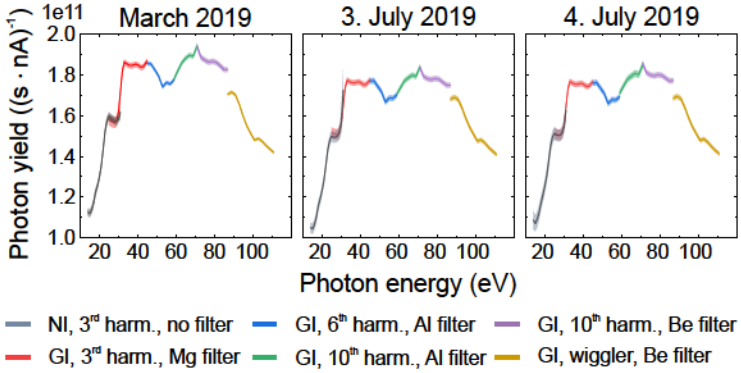

Figure 2.8: Experimental photon yield curve
Calibrated photon yield η for each photon energy recorded in the course of photon-energy-dependent POT data sets in March 2019 (for EMLG) and July 2019 (for QFMLG and QFtBLG). Errors are indicated by shaded area and the colors represent different settings of the beamline (normal incidence NI or grazing incidence GI), undulator harmonics (or wiggler mode), and the used filter. Courtesy of A. Gottwald, H. Kaser and H. Kirschner from PTB, Berlin.

the yellow range at $h\nu = 87$ eV is approximately doubled in March 2019. Crucial at this point is that some photon energies can be set using two different beamline configurations, e.g., 25 eV using the first or second range as can be seen in Tab. 2.1 (15 eV to 31 eV: NI, 3$^{\text{rd}}$ harmonic, no filter or 25 eV to 45 eV: GI, 3$^{\text{rd}}$ harmonic, Mg filter). Thus, the photon-energy-dependent photoemission data measured using different settings of the beamline can be stitched together in order to obtain an extended range of photon energies.

Summarizing, we can conclude that the overall scale and shape of the photon yield is stable and reproducible at the U125 insertion beamline at MLS. Nevertheless, a quantitative study of photon-energy-dependent POT data benefits from prompt yield calibrations because the photon yield does vary over time beyond the calibrated errors for some photon energies.

2.4.7 Treatment of experimental data

The experimental k maps measured at different photon energies need to be normalized properly regarding the photon flux $F_{\mathrm{ph}}(h\nu, \boldsymbol{\epsilon})$ (see Section 2.4.6), the acquisition time (t), and the background intensity. To this end, a step-by-step normalization procedure using the example of EMLG k maps recorded at E_{D} ($E - E_{\mathrm{vac}} = 4.74$ eV) is presented in Fig. 2.9. To trace the intensity of the emission feature in focus, a region of interest (ROI) around the Dirac point is defined in the k map. The intensity within this ROI (white ellipse in Fig. 2.9**a**) is integrated in each k map. For a set of k maps recorded at different photon energies, the integrated photoemission intensity within the ROI is plotted against $h\nu$.

Due to photon-energy-dependent photon flux variations, the measured photoemission intensity changes. As a result, the acquisition time t has to be adopted during the experiment and accounted for in the normalization procedure. If the integrated intensity I is solely divided by the acquisition time t, the intensity distribution shown in Fig. 2.9**c** is obtained. The abrupt jumps in the photoemission intensity at photon energies coinciding with the minimum and maximum photon energies of used beamline configurations indicated by different symbols in Fig. 2.8 suggest a correlation to the measured photon flux $F_{\mathrm{ph}}(h\nu, \boldsymbol{\epsilon})$.

If also the photon flux $F(h\nu, \boldsymbol{\epsilon})$ is taken into account in the normalization ($I/(t{\cdot}F)$), an experimental photon-energy-dependent intensity distribution as presented in Fig. 2.9**d** is obtained. In particular the intensity increase at higher photon energies of the first beamline configuration (15 to 25 eV) points at an insufficiently treated normalization of the integrated photoemission intensity.

Therefore, the intensity of the background is considered in the next step. To this end, four rectangular areas of same size are defined at varying k_x, k_y positions in the k map in Fig. 2.9**a**. The intensities within these rectangular areas are integrated (I_{BG}) and plotted against the photon energy in Fig. 2.9**b** without normalization by the photon flux. One can notice jumps occurring at photon energies where the beamline configurations are to be changed, but also a general variation in the intensity with the photon energy. This is caused by the modified penetration depth of the photons (potentially) enhancing the contribution of photoemission from the substrate for increasing photon energies as well as the cross section. It is important to note that the general evolution of the background intensity is similar for all chosen positions in the k map. This is similarly observed for different background intensities recorded for k maps at other energies $E - E_{\mathrm{vac}}$ of EMLG and QFMLG. For further data analysis, we choose the background area colored in red for this analysis, because it captures I_{BG} in a broad photon energy range. Note that, e.g., the green and blue areas are only non-zero for higher $h\nu$.

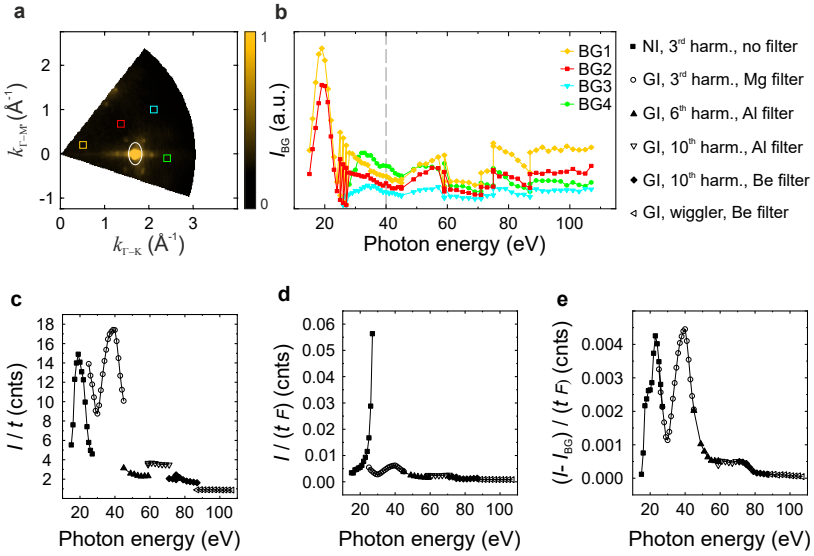

Figure 2.9: Treatment of experimental photon-energy-dependent data **a** Experimental k map of EMLG at E_{D} ($E-E_{\mathrm{vac}} = 4.74$ eV) recorded at $h\nu = 40$ eV. Four rectangular areas representing the background (BG) intensity are drawn in the k maps as well as the ROI for the Dirac point (white ellipse). **b** Integrated intensities of the four BG (I_{BG}) marked in color vs. $h\nu$. **c** Raw integrated intensity of Dirac point taking only the exposure time t for normalization (I/t). **d** Additionally including the photon flux ($I/(t \cdot F)$). **e** $(I - I_{\mathrm{BG}})/(t \cdot F)$.

The final intensity distribution, where the integrated and averaged background intensity I_{BG} is subtracted from the integrated ROI intensity of the emission feature I normalized by the exposure time t and the photon flux F, is presented in Fig. 2.9**e**. The smooth curve shows two clear maxima at $h\nu = 23$ eV and 40 eV, where the first exhibits an additional shoulder at 18 eV. At $h\nu > 57$ eV the integrated intensity remains constant until it further decreases at $h\nu > 73$ eV.

We therefore conclude that in the normalization procedure, of course the exposure time t and the photon flux F have to be taken into consideration, but the background intensity plays an evenly decisive role in the analysis of the photoemission intensity as a function of photon energy. To this end, the analysis software `MOZI` written by X. Yang (former Forschungszentrum Jülich) was extended in this work. The new features in the software are described in Appendix A.

3 | Momentum Space Imaging of σ Orbitals for Chemical Analysis

The applicability of POT to π orbitals is known, but in contrast to σ orbitals they are not always sensitive to local chemical modifications. In this chapter, we show that also σ orbitals can be successfully imaged in POT allowing for a detailed orbital characterization of surface-adsorbed molecules. Therein, experimental binding energies are obtained for multiple π and σ orbitals which are compared to different levels of theory.

The results have been published in two separate journal articles, first in **A. Haags**, X. Yang, L. Egger, D. Brandstetter, H. Kirschner, F. C. Bocquet, G. Koller, A. Gottwald, M. Richter, J. M. Gottfried, M. G. Ramsey, P. Puschnig, S. Soubatch, and F. S. Tautz, "Momentum space imaging of σ orbitals for chemical analysis", Science Advances **8**, 29 (2022) [AH9] focusing on the applicability of POT to σ orbitals to identify reaction products. The second article **A. Haags**, X. Yang, L. Egger, D. Brandstetter, H. Kirschner, A. Gottwald, M. Richter, G. Koller, M. G. Ramsey, F. C. Bocquet, S. Soubatch, F. S. Tautz and P. Puschnig, "Benchmarking theoretical electronic structure methods in a wide binding energy range with photoemission orbital tomography" concentrates on theoretically-derived energies of π and σ orbitals that are compared to experimental projected density of states obtained from the first publication. This article is currently submitted.

The acquisition and analysis of the experimental data as well as writing the first paper have been my contribution in this project. POT experiments were conducted together with colleagues from Karl-Franzens-Universität in Graz, Forschungszentrum Jülich, and Physikalisch Technische Bundesanstalt Berlin. DFT calculations and the development of the analysis software have been performed in the group of P. Puschnig (Karl-Franzens-Universität, Graz, Austria).

3.1 Introduction

The reaction pathway in a chemical reaction can be understood by the modification of the molecular orbitals of the involved molecules. Molecular π orbitals in particular reveal information about the hybridization of a molecule with an underlying substrate, while σ orbitals are sensitive to chemical changes within the molecular backbone. In this chapter, we will show that the latter modifications within a molecule can be traced by POT. This is demonstrated in an Ullmann-type reaction (see Section 3.1.2) where after cleaving C–halide bonds, adjacent biradials are combined by forming C–C bonds. In the reaction under investigation (Section 3.1.3), the formation of C–C bonds is not possible because the molecules are arranged in a brick-wall manner and therefore do not have a bonding partner available. The biradials can instead be saturated with hydrogen or metal adatoms. This is studied by POT of σ orbitals instead of the usually investigated π orbitals. Difficulties in the study of σ orbitals in POT from theoretical and experimental perspectives are summarized in Section 3.1.4. The POT results are presented and discussed in Section 3.2.

3.1.1 Orbitals in surface chemical analysis

It is well-established in literature that the reactivity and the reaction pathway in chemical reactions can be understood using the molecule's orbitals of smallest binding energies – their frontier orbitals. This was already postulated in the 1950's by K. Fukui [107], who won a joint Nobel prize along with R. Hoffmann in 1981 [108–112]. Frontier orbitals of aromatic molecules are usually composed of p_z orbitals building π states with electron density above and below the molecular plane. If the molecule is adsorbed on a metal surface, the spatial proximity of the π states to metal states results in a modification of their electron delocalization. Consequently, the sensitivity of π states toward hybridization with metal states reveals intriguing details of the chemistry at a molecule/metal interface. However, the frontier π orbitals are expected to be less sensitive to local chemical modifications, in particular the making and breaking of bonds at the molecular periphery. For instance, the substitution of a hydrogen atom by an adatom may lead to only minor perturbations of the π orbitals. For such a change in the molecular arrangement, σ bonds would give a clearer picture, because their electron density is accumulated in direct bonds connecting two atoms and therefore serve as fingerprints for the local chemical structure of a molecule. The possibility to image σ orbitals of molecules in surface chemical reaction consequently opens a path to trace their modifications.

The number of experimental methods which allow to differentiate adsorbates of rather similar molecular backbone structure, e.g., a hydrogenated vs. an adatom-substituted species, is limited. Although the effect of the local chemical environment on the core level binding energy is measured in XPS, this traditional technique to describe on-surface chemical reactions is indirect. Instead, it would be far more revealing to determine the orbitals that are directly involved in the bonding. Vibronic spectroscopies, e.g., Fourier-transform infrared spectroscopies, are much more sensitive to local chemical modifications of the molecule [113–115]. However, the interpretation of complex vibration spectra is challenging and often ambiguous [116]. The scanning probe techniques, for example, scanning tunneling microscopy (STM) and atomic force microscopy (AFM) indeed provide valuable information on modifications of molecules, either concerning their orbital geometry [117, 118] or a strongly modified molecular backbone with sub-angström spatial resolution [119–122]. Yet, STM-based orbital imaging is commonly limited to orbitals close to the chemical potential (Fermi energy E_F) in a typical range of $E_\mathrm{F} \pm 2$ eV. Deeper lying orbitals such as σ orbitals are thus extremely difficult to access. In fact, the strength in AFM lays in elucidating the topography of an object, not orbital imaging, because it is not obvious how particular orbitals contribute to the force interaction between the tip and the object [123].

To date, the POT technique introduced in Chapter 2 enables orbital imaging of molecules on surfaces exclusively for π orbitals. However, if the used photon energy is large enough, the ARPES-based method is not limited to a certain binding energy and momentum range. The analysis of σ orbitals with POT consequently appears within reach. Potential challenges that may arise in expansion of the POT technique are summarized in Section 3.1.4.

3.1.2 Ullmann-type reactions on metal surfaces

Carbon is a key element that is able to form various morphologies at the nanoscale. Carbon-based nanomaterials such as nanoribbons, sheets [124–126], macrocycles [AH3, 127, 128], nanographenes [129, 130] or metal-complexes [125] have been studied extensively in the last decade. Their fabrication requires controlled on-surface synthesis routes. A well-known strategy to form these nanomaterials on surfaces is the Ullmann reaction.

In on-surface Ullmann-type coupling reactions, the polymerization via C–C bond formation between halogen-substituted precursor molecules is guided by the metal-substrate as catalyst. The synthesis of 1D [131–133] and 2D [131, 134–141] polymer nanostructures has been achieved with this bottom-up mechanism successfully from suitable halogenated precursor molecules and reactive noble metal substrates.

It is well-established in the literature that the intermediate of this on-surface reaction is a molecule-adatom species with characteristic C–adatom–C bridges connecting former precursor molecules already at room temperature (RT) [135, 140, 142–145]. This intermediate is stable up to temperatures of roughly 530 K [136]. Its formation relies on the alignment of the precursor molecules on the substrate. Only if the halides of two reaction educts face each other, the halide–C bonds can be cleaved, and replaced by a C–adatom–C bridge. Upon further thermal activation, the adatoms are released and neighboring biradicals are coupled by C–C bonds finalizing the Ullmann-type reaction.

If the arrangement of the precursor molecules on the surface is not suitable and a sought-after C–C bond formation is impossible. The initially dehalogenated positions of the precursor molecules can then either be metalated or hydrogenated. Both, hydrogen and Cu adatoms, are abundantly available and mobile at elevated temperature in the reaction environment on the Cu surface [104, 124]. The competing reaction products require an analytic discrimination, which we use as a test case for POT on σ orbitals.

3.1.3 Potential products of DBBA/Cu(110)

The thermal reaction of 10, 10'-dibromo-9,9'bianthracene (DBBA, $C_{28}H_{16}Br_2$) on noble metal surfaces has proven its applicability in the fabrication of graphene nanoribbons (GNR). On Au(111), armchair GNR are formed at temperatures of 400°C [104, 146], while on the more reactive Cu(111) surface GNR is already formed by annealing to lower temperatures [147–149]. The alignment of GNR can be guided by the vicinal Au(788) surface [150]. According to the literature [35, 148], GNR are not formed in the thermal reaction of DBBA on Cu(110) as a consequence of the molecular arrangement on the surface investigated by STM [148]. In the brickwall-stacking of molecules, dehalogenated carbon sites are facing gaps between two neighboring molecules in the molecular rows above or below but no potential molecular bonding partners. C–C bond formation comparable to other Ullmann-type reactions mentioned before is therefore impossible.

As shown in Fig. 3.1, alternative reaction products of DBBA (**1**) on Cu(110) would be a partly dehydrogenated (**2**), fully dehydrogenated (**3**), hydrogenated (**4**) or Cu-substituted (**5**) bisanthene species. A direct chemical bonding of the carbon atoms in the 10, 10'-positions (**2**) or even of all carbon atoms along the zigzag edge (**3**) to the underlying substrate has already been excluded as reaction products by analysis of the frontier π orbitals with POT [35]. The fully hydrogenated bisanthene (**4**) as the final reaction product has been suggested instead by two independent research groups [35, 148]. However, a potential metalation in the

10, 10' positions with Cu adatoms (**5**) has not been taken into account in Ref. [35], while Simonov et al. [148] mention that the participation of native Cu adatoms in the molecular adsorbate layer cannot be excluded. The saturation partner of the dehalogenated carbon atoms in the 10, 10' positions of DBBA is hence still questionable.

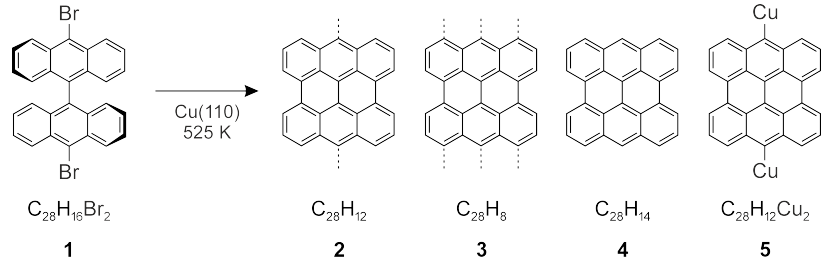

Figure 3.1: DBBA and possible reaction products on Cu(110)
Precursor molecule DBBA and possible reaction products upon adsorption and annealing on Cu(110), namely partly dehydrogenated **2**, fully dehydrogenated **3**, hydrogenated **4** or Cu-substituted/metalated **5** bisanthene species. Dotted lines mark C–substrate bonds.

3.1.4 σ orbitals in POT

The POT technique has only been applied to π orbitals in literature so far. Why the investigation of σ orbitals with POT is challenging from experimental and theoretical point of view is described in the following.

Since the periodicity of the nodal structure of real-space σ orbitals has a smaller length scale compared to π orbitals, the orbital features arise at larger k values in the k maps. Moreover σ orbitals are usually observed at higher binding energies compared to π orbitals due to a greater atomic orbital overlap and thus increased bonding strength. To get access to a sufficiently large photoemission horizon in the k maps and to states of higher binding energies, higher photon energies are required [151]. Exemplary for the case of the topmost $\sigma(0,8)$ orbital, the emission lobes are expected at a $k_{||}$ value of ≈ 2.9 Å^{-1} corresponding to a final-state E_{kin} of about 32 eV. Taking into account the binding energy of this state, the work function, and potential measurement artifacts at the edge of the k maps, a photon energy of approximately 52 eV is required to capture the complete photoemission lobe of this orbital. In this regard, it is important to recall the so-called *universal* curve of the electron mean free path having a minimum at around $h\nu \approx 40$ eV [152].

At higher photon energies the contribution of substrate bulk emission is thus enhanced including the inelastically scattered photoelectrons from the metal. Additionally, for larger photon energies the photoemission crosssections of π [22] as well as presumably σ molecular orbitals drop. As a result the measured experimental intensities will be significantly affected, such as strong emission from the metallic d orbitals of transition metals masks the weak emission from molecular orbitals. This additional background intensity may also hinder the analysis of π states at high binding energies. A good compromise is thus a photon energy where the photoemission horizon captures the complete emission intensities of the orbitals and the emission from the substrate is not too strong. In this work, we thus use a photon energy of 57 eV.

In general, the prediction of orbital binding energies is difficult in DFT calculations, especially for σ states. Due to the only partial correction of the self-interaction error, the binding energies are generally shifted to larger values. This effect is more pronounced for the more localized σ states compared to the rather delocalized π states [153–155]. This may also effect the order of molecular orbitals. The self-interaction error can be counteracted by introducing a certain amount of Hartree-Fock exchange in the functionals. However, using these hybrid functionals is computationally more expensive and their performance depends on the individual molecule/substrate system. It is therefore attractive to measure binding energies of σ orbitals to get an experimental validation of the energy level alignment (see Section 3.3).

3.2 Thermal reaction of DBBA/Cu(110)

The product of the thermal reaction shown in Fig. 3.1 is determined by a sequence of analysis steps. First, experimental band maps in a large binding energy range verify that π and σ orbitals are detectable with POT. For a proper identification of these emissions with k maps, orbitals of an free molecule of bisanthene are calculated. These DFT predictions are followed by a comparison of selected experimental k maps with theoretical ones, finally revealing the actual reaction product after annealing DBBA on Cu(110). Additionally, the experimental data cube $I(E_\mathrm{b}, k_x, k_y)$ measured in a broad binding energy range from about 4.6 eV to 9.6 eV is deconvolved into individual orbital contributions in Section 3.3. The resulting orbital-by-orbital decomposition can be readily compared to the computed MOPDOS which allows to benchmark theoretical simulations of four different functionals.

3.2.1 Band maps

The experimental band maps shown in Fig. 3.2 are recorded along the two high-symmetry directions of Cu(110). Molecular emissions are clearly distinguishable up to $E_b \approx 13$ eV. From earlier experiments we know that the product of the thermal reaction of DBBA on Cu(110) is oriented with its zigzag edges along the substrate [001] direction and with the armchair edges along [1$\bar{1}$0]. The emission along the [001] direction above the metallic d band is identified as the LUMO, which is now occupied due to charge transfer from the metal to the molecule, making it accessible in POT in agreement with Ref. [35]. The characteristic emission lobes of the HOMO and the HOMO−1 are not located along the high-symmetry directions and are consequently not visible in the band maps shown here.

Below the Cu d band, one can clearly identify multiple molecular emissions. At $k_\parallel$ values smaller than 1.5 Å^{-1}, a π band disperses between approximately 4 eV and 10 eV. At $E_b = 5$–13 eV, another band is visible at larger $k_\parallel$, suggestive of σ character. For a precise identification of these molecular emissions, experimental k maps as well as theoretical predictions of all orbitals in a sufficiently large binding energy range and their k maps have to be consulted.

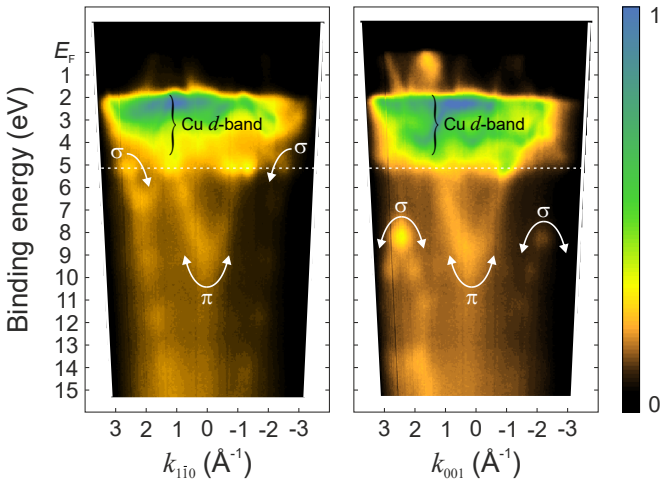

Figure 3.2: Band maps of bisanthene/Cu(110)
Band maps along the [1$\bar{1}$0] and [001] directions of Cu(110) on the left and right, respectively, recorded at $h\nu = 57$ eV. The Cu d band as well as the visible bands of π and σ character are indicated. The white dashed lines denote at which binding energy the k map presented in Fig. 3.6**a** is measured.

3.2.2 Electronic structure calculations

The identification of molecular orbitals is performed by comparison of experimental and theoretical k maps. The latter are calculated based on real-space orbitals of free bisanthene using the Perdew-Burke-Ernzerhof–generalized gradient approximation (PBE-GGA) exchange-correlation functional [156]. The data are available from the online database [157] using the database IDs 406 and 407.

Figure 3.3**a** displays all real-space orbitals of free bisanthene in an energy range from 3.0 eV to 13.5 eV referenced to E_{vac}. The predicted energies $E - E_{\mathrm{vac}}$ are indicated by color shading. The labeling of orbitals first denotes the orbital's π or σ character and second the number of nodal planes along x and y corresponding to the zigzag or armchair directions of the molecule, respectively, and to the [001] and [1$\bar{1}$0] directions of Cu(110). For instance, the LUMO exhibits four (zero) nodal planes along x (y), while the σ(7,3) has seven and three nodes, respectively. One can clearly recognize that with increasing number of nodal planes, the binding energy decreases. In Fig. 3.3, the orbitals are arranged according to the position of their emission lobes closest to the center in their respective k maps. These positions roughly scale with the number of nodal planes along x and y in the real-space orbital. The corresponding k maps of the real-space orbitals are summarized in Fig. 3.3**b**. Note that the emission lobes closest to the center of the k maps move to larger $k_{\parallel}$ values with decreasing E_{b}. It is important to note here that the orbitals of the free molecules are highly similar for hydrogenated ($C_{28}H_{14}$) or metalated ($C_{28}H_{12}Cu_2$) bisanthene. This can be seen for the frontier π orbitals in Fig. 3.4 and in Fig. 3.6 for the orbitals σ(7,3), σ(0,8), and π(0,3).

The presented k maps are used for comparison to experimental ones stemming from the photoemission intensity data cube $I(E_{\mathrm{b}}, k_x, k_y)$. This procedure has been applied successfully to π orbitals in literature [26]. Its effectiveness to σ orbitals is still unknown, especially in view of the fact that its applicability of the PWA is uncertain. The typical comparison of experimental and theoretical k maps by visual inspection or intensity profile scans (e.g, chapter 4, Ref. [AH3]) is extended in this work by deconvolution of the photoemission intensity data cube $I(E_{\mathrm{b}}, k_x, k_y)$. This allows to identify individual orbital contributions in the experimental data. The analysis has been performed in two different approaches, which are explained in Section 3.3. While the first approach originally aimed to identify orbitals, the second procedure focused on the extraction of actual experimental binding energies and spectral lineshapes for each identified orbital. In this work, we mainly present the results of the first approach (Section 3.3), while those of the second are shown in Appendix B (analysis currently still in process).

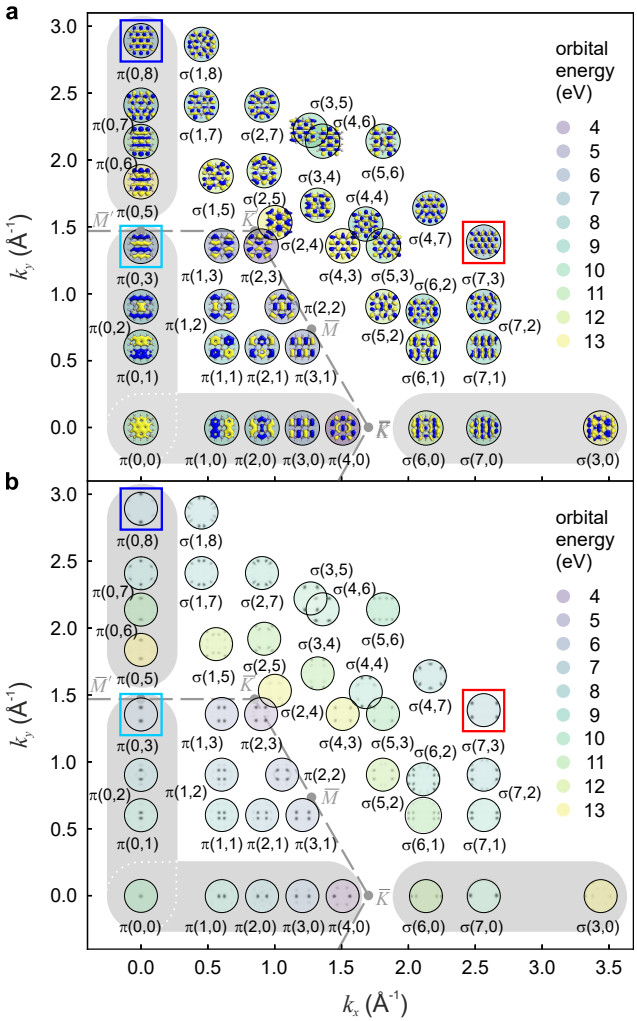

Figure 3.3: Real-space orbitals and DFT k maps of free bisanthene
a Real-space orbitals of free bisanthene and **b** corresponding k maps positioned after the $k_x(k_y)$ position of their emission lobes closest to Γ. Labeling stems from the orbital character – π or σ – and the number of nodal planes along x or y. Color shading represents the predicted energy $E - E_{\mathrm{vac}}$. Gray-shaded areas denote those orbitals visible in the band maps of Fig. 3.2 and gray dashed lines the Brillouin zone (BZ) of graphene.

3.2.3 Identification of adsorption species

Aiming at a distinction between the possible reaction products of hydrogenated ($C_{28}H_{14}$, **4**) or metalated ($C_{28}H_{12}Cu_2$, **5**) bisanthene (see Fig. 3.1), the analysis of multiple orbitals is possible and even required. The identification of the adsorption species proceeds in three steps. In the beginning, we focus on the analysis of frontier orbitals. Later, σ and π orbitals observed directly below the Cu d band are discussed separately in Section 3.2.3.2 and 3.2.3.3, respectively. We will show that a simple comparison of experimental and theoretical k maps is insufficient to distinguish between hydrogenated ($C_{28}H_{14}$, **4**) or metalated ($C_{28}H_{12}Cu_2$, **5**) bisanthene. We therefore call for an experimental density of states projected onto single orbitals that can be directly compared to theoretically-predicted molecular orbital projected density of states (MOPDOS).

A quantitative comparison of theory and experiment is achieved by generating an experimental MOPDOS using the experimental data cube $I(E_\mathrm{b}, k_x, k_y)$ on the one hand and theoretical k maps $\mathrm{I}_i(k_\parallel)$ of considered orbitals calculated for the free molecules on the other. In this *orbital deconvolution* procedure the experimental data cube is decomposed into individual orbital contribution, thus providing an orbital-by-orbital characterization. The experimental MOPDOS $a_i(E_\mathrm{b})$ is obtained by a least squares minimization procedure,

$$\chi^2(a_1, a_2, \cdots, a_i) = \sum_{k_x,k_y} \left[I(E_\mathrm{b}, k_x, k_y) - \sum_{i=1}^{N} a_i(E_\mathrm{b}) I_i(k_x, k_y) \right]^2 . \tag{3.1}$$

The N weights a_i of all considered orbitals i are adjusted for each binding energy E_b separately leading to weight functions $a_i(E_\mathrm{b})$ for each orbital – the experimental MOPDOS which can directly be compared to its theoretically calculated counterpart – the MOPDOS based on molecular/substrate calculations.

3.2.3.1 Frontier π orbitals

Fig. 3.4 displays a comparison of experimental to theoretical k maps and MOPDOS. The experimental k maps in Fig. 3.4**a** are recorded at different E_b of 0.47 eV, 1.16 eV, and 1.97 eV ($h\nu$ = 35 eV) and resemble the theoretical k maps of LUMO, HOMO, and HOMO−1 based on free hydrogenated and metalated bisanthene in **c** and **e**. Although there are minor differences discernible by bare eye, an unambiguous assignment of the calculated to the experimental data to one of the two species is impossible based on the three individual k maps.

An additional opportunity to compare theoretical and experimental data is enabled by deconvoluting the three experimental data cubes $I(E_\mathrm{b}, k_x, k_y)$ at moderate bind-

ing energies presented in **a** using the theoretical k maps based on free hydrogenated bisanthene ($C_{28}H_{14}$) as described in the beginning of this section. The resulting experimental MOPDOS is shown in Fig. 3.4**b** and can be directly compared to the theoretical MOPDOS of $C_{28}H_{14}$ or $C_{28}H_{12}Cu_2$ on Cu(110) in Fig. 3.4**d**, **f**, respectively. Just like the k maps, the experimental MOPDOS does not allow to discriminate between the two scenarios. This corroborates a statement described in the beginning of this chapter, namely that frontier π orbitals are less sensitive to local chemical modifications in a molecule, in particular the making and breaking of bonds at the molecular periphery.

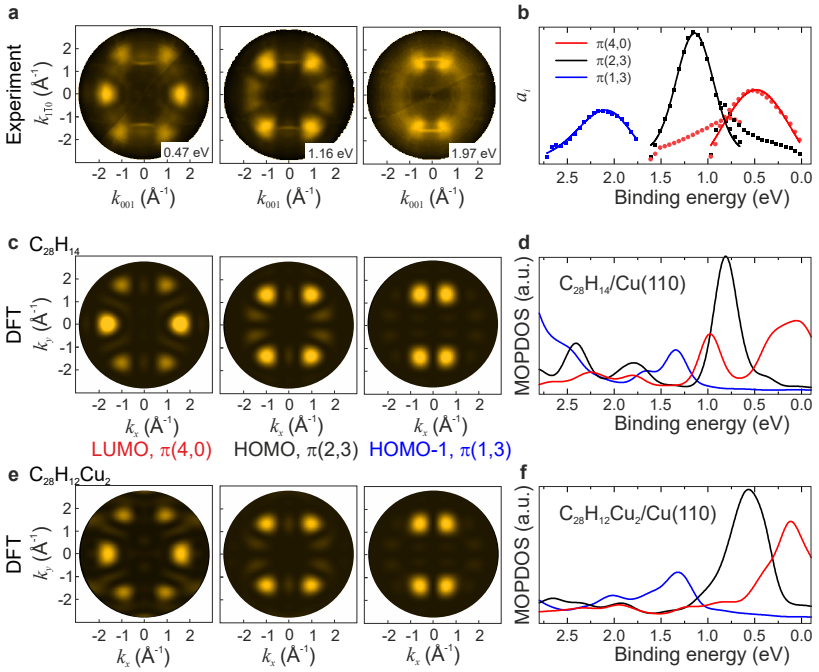

Figure 3.4: k maps and MOPDOS of frontier π orbitals
a Experimental k maps recorded at different binding energies of 0.47 eV, 1.16 eV, and 1.97 eV ($h\nu = 35$ eV). **b** Experimental molecular orbital projected density of states (MOPDOS) from deconvolution of the experimental data cubes $I(E_b, k_x, k_y,)$ using k maps of free $C_{28}H_{14}$ displayed in **c**. Note that qualitatively similar results are obtained when performing the deconvolution with k maps of free $C_{28}H_{12}Cu_2$ in **e**. Theoretical k maps calculated for LUMO, HOMO, and HOMO-1 for free **c** $C_{28}H_{14}$ and **e** $C_{28}H_{12}Cu_2$. DFT-predicted MOPDOS of **d** $C_{28}H_{14}$/Cu(110) and **f** $C_{28}H_{12}Cu_2$/Cu(110).

3.2.3.2 Uppermost σ orbitals

In turn, it is expected that σ orbitals provide clarity in the discrimination between $C_{28}H_{14}$ and $C_{28}H_{12}Cu_2$ as reaction products of DBBA on Cu(110), because they are more sensitive regarding modifications in the molecular periphery. The real-space representations of the orbitals $\sigma(0,8)$ and $\sigma(7,3)$ of smallest σ orbital energy $E - E_{\mathrm{vac}}$ calculated for free $C_{28}H_{14}$ and $C_{28}H_{12}Cu_2$ are displayed in Fig. 3.5. Indeed one of the two uppermost σ orbitals is strongly affected by the choice of the saturation atom in the 10, 10' positions of the molecule as predicted by DFT. Unlike the unaffected lobe structure of $\sigma(7,3)$, a clear modification of electron density is visible for $\sigma(0,8)$ across the whole molecule and in particular in the position of the Cu adatom indicated by the two arrows. A differentiation between the adsorption species $C_{28}H_{14}$ and $C_{28}H_{12}Cu_2$ therefore appears within reach.

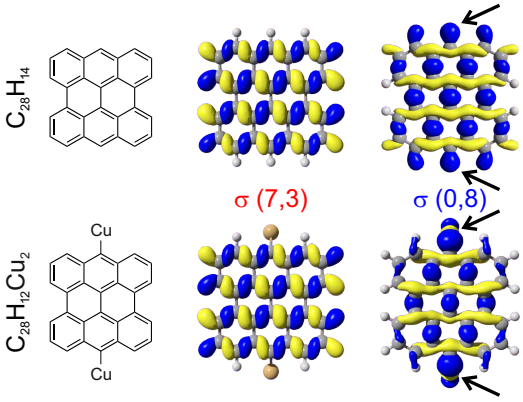

Figure 3.5: $\sigma(0,8)$ and $\sigma(7,3)$ orbitals of $C_{28}H_{14}$ and $C_{28}H_{12}Cu_2$
Skeletal formula and real-space representations of $\sigma(0,8)$ and $\sigma(7,3)$ orbitals of $C_{28}H_{14}$ and $C_{28}H_{12}Cu_2$ in top and bottom rows, respectively. Black arrows indicate obvious changes in the electron density for $\sigma(0,8)$.

To get a qualitative picture, it is worth inspecting the experimental k map measured directly below the Cu d band in direct comparison to the calculated k maps. The measured k map recorded at $E_{\mathrm{b}} = 5.16$ eV has a complex pattern as displayed in Fig. 3.6**a**. The comparison to a k map measured for clean Cu(110) in Fig. 3.6**b** immediately reveals which emissions originate from the substrate or the molecule. Thus, the experimental k map of the bisanthene-like species on Cu(110) in **a** is composed of emissions from several states from the molecular orbitals as well as high-E_{b} tails of the Cu d band indicated by circles and triangles, respectively.

Simulated k maps based on free bisanthene and free metalated bisanthene in Fig. 3.6**c**, **d** reveal that the experimental emissions at $(k_{001},\ k_{1\bar{1}0}) = (0.00,\ \pm 2.89)\text{Å}^{-1}$ (blue circle) arise from the $\sigma(0,8)$, while those at $(k_{001},\ k_{1\bar{1}0}) = (\pm 2.56,\ \pm 1.39)\text{Å}^{-1}$ (red circle) can be from both orbitals, $\sigma(7,3)$ and $\sigma(0,8)$. The emissions at $(k_{001},\ k_{1\bar{1}0}) = (0.00,\ \pm 1.36)\text{Å}^{-1}$ (cyan circle) can be attributed to the $\pi(0,3)$ orbital addressed later in this section (page 61).

A quantitative comparison of theory and experiment is achieved by generating an experimentally-derived MOPDOS using the experimental data cube $I(E_\text{b}, k_x, k_y)$ on the one hand and theoretical k maps $\text{I}_i(k_\parallel)$ of considered orbitals calculated for the free molecules on the other. The experimental data cube is deconvolved (Eq. 3.1) using theoretical k maps of the $\pi(0,3)$, $\sigma(0,8)$, and $\sigma(7,3)$ orbitals of free bisanthene and metalated bisanthene (Fig. 3.6**c**, **d**) in a binding energy range between approximately 5.6 eV and 4.4 eV. The resulting experimental MOPDOS is displayed in Fig. 3.6**e**, **f** using either theoretical k maps of hydrogenated or metalated bisanthene, respectively. We focus on the σ orbitals first and discuss the results of the π orbital later in this section (page 61).

The experimental MOPDOS of the σ orbitals in Fig. 3.6**e**, **f** are remarkably similar, revealing well-defined peaks with related peak widths and energetic positions. In both deconvolution schemes, the $\sigma(7,3)$ orbital is found at smaller E_b than the $\sigma(0,8)$ orbital. The energetic difference is calculated to 0.14 eV and 0.16 eV when deconvoluting with k maps of free $C_{28}H_{14}$ or $C_{28}H_{12}Cu_2$, respectively. The only difference lies in the peak intensities. However, both curves of σ orbitals have higher a_i values than the π orbital. The experimental MOPDOS are compared to theoretical ones of molecule/substrate systems using two different functionals in the next step.

Theoretically-predicted MOPDOS of the $\pi(0,3)$, $\sigma(0,8)$, and $\sigma(7,3)$ orbitals for either bisanthene ($C_{28}H_{14}$) or metalated bisanthene ($C_{28}H_{12}Cu_2$) on Cu(110) are displayed in Fig. 3.7**a**–**d** using PBE-GGA functional [156] and the range-separated hybrid functional due to Heyd, Scuseria and Ernzerhof (HSE) [158, 159]. Focusing on the MOPDOS of the two σ orbitals (blue and red curves), both functionals predict similar shapes of the MOPDOS with peaks of distinct position and comparable width for bisanthene/Cu(110) displayed in Fig. 3.7**a**, **c**. In contrast, in the case of metalated bisanthene on Cu(110) in Fig. 3.7**b**, **d**, the $\sigma(0,8)$ MOPDOS spreads out broadly in energy with its maxima well-separated and at smaller E_b compared to those of $\sigma(7,3)$. This general trend is predicted by both functionals, although the exact shape of the two curves of $\sigma(0,8)$ (blue) is slightly different. The pronounced energy dispersion of $\sigma(0,8)$ indicates a significant hybridization with the substrate also visible in the real-space representation in Fig. 3.5.

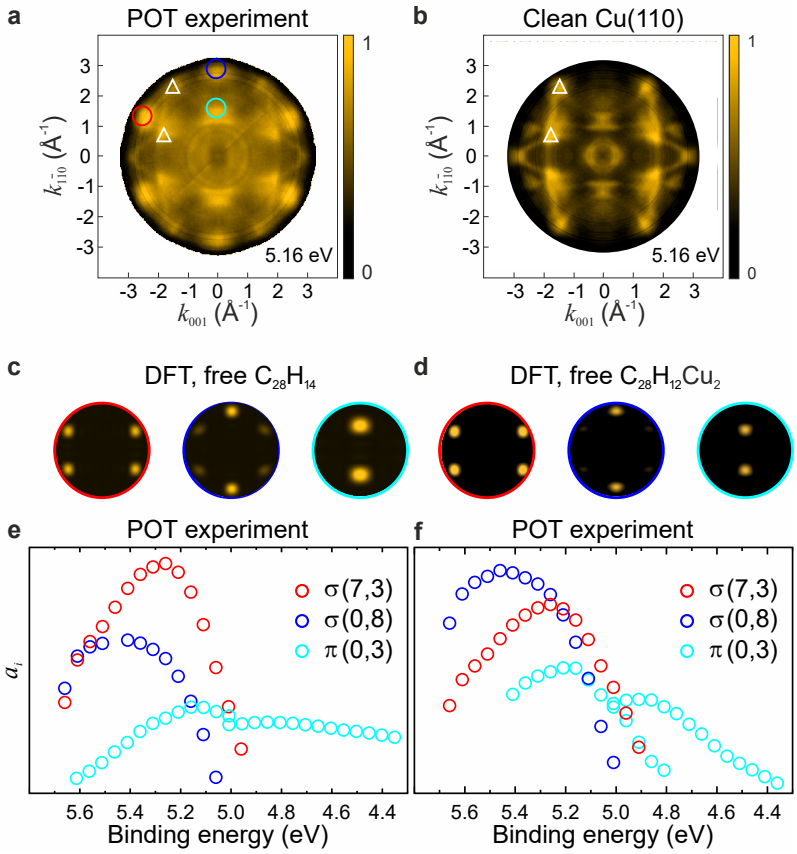

Figure 3.6: *k* maps and experimental MOPDOS
Experimental k maps measured at $E_\mathrm{b} = 5.16$ eV with $h\nu = 57$ eV for **a** bisanthene-like species on Cu(110) and **b** clean Cu(110). Circles and triangles mark emissions from molecular orbitals and metal states, respectively. Calculated k maps of $\sigma(7,3)$, $\sigma(0,8)$, and $\pi(0,3)$ orbitals in red, blue, and cyan based on free **c** $C_{28}H_{14}$ and **d** $C_{28}H_{12}Cu_2$ used for deconvolution. Experimental MOPDOS resulting from the deconvolution using the k maps of free **e** $C_{28}H_{14}$ and **f** $C_{28}H_{12}Cu_2$, respectively. The experimental MOPDOS of $\pi(0,3)$ is discussed on page 61.

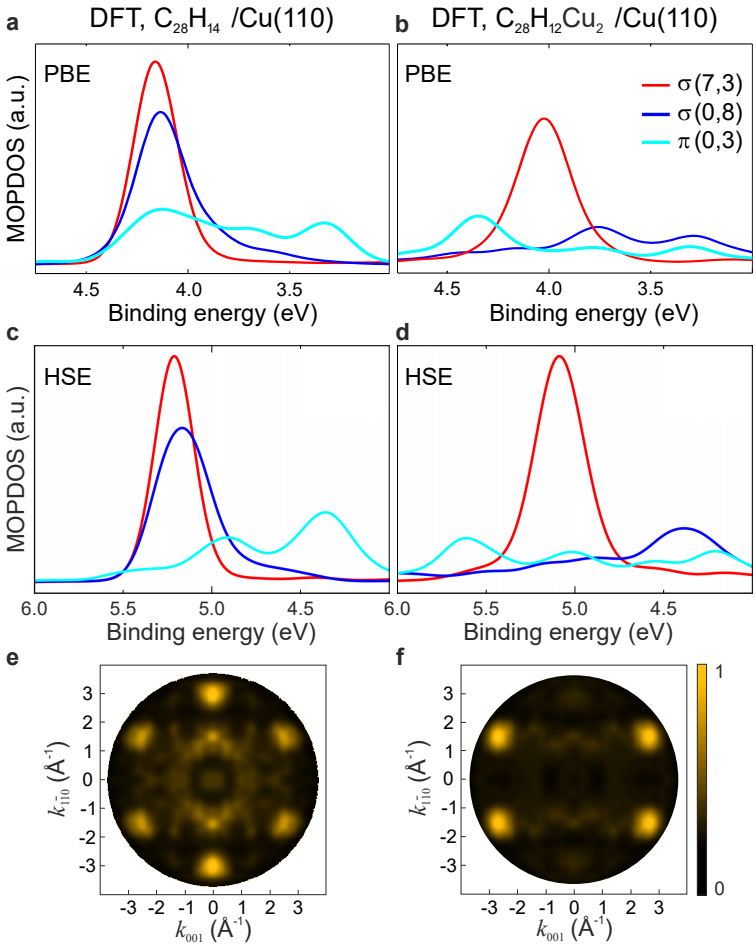

Figure 3.7: MOPDOS and k maps of $C_{28}H_{14}$ and $C_{28}H_{12}Cu_2$ on Cu(110) Theoretical MOPDOS of $\sigma(7,3)$, $\sigma(0,8)$, and $\pi(0,3)$ orbitals in red, blue, and cyan colors for **a** $C_{28}H_{14}$/Cu(110) and **b** $C_{28}H_{12}Cu_2$/Cu(110) using the PBE-GGA functional and **c** $C_{28}H_{14}$/Cu(110) and **d** $C_{28}H_{12}Cu_2$/Cu(110) using the hybrid functional HSE. Theoretical k maps of **e** $C_{28}H_{14}$/Cu(110) and **f** $C_{28}H_{12}Cu_2$/Cu(110) at the calculated $E_b = 3.95$ eV simulated with the PBE-GGA functional.

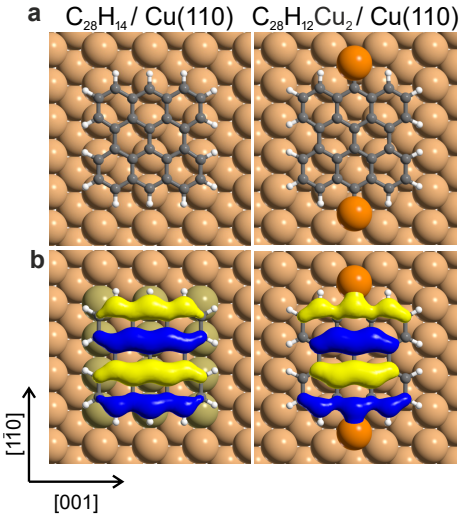

Figure 3.8: Energetically favored adsorption sites
DFT-predicted energetically favored adsorption sites of $C_{28}H_{14}$ (left) at the short bridge and $C_{28}H_{12}Cu_2$ (right) at the hollow site of Cu(110). **a** Backbone of the molecules **b** additionally overlaid with real-space π(0,3) orbital.

The enhanced hybridization of σ(0,8) in the case of metalated bisanthene on Cu(110) is also related to the predicted adsorption site. Namely, geometry relaxations of the two species on the surface either result in the short bridge or the hollow site as the most favorable adsorption sites for bisanthene ($C_{28}H_{14}$) and metalated bisanthene ($C_{28}H_{12}Cu_2$), respectively, as shown in Fig. 3.8**a**, **b**.

In the experimental MOPDOS in Fig. 3.6**e**, **f**, however, we observed well-defined peaks with peak widths and energetic positions in agreement with the predictions of bisanthene ($C_{28}H_{14}$) on Cu(110) (Fig. 3.7**c**, **e**). The metalated product can thus be ruled out, considering the experimental and theoretical MOPDOS.

This is likewise reflected in the calculated k maps of either $C_{28}H_{14}$ or $C_{28}H_{12}Cu_2$ on Cu(110) displayed in Fig. 3.7**e**, **f**, respectively, calculated with van der Waals-corrected DFT using the PBE-GGA functional. The six bright emission lobes at $|k_\parallel| \geq 2$ Å visible in the experimental k map in Fig. 3.6**a** are well-reproduced by the simulated k map for bisanthene/Cu(110) (Fig. 3.7**e**). In contrast, the k map simulated for the metalated adsorption species shows only four emission lobes (Fig. 3.7**f**). The theoretical predictions based on bisanthene/Cu(110) thus agree better with the experimental data considering the MOPDOS and the k maps.

In the experimental k map, an additional emission is visible at smaller $k_{\|}$ values (cyan circle in Fig. 3.6**a**). Moreover, the theoretical MOPDOS predict contributions of the π(0,3) orbitals in the same binding energy range as the σ(0,8) and σ(7,3) orbitals (cyan curves in Fig. 3.7**a**–**d**). We therefore focus on this π(0,3) orbital in the following.

3.2.3.3 π orbitals below Cu *d* band

The experimental k map recorded at E_b = 5.16 eV (Fig. 3.6**a**, $h\nu$ = 57 eV) also exhibits contributions of the π(0,3) orbital with emission along the substrate [1$\bar{1}$0] direction indicated with the cyan circle. According to DFT-predicted MOPDOS (Fig. 3.7**a**–**d**), the energetic dispersion of this orbital extends over a large energy range in contrast to the well-defined σ(7,3) and σ(0,8) orbitals discussed previously. To investigate this noteworthy prediction for the π(0,3) orbital from theory, we record an additional experimental data cube $I(E_\mathrm{b}, k_x, k_y)$ at slightly smaller binding energies in a range of approximately 4.35 – 5.05 eV overlapping with the previous data cube at E_b = 4.95 – 5.75 eV. Since this second measurement is very close in energy to the Cu d band, we use a smaller photon energy of 35 eV to avoid strong substrate contributions and highlight emission from the adsorbate layer.

Fig. 3.9**a** shows a k map from this second experimental data cube recorded at $h\nu$ = 35 eV averaging 15 single k maps in an energy range of 0.2 eV at a mean binding energy of 4.77 eV. Again, the emission lobe of the π(0,3) orbital is visible along k_{001} = 0.00 Å^{-1}. The experimental $k_{1\bar{1}0}$ position of this lobe of ± 1.36 Å^{-1} is in exact agreement with that measured in the k map recorded at $h\nu$ = 57 eV (Fig. 3.6**a**) and with that predicted for free $C_{28}H_{14}$ and $C_{28}H_{12}Cu_2$ (corresponding k maps are shown in Fig. 3.6**c**, **d**, respectively).

π(0,3) orbital

Deconvolution of this experimental data cube ($h\nu$ = 35 eV) using only the k map of the π(0,3) orbital of either free $C_{28}H_{14}$ or $C_{28}H_{12}Cu_2$ results in the experimental MOPDOS plotted in Fig. 3.6**e**, **f**, respectively, in the binding energy range of 4.35 – 5.05 eV. Note that due to the varying photon energies used in the experiment (35 eV and 57 eV), the photon flux changed which also resulted in different acquisition times for the two experimental data cubes $I(E_\mathrm{b}, k_x, k_y)$. The weights a_i resulting from the deconvolution procedures of the two data sets can therefore not directly be compared. Considering the theoretically-predicted MOPDOS, we, however, suspect that the experimental MOPDOS peaks in the higher binding energy range peaking at E_b = 5.16 eV. The important information gained from the deconvolution is, however, more importantly the shape of the curves. Together with the deconvolution results of the experimental data cube recorded at

$h\nu = 57$ eV (Fig. 3.6**a**), we confirm the strong energetic dispersion of the $\pi(0,3)$ orbital predicted by theory in the experiment. In fact, independent of the chosen free species ($C_{28}H_{14}$ or $C_{28}H_{12}Cu_2$), the deconvolution reveals that the contribution of the $\pi(0,3)$ orbital peaks at only slightly smaller binding energy than the two σ orbitals (Fig. 3.6**e**, **f**). A comparison to the theoretically-predicted MOPDOS in Fig. 3.7**a**–**d** shows that this is only correctly predicted for bisanthene/Cu(110) calculated with van der Waals-corrected DFT using the PBE-GGA functional (**a**). Relative to the energetic peak position of the $\sigma(7,3)$ orbital, the HSE functional results in smaller binding energies for bisanthene/Cu(110) (**c**), while both functionals reveal considerably larger binding energies of $\pi(0,3)$ for metalated bisanthene on Cu(110) (Fig. 3.7**b**, **d**). In general, the HSE functional is optimized for self-interaction errors and is therefore expected to perform better in the case of more localized σ orbitals in comparison to PBE. That PBE performs better for delocalized π orbitals is therefore reasonable.

In fact, the strong hybridization of $\pi(0,3)$ provides an intriguing insight into the chemistry at the molecule/metal interface. Its electron density is located on the zigzag chains of bisanthene, which perfectly resembles the periodicity of the substrate lattice in the $[1\bar{1}0]$ direction and bridges three Cu $[\bar{1}\bar{1}0]$ atomic rows along the [001] direction as illustrated in Fig. 3.8**b** (left). This leads to an enhanced hybridization between orbital and metal resulting in the strong energy-broadening observed in the experimental and theoretical MOPDOS. This hybridization is only possible for bisanthene/Cu(110) due to the adsorption site (short bridge). According to DFT relaxations, $C_{28}H_{12}Cu_2$ occupies another adsorption site (hollow) on Cu(110) (Fig. 3.8, right), which has a distinct impact on the hybridization of the orbital with the metal and thus also on the theoretical MOPDOS. The analysis of the deep-lying $\pi(0,3)$ orbital is consequently in full accord with the results of the uppermost σ orbitals. As a result, we confirm fully hydrogenated bisanthene as the final reaction product and validate the investigation of σ orbitals in POT for chemical analysis and validate the investigation of σ orbitals in POT for chemical analysis.

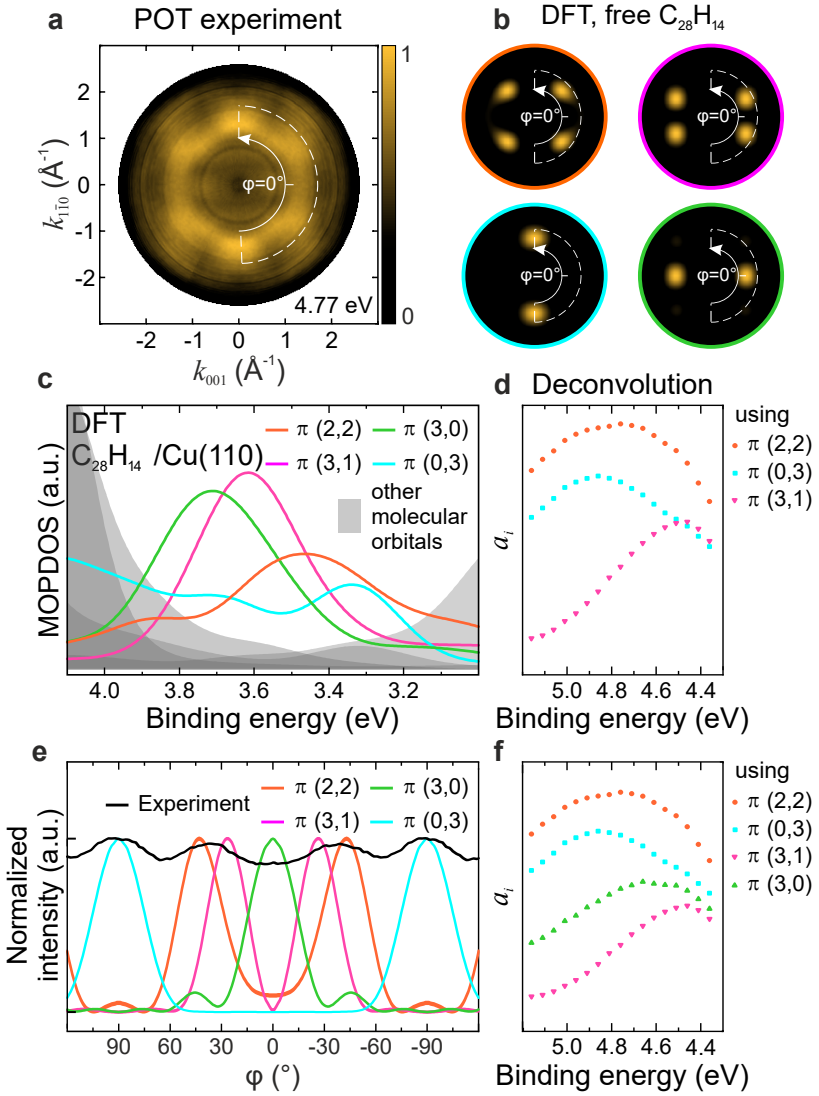

Figure 3.9: Analysis of π orbitals directly below d band
a Experimental k map (E_b =4.77 eV, $h\nu$ =35 eV). **b** Theoretical k maps of π(2,2), π(3,1), π(3,0), and π(0,3) orbitals in orange, magenta, green, and cyan colors calculated for free $C_{28}H_{14}$. **c** Theoretical MOPDOS of these four π orbitals calculated using the PBE-GGA functional for $C_{28}H_{14}$/Cu(110). **e** Normalized radial intensity profiles integrated in the areas marked in white in panel **a** and **c**. Deconvolution results including **d** π(2,2), π(3,1), π(0,3), and **f** additionally π(3,0).

Orbitals π(2,2), π(3,1), and π(3,0)

The experimental k map at E_b = 4.77 eV in Fig. 3.9**a** also shows emissions from other π orbitals. According to the experimental k maps discussed in the beginning of this section, the orbitals LUMO, HOMO, and HOMO−1 (π(4,0), π(2,3), π(1,3)) are observed above the Cu d band and are therefore out of question here. The k maps of the subsequent orbitals HOMO−2, HOMO−3, HOMO−4, and HOMO−5 are shown in Fig. 3.9**b** as π(2,2), π(3,1), π(3,0), and π(0,3) in orange, magenta, green, and cyan, respectively.

According to the DFT-predicted MOPDOS of these orbitals displayed in Fig. 3.9**c**, we expect their contributions in close proximity to each other and within the energetic dispersion range of the π(0,3) orbital (cyan). Indeed, the experimental k map at E_b = 4.77 eV reveals relatively broad but distinguishable emission lobes, in addition to the two lobes of π(0,3) claimed above. These could originate from the overlapping π(2,2) and π(3,1) orbitals with their individual emission lobes located at (k_{001}, $k_{1\bar{1}0}$) = ($\pm$1.00, $\pm$0.95)Å^{-1} and (k_{001}, $k_{1\bar{1}0}$) = ($\pm$1.28, $\pm$0.65)Å^{-1}. If these orbitals would indeed overlap in energy as predicted by DFT, the four emission lobes each of the two orbitals would not be distinguishable anymore but merge into four broad lobes.

Deconvolution

Following the procedure established earlier, a contribution of the four π orbitals would be accessible using deconvolution. This was attempted for this experimental data cube ($h\nu$ = 35 eV) using the four predicted π orbitals in Fig. 3.9**b**, but resulted in ambiguous results concerning the contribution of π(3,0). If this orbital was included, its contribution was strongly exaggerated in the deconvolution scheme recognizable by bare eye looking at the simulated weighted k maps (not shown), while if it was excluded the experimental emission intensity visible along k_{001} (Fig. 3.9**a**) was not captured. The inconclusive deconvolution result is presumably caused by the close proximity to the Cu d band and consequential additional background intensity that is difficult to account for in the deconvolution procedure. In contrast, the contributions of the π orbitals π(2,2), π(3,1), and π(0,3) were unambiguous and resulted in basically the same peak positions at E_b = 4.80 eV, 4.50 eV, and 4.85 eV as can be seen in Fig. 3.9**d**, **f** independent of including/excluding the π(3,0) orbital . If the π(3,0) orbital was included (**f**), its experimental MOPDOS peaked at 4.60 eV.

The unambiguous contribution of the π(3,0) orbital and the overlapping contributions of the π(2,2) and π(3,1) can also be visualized in a more simple way using radial intensity profile scans integrating the emission intensity along the white lines marked in Fig. 3.9**a**, **b**.

Intensity profile analysis

To this end, we extract azimuthal intensity profiles from the experimental and theoretical k maps in Fig. 3.9**a**, **b**. For the intensity analysis, a ring with an inner radius of 1.0 Å^{-1} and fixed width of 0.7 Å^{-1} is defined within the k maps as indicated by the white lines. The intensity along the ring is averaged azimuthally and plotted vs. its azimuthal angle. The angle of $\varphi = 0°$ is indicated in the k maps. Due to the two-fold symmetry of the k maps, the intensity profiles in Fig. 3.9**e** are only plotted in the angular range of $\varphi = \pm 120°$. The profile extracted from the experimental k map is shown in black, while those from the calculated k maps of the orbitals $\pi(2,2)$, $\pi(3,1)$, $\pi(3,0)$, and $\pi(0,3)$ are displayed in orange, magenta, green, and cyan, respectively. Therein, the peaks at $\varphi = \pm 90°$ originate from the $\pi(0,3)$ orbital already identified previously. The peaks in the experimental profile at approximately $\varphi = \pm 37°$ clearly arise from a combination of the peaks from the $\pi(2,2)$ and $\pi(3,1)$ orbitals with their individual maxima located at $\pm 43°$ and $\pm 26.5°$. We therefore confirm the energetic overlap of the orbitals $\pi(2,2)$ and $\pi(3,1)$ as predicted by DFT resulting in four broad emission lobes. These two orbitals are thus identified in the experimental data.

According to the theoretical MOPDOS (Fig. 3.9**c**), the $\pi(3,0)$ orbital is likewise expected within this binding energy window. We would expect its emission in the azimuthal profile at $\varphi = 0°$ (green curve in Fig. 3.9**e**). Yet, the experimental intensity profile does not show a peak at this azimuthal angle for this binding energy (note that the deconvolution shown in panels **d**, **f** would suggest a contribution of the $\pi(3,0)$ at this energy). Nevertheless, there is still intensity along the $k_{1\bar{1}0} = 0.00$ Å^{-1} direction in the experimental k map (Fig. 3.9**a**). A (not shown) intensity profile along a corresponding horizontal line extracted from a k map with $E_\text{b} = 4.96$ eV shows clear peaks at $k_{001} = \pm 1.30$ Å^{-1} in agreement with the position of the emission lobes for the $\pi(3,0)$ orbital. We therefore identify the $\pi(3,0)$ orbital in the experimental data at slightly higher binding energy than the k map shown in Fig. 3.9**a**. This also agrees with the theoretical MOPDOS of $\pi(3,0)$ displayed in Fig. 3.9**c** and the obtained deconvolution curve in **d**, **f**.

In summary, we are able to clearly identify three of the four by theory predicted π orbitals ($\pi(2,2)$, $\pi(3,1)$, and $\pi(0,3)$) in the experimental data cube measured in the binding energy range of approximately 4.35 eV – 5.05 eV. The strong energetic dispersion of the $\pi(0,3)$ orbital even contributes to the identification of the reaction product, namely bisanthene/Cu(110) as opposed to metalated bisanthene. Moreover, we find that explicitly the MOPDOS of $\pi(0,3)$ is only correctly predicted by the PBE-GGA functional, while the HSE fails. The contribution of the $\pi(3,0)$ orbital is ambiguous considering the radial profile scans and the deconvolution.

3.3 Energy level alignment

The deconvolution procedure (Eq. 3.1) used previously to extract experimental MOPDOS and to obtain exact binding energies of orbitals in the experiment opens an additional possibility apart from the identification of reaction products. Namely, our extremely rich set of experimental POT data is ideally suited to benchmark theoretical electronic structure methods. For this purpose, we analyze the complete set of experimental POT data consisting of band maps in an energy range from E_F to $E_\mathrm{b} \approx 15$ eV recorded at $h\nu = 35$ eV, 45 eV, and 57 eV as well as k map data cubes $I(E_\mathrm{b}, k_x, k_y, h\nu = 57\ \mathrm{eV})$ in a binding energy range of approximately 4.1 eV to 10 eV and $I(E_\mathrm{b}, k_x, k_y, h\nu = 35\ \mathrm{eV})$ from $E_\mathrm{b} = -0.4$ eV to $E_\mathrm{b} = 3.2$ eV.

Exact binding energies are either extracted from the band maps resulting in energy distribution curves (EDC) or using deconvolution. The deconvolution of $I(E_\mathrm{b}, k_x, k_y, h\nu = 57\ \mathrm{eV})$ data cubes was performed for π and σ orbitals. The deconvolution of POT data recorded at $h\nu = 35$ eV was, however, only done for π orbitals, because the photoemission horizon of the k maps was too small to capture the emission from σ orbitals (see Section 3.1.4). In this context it is important to note that it is in general difficult to extract the binding energies of the low-lying π orbitals for which the emission intensities are expected at $k_\parallel < 1.15$ Å^{-1} in the k maps due to the diffuse emission intensity in the center therein. Therefore, we additionally use band maps and EDCs as presented in Section 3.3.3.

The deconvolution procedure is performed following two different approaches. While the first approach originally aimed to identify orbitals (Ref. [AH3]), the second procedure focused on the extraction of actual experimental binding energies and spectral lineshapes for each identified orbital. The first approach is applied to frontier π orbitals ($h\nu = 35$ eV) and σ orbitals ($h\nu = 57$ eV). The second approach is applied to both experimental data cubes ($h\nu = 35$ eV: π orbitals and $h\nu = 57$ eV: σ orbitals) in the complete energy ranges. Both approaches are briefly explained in the following Section 3.3.1.

At last in this chapter, the experimentally-derived binding energies are compared to the results of electronic structure calculations based on four widely used functionals. A detailed theoretical evaluation is beyond the scope of this thesis and therefore only described shortly in this chapter. For a complete description of theoretical data, we refer to Ref. [AH13].

3.3.1 Approaches 1 & 2

In the deconvolution analysis, it is crucial to decide which initial state orbitals are included in the fitting process. To this end, two different approaches are used. While approach 1 originally aimed to identify orbitals, approach 2 (still in progress) focused on the extraction of actual experimental binding energies and spectral lineshapes for each identified orbital. In this work, we mainly present the results of approach 1 (Section 3.3), while preliminary results of approach 2 are shown in Appendix B.

The analysis following approach 2 has been revived recently, because details in the deconvolution calculation scheme are still to be optimized due to two problems that were not noticed up to now. One is that the fitted weights a_i of the individual orbitals were allowed to be negative, which has, however, no physical meaning. The other issue only appears, if multiple k maps used in the deconvolution fit are highly similar or even the same. This is, e.g., the case for the two orbitals σ(4,6) and σ(3,5). Logically, if the emission pattern is in general included in the experimental k maps, the contribution of the two orbitals should be similar. However, in the current calculation procedure, the weight of one orbital is set to zero, while the contribution of the other orbital is somewhat exaggerated. The adjustment of both problems is currently in process. Nevertheless, after several preliminary analyses, the so-far extracted binding energies are not expected to change much and are therefore also included in the results in Tabs. 3.6, 3.7, and 3.5. The corresponding preliminary spectral lineshapes for the σ orbitals are shown in Appendix B, while the updated deconvolution curves will be included in Ref. [AH13].

In the following, the two approaches to deconvolve the experimental data cubes $I(E_\mathrm{b}, k_x, k_y)$ are explained.

Approach 1

In the first approach, the decision which initial state orbitals are included in the fitting process depends on the predicted $E - E_\mathrm{vac}$ of the free molecule. In an initial fitting attempt, a broad range of orbitals is included in the fitting procedure resulting in some specific χ^2 which is intended to be minimized. In a next step, several fit models are tested in which single orbitals are included or excluded in order to mainly optimize χ^2 and also to obtain a reasonable qualitative fit between experimental and theoretical $\sum_i a_i(E_\mathrm{b}) \cdot I_i(\boldsymbol{k}_\parallel)$ maps. The final deconvolution result consists of an experimental MOPDOS of multiple orbitals in one energy range of one experimental data cube. The obtained weights from varying measurements (energy ranges), however, can not be directly related. On the one hand, this is due to the single measurement, which were recorded at a certain time lag. There-

fore the experimental data cubes were not taken at the exact same photon flux which influence the emission intensity. On the other hand, a constant background intensity is additionally fitted to the chosen orbitals. A high background intensity would then potentially result in a smaller weighting of the orbitals at certain energies. The results of approach 1 are therefore shown for each range separately in Figs. 3.11, 3.12, 3.13, 3.14, and 3.15.

Approach 2

In the second approach, the only initial input is the experimental data cube and all individual k maps of the orbitals of the free molecule bisanthene. In a first step, a data cube $I(E_\mathrm{b}, k_x, k_y)$ is fitted with a single theoretical k map $I_i(k_x, k_y)$, where the index i labels the orbitals. This is repeated for all orbitals (e.g., $i = 1, \ldots 27$ for σ orbitals see Tab. 3.6). These initial fits with single k maps result in broad peaks that allow to narrow down the binding energy range in which the respective orbital is to be expected. This is done for each energy range separately. In the second step, each data cube is deconvolved using its so-obtained set of contributing orbitals. In these curves, however, the contribution of some orbitals is negligibly small or unstructured in particular energy ranges or the features in the theoretical k maps obviously do not match the experimental one. In such cases, the orbitals are excluded in the next analysis step. Single case-to-case judgments can be found in the SI of Ref. [AH13]. After finding an appropriate fitting model for each energy range, there are multiple deconvolution results $a_i(E_\mathrm{b})$ for each orbital from neighboring energy ranges.

For the same reasons as in approach 1, the obtained MOPDOS from varying measurements (energy ranges) can not be directly related. To overcome this incompatibility in between energy ranges, we interpolate the deconvolution results in neighboring energy ranges (and in some cases of different fitting models in one energy range) for each orbital individually in approach 2. This is exemplary shown in Fig. 3.10 with the original deconvolution results as gray curves and the final MOPDOS in red. The results of all orbitals are shown in Appendix B.

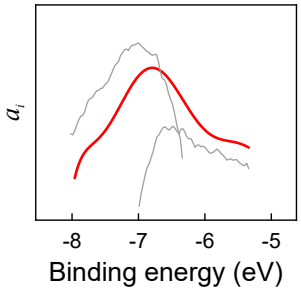

Figure 3.10: Interpolation
Interpolation of original deconvolution results (gray) to obtain final MOPDOS (red) for one orbital from neighboring energy ranges in approach 2.

3.3.2 Experimental MOPDOS of σ orbitals

To identify σ orbitals in the experimental data, we apply the deconvolution procedure to five individual experimental data cubes that overlap in binding energy and were all recorded at $h\nu = 57$ eV. Since the emissions of σ orbitals arise at large $k_\parallel$ in the k maps, we can restrict the deconvolution to well-defined rings within the k maps that only include emissions from σ states. The inner radius of these rings is given in the captions of the deconvolution results for each energy range individually, e.g., $k_\parallel = 2.2$ Å^{-1} in range 1 (Fig. 3.11). Intensities of potential π states in the center of the k maps that would complicate the fitting process are thus omitted.

The results of the deconvolution procedures according to approach 1 are displayed in Figs. 3.11–3.15, which are all constructed in the following way. Four experimental k maps $I(\boldsymbol{k}_\parallel)$ at individual E_b within one data cube are displayed in panels **a**. **b** show the constructed k maps $\sum a_i(E_\mathrm{b})I_i\ (\boldsymbol{k}_\parallel)$ based on the used individual k maps of the orbitals I_i from **d** and the weight factors a_i plotted in **e**. All k maps in **a**, **b** are plotted according to the same color scale in one figure to allow direct comparison. The difference between experimental and constructed k maps $I(\boldsymbol{k}_\parallel) - \sum a_i(E_\mathrm{b})I_i\ (\boldsymbol{k}_\parallel)$ is presented in panels **c** to judge the performed deconvolution procedure. The color scales of these residual k maps is individually adjusted to each binding energy to express the success rate of the deconvolution scheme. Color scale boundaries closer to zero consequently indicate high similarity between experimental and constructed k maps, while larger color scale boundaries imply the opposite and therefore a lacking deconvolution. The theoretical k maps used for deconvolution I_i are displayed in panels **d** and are chosen according to their calculated $E - E_\mathrm{vac}$ as explained in Section 3.3.1. For example orbitals predicted at large $E - E_\mathrm{vac}$ are not taken into consideration in the deconvolution of the experimental data cube in a smaller binding energy range. Thereby, initial mistakes in the choice of the orbitals are immediately prevented. However, this also constitutes an additional initial input apart from with the initial-state orbitals. Information about which orbital is fitted in which energy range is given in Tabs. 3.1, 3.2. To obtain defined E_b for each identified orbital, the experimental MOPDOS of individual orbitals in varying energy ranges are inspected closely. MOPDOS with clear peaks are then fitted with Gaussians which peak positions define the E_b of single orbitals. For clarity, the Gaussian fits are not included in Figs. 3.11–3.15. Yet, the used energy range for E_b identification is indicated in Tabs. 3.1, 3.2 in bold text, e.g., in the case of $\sigma(4,7)$, the orbital is included in the fitting for the energy ranges 1,2, and 3, while E_b of this orbital is extracted from energy range **2**. The $\sigma(2,7)$ is fitted in the ranges 2,3, and 4 and its final E_b is an average of the Gaussian peak positions from the ranges **3** and **4** resulting in E_b =7.54 eV.

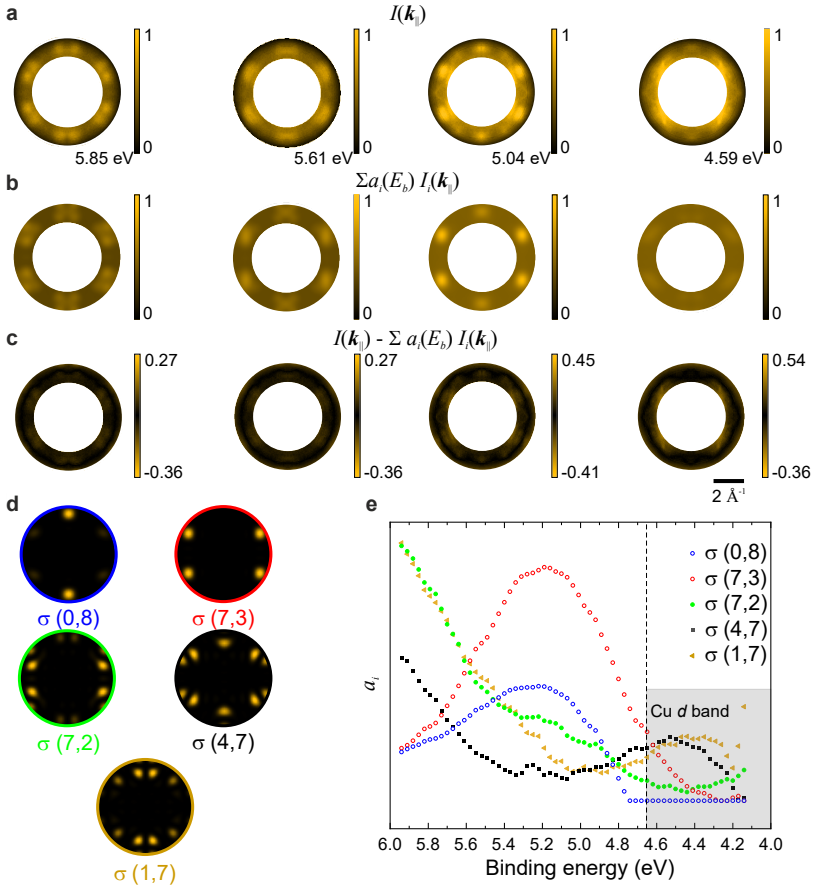

Figure 3.11: Deconvolution of the experimental POT results in the E_b range 1 from 4.15 to 6.00 eV

a Experimental k maps $I(E_b, \boldsymbol{k}_\parallel)$ recorded at binding energies given in the figure. **b** Theoretical k maps $\sum_i a_i(E_b) \cdot I_i(\boldsymbol{k}_\parallel)$ from the deconvolution using the k maps $I_i(\boldsymbol{k}_\parallel)$ of free bisanthene shown in **d** and the fitting parameters $a_i(E_b)$ plotted in **e**. **c** Deconvolution residual $I(E_b, \boldsymbol{k}_\parallel) - \sum_i a_i(E_b) \cdot I_i(\boldsymbol{k}_\parallel)$. **d** Theoretical k maps based on free bisanthene ($C_{28}H_{14}$, **4**) used for deconvolution. **e** Fitting parameters $a_i(E_b)$ – experimental MOPDOS resulting from the deconvolution. All k maps are restricted to $k_\parallel \geq 2.2$ Å^{-1} to exclude emission from π states at small $k_\parallel$.

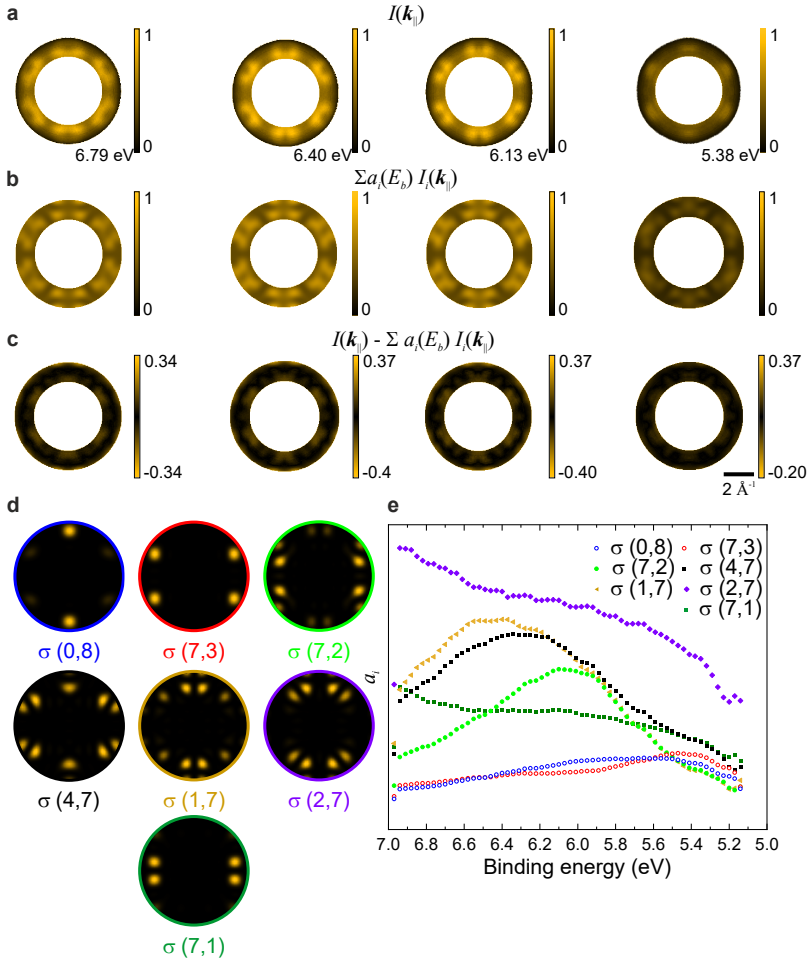

Figure 3.12: Deconvolution of the experimental POT results in the E_b range 2 from 5.15 to 7.00 eV

a Experimental k maps $I(E_b, \boldsymbol{k}_\parallel)$ recorded at binding energies given in the figure. **b** Theoretical k maps $\sum_i a_i(E_b) \cdot I_i(\boldsymbol{k}_\parallel)$ from the deconvolution using the k maps $I_i(\boldsymbol{k}_\parallel)$ of free bisanthene shown in **d** and the fitting parameters $a_i(E_b)$ plotted in **e**. **c** Deconvolution residual $I(E_b, \boldsymbol{k}_\parallel) - \sum_i a_i(E_b) \cdot I_i(\boldsymbol{k}_\parallel)$. **d** Theoretical k maps based on free bisanthene ($C_{28}H_{14}$, **4**) used for deconvolution. **e** Fitting parameters $a_i(E_b)$ – experimental MOPDOS resulting from the deconvolution. All k maps are restricted to $k_\parallel \geq 2.2$ Å^{-1} to exclude emission from π states at small $k_\parallel$.

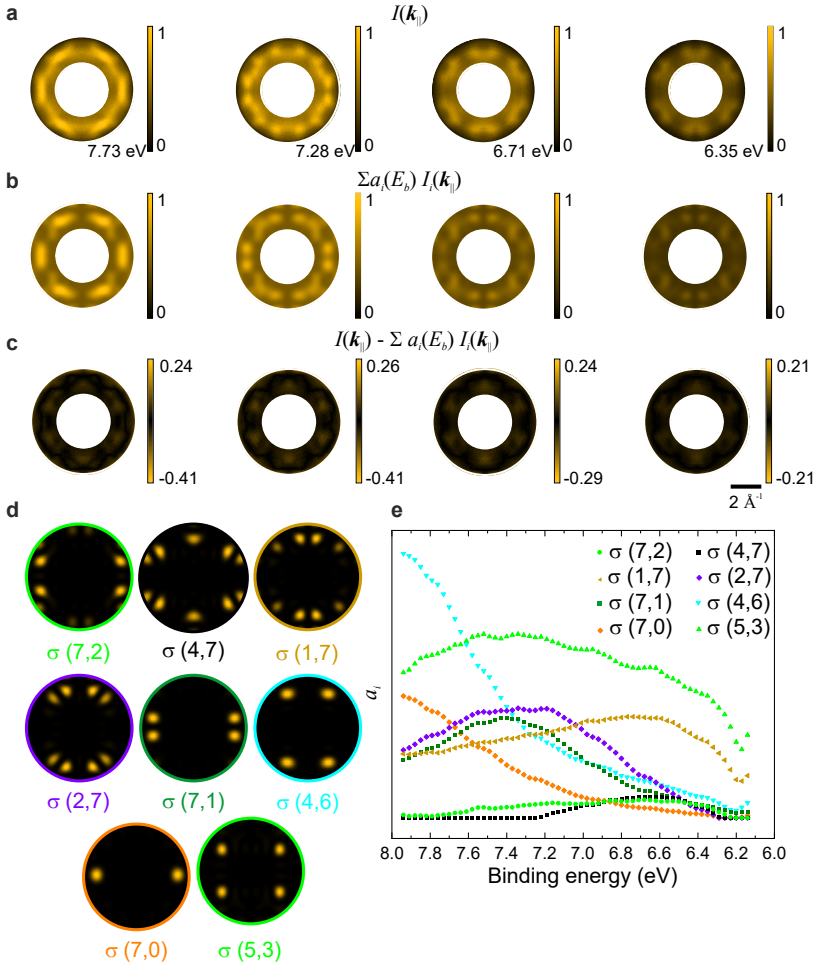

Figure 3.13: Deconvolution of the experimental POT results in the E_b range 3 from 6.15 to 8.00 eV

a Experimental k maps $I(E_b, \boldsymbol{k}_\parallel)$ recorded at binding energies given in the figure. **b** Theoretical k maps $\sum_i a_i(E_b) \cdot I_i(\boldsymbol{k}_\parallel)$ from the deconvolution using the k maps $I_i(\boldsymbol{k}_\parallel)$ of free bisanthene shown in **d** and the fitting parameters $a_i(E_b)$ plotted in **e**. **c** Deconvolution residual $I(E_b, \boldsymbol{k}_\parallel) - \sum_i a_i(E_b) \cdot I_i(\boldsymbol{k}_\parallel)$. **d** Theoretical k maps based on free bisanthene ($C_{28}H_{14}$, **4**) used for deconvolution. **e** Fitting parameters $a_i(E_b)$ – experimental MOPDOS resulting from the deconvolution. All k maps are restricted to $k_\parallel \geq 1.6$ Å^{-1} to exclude emission from π states at small $k_\parallel$.

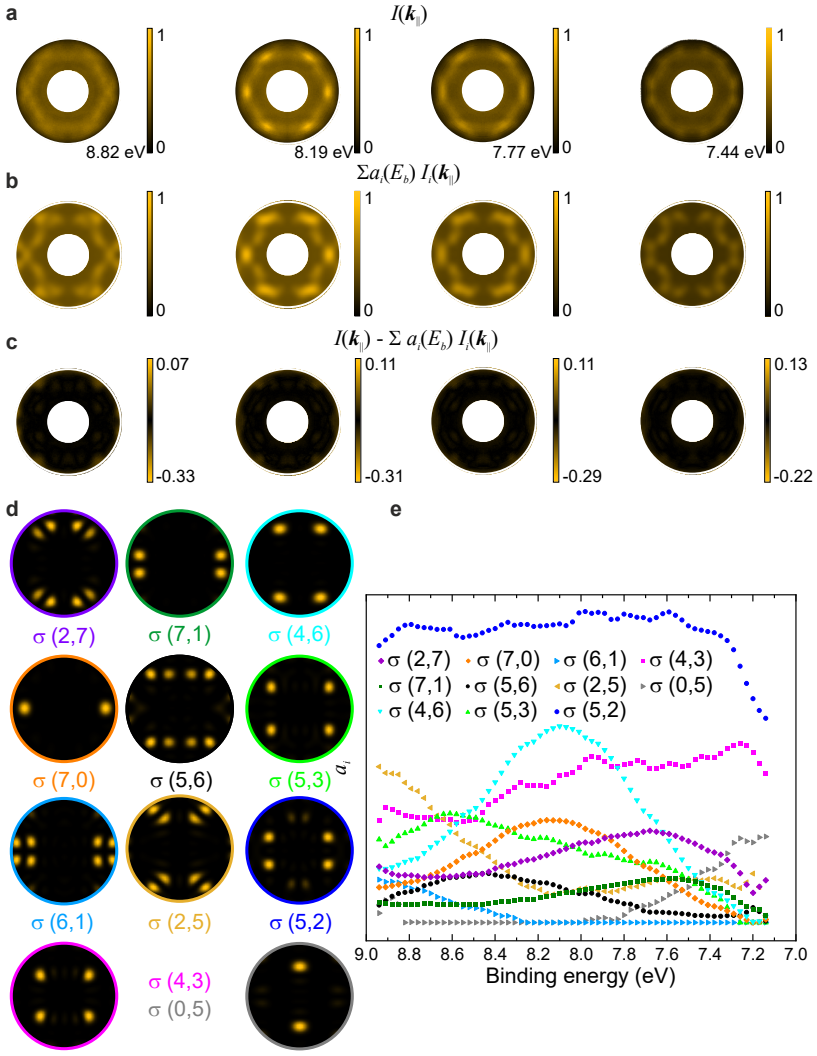

Figure 3.14: Deconvolution of the experimental POT results in the E_b range 4 from 7.15 to 9.00 eV

a Experimental k maps $I(E_\mathrm{b}, \boldsymbol{k}_\parallel)$ recorded at binding energies given in the figure. **b** Theoretical k maps $\sum_i a_i(E_\mathrm{b}) \cdot I_i(\boldsymbol{k}_\parallel)$ from the deconvolution using the k maps $I_i(\boldsymbol{k}_\parallel)$ of free bisanthene shown in **d** and the fitting parameters $a_i(E_\mathrm{b})$ plotted in **e**. **c** Deconvolution residual $I(E_\mathrm{b}, \boldsymbol{k}_\parallel) - \sum_i a_i(E_\mathrm{b}) \cdot I_i(\boldsymbol{k}_\parallel)$. **d** Theoretical k maps based on free bisanthene used for deconvolution. **e** Fitting parameters $a_i(E_\mathrm{b})$: experimental MOPDOS resulting from the deconvolution. All k maps are restricted to $k_\parallel \geq 1.3$ Å^{-1} to exclude emission from π states at small $k_\parallel$.

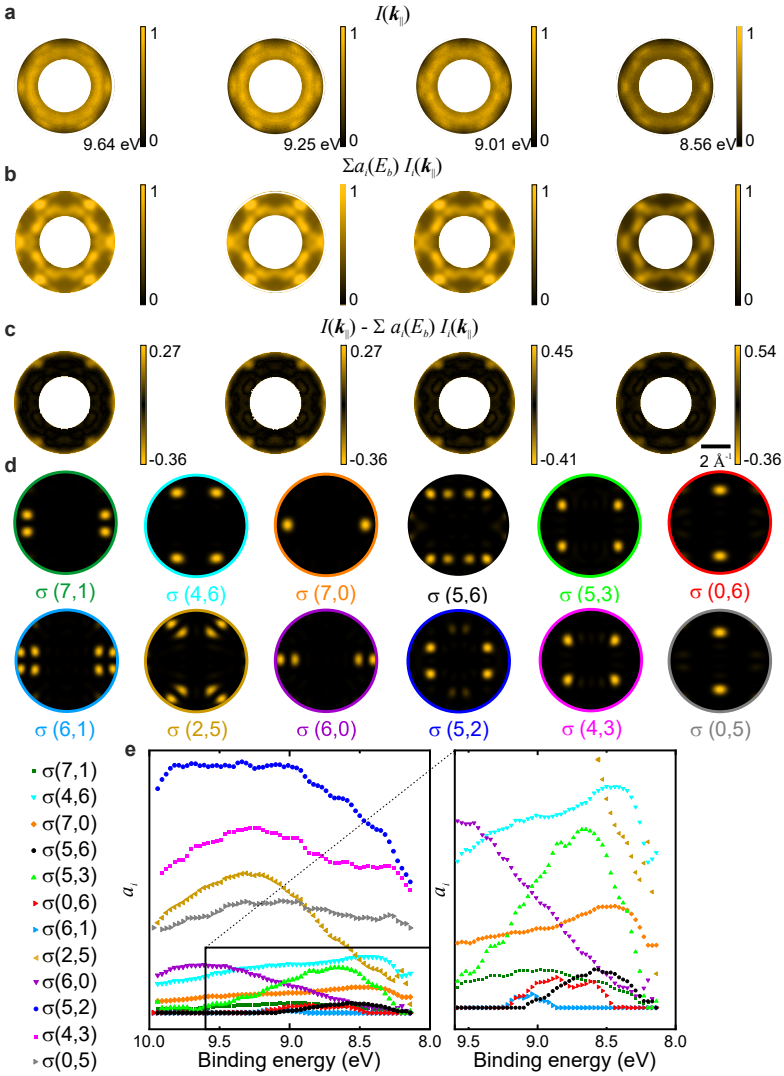

Figure 3.15: Deconvolution of the experimental POT results in the E_b range 5 from 8.15 to 10.00 eV

a Experimental k maps $I(E_\mathrm{b}, \boldsymbol{k}_\parallel)$ of E_b given in the figure. **b** Theoretical k maps $\sum_i a_i(E_\mathrm{b}) \cdot I_i(\boldsymbol{k}_\parallel)$ from the deconvolution using the k maps $I_i(\boldsymbol{k}_\parallel)$ of free bisanthene shown in **d** and the fitting parameters $a_i(E_\mathrm{b})$ plotted in **e**. **c** Deconvolution residual $I(E_\mathrm{b}, \boldsymbol{k}_\parallel) - \sum_i a_i(E_\mathrm{b}) \cdot I_i(\boldsymbol{k}_\parallel)$. **d** Theoretical k maps based on free bisanthene used for deconvolution. **e** Fitting parameters $a_i(E_\mathrm{b})$: experimental MOPDOS resulting from the deconvolution. All k maps are restricted to $k_\parallel \geq 1.7$ Å^{-1}.

The following Tabs. 3.1 and 3.2 show in which energy range each orbital was fitted in both approaches as well as its determined E_b (eV). The numbers 1 to 5 in the second and 5th columns refer to the energy ranges **1**: 4.14 eV – 5.97 eV; **2**: 5.14 eV – 6.97 eV, **3**: 6.14 eV – 7.97 eV, **4**: 7.14 eV – 8.94 eV, and **5**: 8.14 eV – 9.97 eV of the five experimental data sets. The bold numbers in the case of approach 1 denote in which energy range a clear peak is observed that is used to determine the E_b of the corresponding orbital by Gaussian fits. In some cases, no clear peak is obtained from the deconvolution fitting, which is expressed in more detail in the column "Peak shape" in the tables. In the case of approach 2, the deconvolution result of sometimes more than one energy range from one orbital is used to calculate its E_b by interpolation (see Fig. 3.10). Therefore, no energy range is marked bold in that case. The E_b difference between the two approaches given in the last column of the two tables is calculated as $\Delta E = E_b$ (Approach 2) $- E_b$ (Approach 1).

	Approach 1			**Approach 2**		
σ **orbital**	**Fitted in range**	E_b **(eV)**	**Comment**	**Fitted in range**	E_b **(eV)**	ΔE **(eV)**
0,8	**1**, 2	5.37	clear peak	1	5.31	−0.06
7,3	**1**, 2	5.24	clear peak	1, 2	5.29	0.05
1,8	–	–	–	1,2	6.04	–
7,2	1, **2**, 3	6.09	clear peak	1, 2, 3	6.24	0.15
4,7	1, **2**, 3	6.44	clear peak	1, 2, 3	6.40	−0.04
1,7	1, **2**, **3**	6.56	clear peaks	2, 3	6.79	0.23
0,7	–	–	–	2, 3	6.79	–
2,7	2, **3**, **4**	7.54	clear broad peak	3	7.35	−0.19

Table 3.1: Energy ranges and E_b of individual σ orbitals
σ orbital label, namely the number of nodal planes n and m along the x and y directions. Used energy ranges and determined E_b of σ orbitals using deconvolution according to approaches 1 and 2. The numbers refer to the energy ranges of the experimental data cubes $I(E_b, k_x, k_y)$: **1**: 4.14 eV – 5.97 eV, **2**: 5.14 eV – 6.97 eV, **3**: 6.14 eV – 7.97 eV, **4**: 7.14 eV – 8.94 eV, and **5**: 8.14 eV – 9.97 eV. ΔE is the difference in E_b between the two approaches calculated as $\Delta E = E_b$(Approach 2) $- E_b$(Approach 1). The ordering of the orbitals is adapted from the energies $E - E_{vac}$ from the free bisanthene molecule.

	Approach 1			Approach 2		
σ orbital	Fitted in range	E_b (eV)	Comment	Fitted in range	E_b (eV)	ΔE (eV)
6,2	–	–	–	3	7.31	–
7,1	2, **3**, 4, 5	7.52	clear peak	3, 4	7.51	−0.01
4,4	–	–	–	3, 4	7.75	–
4,6	3, **4**, 5	8.13	sharp peak	4	8.17	0.04
7,0	3, **4**, 5	8.18	clear peak	3, 4	8.26	0.08
3,5	–		–	3, 4	8.18	–
5,6	4, **5**	8.52	small peak	3, 4	8.20	−0.32
5,3	3, 4, **5**	8.66	clear peak	4, 5	8.80	0.14
0,6	**5**	8.91	small double peak	5	9.14	0.23
6,1	4, **5**	9.07	small peak	5	9.18	0.11
3,4	–		–	5	9.33	–
2,5	4, **5**	9.31	clear peak	5	9.36	0.05
6,0	**5**	9.63	broad peak	5	9.65	0.02
5,2	4, **5**	9.27	very broad peak	5	9.84	0.57
1,5	–	–	–	–	–	–
4,3	4, 5	9.27	broad peak	–	–	–
2,4	–	–	–	–	–	–
0,5	4, 5	9.18	very broad	–	–	–

Table 3.2: Energy ranges and E_b of individual σ orbitals
σ orbital label, namely the number of nodal planes n and m along the x and y directions. Used energy ranges and determined E_b of σ orbitals using deconvolution according to approaches 1 and 2. The numbers refer to the energy ranges of the experimental data cubes $I(E_b, k_x, k_y)$: **1**: 4.14 eV – 5.97 eV, **2**: 5.14 eV – 6.97 eV, **3**: 6.14 eV – 7.97 eV, **4**: 7.14 eV – 8.94 eV, and **5**: 8.14 eV – 9.97 eV. ΔE is the difference in E_b between the two approaches calculated as $\Delta E = E_b(\text{Approach 2}) - E_b(\text{Approach 1})$. The ordering of the orbitals is adapted from the energies $E - E_{vac}$ from the free bisanthene molecule.

In total, we are able to experimentally derive the binding energies of 18 and 22 σ orbitals in approach 1 and 2, respectively, in a binding energy range of approximately 4.1 – 10 eV. While at smaller binding energies in approach 1, the deconvolution results in clear peaks in the MOPDOS, broad, small or sometimes double peaks are obtained at larger binding energies $\gtrapprox$ 8.5 eV which concerns 7 σ orbitals (σ(5,6), σ(0,6), σ(6,1), σ(6,0), σ(5,2), σ(4,3), and σ(0.5)). Nevertheless, orbitals identified in both approaches result at similar E_b rather independent on the peak shape. The largest discrepancies $\Delta E = E_\mathrm{b}$(Approach 2) $- E_\mathrm{b}$(Approach 1) are observed for the orbitals σ(5,2) (very broad peak, ΔE =0.57 eV) and σ(5,6) (small peak, $\Delta E = -0.32$ eV), while at the same time one of the smallest ΔE =0.02 eV is obtained for a broad peak (σ(6,0)). In general, the extracted E_b of approach 2 is mostly (for 11 σ orbitals) larger compared to that obtained from approach 1.

The agreement between experimental and theoretical binding energies calculated for the molecule/substrate system is examined in Section 3.3.4 after exact binding energies are obtained for π orbitals in the following section.

3.3.3 Binding energies of π orbitals

In total, theory predicts 14 occupied π orbitals for free bisanthene in the D_Dh point group. Two of those (HOMO and HOMO−1) as well as the formerly unoccupied LUMO are identified at binding energies between E_F and the onset of the Cu d band (see Section 3.2.3.1). Additional four π orbitals are observed directly below the Cu d band according to approach 1 as described in Section 3.2.3.3, which leaves 8 π orbitals to be identified in the experimental data at larger binding energies. Five of those orbitals exhibit no node in either x or y direction, which makes them accessible in the experimental band maps recorded in the high symmetry directions of Cu(110). This is indicated in Figs. 3.2 and 3.16**a** in the band maps recorded at $h\nu$ = 57 eV and 45 eV, respectively. In the four band maps, white lines mark a broad, energy-dispersing intensity that we attribute to the π band. Predominantly, there is no clear emission visible but rather a diffuse band.

Since the band maps are recorded in the high-symmetry directions of the substrate, only molecular orbitals with emission intensity along the same momentum are visible in the band maps. Namely, we observe orbitals with no node along the k_x direction in the band map along the [1$\bar{1}$0] direction of Cu(110) (π(0,0), π(0,1), and π(0,2)), while the orbitals π(0,0), π(1,0), and π(2,0) are visible in the [001] direction. To be able to estimate the binding energies of the five predicted π orbitals ((0,0), (0,1), (1,0), (0,2), and (2,0)), we first consult their calculated k maps based on free bisanthene. The k maps are shown in Fig. 3.16**b** with the π(0,2) (red, dashed) and π(0,1) orbitals (blue, dashed) on the left.The π(2,0) and

π(1,0) orbitals are displayed in Fig. 3.16**b** on the right.The π(0,0) orbital of lowest binding energy has no node perpendicular to the molecular plane in its real-space representation. Therefore, its k map only exhibits one emission lobe in the center of the k maps and defines the bottom of the π band in both band maps.

Note that the positions of the emission lobes in the k maps of orbitals with different number of nodes in one direction (e.g. π(1,0) and π(2,0)) vary, which is exploited in this analysis to obtain the experimental binding energies of the five orbitals. To this end, we integrate the photoemission intensity in the band maps in specific $k_{\parallel}$ ranges according to the position of the emission lobes in their k maps. The individual k positions and $k_{\parallel}$ ranges also indicated in Fig. 3.16**a** are summarized in Table 3.3. The k range is always chosen in a $\pm$ 0.2 Å^{-1} window around the k position of the emission lobe.

Orbital	k **position**	$k_{\parallel}$ **range**
π(0,0)	(0.00 Å^{-1}, 0.00 Å^{-1})	$k_{\parallel} = \pm 0.2$ Å^{-1}
π(1,0)	(0.58 Å^{-1}, 0.00 Å^{-1})	$k_{[001]} =$ 0.78−0.38 Å^{-1}
π(2,0)	(0.92 Å^{-1}, 0.00 Å^{-1})	$k_{[001]} =$ 1.12−0.72 Å^{-1}
π(0,1)	(0.00 Å^{-1}, 0.60 Å^{-1})	$k_{[1\bar{1}0]} =$ 0.80−0.40 Å^{-1}
π(0,2)	(0.00 Å^{-1}, 0.92 Å^{-1})	$k_{[1\bar{1}0]} =$ 1.12−0.75 Å^{-1}

Table 3.3: k positions of deep π orbitals
Calculated k positions of the emission lobes in the k maps (Fig. 3.16**b**) of the π orbitals (0,0), (0,1), (1,0), (0,2), and (2,0) of free bisanthene. k ranges denotes the used momentum range used to integrate the photoemission intensity in the experimental band maps (Fig. 3.16**a**). The resulting energy distribution curves (EDCs) are shown in Fig. 3.16**c**.

EDCs of the five orbitals are extracted from three sets of band maps all measured along the high symmetry directions of Cu(110) but using different photon energies, namely 35 eV, 45 eV, and 57 eV. The corresponding band maps are displayed in Fig. 3.16**a** for 45 eV and in Fig. 3.2 for 57 eV. Note that the maximum E_{b} of the band map recorded along [001] at $h\nu = 35$ eV was 9 eV. The extracted EDCs are plotted in Fig. 3.16**c**.

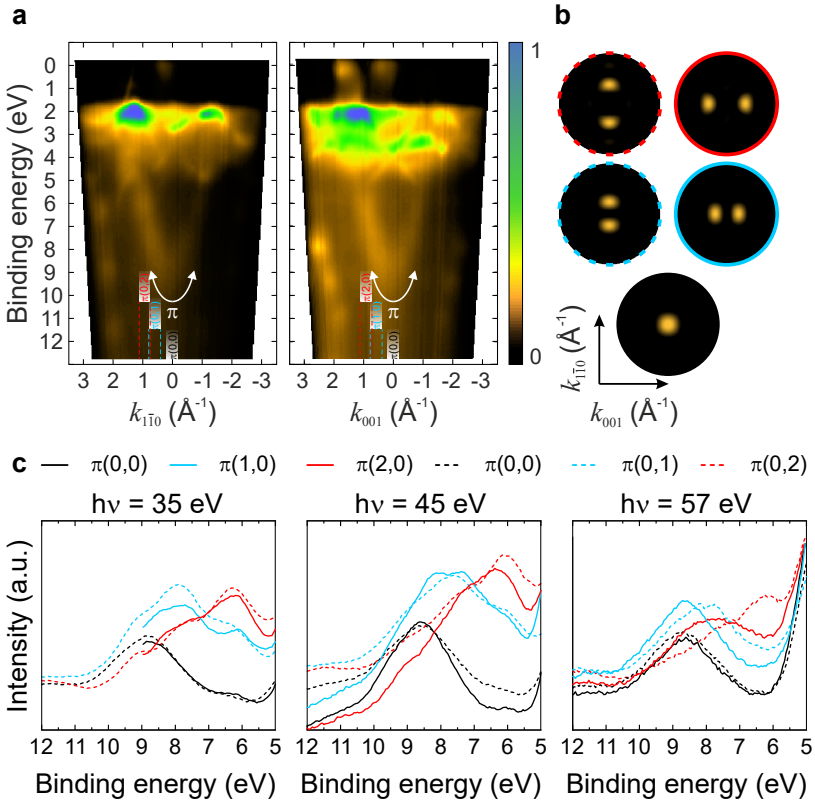

Figure 3.16: Band maps and EDC of deep-lying π orbitals
a Band maps along the [1$\bar{1}$0] and [001] directions of Cu(110), respectively, recorded at $h\nu$ = 45 eV. The π band is indicated with white lines. k ranges for EDC extraction are marked. **b** k maps based on free bisanthene for π orbitals expected to see in the band maps. **c** Integrated EDC extracted from band maps recorded at $h\nu$ = 35, 45, and 57 eV in the [1$\bar{1}$0] and [001] directions of Cu(110) plotted in dashed and solid lines, respectively. $k_{\|}$ ranges for integration are adopted to positions of emission lobes for explicit orbitals under investigation. See text and Table 3.3 for details. EDC of π orbitals (2,0), (1,0) in red and blue solid lines; π orbitals (0,2), (0,1) in red and blue dashed lines. π(0,0) in black.

At first glance, the so-obtained EDCs for single orbitals predominantly show clear maxima that give rise to the exact binding energies of the orbitals. The curves are analyzed separately and fitted by Gaussians to obtain peak maxima. Yet, some EDCs are not taken into account to calculate E_b, because of, e.g., vertical artifacts in the band maps in the required $k_\parallel$ range or no distinct maximum. The final binding energies from the maxima in the EDCs are averaged and summarized in Tab. 3.4 for the π orbitals (0,0), (0,1), (1,0), (0,2), and (2,0).

The remaining so far not mentioned π orbitals (1,1), (2,1), and (1,2) are not visible in the recorded band maps. Initial attempts to deconvolve the corresponding k maps in the experimental data sets recorded at $h\nu = 57$ eV did not succeed using approach 1 explained in the previous section. Using approach 2, we were able to extract exact binding energies, summarized in Tab. 3.4. To date, details in the deconvolution procedure of approach 2 are still to be optimized. Nevertheless, the extracted binding energies up to date are not expected to change and are therefore also included in Tab. 3.4. The corresponding preliminary spectral lineshapes are shown in Appendix B.

Tab. 3.4 thus includes all obtained E_b of the π orbitals of bisanthene. Using approach 1, we are able to identify 12 of the 15 predicted orbitals, while using approach 2 E_b of all orbitals are extracted. The results of approach 1 are either obtained using deconvolution of experimental data cubes recorded at $h\nu = 35$ eV or using EDCs (see table for details). In approach 2, data cubes recorded at $h\nu = 57$ eV and $h\nu = 35$ eV are deconvolved resulting in the E_b indicated with * or **, respectively. In the following, E_b of approach 2 obtained at smaller photon energy are used, because on the one hand, the extracted energy agree better with those of approach 1 and on the other hand, smaller photon energies are expected to be more sensitive to π orbitals, because the contribution from the substrate is diminished. As will be seen later, those E_b^{**} in fact also agree better with theory than E_b^{*} (see Fig. 3.17). To compare the two approaches in the last column, ΔE is calculated as $\Delta E = E_\mathrm{b}^{**}(\text{Approach 2}) - E_\mathrm{b}(\text{Approach 1})$.

In the next section, we compare the extracted E_b from both approaches to theoretical energies calculated for the molecule/substrate system.

π	Approach 1		Approach 2		ΔE
orbital	Identification	E_b (eV)	E_b^* (eV)	E_b^{**} (eV)	(eV)
4,0	Deconvolution	0.5 ± 0.1	–	0.36	−0.14
2,3	Deconvolution	1.2 ± 0.1	–	1.10	−0.10
1,3	Deconvolution	2.1 ± 0.1	–	2.14	0.04
2,2	Deconvolution	4.80 ± 0.1	–	2.34	−2.45
3,1	Deconvolution	4.50 ± 0.1	4.39	4.54	0.07
3,0	Deconvolution	4.60 ± 0.1†	4.79	4.69	0.07
0,3	Deconvolution	5.16*/4.85**	5.18	4.86	0.01
1,2	–		6.34	6.28	–
2,1	–		7.01	6.29	–
2,0	EDC [001]	6.4 ± 0.1	7.74	6.65	0.25
0,2	EDC [1$\bar{1}$0]	6.2 ± 0.1	6.87	6.55	0.35
1,1	–		8.04	6.93	–
1,0	EDC [001]	8.1 ± 0.5	8.83	7.95	−0.15
0,1	EDC [1$\bar{1}$0]	7.9 ± 0.2	8.64	8.00	0.10
0,0	EDC [001] & [1$\bar{1}$0]	8.7 ± 0.1	8.66	9.09	0.39

Table 3.4: E_b of individual π orbitals
Column 1: π orbital label, namely the number of nodal planes n and m along the x and y directions. Column 2: Approach 1: Identification of experimental binding energies using either deconvolution (Fig. 3.4 and 3.9) with k maps recorded at $h\nu = 35$ eV , radial profile scans at one binding energy (Fig. 3.9) or EDCs (Fig. 3.16**c**). Column 3: Resulting experimental binding energy or estimated binding energy range. The results of approach 2 are thoroughly obtained using deconvolution. Deconvolution results using either k maps recorded with Column 4: $h\nu = 57$ eV or Column 5: $h\nu = 35$ eV are indicated by * or **, respectively. Column 6: ΔE is the difference in E_b between the two approaches calculated as $\Delta E = E_b^{**}$(Approach 2) $- E_b$(Approach 1). The ordering of the orbitals is adapted from the energies $E - E_{vac}$ from the free molecule.

3.3.4 Benchmarking theory

We use the extracted experimental binding energies of bisanthene's orbitals in the next step to benchmark the performance of four widely used exchange-correlation functionals within DFT. The detailed orbital-by-orbital assessment of theory and experiment allows to test the different theoretical approaches with regards to the $E-E_{\mathrm{F}}$ alignment of organic/metal interfaces. For more detailed information about the theory, we refer to Ref. [AH13].

Our experimental MOPDOS is compared to the results of four different exchange correlation functionals that are frequently used to describe molecule/metal interfaces, namely (i) PBE-GGA [156], (ii) the range-separated hybrid functional HSE [158, 159], (iii) the popular B3LYP hybrid functional due to Becke et al. [160] as well as (iv) the global hybrid PBE0 [161]. The theoretical data of free bisanthene calculated by these four functionals are available from the online database of P. Puschnig [157]. Note that the simulated orbitals and k maps of the free molecule are robust by the choice of the exchange-correlation functional (see Fig. 4 in Ref. [AH13]). The simulated k maps turn out to be virtually indistinguishable. Nevertheless, the extracted binding energies for the molecule/substrate system referenced to E_{F} vary as can be seen in Tabs. 3.5, 3.6, and 3.7. The tables also include the experimental E_{b} of both approaches. The ordering of the orbitals is adapted from the energies $E-E_{\mathrm{vac}}$ from the free molecule to evaluate whether the energy ordering in the calculation changes if the complete molecule/substrate system is inspected.

Comparing the individual energies of the orbitals, most experimental outcomes agree qualitatively with theory, while the results of some orbitals stand out and are therefore shortly discussed. Concerning π orbitals, the predicted energy of the $\pi(2,2)$ changes significantly if the substrate us included. As a result, approach 1 – in which the orbitals of the initial fit are chosen according to the energies of the free molecule – suggests it to be located below the Cu d band, while in approach 2 this orbital is observed above the Cu d band in rough agreement with the calculated energies of HSE, B3LYP, and PBE0. However, theory still predicts the orbital at higher binding energy compared to that obtained from approach 2. Moreover, the experimental E_{b} of $\pi(1,2)$ obtained from approach 2 occurs to be significantly different than the predicted energies as the experiment suggests it to be at approximately the same E_{b} as the $\pi(2,1)$ orbital, while theory predicts an energetic difference of roughly 0.6 eV. The $\pi(1,2)$ is thus observed at a significantly larger E_{b} compared to the prediction (0.56 eV larger than the largest predicted $|E-E_{\mathbf{F}}|$ using PBE0). In the case of the other π orbitals, the experimental energies are usually within the predicted energy ranges of the four functionals.

Considering the energy level alignment of the π orbitals, the experiment suggests minor rearrangements. Namely, the symmetry equivalent orbitals $\pi(1,2)$ and $\pi(2,1)$ are proposed to be approximately degenerate. Also, both approaches result in a smaller binding energy for the $\pi(0,2)$ compared to the $\pi(2,0)$, while this is reversed for the free molecule. In the case of $\pi(0,1)$ and $\pi(1,0)$, only approach 2 agrees with the predicted order, while approach 1 suggests a larger E_b for $\pi(1,0)$.

	Theory				**Experiment**	
$\boldsymbol{\pi}$	$\boldsymbol{\lvert E - E_\mathrm{F}\rvert}$ **(eV)**				$\boldsymbol{E_\mathrm{b}}$ **(eV)**	
	PBE	**HSE**	**B3LYP**	**PBE0**	**Approach 1**	**Approach 2**
4,0	0.06	0.46	0.63	0.75	0.5 ± 0.1	0.36
2,3	0.81	1.28	1.47	1.64	1.2 ± 0.1	1.10
1,3	2.92	2.27	2.43	2.65	2.1 ± 0.1	2.14
2,2	3.47	2.58	2.74	2.97	4.79	2.34
3,1	3.62	4.57	4.68	4.97	4.47	4.54
3,0	3.71	4.57	4.68	4.98	4.62	4.69
0,3	4.13	4.37	4.50	4.77	4.85	4.86
1,2	4.33	5.31	5.34	5.72		6.28
2,1	4.9	5.82	5.92	6.23		6.29
2,0	5.75	6.66	6.75	7.08	6.4 ± 0.1	6.65
0,2	5.43	6.36	6.44	6.78	6.2 ± 0.1	6.55
1,1	5.86	6.94	7.02	7.36		6.93
1,0	6.59	7.70	7.77	8.11	8.1 ± 0.1	7.95
0,1	6.80	7.88	7.9	8.3	7.9 ± 0.1	8.00
0,0	7.65	8.95	8.79	9.38	8.7 ± 0.1	9.09

Table 3.5: Theoretical and experimental π orbitals
π orbital symmetry label as well as the number of nodal planes n and m along the x and y directions. Calculated π $E - E_\mathrm{F}$ (eV) of bisanthene adsorbed on Cu(110) calculated with the four functionals PBE, HSE, B3LYP, and PBE0. Experimental binding energies $E - E_\mathrm{F}$ obtained using approaches 1 and 2 in the two rightmost columns. The ordering of the orbitals is adapted from the energies $E - E_\mathrm{vac}$ from the free molecule.

σ	DFT: $\lvert E - E_F \rvert$ (eV)				Experiment: E_b (eV)	
	PBE	HSE	B3LYP	PBE0	Approach 1	Approach 2
0,8	4.14	5.17	5.43	5.56	5.37	5.31
7,3	4.16	5.22	5.46	5.61	5.24	5.29
1,8	4.93	6.05	6.27	6.45	–	6.04
7,2	4.98	6.10	6.31	6.49	6.09	6.24
4,7	5.14	6.26	6.47	6.66	6.44	6.40
1,7	5.29	6.43	6.64	6.83	6.56	6.79
0,7	5.38	6.56	6.76	6.96	–	6.79
2,7	5.81	7.00	7.18	7.39	7.54	7.35
6,2	6.02	7.23	7.41	7.63	–	7.31
7,1	6.29	7.48	7.64	7.88	7.52	7.51
4,4	6.25	7.46	7.63	7.86	–	7.75
4,6	6.63	7.88	8.04	8.28	8.13	8.17
7,0	7.02	8.24	8.33	8.65	8.18	8.26
3,5	6.90	8.20	8.34	8.60	–	8.18
5,6	6.88	8.17	8.33	8.57	8.52	8.20
5,3	7.19	8.53	8.66	8.94	8.66	8.80
0,6	7.52	8.88	9.00	9.29	8.91	9.14
6,1	7.61	8.95	9.07	9.35	9.07	9.18
3,4	7.86	9.38	9.48	9.79	–	9.33
2,5	8.01	9.22	9.32	9.62	9.31	9.36
6,0	8.21	9.60	9.69	10.01	9.63	9.65
5,2	8.33	9.81	9.89	10.21	9.27	9.84

Table 3.6: Theoretical and experimental energies of σ orbitals
σ orbital symmetry label as well as the number of nodal planes n and m along the x and y directions. Calculated π $E - E_F$ (eV) of bisanthene adsorbed on Cu(110) calculated with the four functionals PBE, HSE, B3LYP, and PBE0. Experimental binding energies E_b obtained using approaches 1 and 2. The ordering of the orbitals is adapted from the energies $E - E_{vac}$ from the free molecule.

σ	DFT: $\lvert E - E_F \rvert$ (eV)				Experiment: E_b (eV)	
	PBE	HSE	B3LYP	PBE0	Approach 1	Approach 2
1,5	8.66	10.08	10.16	10.49	–	–
4,3	9.30	10.87	10.92	11.28	9.27	–
2,4	9.51	11.00	11.03	11.41	–	–
3,0	9.75	11.25	11.28	11.66	–	–
0,5	9.97	11.57	11.60	11.98	9.18	–

Table 3.7: Theoretical and experimental energies of σ orbitals
σ orbital symmetry label as well as the number of nodal planes n and m along the x and y directions. Calculated π $E - E_F$ (eV) of bisanthene adsorbed on Cu(110) calculated with the four functionals PBE, HSE, B3LYP, and PBE0. Experimental binding energies E_b obtained using approaches 1 and 2. The ordering of the orbitals is adapted from the energies $E - E_{vac}$ from the free molecule.

The comparison of experimental and theoretical σ orbitals energies is more complicated than the discussion of the π orbitals. This is due to the increased number of orbitals fitted simultaneously in the deconvolution procedure, but also because of the two different approaches used in the analysis. Nevertheless, the experimentally-obtained binding energies allow to amend the theoretically-predicted energetic ordering of individual orbitals. This is examined in the following by going through the orbitals in Tab. 3.6, 3.7 from smallest to largest E_b. Since experimental results of orbitals identified using both approaches are supposed to be more reliable, we focus on these orbitals first.

The first discrepancy between experiment and theory is the reverse order of the σ orbitals (0,8) and (7,3) already discussed in Section 3.2.3. Moreover, the energetic difference between these two orbitals is proposed to be much larger in approach 1 (0.13 eV) in comparison to approach 2 (0.02 eV).

The energies of the orbitals σ(2,7) and σ(7,1) are also noticeable, since approach1 proposes them to about degenerate (E_b (2,7) = 7.54 eV and E_b (7,1) = 7.52 eV). Since the MOPDOS of both orbitals are observed as clear peaks (see Tabs. 3.1, 3.2), this appears reliable in contrast to theory predicting energy differences of about 0.5 eV for all four functionals.

Moreover, it is noticeable that the orbitals $\sigma(5,6)$, $\sigma(3,5)$, and $\sigma(7,0)$ are predicted in an energy range of only a few meV. Although approach 2 suggests a similar assimilation of energies, approach 1 does not identify $\sigma(3,5)$ and proposes a significantly larger E_b for $\sigma(5,6)$. This must, however, be regarded carefully considering the peak shape of this orbital discussed in Tab. 3.2. Namely, the MOPDOS of $\sigma(5,6)$ is only a "small peak". The result of approach 1 considering this orbital should thus be taken with care.

Another discrepancy is observed for the three deepest-lying identified σ orbitals under investigation in this energy range, namely $\sigma(5,2)$, $\sigma(4,3)$, and $\sigma(0,5)$. These orbitals are found at significant smaller E_b using approach 1 in comparison to the predicted energies. Checking the peak shapes in Tab. 3.7, however, reveals that their MOPDOS are all "(very) broad peaks" making the determination of exact E_b error-prone and uncertain.

To adequately compare theoretical and experimental binding energies, we compute the mean errors (ME) and mean absolute errors (MAE) with the experimental E_b of orbital i from the deconvolution E_i^exp and the DFT calculation E_i^DFT. This is calculated for both approaches using E_i^DFT of four widely used functionals, namely PBE, HSE, B3LYP, and PBE0. The predicted energies of single π and σ orbitals are included in Tab. 3.5, 3.6, and 3.7.

$$\mathrm{ME} = \frac{1}{N}\sum_i (E_i^\mathrm{exp} - E_i^\mathrm{DFT}) \tag{3.2}$$

$$\mathrm{MAE} = \frac{1}{N}\sum_i |E_i^\mathrm{exp} - E_i^\mathrm{DFT}|. \tag{3.3}$$

The resulting ME and MEA are presented as bar diagrams for π and σ orbitals separately in Figs. 3.17 and 3.18, respectively. The ME is presented in cross-hatched bars, while the MAE is shown in colored bars. The results of approach 1 are shown in red and orange and those of approach 2 in different shades of blue. Since the discrepancy of the $\pi(2,2)$ orbital is particularly severe due to a wrong assignment above/below the Cu d band, the ME and MAE are calculated with and without this orbital. The results with $\pi(2,2)$ are shown in darker color while those without $\pi(2,2)$ are in lighter color.

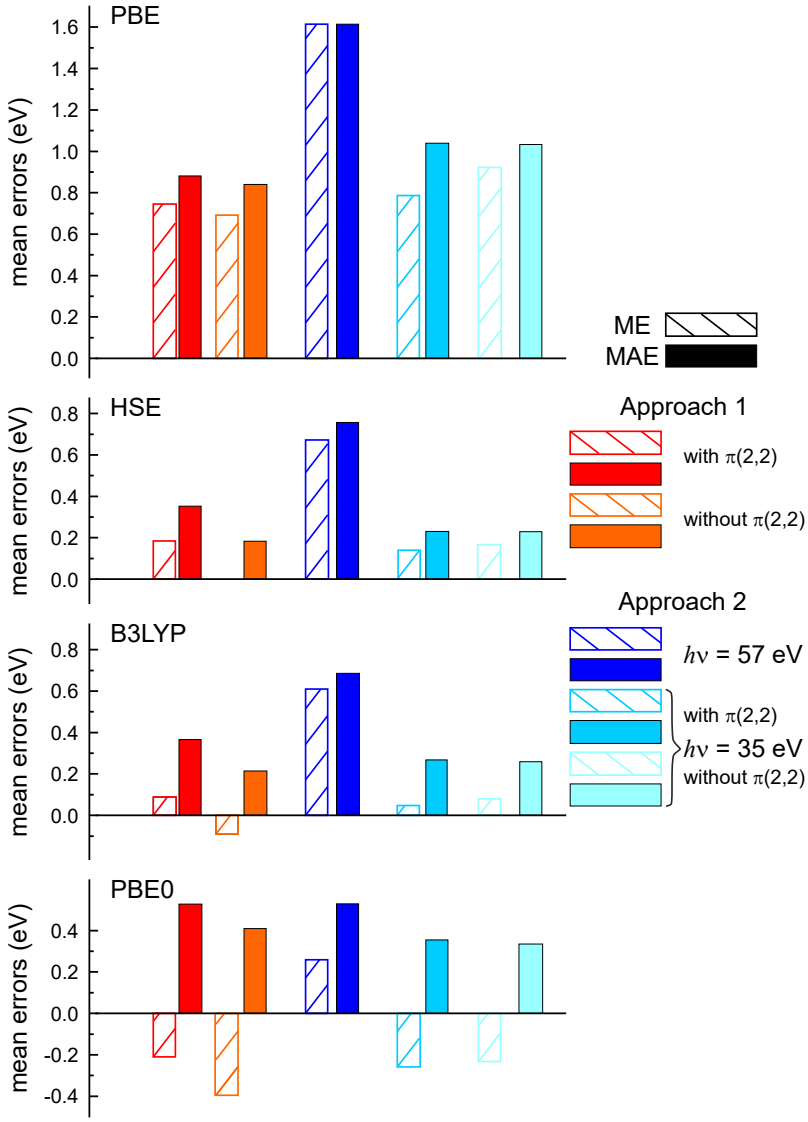

Figure 3.17: Mean and mean absolute errors of π orbitals
Mean errors (ME) (cross-hatched bars) and mean absolute errors (MAE) (colored bars) for π orbitals calculated by Eqs. 3.2 and 3.3 using calculated energies $E - E_{\mathrm{F}}$ of four different exchange-correlation functionals. Since the binding energy of the $\pi(2,2)$ orbital is significantly different in the two approaches, ME and MAE are either calculated with or without this orbital.

For the π orbitals, we see that the largest discrepancies between all single functionals and the experiment arise for the data extracted using approach 2 and the experimental data cube recorded at $h\nu = 57$ eV, which is presumably due to the increased substrate contribution and the reduced sensitivity towards π orbitals at larger photon energies. The largest errors are in general found for the generalized gradient approximation PBE.

The best agreement between experiment and theory is found for approach 1 and the hybrid functional HSE, where we notice a significant reduction of ME if the $\pi(2,2)$ orbital is excluded (ME = 0.19 eV vs. ME = 0.0005 eV – explaining why there is no orange cross-hatched bar for the ME of approach 1 without $\pi(2,2)$). Nevertheless, the performance of B3LYP is similarly satisfying with errors of only 0.05 eV and 0.08 eV with and without the $\pi(2,2)$ orbital in comparison to approach 2.

In the case of the σ orbitals presented in Fig. 3.18, the best agreement is found for the hybrid functional B3LYP. The remarkable agreement is observed for both approaches. Importantly, the ME is only -0.05 eV for approach 1 in comparison to -0.01 eV for approach 2, although approach 2 identified four additional orbitals. If only those orbitals are included found in both approaches (16 orbitals), however, the best agreement is found for approach 2 and B3LYP. That B3LYP performs best for σ orbitals is thus unambiguous. Following the classification of peak shapes from Tab. 3.1, 3.2, we also calculate the ME and MAE for all "clear" peaks (11 orbitals) separately from "broad" or "small" peaks (7 orbitals) for approach 1. As expected the error between clear peaks and the B3LYP functional remains small (-0.04 eV), while for the other peaks the disagreement between theory and experimental increases significantly to -0.66 eV. This means that in the analysis, it is particularly important to ensure reasonable peak shapes and widths.

The largest errors are again found for PBE, for which we observe also a significant difference between the π and σ orbitals. The reason that PBE errors for the σ orbitals are about 0.7 eV larger than for π orbitals can be attributed to the self-interaction error. Namely, the σ orbitals are more localized than π orbitals and therefore more vulnerable to self-interaction errors.

This self-interaction error is clearly weakened in the hybrid functionals by incorporating a fraction α of Hartree-Fock (HF) exchange, which is set to 0.25 for HSE and PBE0 and 0.2 for B3LYP. Since B3LYP performs best for the σ orbitals of the bisanthene/Cu(110) system studied in this work, we conclude that the smaller fraction of HF exchange partly corrects for the overshooting in the ME of PBE0 and compensates for the long-range screening of HSE. That the range-separated HSE functional performs slightly better for π orbitals is presumably because HF exchange is only included in the short range and that in the language of optimally-

tuned range separated hybrid functionals [153, 162, 163], the HSE functional can be viewed as having effectively infinite dielectric screening in the long-range, which seems appropriate for the π orbitals of this system.

That varying functionals perform better for either π or σ orbitals shows that the choice of the functional always needs to be adapted to the investigated system including, e.g., the type of substrate, the molecule-substrate distance, and the orbital under investigation.

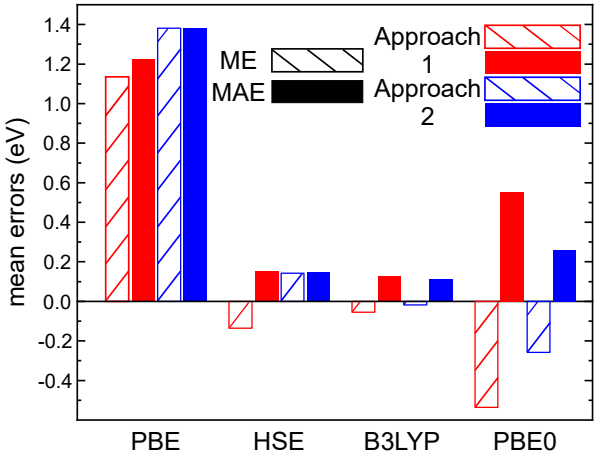

Figure 3.18: Mean and mean absolute errors of σ orbitals
Mean errors (ME) (cross-hatched bars) and mean absolute errors (MAE) (colored bars) for σ orbitals calculated by Eqs. 3.2 and 3.3 using calculated energies $E - E_\mathrm{F}$ of four different exchange-correlation functionals.

3.4 Conclusion

In this chapter, we learn that POT cannot only be applied to π orbitals, but σ orbitals at higher binding energies can also be measured successfully. This results in several new applications of POT. Using the example of bisanthene/Cu(110), the analysis of σ orbitals allows to differentiate between a fully hydrogenated and a metalated reaction product. We identify the fully hydrogenated bisanthene as final product of the thermal reaction of DBBA on Cu(110), which was not possible using frontier π orbitals typically investigated in POT studies. Additionally, employing the orbital deconvolution on several experimental data cubes $I(E_\mathrm{b}, k_x, k_y)$, experimental energies for a extraordinary large binding energy range is obtained.

The analysis is done using two different approaches, which differ in their initial input information and the post-processing of MOPDOS of individual orbitals. The complexity in the approaches and the expenditure of time is clearly smaller in approach 1, where the experimental data cubes are directly fit with multiple orbitals and single MOPDOS curves obtained in one energy range are fitted with Gaussians to extract the binding energies of the single orbitals.

The experimental energies are compared to those calculated for the complete molecule/substrate system using four widely used functionals in order to benchmark the different theories and to validate which approach agrees best with theory.

We conclude that for π and σ orbitals, approach 1 achieves a remarkable agreement to those functionals with fractionally-included HF exchange. While B3LYP matches the experimental σ orbital energies of approach 2 slightly better, HSE is in excellent agreement with π orbitals energies extracted using approach 1. The generalized gradient approximation PBE and the global hybrid functional PBE0, however, do not agree with the experiment. Since the energy level alignment – independent from the exact energies – is the same for all functionals under investigation, the experimentally-observed new order is not correctly predicted in all functionals.

Finally, this chapter shows that measuring and identifying orbitals below the metal d states opens a completely new applicability of POT. We envision that this will provide equally stringent experimental information for benchmarking the performance of electronic structure methods in the future also for other molecule/metal interfaces.

4 | Aromatic Stabilization in Kekulene

The question about kekulene's aromaticity, whether it is better described by Clar's sextet rule or as "superaromatic", is recalled in this chapter focusing on the molecule's frontier orbitals. Conclusions of this chapter are based on information gained by POT of kekulene synthesized on Cu(111) in combination with experimental STM images and DFT calculations.

The results presented in this chapter are partly published in the following journal article: **A. Haags**, A. Reichmann, Q. Fan, L. Egger, H. Kirschner, T. Naumann, S. Werner, T. Vollgraff, J. Sundermeyer, L. Eschmann, X. Yang, D. Brandstetter, F. C. Bocquet, G. Koller, A. Gottwald, M. Richter, M. G. Ramsey, M. Rohlfing, P. Puschnig, J. M. Gottfried, S. Soubatch, and F. S. Tautz, "Kekulene: On-Surface Synthesis, Orbital Structure, and Aromatic Stabilization", ACS Nano **14**, 15766 (2020) [AH3].

The acquisition and analysis of the experimental data POT as well as writing the paper have been my contribution in this project. POT experiments were conducted together with colleagues from Karl-Franzens-Universität in Graz, Forschungszentrum Jülich, and Physikalisch Technische Bundesanstalt Berlin. The synthesis of the precursor molecule and the acquisition of STM data were achieved in the groups of J. Sundermeyer and J. M. Gottfried, respectively (Philipps-Universität Marburg). Theoretical contributions were provided in terms of density functional theory and Hückel theory calculations performed in the group of P. Puschnig (Karl-Franzens-Universität, Graz, Austria) and bond order analysis by M. Rohlfing (Westfälische Wilhelms-Universität, Münster).

4.1 Introduction

Aromaticity is a fundamental concept that is indispensible in modern chemistry [164] ever since the cyclic structure of benzene has been proposed by August Kekulé in 1865 [165]. It is used in organic chemistry in order to explain the stabilization of cyclic, planar molecules by delocalization of electrons in conjugated π electron systems. If in those kind of molecules the number of contributing π electrons is $4n + 2$, where n is a non-negative integer, Hückel's rule predicts aromatic properties. π systems with smaller n are supposed to be more stable.

An exceptional type of aromaticity has been proposed for the prototypical cycloarene kekulene ($C_{48}H_{24}$), namely the so-called "superaromaticity". It involves the π conjugation in two concentric macrocyclic conjugation paths of different sizes [166–174] denoted as [18]annulene and [30]annulene in the case of kekulene as illustrated in Fig. 4.1**a**. In these macrocycles, the number of contributing π electrons is 18 and 30, respectively, which gives $n = 4$ and $n = 7$ applying Hückel's $4n + 2$ rule. Note that the C–C bond lengths are equalized in aromatic π systems indicated by dashed lines for superaromatic kekulene in Fig. 4.1. Whether the concept of superaromaticity exists at all as a mechanism of molecular stabilization has been debated for many years [166–170, 173, 175, 176]. The dispute in literature dealt with the prototypical kekulene molecule, but also with other larger molecules [169, 171].

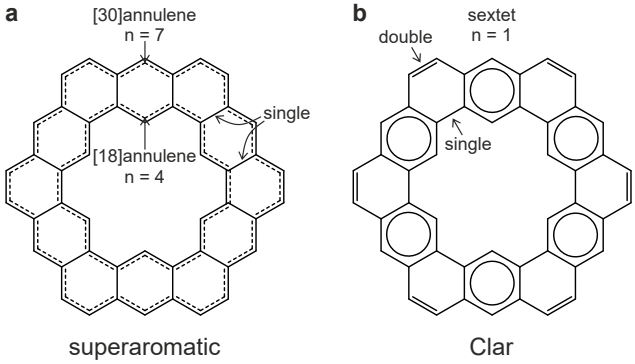

Figure 4.1: Aromaticity models of kekulene
Skeletal formula of **a** "superaromatic" kekulene with two concentric aromatic rings indicated by dashed lines on the left and **b** the Clar configuration with six aromatic benzene rings separated by non-aromatic linkers on the right. Single and double bonds are indicated by "single" and "double", respectively. n refers to Hückel's $4n + 2$ rule.

Following an alternative idea, kekulene is thought to be based on six disjoint aromatic sextets (6 π electrons $\widehat{=}$ n =1) which are indicated by circles in Fig. 4.1**b** [166, 167, 169–174, 177]. According to Clar's sextet rule, the number of disjoint aromatic benzene rings in benzoic molecules should be maximized, while the number of double bonds should be minimized to achieve the highest possible aromatic stabilization.

In both models, aromaticity comes along with geometric and electronic properties of the molecule. While in superaromatic kekulene, all bond lengths contributing to the aromatic stabilization should be equal (dashed lines in Fig. 4.1**a**), this is only valid for benzoic ring units in Clar's model separated from adjacent rings by formal C–C single and double bonds. Electronically, cyclic π electron delocalization responsible for the aromatic character of the molecule is confined to either the [18]annulene or the [30]annulene circuit in the superaromatic model of kekulene and to the six benzoic units in the alternative Clar model. It is crucial to note that both, geometric and electronic properties of kekulene, have to be taken into account when assessing the molecule's aromaticity theoretically and experimentally in order to gain full understanding.

For over 40 years, only one experimental study of kekulene was available [174, 178, 179] which was used as basis for many theoretical investigations on the molecule's aromaticity. The study of the second successful synthesis of kekulene [43] basically focused on structural properties of the molecule. The authors drew conclusions regarding the molecule's aromaticity comparing experimentally and theoretically predicted interatomic distances. Thus, an electronic view on the subject based on experimental data has not been substantiated so far.

In this work, the electronic nature of kekulene is assessed experimentally by angle-resolved photoemission spectroscopy of the molecule's frontier orbitals. The results are compared to two theoretical simulations which describe either the superaromatic or Clar model of kekulene. Thereby, we are able to evaluate kekulene's aromaticity geometrically and electronically.

For the area-averaging technique POT, several requirements of the adsorbate-substrate-system must be fulfilled. Importantly, a sufficient number of the desired adsorbate species must be present on the surface to ensure a sufficiently strong photoemission intensity. This also excludes potential byproducts which would alter the photoemission signal and complicate data analysis. Also, the study in POT becomes more straightforward when the majority of molecules is oriented in the same way, preferably aligned with the underlying substrate. To this end, an on-surface synthesis of kekulene from a specially designed precursor molecule is developed leading to a well-ordered complete monolayer of the desired species.

4.1.1 Literature review

Apart from our publication about kekulene on Cu(111) [AH3], to out knowledge only two other experimental studies about kekulene are reported in the literature. The first study elaborated a synthesis route of kekulene and investigated its properties using analytical chemistry. In the second approach, the synthesis of kekulene was reproduced. Additionally, the authors achieved to evaporate and deposite the molecule onto a metal surface for the first time. The results of both studies are briefly described in the following.

The first reliable synthesis route for kekulene was developed by F. Diederich and H. A. Staab in 1978 [174]. The resulting microcrystals were analyzed by mass spectrometry, infrared adsorption and electron spectroscopies, proton nuclear magnetic resonance (^{1}H-NMR), x ray diffraction (XRD) and optically detected magnetic resonance (ODMR) [179]. Yet, with its "extreme insolubility in solvents of all kinds" [174], the analysis of the product turned out to be extremely difficult. Nevertheless, the authors came to a conclusion concerning kekulene's type of aromaticity. A substantial variation of bond lengths in XRD, a partial compartmentation of the π system in ODMR and strong coupling between the outer and inner circuits of the molecule observed in ^{1}H-NMR lead Krieger et al. [178] to conclude that Clar's sextet model is the better representation for kekulene's bonding situation.

41 years after the first publication of Diederich et al. [174], I. Pozo and coworkers [43] recalled their synthesis route, improved it, and finally achieved a 19.5% yield of kekulene. They sublimated kekulene by rapid heating from a Si wafer and deposited the molecules onto a Cu(111) substrate held at 10 K. An increased fragmentation rate due to the high sublimation temperature resulted in small and often mobile molecules with only a few of them showing the expected size and hexagonal shape of kekulene molecules. The analysis therefore required a locally resolved scanning probe method such as constant-height atomic force microscopy (AFM) with a CO-functionalized tip imaging the geometry of single adsorbed molecules. Details of the contrast in the AFM images were related to bond order, where bonds of highest bond order were identified at the peripheral C(H)–C(H) bonds in agreement with gas phase simulations and on-surface calculations. The bonding patterns matched the predictions of the π sextet rule and therefore corroborated Clar's model. Nonetheless, there may be two difficulties in the interpretation of their experimental results. First, as Pozo et al. [43] already recognized, the bond-order-related contrast may be difficult to interpret considering the nonplanar background from van der Waals and electrostatic forces. Moreover, they focused on solely structural properties to assess kekulene's aromaticity, although this fundamental concept is a unique interplay of structural *and* electronic prop-

erties of the molecule. Therefore, the electronic nature of aromaticity should not be neglected, if a full understanding of the molecule's aromaticity is desired.

To shed light on the aromaticity of kekulene from a geometric and electronic point of view to verify to which extent if at all the proposed superaromatic stabilization may play a role, we performed STM and POT measurements. The STM experiments serve to check the structure on the surface, but does not provide information about the molecule's aromaticity. A comparison of multiple theoretical predictions to the experiment in POT allows us to rule out the superaromatic model of kekulene and verify the Clar model of aromaticity. Therein, it is particularly intriguing that we can rule out superaromaticity by only looking at frontier orbitals.

4.1.2 Experimental details

Synthesis of precursor molecule

The synthesis and analysis of the precursor molecule used in our experiments is schematically shown in Fig. 4.2**a** and described in detail in the SI of Ref. [AH3]. The four-step reaction sequence begins with a regioselective bromination of 9,10-dihydrophenanthrene (**1**) to 2,7-dibromo-9,10-dihydrophenanthrene (**2**) after a protocol from Tian et al. [180]. After oxidation to 2,7-dibromophenanthrene (**3**), the aromatic compound is subsequently converted into bis-aldehyde (**4**). Using a McMurry reaction protocol for similar reactions established by Majewski et al. [181], **4** is finally oligomerized to the nonplanar kekulene precursor 1,4,7(2,7)-triphenanthren-acyclononaphane-2,5,8-triene (**5**) which is obtained as a colorless solid. The chemical synthesis of the precursor molecules was carried out in the group of J. Sundermeyer (Marburg University). The molecular structure of the precursor was analyzed and proved by XRD, revealing a highly distorted nonplanar geometry with three phenanthrene moieties rotated out of the molecular plane.

On-surface synthesis of kekulene on Cu(111)

The on-surface synthesized kekulene/Cu(111) was prepared for photoemission and STM experiments under UHV conditions.First, the Cu(111) crystals were cleaned by repeating sputter/anneal cycles. The protocol of the on-surface synthesis of kekulene/Cu(111) from the precursor molecule developed in the group of J. M. Gottfried (University of Marburg) involves the thermal evaporation of the precursor molecules in vacuum at 550 K to deposit intact molecules on the Cu(111) surface held at room temperature. Subsequent annealing of the as-deposited monolayer of precursor molecules at 500 K triggers the cyclodehydrogenation reaction to form the final product kekulene (Fig. 4.2**a**, **6**) on Cu(111).

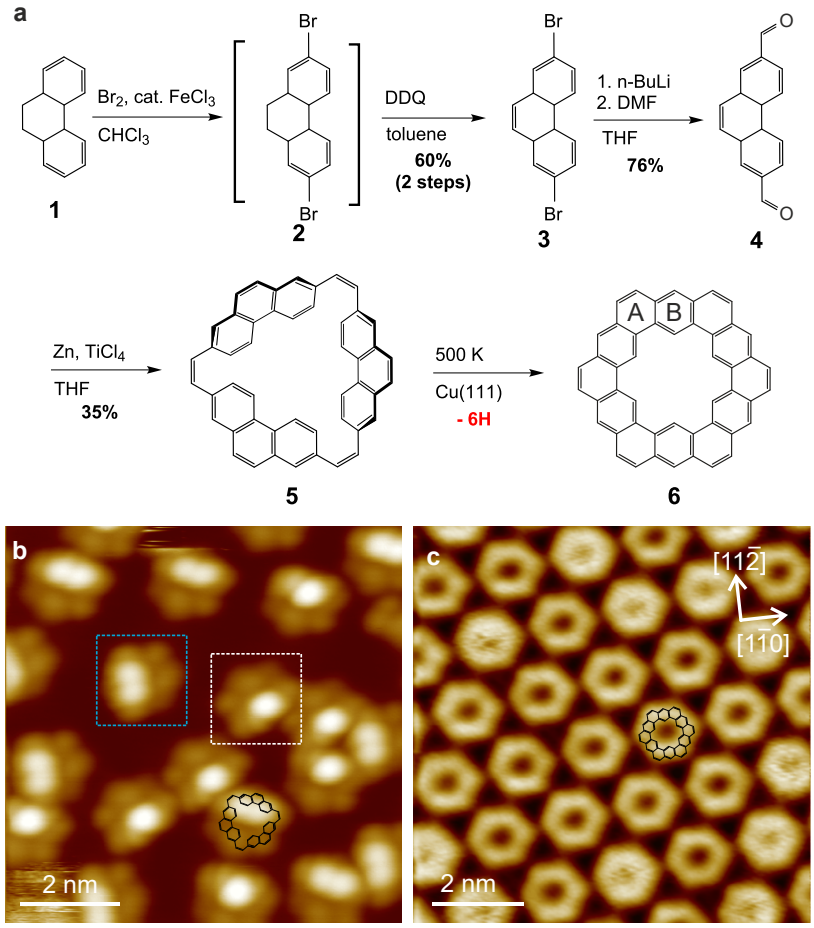

Figure 4.2: Synthesis route and STM results
a Synthesis route for kekulene precursor **5** by four-step reaction sequence followed by on-surface synthesis of kekulene (**6**) on Cu(111). STM micrographs of **b** precursor (**5**, U = −2.8 V, I = 0.11 nA) and **c** kekulene (**6**, U = −2.9 V, I = 0.26 nA) on Cu(111), respectively, recorded at 100 K. Skeletal formula of the molecules are added to illustrate the nonplanar and planar conformations of **5** and **6**, respectively. White and blue frames in **b** mark different conformers of the precursor molecule. Varying appearances of kekulene in **c** arose by slight motion of the molecules usually related to the STM tip. After Fig. 1 and 2 of Ref. [AH3]. The synthesis part and STM measurements were performed at Marburg University in the groups of J. Sundermeyer and J. M. Gottfried, respectively.

4.2 STM

To gain insight into the structural conformation of the molecules before and after the thermal treatment of the precursor molecules, low temperature (100 K) STM measurements were performed by Q. Fan at the University of Marburg.

Figure 4.2**b** displays an exemplary STM image of the as-deposited precursor molecules on Cu(111). A number of asymmetric adsorption species are discernible which are attributed to intact precursor molecules. The bright protrusions are ascribed to the tilted phenanthrene moieties already observed in the XRD measurements of the precursor microcrystals. The nonplanar geometry of the precursor with phenanthrene units tilted out of the substrate plane is therefore preserved upon adsorption on the metal surface. A closer look to the bright protrusions reveals that there are two different conformations of the precursor molecule on the surface, either showing one or two bright features per molecule marked with white and blue frames in Fig. 4.2**b**, respectively. This can be explained by the degree of rotation of the phenanthrene units in the precursor molecules. It suggests that in both cases, two phenanthrene units lie flat on the sample surface. The third unit is either rotated such that it is completely pointing away from the substrate or only with its central part. This results in either two or one bright protrusion in the STM images, respectively, leading to the conformers C1 and C2. A statistical evaluation of large-scale STM images reveals that the Cu(111) is covered nearly evenly by both conformers; 50.2% by C1 and 49.8% by C2. None of them is thus preferred over the other.

Annealing the sample to 500 K modifies the adsorbate layer as illustrated in Fig. 4.2**c**. A long-range ordered lattice consisting of planar and aligned hexagonal species is observed with domain sizes up to 100 nm. The individual units of the adsorbate exhibit an empty pore in the center with strong resemblance to the molecular structure of kekulene. Note that the free molecule belongs to the symmetry group D_{6h} for a planar configuration and to D_{3d} if the small alternating out-of-plane bending of the inner hydrogen atoms is taken into account. The STM micrographs convey a successful reaction and planarization of the precursor molecule. In fact, a statistical analysis of large-scale STM images reveals that more than 99% of the adsorption species are identified as kekulene molecules. This means that on Cu(111) the thermal treatment of both precursor conformers C1 and C2 results in a formation of flat kekulene molecules.

The monolayer is closely packed with its lattice vectors of the superstructure slightly deviating from the high-symmetry directions of the underlying substrate, which results in symmetry-equivalent molecular mirror domains. The mirror plane between these two domains coincides with a molecular mirror plane within the

kekulene molecules, therefore all molecules are oriented in the same azimuthal direction with one zigzag-edge parallel to the $[1\bar{1}0]$ orientation of the substrate, which facilitates POT experiments. The second and third requirements mentioned for POT are satisfied given the density of the monolayer film confirming a high reaction yield with no detectable amount of byproducts.

4.3 Aromaticity of kekulene from geometric perspective

In a first step, the aromaticity of kekulene is approached using the geometry of the molecule simulated by DFT, namely the internuclei distances commonly referred to as bond lengths.

The electronic structure calculations of kekulene/Cu(111) are obtained by structural optimization using the Vienna *Ab Initio* Simulation Package (VASP) code. These results and analysis of the harmonic oscillator model of aromaticity (HOMA) to determine the degree of aromaticity in the molecule for the adsorbed and free molecules in this section have been performed in the framework of A. Reichmann's Master's thesis [182] in the group of P. Puschnig (University of Graz). The results of these calculations have been cross-checked independently using the Spanish Initiative for Electronic Simulations with Thousands of Atoms (SIESTA) code performed in the group of M. Rohlfing (University of Münster) discussed in the SI of Ref. [AH3]. Both approaches are consulted and put into context in this section.

4.3.1 DFT optimization

The configuration of the kekulene molecule on Cu(111) concerning its most favorable adsorption site is addressed using two different theoretical methodologies within DFT.

First, the VASP code is employed by A. Reichmann (University of Graz) with exchange and correlation effects treated by the PBE-GGA functional and van der Waals forces included according to Tkatchenko and Scheffler [183, 184]. This approach is employed in two variants. Using either a separately optimized Cu lattice parameter of 3.55 Å and three Cu layers mimicking the substrate, we evaluate the correct adsorption site of kekulene on Cu(111). To test the robustness of the found optimal adsorption configuration, the second variant uses an experimentally-derived lattice parameter of 3.61 Å [185] and six Cu layers as substrate, calculating only the previously evaluated most stable adsorption site. We compare the two

variants using the adsorption energy E_{ad}, which is defined by the energy gain when two initially separated systems form a combined system following

$$E_{\mathrm{ad}} = E_{\mathrm{tot}} - (E_{\mathrm{surf}} + E_{\mathrm{mol}}) \tag{4.1}$$

, where E_{tot} is the total energy of the combined system, E_{mol} the total energy of the free molecule, and E_{surf} the energy of the isolated substrate. We find varying adsorption energies of -6.20 eV (3 Cu layers) and -5.93 eV (6 Cu layers), while the adsorption height remains almost unaffected (2.92 Å vs. 3.05 Å), proving the applicability of the first approach and confirming the simulated adsorption position. In the second theoretical approach by colleagues at the University of Münster, the SIESTA code is utilized. A detailed description of the method can be found in the SI of Ref. [AH3]. The calculations are used in the course of this chapter dealing with bond order analysis (Section 4.4.3).

The geometry relaxations are started at the four principle adsorption positions on Cu(111): top, bridge, hollow (H) *face centered cubic (fcc)*, and H *hexagonal closed packed (hcp)*. For all possible adsorption sites, the azimuthal orientations of one molecule's zigzag edge parallel to both principal directions of the substrate are investigated, resulting in overall eight considered configurations. The results of the average carbon atom adsorption heights $\bar{h}_{\mathrm{C}}$ and the total adsorption energies E_{ad} are summarized in Tab. 4.1. Note that the simulations of the bridge site using the SIESTA code did not converge at the initial adsorption position. Instead the molecule shift towards the H *hcp* site for both azimuthal orientations. It is important to mention that the exact numbers for the most stable adsorption site calculated by the VASP or the SIESTA code in Tab. 4.1 are slightly different ($\Delta\bar{h}_{\mathrm{C}} = 0.14$ Å, $\Delta E_{\mathrm{ad}} = -0.52$ eV). That the molecule is predicted to be closer to the surface but slightly less bound in terms of adsorption energy reflects the well-known uncertainty of computational physisorption. Nevertheless, both methodologies suggest a rather weak interaction between molecule and substrate.

Both methodologies confirm that the most preferable adsorption configuration is the *hcp* H site with one kekulene zigzag edge parallel to the $[1\bar{1}0]$ direction of Cu(111). Fig. 4.3 displays the resulting top and side views of kekulene on Cu(111) based on the VASP simulation. The simulated orientation of the molecule agrees with the STM measurements presented earlier. The large mobility of the molecules on the Cu(111) surface observed in low-temperature STM reported in Ref. [43] and also in our own STM experiments (Q. Fan, University of Marburg) suggests a rather weak interaction strength between molecule and metal surface. This can be checked by evaluating the adsorption energy and adsorption height of the molecule predicted by DFT in comparison to other well-known systems.

Adsorption site	Kekulene zigzag edge parallel to	VASP code $\bar{h}_C$ (Å)	VASP code E_{ad} (eV)	SIESTA code $\bar{h}_C$ (Å)	SIESTA code E_{ad} (eV)
top	along [$\bar{1}$12]	3.14	−5.99	2.98	−5.28
bridge	along [$\bar{1}$12]	3.15	−6.05	shift to H *hcp*	
H *fcc*	along [$\bar{1}$12]	3.14	−6.04	2.95	−5.40
H *hcp*	along [$\bar{1}$12]	3.15	−6.05	2.94	−5.45
top	along [1$\bar{1}$0]	3.28	−5.86	2.99	−5.07
bridge	along [1$\bar{1}$0]	3.11	−6.17	shift to H *hcp*	
H *fcc*	along [1$\bar{1}$0]	3.11	−6.19	2.94	−5.53
H *hcp*	along [1$\bar{1}$0]	**3.06**	**−6.20**	**2.92**	**−5.68**

Table 4.1: Adsorption energies and heights of kekulene/Cu(111)
Average carbon adsorption heights $\bar{h}_C$ and adsorption energies E_{ad} of kekulene on Cu(111) predicted for different adsorption sites along the two high-symmetry directions of the substrate tested with two theoretical approaches. See text and Supplementary Material of Ref. [AH3] for details. After Tab. 3.1 of Ref. [182]. Calculations using the VASP and SIESTA codes performed in the groups of P. Puschnig, Graz and M. Rohlfing, Münster, respectively.

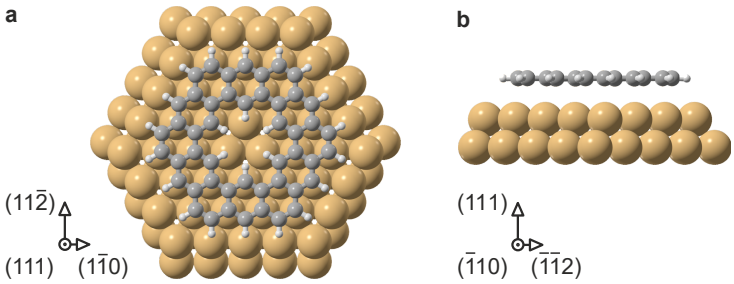

Figure 4.3: Simulated relaxed kekulene/Cu(111) configuration
a Top and **b** side views of the relaxed adsorption geometry of kekulene on Cu(111) as obtained by DFT. After Fig. 2 of Ref. [AH3]. Calculations by P. Puschnig.

In the most favorable adsorption site, an adsorption energy of −5.93 eV per molecule is simulated within PBE-GGA+TS using six Cu layers and an experimentally measured lattice parameter of Cu which breaks down to 123 meV per C atom. In comparison, the simulation of bisanthene ($C_{28}H_{14}$) on its preferred adsorption site on Cu(110) results in a higher value of 188 meV per C atom [35]. Since the LUMO of bisanthene is occupied on this surface, this adsorption energy represents a stronger interaction between molecule and substrate. The interaction between kekulene and Cu(111) is consequently weaker and the LUMO not occupied (see POT results in Section 4.4.1). Considering the adsorption height, PTCDA on three different (111) metal surfaces serves as a reasonable comparison. The molecule is charged on Cu(111) and Ag(111) with experimentally-derived adsorption heights of 2.66 Å and 2.86 Å in agreement with DFT predictions (2.68 Å and 2.87 Å , respectively) [186]. These adsorption heights are considerably smaller than the sum of van der Waals radii (3.17 Å and 3.42 Å for C–Cu and C–Ag). On Au(111), the theoretical and experimental adsorption heights of neutral PTCDA (both 3.27 Å) are further away from the surface, but still smaller than the sum of van der Waals radii C–Au of 3.36 Å. In our case, the sum of van der Waals radii (3.17 Å) from carbon in benzene $r^{\mathrm{C}}_{\mathrm{vdW}} = 1.77$ Å [187] and that of copper $r^{\mathrm{Cu}}_{\mathrm{vdW}} = 1.4$ Å deduced from organo-metallic compounds (methodologically least reliable) [187] is only slightly larger than the predicted adsorption height of kekulene (3.06 Å). Therefore, the interaction between kekulene and Cu(111) is indeed well-described as weak. This explains the mobility of the molecules on the surface observed in STM. It also gives a reason for the molecule's predicted small vertical distortion of $\Delta\bar{h}_{\mathrm{C}} = 0.06$ Å which is not altered by the metal surface due to the low interaction strength.

4.3.2 Quantitative analysis of aromaticity

On the basis of the geometry relaxations obtained by the VASP code and introduced in the previous section, the internal geometry of the relaxed molecular structure is examined with regard to its aromaticity. There are various strategies to quantify aromaticity in molecules, e.g., the harmonic oscillator model of aromaticity (HOMA) [172, 188, 189], the nucleus independent chemical shifts (NICS) [176, 190], the para-delocalization index (PDI) [191] or the density, degeneracy, delocalization-based index of aromaticity (D3BIA) [192]. A purely geometric measure that is frequently used in the literature is provided by the HOMA, which solely relies on bond lengths. These can easily be obtained from the available DFT simulations. In the following, the internuclei distances (bond lengths) obtained by the VASP calculations for kekulene are used for a quantitative analysis of the molecule's aromaticity based on the HOMA approach.

The strength of a bond between two atoms can be quantified by the bond length. The longer C–C single bonds, corresponding to a weaker interaction between the atoms, are composed of s, p_x and p_y orbitals. These bonds are called σ bonds with bond lengths of approximately $R_{single} = 1.522$ Å as in ethane (C_2H_6) [193]. An additional stabilization between the two atoms is achieved when p_z orbitals are involved as well. These resulting stronger π bonds are shorter ($R_{double} = 1.331$ Å in ethylene C_2H_4) [194] and represented as double bonds C=C in skeletal formulae.

In aromatic systems, the C atoms are connected along a circle with their bond lengths assimilated for perfect aromatic stabilization. Therefore, there is no typical single or double bond length anymore in an aromatic system but only one bond length. As a consequence, single bonds are compressed and double bonds are stretched. The resulting equal bond length of all bonds is the optimum bond length R_{opt}.

To quantify this aromatic character within the system, we use the HOMA approach in which the energy cost, due to stretching the double bond and compressing the single bond, scales quadratically. The HOMA value H is calculated by:

$$H = 1 - \frac{\alpha}{j} \sum_{i=1}^{j} (R_{opt} - R_i)^2 \tag{4.2}$$

The formula requires the bond lengths R_i of all considered bonds j, the optimum C–C bonding distance R_{opt}, and an additional normalization factor $\alpha(n)$ taken from Ref. [195]. H can vary finally between zero and one with $H = 1$ indicating perfect aromaticity, while smaller HOMA values correspond to weaker aromatic stabilization. This model can be applied to the entire molecule or any cyclic conjugation path within it, which brings great benefit to the aromaticity analysis. Only condition for the regarded parts of the molecule is that Hückel's $4n + 2$ rule ($n = 0, 1, 2, ...,$) considering the number of electrons involved in the π system has to be fulfilled.

We calculate R_{opt} as the average of single- and double-bond lengths in free *trans*-1,3-butadiene (C_4H_6). Our DFT calculations using PBE-GGA reveal individual bonds of $R_{single} = 1.456$ Å and $R_{double} = 1.350$ Å in agreement with two individual experimental studies [194]. The optimal bond length is hence $R_{opt} = 1.403$ Å. However, the bond lengths in kekulene predicted by DFT geometry relaxations differ from R_{opt}. Fig. 4.4**a** shows the bond lengths within the kekulene molecule relaxed on the Cu(111) surface by the blue color scale. The predicted bond lengths vary between 1.370 and 1.452 Å with some bonds close to R_{opt}. These are often adjacent to each other at the central benzoic unit along the molecules edges (ring

B in the skeletal formula of kekulene (**6**) in Fig. 4.2 **a**). Qualitatively, this already suggests an enhanced aromatic character at these benzoic units of the molecule.

For the kekulene molecule specifically, three different paths are taken into account, namely localized individual benzoic units ($n = 1$), or peripheral units for the proposed inner ($n = 4$) and outer ($n = 7$) annulene circuits in the superaromatic model (see Fig. 4.1). All evaluated circuits follow Hückel's $4n + 2$ condition of aromaticity and are therefore reasonable representatives for aromaticity stabilization in kekulene.

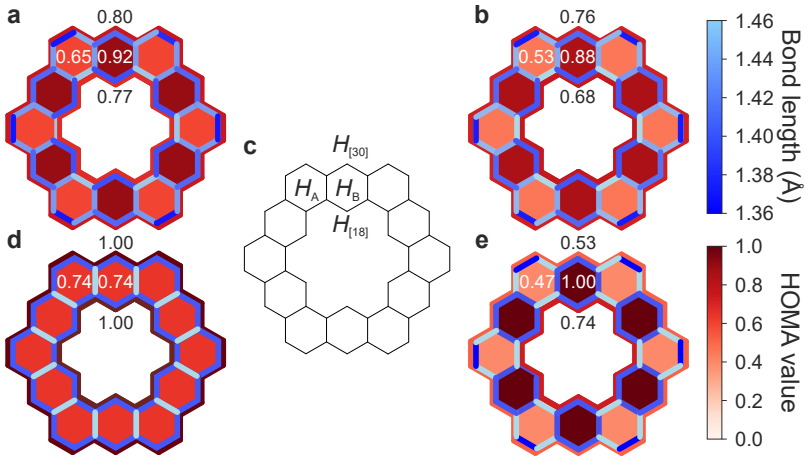

Figure 4.4: Bond lengths and *H* for four kekulene configurations
Bond lengths in blue schemes with light blue indicating larger bond lengths. Red color illustrates the calculated HOMA values for individual benzoic units or inner and outer annulene circuits. Dark red indicates a HOMA value close to one, i.e., perfect aromaticity. Lighter color means smaller aromatic stabilization. **a** DFT optimized kekulene in geometry as adsorbed on Cu(111). **b** DFT geometry-optimized gas phase kekulene. **c** Basic framework of kekulene molecule to show for which conjugation paths the HOMA value is calculated. Kekulene fixed in **d** superaromatic and **e** Clar models, respectively. After Fig. 3.4 of Ref. [182]. Calculations by A. Reichmann (University of Graz).

Considering the Clar model, two inequivalent ring units are discerned denoted as rings A and B in Fig. 4.2**a** (**6**) and Fig. 4.4**c**. Calculated for the relaxed kekulene on Cu(111) shown in Fig. 4.4**a**, H yields $H_{\mathrm{A}} = 0.65$ and $H_{\mathrm{B}} = 0.92$ indicating a tendency towards Clar's limit, i.e., ring B more aromatic than ring A.

The evaluation of the relaxed kekulene structure concerning the superaromatic model is approached with HOMA values of the inner ([18]) and outer ([30]) annulene circuits as indicated in Fig. 4.4**c**. According to the Hückel rule, π systems with $4n + 2$ electrons are more stable with smaller n. Accordingly, $H_{[18]}$ is expected to be larger than $H_{[30]}$. However, with the calculated values for adsorbed kekulene of $H_{[18]} = 0.77$ and $H_{[30]} = 0.80$, this trend is reversed. The HOMA calculation obviously exaggerates the peripheral aromaticity of kekulene, which is a well-known problem of this concept [172].

To compare the calculated H based on adsorbed kekulene on Cu(111) clearly to the two aromaticity models, H are calculated of four different kekulene configurations illustrated in Fig. 4.4 and summarized in Table 4.2. For these calculations, configurations of the free kekulene molecule following the ideal bond lengths according to the superaromatic or Clar model were fixed as illustrated in Fig. 4.4**d**, **e**, respectively. For the former molecular geometry, the C–C bonds along the annulene circuits were set to $\mathrm{R}_{\mathrm{opt}}$ such that $H_{[18]} = H_{[30]} = 1.00$, while for the latter only the bonds in ring B were fixed to $\mathrm{R}_{\mathrm{opt}}$ aiming at $H_{\mathrm{B}} = 1.00$. All other bonds were allowed to relax in the calculation. Details about the calculation of bond lengths can be found elsewhere [AH3, 182].

H	superaromatic model	free kekulene	kekulene/Cu(111)		Clar model
H_{A}	0.735	0.527	0.651	more superaromatic	0.472
H_{B}	0.735	0.878	0.923	more Clar	1.000
$H_{[18]}$	1.000	0.678	0.767	more Clar	0.735
$H_{[30]}$	1.000	0.756	0.802	more superaromatic	0.526

Table 4.2: HOMA values of kekulene
Calculated HOMA values for fixed superaromatic and Clar configurations of kekulene as well as relaxed free kekulene and kekulene/Cu(111). After Tab. 3.2 of Ref. [182].

Correlating the individual H of the different structures, it is important to note that the four H of free kekulene tend towards none of the two models, since neither H_{B} nor $H_{[18]}$ and $H_{[30]}$ are close to one. Yet adsorbed on the substrate, all values are increased even rising by 13 and 24 % in the cases of $H_{[18]}$ and H_{A} pointing at an "enhanced" superaromatic character. Actually, the calculated H_{A} and $H_{[30]}$ values of adsorbed kekulene indicate a more superaromatic tendency on the surface, while H_{B} and $H_{[18]}$ suggest a more Clar-like character. The purely structural analysis is hence ambiguous and a clear classification of kekulene towards superaromatic or Clar model cannot be inferred.

4.4 Aromaticity of kekulene from electronic perspective

Up to this point, the aromaticity of kekulene was solely regarded on the basis of DFT-optimized bond lengths. Nevertheless, aromaticity is a complementary concept of mutually related geometric and especially electronic properties of a molecule. The latter aspect is tackled in this section using POT. The photoemission results of the molecule's HOMO are compared to various simulated k maps in Section 4.4.2 to evaluate whether the aromaticity of kekulene is primarily of superaromatic or Clar type. Using bond order analysis in Section 4.4.3, it is further shown that indeed the emission of the molecule's HOMO can be taken as measure for the aromaticity of the molecule.

4.4.1 POT

We start by comparing band maps recorded for the clean Cu(111) surface and the sample with deposited and annealed precursor molecules on the Cu(111) surface as shown in Fig. 4.5**a**,**b**, respectively. The sample was prepared according to the same protocol as STM experiments (see page 4.1.2). In the band maps of the clean metal surface (Fig. 4.5**a**), the *sp* band is clearly visible dispersing from $E_{\mathrm{b}} = 0$ eV to the onset of the *d* band at a $E_{\mathrm{b}} \approx 2$ eV.

After adsorption of the kekulene precursor molecules and annealing the molecular layer, the band map measured along the $[1\bar{1}0]$ direction of the substrate changes (Fig. 4.5**b**). The intensity of the metal *sp* bands is diminished and an additional broad photoemission becomes visible between approximately $1.0\ \text{Å}^{-1} < k_{1\bar{1}0} < 1.9\ \text{Å}^{-1}$. Due to the close vicinity to the substrate *d* band emission, a clear molecular state is barely resolved in the EDC and the band map. An indication for the presence of molecular states above the Cu *d* band is shown

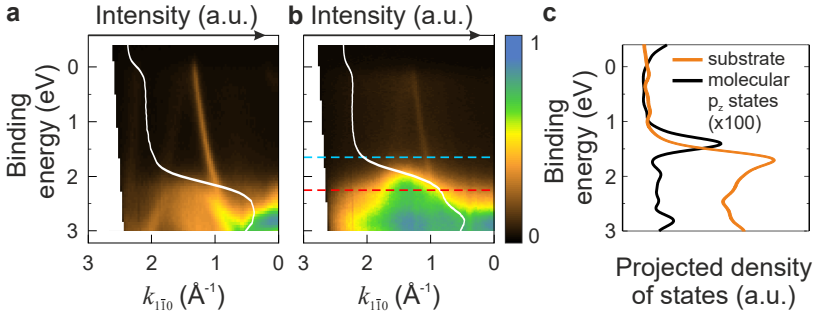

Figure 4.5: Band maps and EDC of clean Cu(111) and kekulene/Cu(111) Band maps along the $[1\bar{1}0]$ direction of Cu(111) for **a** clean Cu(111) and **b** Cu(111) after adsorbing and annealing kekulene precursor molecules. White lines are angle-integrated EDCs integrated between $1.0 < k_{1\bar{1}0} < 1.9$ Å^{-1}. Light blue and red dashed lines indicate the experimental binding energies, where we measured the k maps shown in Fig. 4.6**a**, **d**, respectively. **c** Density of states projected onto the substrate (orange) and molecular p_z states (black) predicted by DFT. After Fig. 3 of Ref. [AH3]. Calculations by A. Reichmann (University of Graz).

by the computed pDOS for kekulene/Cu(111) in Fig. 4.5**c**. There is an emission from molecular p_z-derived state (black curve) predicted at slightly smaller binding energy than the Cu d band (orange curve) between 1.2 eV and 1.6 eV. Projected onto the individual orbital contributions [182], this feature is attributed to two doubly degenerate states of kekulene.

To confirm the assignment of the molecular emissions in the experimental band map to molecular orbitals predicted by DFT, k maps of the photoemission intensity distribution are measured for two different binding energies shown in Fig. 4.6**a**, **d**. At the smaller binding energy of $E_\mathrm{b} = 1.65$ eV (4.6**a**), the k map exhibits clear signatures with six major lobes at $k_\parallel \approx 1.6$ Å^{-1} and six interjacent minor lobes at slightly smaller $k_\parallel \approx 1.5$ Å^{-1}. The sharp sp bands of the metal are clearly visible at this binding energy. Recording k maps at larger binding energy closer to the Cu d states (4.6**d**) reduces the intensity of the sp bands and alters the shape of the emission lobes. The major features appear more elongated, split up into two lobes, and the previous minor lobes vanish. At their position in k space, no photoemission intensity is visible anymore. We therefore conclude that two different states are observed above the Cu d states.

Comparison to DFT calculations shows that these two emissions belong to kekulene's HOMO and HOMO−1 which are both doubly degenerate states. The respective theoretical k maps based on the DFT-optimized structure of free kekulene are displayed in Fig. 4.6**b**, **e**. Note that the two orbitals with irreducible representations of e_{1g} and e_{2u} are energetically only 0.12 eV apart (Orbital energies $E-E_{\mathrm{vac}}$: $\mathrm{HOMO_a}$ + $\mathrm{HOMO_b}$ ($E-E_{\mathrm{vac}}$ = 4.81 eV) and $\mathrm{HOMO-1_a}$ + $\mathrm{HOMO-1_b}$ ($E-E_{\mathrm{vac}}$ = 4.93 eV)). To further verify the orbital assignment, the simulated k maps of kekulene/Cu(111) at binding energies of 1.45 eV and 1.70 eV shown in Fig. 4.6**c**, **f**, respectively, are in good agreement with the experimental data (Fig. 4.6**a**, **d**).

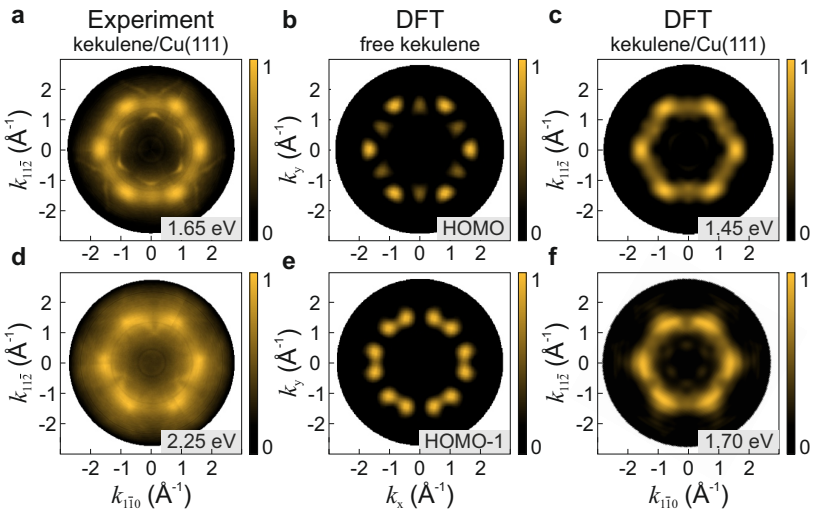

Figure 4.6: Experimental and theoretical k maps of kekulene/Cu(111) Top row: doubly degenerate HOMO, bottom row: doubly degenerate HOMO−1. **a, d** Experimental k maps at the respective binding energies indicated in Fig. 4.5**b** as blue and red dashed lines of the HOMO and HOMO−1, respectively. **b, e** DFT simulated k maps of free kekulene for the doubly degenerate states $\mathrm{HOMO_a}$ + $\mathrm{HOMO_b}$ ($E-E_{\mathrm{vac}}$ = 4.81 eV) and $\mathrm{HOMO-1_a}$ + $\mathrm{HOMO-1_b}$ ($E-E_{\mathrm{vac}}$ = 4.93 eV), respectively. **c, f** DFT simulated k maps of kekulene/Cu(111) considering either six or three Cu layers at binding energies of 1.45 eV and 1.70 eV representative for HOMO and HOMO−1, respectively. After Fig. 3 of Ref. [AH3] and Fig. 3.10 of Ref. [182].

This agreement between experiment and theory also unambiguously confirms the successful on-surface synthesis of kekulene/Cu(111) in sufficiently large well-ordered domains. Moreover, the azimuthal alignment of the adsorbed molecules with one zigzag-edge parallel to the substrate's $[1\bar{1}0]$ direction previously inferred from STM and DFT geometry relaxation, is confirmed by POT results considering the relative orientation of the Cu *sp* bands and the molecular emissions in the experimental k maps.

The results of POT are directly related to the orbital structure and hence the electronic properties of the adsorbed kekulene molecules. The two observed electronic states therefore provide substantial insight into the molecule's aromaticity. However, the binding energy of HOMO−1 is relatively close to the Cu *d* states resulting in an enhanced background intensity in its k map. The emission pattern of the HOMO is less affected and is therefore used in the following to address the primary goal of this chapter. Namely, we aim to demonstrate that POT, which is directly related to the orbital structure of frontier molecular orbitals, provides substantial insight into the molecule's aromaticity.

4.4.2 POT analysis of the HOMO

To this end, we compare experimental HOMO k maps to various theoretical ones reflecting the two proposed aromaticity models in Fig. 4.8. The experimental and theoretical k maps are compared by azimuthal intensity profiles passing through the major (L1) and minor (L2) lobes in the k maps. For the intensity analysis, a ring with an inner radius of 1.3 Å^{-1} and fixed width of 0.5 Å^{-1} is defined within the k maps as indicated in the k maps in Fig. 4.8. The intensity along the ring is averaged azimuthally and plotted vs. its azimuthal angle. Since the k maps are threefold symmetric, only a defined azimuthal angle range is plotted with $\varphi = 0°$ located at the major lobe L1 at $(k_x, k_y) = (\approx 1.6\ \text{Å}^{-1}, 0.0\ \text{Å}^{-1})$. The minor lobes L2 are correspondingly found at $\varphi = \pm 30°$.

The results are presented in Fig. 4.8 with the experimental intensity profile shown in panel **a** (filled symbols) in comparison to the corresponding simulation result for kekulene/Cu(111) (open symbols) extracted from the already presented k maps in Fig. 4.8**b**, **c** (same k maps as in Fig. 4.6**a**, **c**, respectively). The profiles coincide qualitatively, however, a quantitative analysis of the intensity ratio between lobes L1 and L2 is impossible, due to the barely comparable backgrounds of experimental and theoretical data. The intensity variation of L2 lobes in the experimental k map originates from the *sp* bands of the underlying Cu found at $\varphi = -30°$ reducing the emission from the molecule in this direction. This is less pronounced but still visible in the DFT calculation of kekulene/Cu(111).

Following the characteristics of the two proposed aromaticity models of kekulene, we now inspect the influence of geometric and/or electronic modifications of kekulene on the k maps of the HOMO emission.

To this end, we fix the bond length to what is expected for the two models. Namely, in the Clar model, the bond lengths c, d and f – those inside of the aromatic sextet as in Fig. 4.7 – are set to R_{opt} (R_{sextet} =R_{opt}) leading to maximal aromaticity in the sextets ($H_B = 1$). In the superaromatic model, all bonds along the two annulene circuits (bonds a, b, c, e, and f) are set to R_{opt} ($R_{[18]} = R_{[30]} = R_{opt}$) in order to constrain $H_{[18]} = H_{[30]} = 1.00$. The bonds which are not fixed are allowed to relax in the calculation.

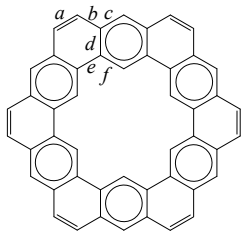

Figure 4.7: Labeling of bonds in kekulene
Skeletal formula of kekulene in the Clar model with six different C–C bonds labeled a to f.

These two fixed hypothetical geometries of free kekulene are employed in DFT calculations to calculate the corresponding charge density distributions and simulate the molecule's HOMO k maps.

As is evident from the k maps (Fig. 4.8**e**, **f**), the corresponding intensity profiles in Fig. 4.8**d** and the charge density distributions in Fig. 4.9**a**, **b**, the overall symmetry and emission patterns of Clar and superaromatic model are very similar. Note that the intensity relation between lobes L1 and L2 (I(L1) > I(L2)) as observed in the experimental k map and that of kekulene on Cu(111) in panels **b** and **c**, respectively, is preserved in both model calculations where the substrate is neglected. This again points at a rather weak interaction strength between molecule and substrate in agreement with STM results presented in Section 4.2. Neglecting the substrate in the discussion about kekulene's aromaticity therefore seems to be a reasonable approach. Nevertheless, the intensity difference between I(L1) and I(L2) is much stronger in the intensity profile of kekulene/Cu(111) compared to those of free kekulene. This is attributed to the background intensity and an additional broadening of molecular states due to the coupling to the metal states.

Fixing the bond lengths as performed in this approach, hence, does not lead to changes in the electronic structure, i.e., the nodal structure of the wave function. The superaromatic kekulene is thus not correctly described in this way.

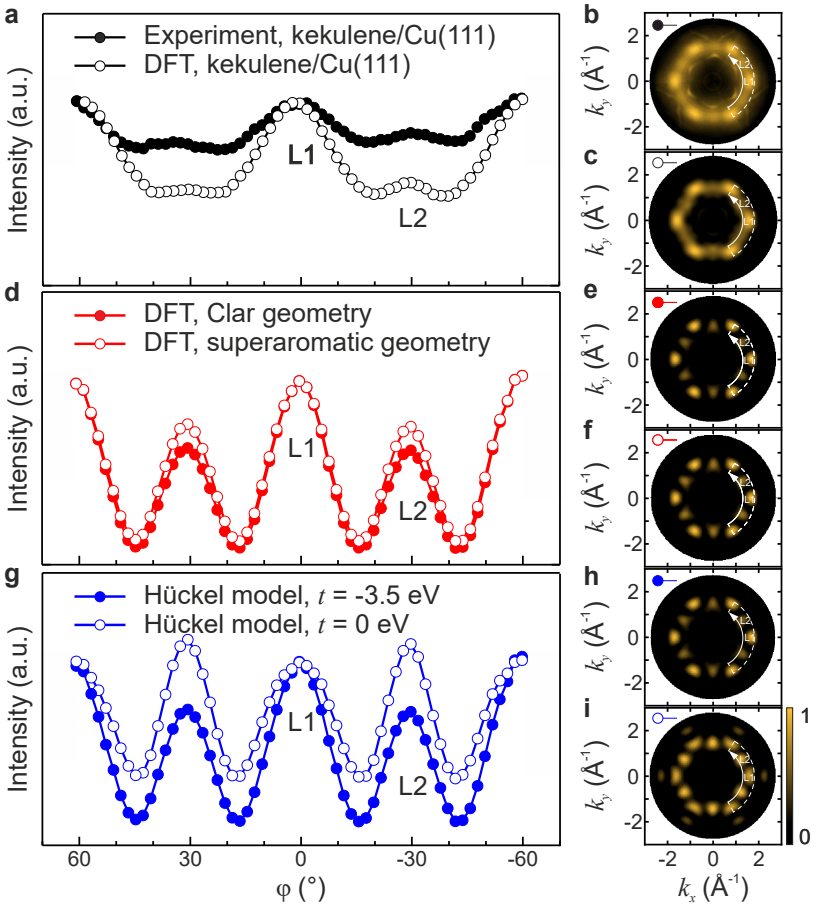

Figure 4.8: Intensity profiles in experimental and theoretical k maps
a Azimuthal intensity profiles based on the experimental (full symbols) and by DFT predicted (open symbols) data of kekulene/Cu(111) extracted from the corresponding k maps in **b, c**, respectively. **d** Simulated profiles from DFT calculations of free kekulene from the k maps based on the **e** Clar (full symbols) and **f** superaromatic (open symbols) geometries. **g** Simulated profiles from the Hückel model where the coupling between the inner and outer annulene rings is fully intact ($t = -3.5$ eV, full symbols) or extinguished ($t = 0$ eV, open symbols). The corresponding k maps are shown in **h** and **i**, respectively. Emission lobes are labeled as L1 and L2 in the profiles and k maps. The white lines in the latter display the areas used for intensity averaging. Profiles are normalized to the intensity of L1. After Fig. 4 of Ref. [AH3]. Calculations by P. Puschnig.

To model the superaromatic state of kekulene reasonably from electronic point of view, we need to switch off the coupling between the inner and outer circuit. Geometrically, we again fix the bond lengths $R_{[18]} = R_{[30]} = R_{opt}$. In this way we can enforce the desired separated superaromatic conjugation paths.

This approach is realized using a simple tight binding Hückel model. Therein, the molecular orbitals are described as linear combinations of atomic p_z orbitals. The Hamiltonian matrix of the linear combination of planar, unsaturated hydrocarbons is given by the following :

$$H_{ij} = \begin{cases} E - E_{\text{vac}} & i = j \\ t & i, j \ \textit{adjacent} \\ 0 & \textit{otherwise} \end{cases} \tag{4.3}$$

The eigenvalues of the Hamiltonian correspond to the molecular orbital energies expressed by $E - E_{\text{vac}}$ and t. The former, $E - E_{\text{vac}}$, describes the energy of a $2p$ electron at one carbon atom relative to its unbound counterpart and is given by an on-site integral localized at one atom. The latter, t, represents the energy of an electron located at a $2p$ orbital in comparison to a delocalized π orbital built from two adjacent carbon atoms. t therefore describes the interatomic coupling in each bond connecting two carbon atoms.

In the kekulene molecule, bond d (see Fig. 4.7 **a**) connects the inner and outer annulene paths. The interatomic coupling in this bond is described by its energy t_d referred to as hopping parameter in the following. t_d is essential for the coupling between the two conjugation paths in kekulene. Setting this hopping parameter t_d to zero will suppress the coupling between the two circuits which is expected to resemble the superaromatic model of kekulene.

To check whether this simple Hückel model is in general appropriate to be compared to DFT calculations, the Hückel simulation is performed with $t_d = -3.5$ eV mimicking the typical coupling between C atoms in graphene. In this kekulene variant, the geometry is fixed to the superaromatic model but the electronic coupling between inner and outer annulene circuits is allowed. We expect it to have a similar charge density distribution and k map as the DFT simulation discussed previously where only the bonds are fixed according to the superaromatic model ("DFT superaromatic geometry" in Fig. 4.9**b**, **f** and Fig. 4.8**d**, **f**). A reasonably good agreement between results based on the Hückel model compared to DFT is achieved when setting the t energies of all other bonds (t_a, t_b, t_c, t_e, and t_f) to $t = -4.1$ eV and $t_d = -3.5$ eV.

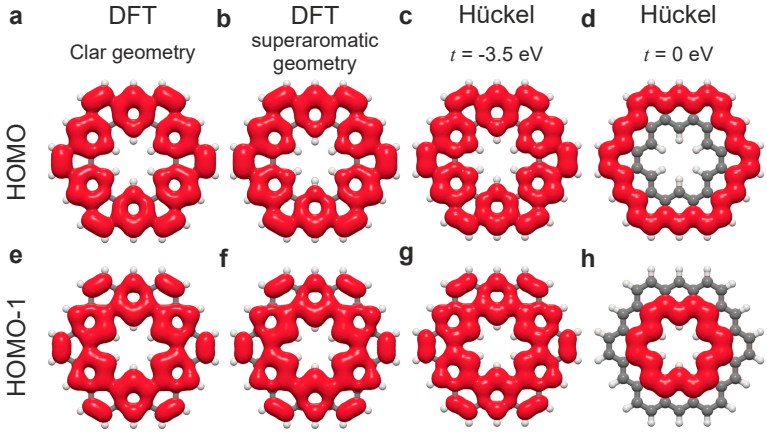

Figure 4.9: Charge density distributions of kekulene
DFT simulations of kekulene's HOMO in the geometries of the **a** Clar and **b** superaromatic models. Calculations in the Hückel model using **c** $t = -3.5$ eV and **d** $t = 0$ eV corresponding to the Clar and the superaromatic models, respectively. Analogous charge distributions of the HOMO-1 are displayed in **e**, **f**, **g**, and **h**. After Fig. S7 of Ref. [AH3]. Calculations by P. Puschnig.

The results of the charge density distributions of HOMO and HOMO-1 based on the Hückel model with $t_d = -3.5$ eV are displayed in Fig. 4.9**c**, **g**. It is clearly visible that its charge density distributions are localized at the benzoic unit B and at bond a – indistinguishable from those based on both DFT simulations in **a**, and **e** or **b** and **f** either using Clar or superaromatic geometries, respectively. The similarity between DFT and Hückel model with $t_d = -3.5$ eV is likewise reflected in Fig. 4.8**g** displaying the intensity profile of the latter in full symbols based on the theoretical k map in **h** of the doubly degenerate HOMO, where again $I(\mathrm{L1}) > I(\mathrm{L2})$. These agreements allow us consider the Hückel model as a reasonably good approach to finally be able to access the true superaromatic configuration of kekulene in a next step.

To mimic the true superaromatic kekulene case, the coupling between the two conjugation paths has to be turned off artificially. Thereby two independent cyclic aromatic conjugation paths are created. This is achieved by setting $t_d = 0$ eV, resulting in HOMO and HOMO-1 charge density distributions illustrated in Fig. 4.9**d**, **h**, respectively. The doubly degenerate HOMO is now confined to exclusively around the outer [30]annulene path, while the electron density of HOMO-1 is fixed to the inner [18]annulene. From an electronic point of view,

this Hückel model now indeed describes the superaromatic model correctly. This also affects the photoemission k map of the HOMO displayed in Fig. 4.8**i**. In particular, the intensity of the former minor lobes L2 is enhanced becoming the leading features in the emission pattern. Moreover, six additional intensity lobes arise at larger $k_{\parallel} \approx 2.1$ Å^{-1} which are a result of the confinement of the electrons to the outer annulene circuit reflected in a larger spread in k space.

Comparing this k map to the experimental one in Fig. 4.8**b**, multiple difference are discernible. First, there are no low-intensity emission lobes visible at larger $k_{\parallel} \approx 2.1$ Å^{-1} in the experiment. Moreover, as illustrated in the intensity profiles in Fig. 4.8**a** and **g** for the experiment and the correctly simulated superaromatic kekulene, respectively, the most intense feature should be located at $\varphi = 0°$, but in the simulation this peak is of lowest intensity. Finally, using a correct description of the superaromatic state in the Hückel model allows us to unambiguously rule out this superaromatic configuration of kekulene.

Instead, the experimental intensity profiles are well-reproduced by the theoretical results based on relaxed kekulene/Cu(111) and the artificial configuration of the Clar model in its ideal geometry. Consequently, our POT results exclude the superaromatic state of kekulene and point toward the Clar model from an electronic structure perspective.

This conclusion that kekulene's aromaticity is better described by the Clar model on the basis of POT analysis is drawn from the assumption that the HOMO alone serves as a sufficient measure for the molecule's aromaticity. This apparently does not include other π orbitals. To corroborate this approach, we inspect the orbital structures of the doubly degenerate HOMO of kekulene, denoted as $\mathrm{HOMO_a}$ and $\mathrm{HOMO_b}$ calculated using the Hückel model with $t_d = -3.5$ eV in Fig 4.10**a**, **b**.

Apparently, the electrons in the HOMO are delocalized over both annulene paths and not confined to either the outer or inner ring. More precisely, the pair of kekulene HOMOs locally consists of benzene-like patterns as indicated by the dashed lines in Fig. 4.10**a**, **b**. This pattern coincides with those hexagonal carbon rings that we initially denoted as ring B in Fig. 4.4**c** where the Clar model predicts aromatic sextets. The dotted lines in Fig. 4.10**a**, **b** indicate the location of the pronounced double bonds at the corners of kekulene.

The sum of $\mathrm{HOMO_a}$ and $\mathrm{HOMO_b}$ yields the total charge density of kekulene's HOMO displayed in Fig. 4.10**c**. Now, the six aromatic sextets and the isolated double bonds at the corners characteristic for the Clar model are clearly visible. In fact, the development of the Clar-like structure is an immediate consequence of turning on the coupling between [18]- and [30]-annulene which can be visually traced in a video provided in the SI of Ref. [AH3].

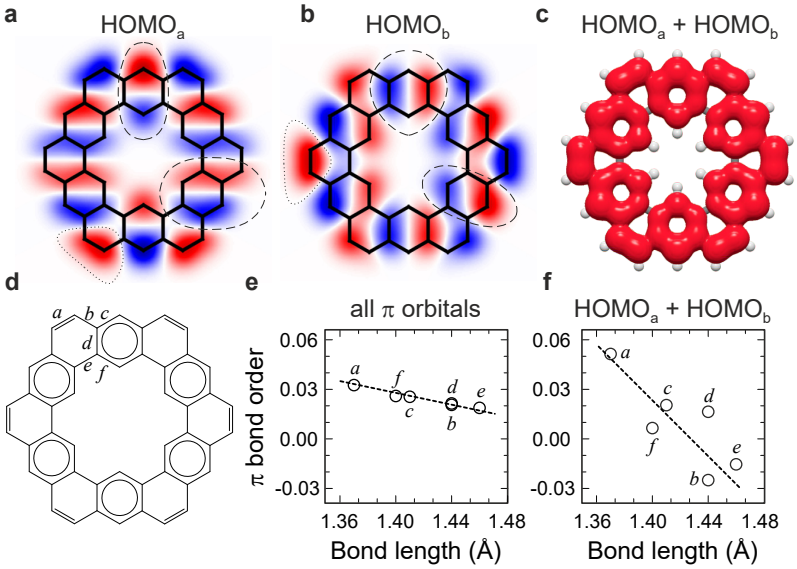

Figure 4.10: Bond order analysis and charge density of free kekulene
a, b Nodal structure of the two degenerate orbitals comprising the HOMO, denoted $HOMO_a$ and $HOMO_b$, respectively, calculated with the Hückel model. **c** Charge density distribution of the HOMO. **d** Skeletal formula of kekulene in the Clar model with the six different C–C bonds labeled *a* to *f*. Correlation between C–C bond lengths of free kekulene simulated by DFT and bond order parameter taking into account either **e** all 24 occupied π orbitals or **f** only the degenerate HOMO ($m = 23$ and 24) orbital, respectively. Linear fits drawn as dashed lines. After Fig. 5 of Ref. [AH3]. Calculations for bond order analysis by M. Rohlfing and charge density distributions by P. Puschnig.

4.4.3 Bond order analysis

The assumption that the HOMO alone can serve as a sufficient measure for kekulene's aromaticity is corroborated by looking at its contribution to the bond order.

In a simplified way, the bond order describes the number of chemical bonds between a pair of atoms. For single, double or triple bonds, the bond order is one, two, or three, respectively. In an aromatic hydrocarbon, two carbon atoms are not connected between strict single or double bonds. Instead the bond lengths is in between that of a single and a double bond. The bond order consequently varies between one and two. More precisely, the bond order directly relates the orbital

structure to the bond lengths in a π conjugated molecule. At the same time, the bond lengths are correlated to the molecule's aromaticity as described in the HOMA analysis. Given that the bond order analysis can be applied to individual orbitals in a molecule, it is possible to evaluate if single orbitals can be taken as a measure for the aromaticity of a complete molecule.

The bond order analysis is based on the bond order parameter b_{ij}:

$$b_{ij} = \frac{2}{N} \sum_{m=1}^{N} a_i(m) a_j(m). \tag{4.4}$$

It is normalized by the number of contributing π electrons N for a given bond between two carbon atoms labeled i and j. The parameter a_i (a_j) describes the contribution of the p_z orbital at carbon atom i (j) to the molecular π orbital m and is obtained from the solution of the Hückel model. A stronger contribution of a p_z orbital representative for double bond character would result in a larger bond order parameter. In this Hückel model, $m = 23$ to 24 denotes the molecule's degenerate HOMO composed of $\mathrm{HOMO_a}$ and $\mathrm{HOMO_b}$ and $m < 22$ consequently orbitals of higher binding energy.

The bond order analysis in this section was performed in the group of M. Rohlfing (University of Münster) who used the Hückel model to calculate the parameters a_i and a_j for Eq. 4.4 and the SIESTA code introduced in Section 4.3 to get bond lengths of the kekulene molecule. The calculation of b_{ij} is performed for all chemically different bonds in the kekulene molecule indicated in Fig. 4.10**d**. This skeletal formula already hints to the bond lengths of these bonds a–f giving rise to single, double or "aromatic" bond character.

The results of bond order analysis are shown in Figs. 4.10 and 4.11. We plot the bond order vs. the DFT-optimized bond lengths of the bonds a–f based on the in total 24 predicted π orbitals resulting in a linear relation with negative slope as shown in Fig. 4.10**e**. In particular, the highest bond order is calculated for bond a representative for strong double bond character. The DFT calculation results in a bond length of $d_a = 1.370$ Å which is close to the double bond length of $\mathrm{R_{double}}$ =1.350 Å in *trans*-1,3-butadiene. Note that this molecule was used to calculated the optimum bond length $\mathrm{R_{opt}}$ for an aromatic system in the HOMA analysis. The smallest bond order suggestive for single bond character is calculated for bond e. Its length is optimized to $d_e = 1.452$ Å for free kekulene by DFT in excellent agreement with $\mathrm{R_{single}}$ =1.456 Å in *trans*-1,3-butadiene.

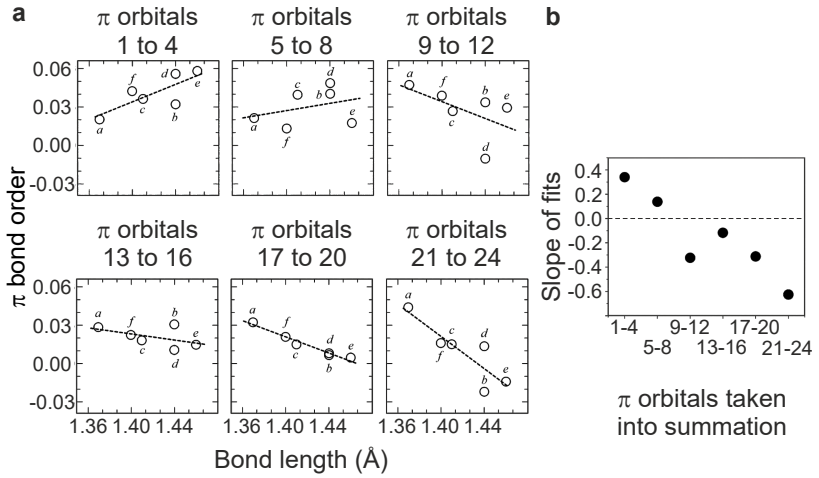

Figure 4.11: Bond order parameter vs. bond lengths
a Bond order parameters of bonds a to f plotted vs. their bond lengths for occupied π orbitals in groups of four. $m = 23$ to 24 is the degenerate $\mathrm{HOMO_a}/\mathrm{HOMO_b}$, $m = 21$ to 22 the degenerate $\mathrm{HOMO{-}1_a}/\mathrm{HOMO{-}1_b}$ and so on. Linear fits are drawn as dashed lines. **b** Slopes of these linear fits plotted vs. groups of π orbitals. Dashed line at zero slope. After Fig. S9 of Ref. [AH3]. Calculations by M. Rohlfing (University of Münster).

The initial intention of this bond order analysis was to see, whether the frontier π orbitals which we measure in the experiment, e.g., HOMO, is sufficient to characterize the aromaticity of the molecule. For this, the bond order parameter is calculated taking only the degenerate $\mathrm{HOMO_a}$ and $\mathrm{HOMO_b}$ ($m = 23$ to 24) orbitals into consideration. Indeed, the linear behavior with negative slope observed when taking all orbitals into account is reproduced as shown in Fig. 4.10**e**, **f**. This verifies to use the degenerate HOMO orbitals as measure for kekulene's aromaticity. Moreover, the nodal pattern of the combined HOMO illustrated in Fig. 4.10**c** shows that the π orbital electron density is enhanced at the shortest C–C bond a, but not at the longest bond e. The contribution of the HOMO to the bonding pattern is thus even astonishingly large.

In fact, the charge distribution of the doubly degenerate state HOMO-1 ($m = 21$ to 22) in Fig. 4.9**e–g** already shows another trend with charge density enhanced at bond e.

Fig. 4.11**a** displays this bond order analysis taking π orbitals of higher binding energy into account. The 24 π orbitals are partitioned into groups of four orbitals in this representation. For the four orbitals in one group, the bond order parameter is calculated and plotted vs. the bond lengths similar to Fig. 4.10**e**, **f**. Interestingly, the negative slope of the relation between bond lengths and bond order parameters found for the complete molecule in Fig. 4.11**b** is not found for orbitals with $m < 9$ indicating that their contribution to the overall bonding pattern is relatively small.

4.5 Conclusion

In this chapter, a reliable on-surface synthesis route of kekulene on Cu(111) using a specially designed precursor is presented. The high reaction yield of the well-oriented monolayer film is observed in STM and could be confirmed by the area-averaging technique of POT. In the photoemission data, we observe two molecular emissions identified as the doubly degenerate states of kekulene's HOMO and HOMO-1. This is confirmed by DFT calculations. Due to a correct bond order pattern already present in kekulene's HOMO, we infer that the orbital's nodal pattern which we measure in POT is indicative of the molecule's aromaticity. Comparing the experimental k map of the HOMO to various configurations of kekulene in theory allows for an unambiguous description of the molecule's aromatic state. The investigation in DFT using the geometric constraint of the Clar or superaromatic model reveals that the charge density is not affected by solely changing the bond lengths. This is also reflected in the simulated photoemission data. An configuration mimicking the geometric and electronic properties of a superaromatic state is achieved by switching off the coupling between the inner and outer circuits and thus enforcing the superaromatic conjugation paths. The corresponding k map does not resemble the experimental one, which finally rules out the superaromatic state of kekulene. Instead the Clar-type structure is favored – finally considering both, geometric and electronic constraints.

The assessment of kekulene's electronic nature in this work is enabled by using POT. It turns out that this method not only allows the identification of individual orbitals by assigning particular experimentally observed emissions to theoretical data. A careful analysis of the intensities and emission maxima in experimental k maps compared to those calculated for specific, hypothetical geometric and electronic states of a molecule can gain further insight into a molecule's aromatic state. The range of applications in the POT technique is thereby extended from the identification of single orbitals to an actual insight into a more fundamental concept: aromatic stabilization in polycyclic hydrocarbons.

5 | Identification of Nonplanar Iso-kekulene on Cu(110)

In this chapter, we investigate molecular, in particular, isomeric reaction products of the thermal reaction of specific precursor molecules on Cu(110). The formation of the three molecular species is observed experimentally by STM and confirmed by DFT calculations. Iso-kekulene is found to be the predominant reaction product on Cu(110) as concluded from POT experiments, which additionally reveal charge transfer from the metal to the adsorbate.

A dedicated journal article including additional STM measurements obtained with a CO-decorated tip by S. Wenzel is currently in preparation.

The acquisition and analysis of the experimental POT data have been my contribution in this project. POT experiments were conducted together with colleagues from Karl-Franzens-Universität in Graz, Forschungszentrum Jülich, and Physikalisch Technische Bundesanstalt Berlin. The synthesis of the precursor molecule and the acquisition of STM data were achieved in the groups of J. Sundermeyer and J. M. Gottfried, respectively (Philipps-Universität Marburg). DFT calculations have been performed in the group of P. Puschnig (Karl-Franzens-Universität, Graz, Austria).

5.1 Introduction

Building covalent bonds within single molecules or between molecular building blocks is the essence of reactions in organic chemistry. Some of these reactions can also be realized on single crystal surfaces in UHV by on-surface syntheses [AH3, 124–130, 196] using specially designed precursor molecules as demonstrated in the previous chapters 3 and 4. Especially the efficient synthesis of polycyclic aromatic hydrocarbons (PAH) on metal surfaces such as Cu, Ag, Au, and Pt resulting in nanographenes [43, 125, 130, 197–201], GNR [104, 124–126, 146, 148, 202–206], or coronoids/cycloarenes [127, 133, 207] has been studied in the last decade.

The resulting reaction products are influenced by an interplay of multiple aspects, e.g., the design of the molecular precursors, the chemical nature, and lattice of the underlying substrates or the sample temperature. A case in point is the correlation of symmetries – of the molecular precursor molecules and the metal substrate. In on-surface syntheses, the final reaction product using the same precursor molecule can therefore vary depending on the used surface orientation. The same surface orientations of different metal surfaces have reported to show considerable influence on the reaction pathways of on-surface synthesized PAHs [137, 139, 208] as well as varying crystal orientations of the same metal [148, 209]. For example, the brominated precursor molecule DBBA also discussed in Chapter 3 forms GNR on Au(111) [104, 146] and Cu(111) [147–149], which are, however, of different structures. On Cu(110), the reaction proceeds even differently and results in molecular bisanthene molecules ($C_{28}H_{14}$) [AH9, 35, 148] instead of GNR.

In this work, we show that POT is capable to differentiate varying conformational isomers of planar and nonplanar configuration. We do this using the example of the on-surface reaction of the precursor molecule 1,4,7(2,7)-triphenanthrenacyclononaphane-2,5,8-triene, further simply referred to as precursor molecule, which is deposited onto two different Cu surfaces separately: (111) and (110). Thereby, we are able to investigate the influence of the substrate's symmetry on the final reaction product. After thermal treatment of the as-deposited layers, we find ordered monolayers of two different isomers of kekulene on the two Cu surfaces. Exclusively kekulene is formed on Cu(111) as discussed in Chapter 4. In the present chapter, we will identify the isomeric state of the reaction products on Cu(110).

In the previous chapter, we find that more than 99% of the Cu(111) surface is covered by kekulene molecules formed in a thermally induced reaction of the precursor molecules. In that case, the three-fold symmetric Cu(111) surface matches the D_{6h} or, if the small alternating out-of-plane bending of the inner hydrogen atoms is taken into consideration, D_{3d} symmetry group of free kekulene. The on-

surface synthesis from the specially designed precursor molecules correspondingly results in a reaction product in line with the chosen Cu surface orientation. In the current chapter, we choose the two-fold symmetric Cu(110) surface to investigate the influence of the substrate's symmetry on the final reaction product after cyclodehydrogenation. We find that not only kekulene is formed on Cu(110), but the majority of the reaction products are identified as iso-kekulene – a conformational isomer of kekulene which adsorbs in tow different ways on the surface. In fact, the iso-kekulene-down configuration is favored over iso-kekulene-up. Interestingly, the molecules are charged on Cu(110) in contrast to previously reported neutral kekulene on Cu(111). The interaction between the molecules and the Cu(110) or Cu(111) substrate is therefore considerably different.

The precursor molecule 1,4,7(2,7)-triphenanthren-acyclononaphane-2,5,8-triene (**0**, Fig. 5.1**a**) is built out of three phenanthrene units marked with blue ellipses, which are freely rotatable around the adjacent single C–C bonds. The individual phenanthrene units can hence face with their central rings towards the center of the molecule or outwards. Upon adsorption on the surface, as revealed by STM measurements later, two different conformers are observed depicted in Fig. 5.1**b**. The molecule correspondingly adsorbs with two phenanthrene units flat, while the third unit bends out of the molecular plane, either rotated away (**C1**) or towards (**C2**) the central pore.

After detachment of six hydrogen atoms due to thermal treatment, the highly twisted precursor molecule (**0**) can in general result in four isomers with different symmetries as indicated in Fig. 5.1**c**. The newly formed C–C bonds are marked in red. If all phenanthrene units of **0** are rotated outwards reducing the sterical hindrance of the hydrogen atoms in the central pore, kekulene (**1**) is formed as already reported as a reaction product on Cu(111) (Chapter 4).

Notably, if one phenanthrene unit is rotated toward the center of the molecule, the symmetry of the reaction product changes. Iso-kekulene (**2**) has only one mirror plane (Fig. 5.1**c**). This different structure has high impact on the molecules conformation, because the two carbon atoms marked with C_1 and C_2 as well as the attached hydrogen atoms require space and therefore do not lay in the molecular plane. Iso-kekulene (**2**) is consequently not planar in contrast to kekulene (**1**). The vertical position of the two carbon atoms marked with C_1 and C_2 in Fig. 5.1**c**, **2** will later aid to quantify the degree of nonplanarity for this phenanthrene unit when turning to theoretical predictions of the molecules on the Cu(110) surface.

The rotation of more than one phenanthrene unit towards the center of the precursor molecules (Fig. 5.1**a**, **0**) results in the even more sterically demanding products **3** and **4** having one mirror plane and three-fold symmetry, respectively.

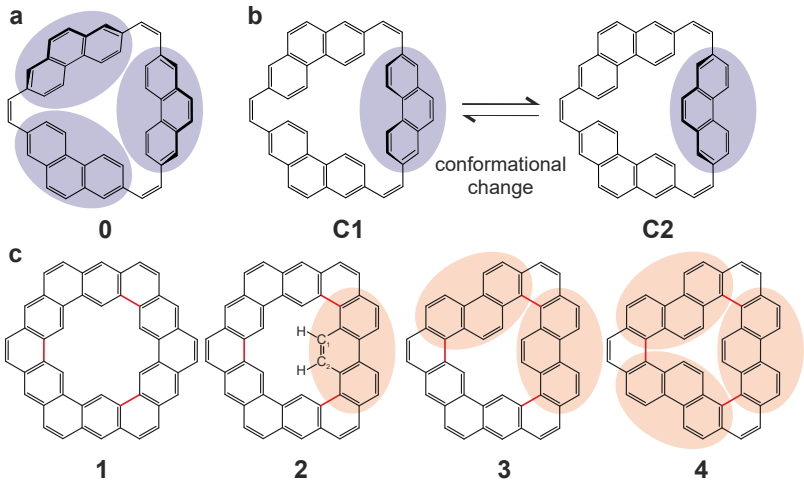

Figure 5.1: Molecular precursor and possible reaction products
Skeletal formula of **a** precursor molecule (**0**) with rotatable phenantrene units indicated with blue ellipses. **b** Conformational changes of **0** upon deposition on the surface. Two phenanthrene units flat and the third unit either rotated away (**C1**) or towards (**C2**) the central pore. **c** Possible reaction products after dehydrogenation of **0** with phenanthrene units rotated towards the center of the molecule marked with orange ellipses. Kekulene, **1**; iso-kekulene, **2**. Labeled carbon atoms C_1 and C_2 important in Section 5.4. Sterically demanding products **3** and **4**. Established C–C bonds after dehydrogenation are marked in red.

The azimuthal orientation of the on-surface synthesized molecules is described using one edge of the molecule and the substrate's high symmetry directions. In the six-fold symmetric kekulene (Fig. 5.1**c**, **1**), all molecular edges are C–C zigzag-edges and equivalent. In iso-kekulene (Fig. 5.1**c**, **2**), there are only four zigzag-edges. The edge where one phenanthrene unit is rotated towards the center of the molecule marked with an orange ellipse is transformed into an armchair edge. Since two zigzag-edges (top and bottom) in **2** are connected to the rotated phenanthrene unit and two border to other zigzag-edges, the four edges are not equivalent. Describing the orientation of the iso-kekulene molecule using any zigzag-edge in the molecule would thus not be precise. For that reason, we use the armchair edge of iso-kekulene to describe its azimuthal orientation on the surface in the following. Note here that the armchair edges of graphene are expected to possess spin-polarized edge states [210]. Therefore, an isomeric transformation from the all-zigzag-edged kekulene to iso-kekulene with an additional armchair edge might be interesting for exotic electronic applications.

As we will see later in this chapter, iso-kekulene and kekulene molecules are the main products of this reaction on the Cu(110) surface, which is why we omit to describe how the orientation of the products **3** and **4** presented in Fig. 5.1**c** would be described.

5.2 Experimental details

5.2.1 Synthesis of precursor molecule

The synthesis and analysis of the precursor molecules (**0**, Fig. 5.1**a**) as a solid material are described in detail in the previous chapter 4.1.2. The chemical synthesis of the precursor molecules was carried out in the group of J. Sundermeyer (Marburg University).

5.2.2 On-surface synthesis on Cu(110)

The on-surface synthesis on Cu(110) was carried out under UHV conditions in the preparation chamber of the toroidal electron analyzer (Section 2.4.4). In the beginning, the Cu(110) crystal was cleaned by repeating sputter/anneal cycles. We use the same protocol as for the on-surface synthesis of kekulene on Cu(111) (Section 4.1.2) developed in the group of J. M. Gottfried (University of Marburg) and replicate the procedure on Cu(110). It involves the thermal evaporation of the precursor molecules in vacuum at 550 K to deposit intact molecules on the Cu(110) surface held at RT. Subsequent annealing of the layer of precursor molecules at 500 K triggers the cyclodehydrogenation reaction on Cu(110).

5.3 Experimental results

5.3.1 STM

Figure 5.2 displays STM images before and after thermal treatment of the molecular precursor layer on the Cu(110) surface. STM experiments were carried out at 100 K. The as-deposited submonolayer of the precursor molecules is displayed as overview and zoom-in images in Fig. 5.2**a**, **b**, respectively. The nonplanar molecules adsorb disordered in two different preferential adsorption configurations marked with white and blue frames in Fig. 5.2**b**. The white-framed species is of irregular pentagonal shape with one bright protrusion in the center of the longest edge of the pentagon.

The second species marked with a blue frame has a distorted hexagonal shape and two adjacent bright protrusions. The conformation of the two adsorption species can be explained by the angle of rotation of the phenanthrene units in the precursor molecule (Fig. 5.1**a**, **0**). It suggests that in both cases, two phenanthrene units lie flat on the sample surface. The third unit either points away from the center of the molecule or towards it (Fig. 5.1**b**, **C1** vs. **C2**). In the first case, the phenanthrene unit is rotated away from the central pore and therefore has more space, while due to sterical hindrance in the second case, the complete phenanthrene unit is pointing out of the molecular plane. As might be naturally assumed from the skeletal geometry of the conformers, this results in either two or one bright protrusions in the STM images. We label these conformers C1 (two bright protrusions, hexagonal, blue frame) and C2 (one bright protrusion, pentagonal, white frame), respectively.

A statistical analysis of overview STM images (Q. Fan, University of Marburg) focusing on the coverage of the two conformers shows that on the Cu(110) surface conformer C2 is favored ($\approx$ 72 %) over C1. The higher stability and therefore increased coverage of C2 on the Cu(110) surface in comparison to C1 may be due to the different registry of C2.

After annealing the submonolayer of the precursor molecules to 500 K, the bright protrusions disappear, suggesting the formation of more planar reaction products (Fig. 5.2**c**). Closer inspection on the magnified image in Fig. 5.2**d** reveals that two reaction products are formed after cyclodehydrogenation. The four potential products after dehydrogenation of the precursor molecule are introduced in Fig. 5.1**c**, yet only two of those resemble the shapes of the molecules found in the STM measurements. The species marked with the blue frame and superimposed with a blue hexagon in the bottom of Fig. 5.2**d** is of regular hexagonal shape in agreement with the hexagonal topology of kekulene (Fig. 5.1**c**, **1**). The second product (white frame and white pentagon in the bottom of Fig. 5.2**d**) is of pentagonal shape. This shape resembles iso-kekulene (Fig. 5.1**c**, **2**) in which one phenanthrene unit is rotated towards the central pore leading to a product with one mirror plane. Note that this iso-kekulene has not been reported in literature up to date.

Careful analysis of overview STM images indicates that the sub-monolayer molecular film on Cu(110) consists of approximately 83 % iso-kekulene and 17 % kekulene molecules. From a general point of view, the ratio between different conformers and/or isomers is related to a gain of global energy within the system. Nevertheless, kinetic aspects as well as stochastic variations may play a role, especially taking into account the limited field of view in STM.

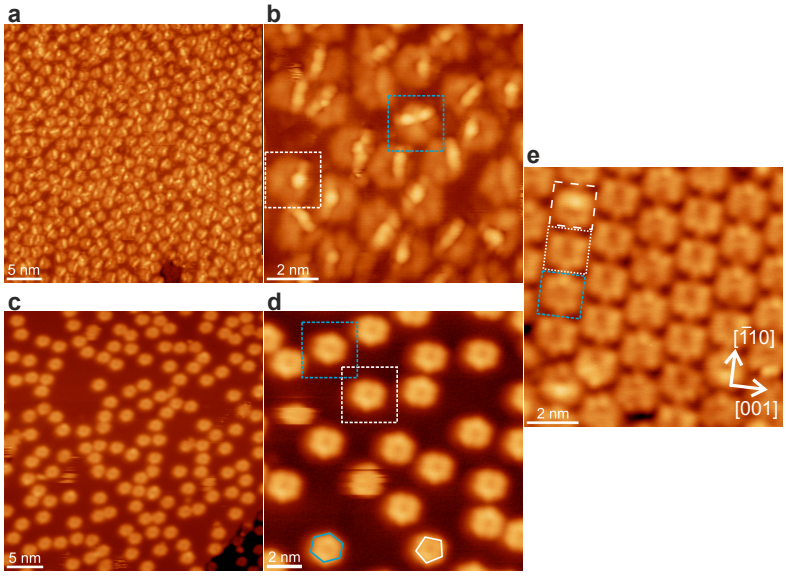

Figure 5.2: STM before and after annealing of precursor/Cu(110)
STM image after deposition of intact precursor molecules on the Cu(110) surface in **a** overview (U = 1.7 V, I = 0.08 nA) and **b** magnified STM images (U = −3.4 V, I = 0.11 nA). **c** and **d** show the respective overview and magnified STM images after subsequent annealing of the submonolayer of precursor molecules to 500 K (U = 1.4 V, I = 0.09 nA and U = −3.4 V, I = 0.11 nA). White and blue frames mark different conformers C1 and C2 after adsorption or resulting reaction products kekulene and iso-kekulene, respectively, also indicated by blue hexagon and white pentagon in **d**. **e** Monolayer after thermal reaction on Cu(110) resulting in iso-kekulene-up (dashed, white frame), iso-kekulene-down (dotted, white frame), and kekulene (blue frame). U = −1.0 V, I = 0.21 nA. STM images by Q. Fan.

We infer that the predominant precursor species with one bright protrusion (C2) transforms into the preferred reaction product, iso-kekulene (**2**), after thermal treatment. Conformer C1 consequently converts into the less prominent reaction product, the hexagonally shaped kekulene (**1**) molecules. Note however, that the ratio of precursor conformers on the surface (C1 : C2 = 28% : 72%) results in a ratio of reaction products of 17% : 83% favoring iso-kekulene over kekulene. This discrepancy can be due to a different position at the sample. It could also mean that, e.g., C1 conformers can also transform into iso-kekulene, or that the desorption rate of one conformer is higher compared to the other one.

In experiments with higher coverage, we observe that the ratio of isomers is different. Fig. 5.2**e** displays an STM micrograph of the Cu(110) surface after annealing a precursor monolayer at 500 K. Clearly, we see more pentagonal species assigned to iso-kekulene (white frames) in comparison to hexagonal species ascribed to kekulene (blue frame). In fact, we observe two different types of pentagonal molecules (iso-kekulene). In the upper molecule of Fig. 5.9**a** marked with a dashed, white frame, one bright protrusion is visible which is missing in the molecule below (dotted white frame).

As DFT simulations (Fig. 5.9**b**) confirm later in Section 5.5.3, these are iso-kekulene molecules with the inwards rotated phenanthrene unit tilted out of the molecular plane pointing either away from the substrate ("up") or towards it ("down"). The geometries of these two conformers are discussed again in Section 5.4. The total ratio of iso-kekulene (white frames) vs. kekulene (blue frame) molecules is determined to 92 % : 8 % according to STM. Of these 92 % iso-kekulene molecules, approximately 11 % are iso-kekulene-up and 81 % iso-kekulene-down. Overall, iso-kekulene-down is thus the preferred adsorption species.

The observed higher reaction yield of iso-kekulene molecules can be understood by an increased in-plane pressure at monolayer coverages and the relative sizes of the reaction products. Iso-kekulene in general requires less space on the surface in comparison to kekulene, which has a large pore in the center (see Fig. 5.1**c** **1** vs. **2**). Considering the total energy of the system, iso-kekulene is thus more preferred when the coverage reaches saturation.

Interestingly, the three observed molecular species form rows on the Cu(110) surface in which they are aligned in one orientation (Fig. 5.2**e**). Namely, the kekulene molecules are oriented with one zigzag-edge parallel to the substrate's $[\bar{1}10]$ direction. Iso-kekulene molecules orient with their armchair-edges parallel to the [001] direction. The distance between the centers of the molecules is always the same, which suggests that all molecules are positioned at the same Cu adsorption site. According to low-energy electron diffraction (LEED), the molecular layer is in good commensurate registry with the substrate. The LEED image is shown in Appendix C.

The superstructure matrix is $\begin{pmatrix} 6 & 0 \\ 3 & 4 \end{pmatrix}$ with unit cell vectors of $a = 16.35$ Å and $b = 15.34$ Å ($\theta = 62°$). This unit cell will be used later to develop a reasonable adsorption geometry in the DFT calculations (see Section 5.4).

5.3.2 Band maps

The band maps of clean Cu(110) and of the organic monolayer formed after annealing the precursor on Cu(110) measured along the substrate's [1$\bar{1}$0] directions are presented in Fig. 5.3**a**, **b**, respectively. Note that along this particular direction, DFT predicts the emission of the molecule's LUMO and HOMO−1 orbitals (see Fig. 5.5**a**, **b**).

In the band map of the clean metal surface displayed in Fig. 5.3**a**, the *sp* band is clearly visible as a sharp bright line. The high intensity at $E_\mathrm{b} > 2$ eV indicates the onset of the Cu *d* band. After depositing and annealing a monolayer of precursor molecules on the Cu(110) surface, the band map shows additional intensities between E_F and the onset of the Cu *d* band (Fig. 5.3**b**). There are two emissions visible, one close to E_F and another close the metal *d* band. The corresponding *k* maps at $E_\mathrm{b} = 0.11$ eV and 1.83 eV are displayed in Fig. 5.3**c**, **d**, respectively. The clear features in the *k* maps prove the successful on-surface synthesis after annealing the as-deposited precursor molecules. Additionally to the molecular emissions, the *sp* band of the metal is still visible as a sharp line in both *k* maps along $k_{001} = 0.00$ Å^{-1}. The exact positions of these sharp lines in $k_{1\bar{1}0}$, however, vary depending on E_b from 1.30 Å^{-1} (at $E_\mathrm{b} = 0.11$ eV, Fig. 5.3**c**) to 1.55 Å^{-1} (at $E_\mathrm{b} = 1.83$ eV, Fig. 5.3**d**). This minor shift is in agreement with the parabolic dispersion of the *sp* band visible in both band maps in Fig. 5.3**a**, **b**.

5.3.3 POT

Fig. 5.3**c**, **d** shows the *k* maps of the sample after the successful chemical reaction corresponding to binding energies of $E_\mathrm{b} = 0.11$ eV and 1.83 eV indicated by light blue and red dashed horizontal lines in the band map of Fig. 5.3**b**. The *k* map at $E_\mathrm{b} = 0.11$ eV (Fig. 5.3**c**) displays two bright, round emissions at (± 1.8, 0.0) Å^{-1} and two pairs of elongated emission lobes at (± 1.0, ± 1.6) Å^{-1} suggesting a reasonably well-organized organic film. Yet, some degree of disorder in the layer is observed, considering the radial emission at a radius of $k_\parallel = 1.6$ Å^{-1}. The *k* map measured at $E_\mathrm{b} = 1.83$ eV appears rather diffuse due to the vicinity of the Cu *d* band. Nevertheless, six emission lobes are clearly visible.

Note that due to the diffuse emission intensity in both *k* maps, the comparison of experimental and theoretical *k* maps is hindered if deconvolution is considered (see Section 5.5.1). We therefore additionally compare the experimental *k* map recorded at $E_\mathrm{b} = 0.11$ eV to theoretical *k* maps of four different molecule/substrate systems using radial intensity profiles (Section 5.5.2). Since both of these approaches require simulations, these are presented in the following section.

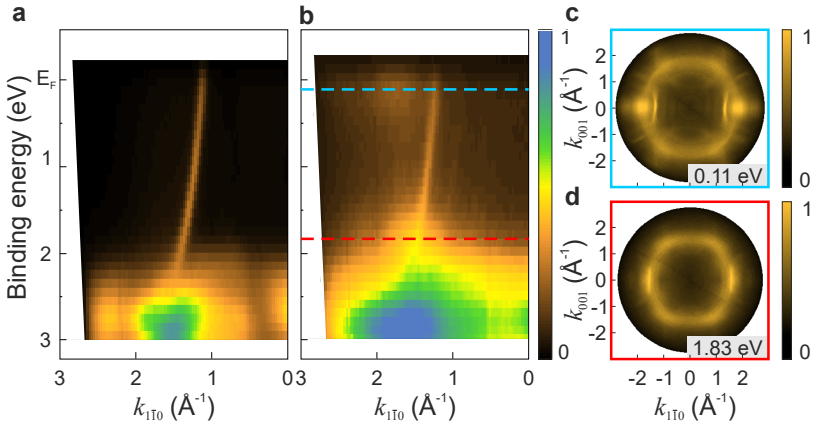

Figure 5.3: Band maps and k maps
Band maps measured along the $[1\bar{1}0]$ direction of Cu(110) in an energy range of 3 eV below E_F for **a** clean Cu(110) and **b** after adsorbing and annealing the precursor molecules. **c**, **d** k maps of the sample after the chemical reaction at $E_b = 0.11$ eV and 1.83 eV corresponding to the light blue and red dashed horizontal lines in **b**.

5.4 DFT calculations

For the three reaction products, namely kekulene, iso-kekulene-down, and iso-kekulene-up, observed by STM after the thermal reaction of the precursor on Cu(110), DFT calculations are performed to find the energetically favored adsorption site as well as the electronic structure of the molecule/metal interface. Calculations of the three molecule/Cu(110) interfaces are used to compare simulated and experimental k maps as well as STM contrast in Section 5.5.

Geometry relaxations are performed using the PBE-GGA functional including van der Waals corrections according to Tkatchenko and Scheffler (TS) [183]. Five layers of Cu(110) were used in the simulation with atoms in the bottom three layers fixed, while the topmost two layers were allowed to relax. For iso-kekulene (up and down configurations), the unit cell dimensions of $a = 16.07$ Å and $b = 15.06$ Å ($\theta = 62°$) are used in the calculation in agreement with the values from experimental LEED data ($a = 16.35$ Å, $b = 15.34$ Å, $\theta = 62°$). A flat-lying kekulene molecule, however, does not fit into this unit cell. Since STM does not show any significant asymmetry, a tilted kekulene molecule can also be ruled out. Therefore, an enlarged unit cell is used in the calculations of kekulene/Cu(110) ($a = 17.75$ Å and $b = 17.57$ Å, $\theta = 90°$), which fits best to the experimental STM data (Section 5.3.1).

The calculations were by performed by A. Reichmann in the framework of his Master's thesis [182]. The resulting most favorable adsorption sites are judged by the total energies of the system E_{tot}, the adsorption energies E_{ad} defined in the previous chapter (page 99, Eq. 4.1) and the simulated adsorption heights discussed first in this section. This is followed by the calculated electronic properties of the adsorbate layers performed by P. Puschnig and analyzed in this work in Section 5.4.2. k maps of the molecule/substrate systems at two binding energies are discussed in the end of this chapter, which will be compared to experimental data in Section 5.5.

5.4.1 Geometry relaxations

In the beginning, geometry relaxations are performed for kekulene on Cu(110) located at the top, short bridge (SB), long bridge (LB), and hollow (H) sites oriented with its zigzag-edges either along the substrate's [001] or [$\bar{1}$10] directions. For these 8 different adsorption configurations, the most stable configuration is found to be the LB site with kekulene's zigzag-edge parallel to the [001] direction of the Cu(110) substrate considering the total energies E_{tot} of the systems.

Adsorption site	**zigzag along**	$\boldsymbol{E_{\mathrm{tot}}}$ **(eV)**	$\boldsymbol{\Delta E_{\mathrm{tot}}}$ **(eV)**	$\boldsymbol{E_{\mathrm{ad}}}$ **(eV)**	$\boldsymbol{E_{\mathrm{ad}}}$ **(eV/nm²)**	$\boldsymbol{\bar{h}_{\mathrm{C}}}$ **(Å)**
top	[001]	−1185.76	0.73	–	–	2.52
SB		−1185.93	0.55	–	–	2.39
LB		−1186.75	0.73	–	–	2.43
H		−1185.70	0.79	–	–	2.37
top	[$\bar{1}$10]	−1185.21	1.28	−7.94	−2.55	2.54
SB		−1185.82	0.67	−8.55	−2.74	2.46
LB		**−1186.49**	**0**	**−9.22**	**−2.96**	**2.41**
H		−1185.98	0.51	−8.71	−2.79	2.48

Table 5.1: Total and adsorption energies of kekulene/Cu(110)
Total energies E_{tot} and adsorption energies E_{ad} in eV and eV/nm^2. Average adsorption heights of carbon atoms $\bar{h}_{\mathrm{C}}$ in Å. Calculations were performed for kekulene in the top, short bridge (SB), long bridge (LB), and hollow (H) sites of Cu(110) oriented with its zigzag-edge along the substrate's [$\bar{1}$10] and [001] directions.

This is in agreement with the molecule's orientation observed in STM measurements of full monolayer coverage (see Fig. 5.2**e**). This configuration is $\Delta E_{\mathrm{tot}} = 0.51$ eV more stable than the second stable H site. All calculated total and adsorption energies of kekulene on Cu(110) can be found in Table 5.1.

For both iso-kekulene species, the orientation of the molecules on the Cu(110) is found to be same as for kekulene from STM experiments. Therefore, we use the same preferential azimuthal orientation from the geometry relaxations of kekulene for the geometry relaxations of both iso-kekulene configurations. Geometry relaxations for iso-kekulene oriented in the other high symmetry reaction are therefore not performed, which leaves the investigation of four adsorption sites with the molecule oriented in the same direction as kekulene. This is iso-kekulene's armchair edge parallel to the [001] direction.

The calculated total energies E_{tot} and adsorption energies E_{ad} for iso-kekulene on Cu(110) are presented in Tab. 5.2. For iso-kekulene-up/Cu(110), DFT predicts the LB site as the most favorable adsorption site considering E_{tot} – the same as for kekulene – with a clear energetic difference of 0.42 eV to the second stable adsorption site (H). Contrary, in the case of iso-kekulene-down/Cu(110), the H position is calculated as the most favorable adsorption site – 0.52 eV more stable than the LB site of iso-kekulene-down/Cu(110).

In the course of this chapter, we will show that theoretical predictions of iso-kekulene-down at the H site do not agree with experimental POT data. Instead, predictions based on iso-kekulene-down at the LB site – the same adsorption site as iso-kekulene-up and kekulene – matches the experimental data. Therefore, we will show the simulations of iso-kekulene-down/Cu(110) in both adsorption sites – H and LB – to be compared to experimental POT data in Section 5.4.2.

To correlate the theoretical results from the geometry relaxations to the experiment, the total energies of the systems are not suitable, because the calculations for kekulene required a larger unit cell than those for iso-kekulene. The obtained E_{tot} and E_{ad} are therefore not comparable. To this end, E_{ad} is divided by the unit cell areas (kekulene/Cu(110): 311.9Å^2; iso-kekulene/Cu(110): 213.9Å^2) resulting in the adsorption energies per area given in the last columns of Tabs. 5.1, 5.2.

According to these comparable quantities, kekulene is predicted to be least stable on the Cu(110) surface ($E_{\mathrm{ad}} = -2.96$ eV/nm^2). This is in agreement with experimental STM data, where for a complete monolayer only 8 % of the metal surface is covered with kekulene molecules and 92 % with iso-kekulene. The values of E_{ad}/nm^2 for iso-kekulene-up (LB) and -down (H and LB) show a preference for iso-kekulene-up at the LB site ($E_{\mathrm{ad}} = -4.07$ eV/nm^2). We can thus unambiguously conclude that on Cu(110), iso-kekulene is more stable than kekulene

considering E_{tot} and E_{ad}. Nevertheless, a preference of either iso-kekulene-up or iso-kekulene-down has to be taken with care due to the different possibilities of calculating E_{mol} and E_{surf} in Eq. 4.1 which would presumably slightly change the computed E_{ad}. Namely, E_{mol} and E_{surf} could either be calculated in the geometries as in the molecule/substrate system or in geometries that are separately relaxed for either the molecule or the substrate. In this work, the first variant is computed.

The simulated relaxed adsorption configurations of iso-kekulene-up, iso-kekulene-down, and kekulene in the LB positions of Cu(110) as well as iso-kekulene-down at the H site as obtained by DFT are illustrated in Fig. 5.4. The figure displays the adsorption configurations in top views as well as in two side views.

Iso-kekulene	Adsorption site	E_{tot} (eV)	ΔE_{tot} (eV)	E_{ad} (eV)	E_{ad} (eV/nm^2)	$\bar{h}_{\mathrm{C}}$ (Å)
up	top	−979.38	1.09	−7.62	−3.56	2.69
	SB	−979.76	0.71	−8.00	−3.74	2.59
	LB	**−980.47**	**0**	**−8.71**	**−4.07**	**2.48**
	H	−980.05	0.42	−8.29	−3.88	2.57
down	top	−978.87	1.44	−6.78	−3.17	2.87
	SB	−978.97	1.34	−6.88	−3.22	2.87
	LB	−979.79	0.52	−7.70	−3.60	2.67
	H	**−980.31**	**0**	**−8.22**	**−3.84**	**2.60**

Table 5.2: Total and adsorption energies of both iso-kekulene conformers on Cu(110)

Total energies E_{tot} and adsorption energies E_{ad} in eV and eV/nm^2. Average adsorption heights of carbon atoms $\bar{h}_{\mathrm{C}}$ in Å. Calculations were performed for iso-kekulene-up and iso-kekulene-down in the top, short bridge (SB), long bridge (LB), and hollow (H) sites of Cu(110).

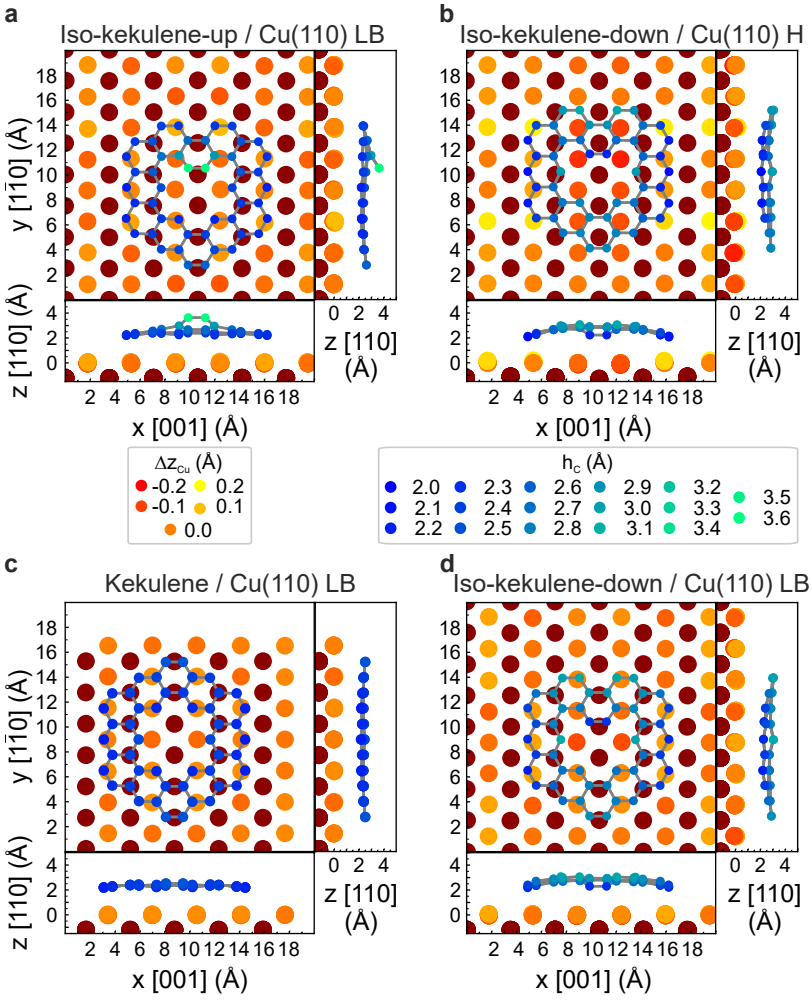

Figure 5.4: Simulated iso-kekulene and kekulene on Cu(110)
Top and side views of the relaxed adsorption geometries to be most stable according to DFT. **a** Iso-kekulene-up in long bridge (LB) site, **b** iso-kekulene-down in hollow (H) site, **c** kekulene in LB site on Cu(110) as well as **d** iso-kekulene-down in LB site. The color codes of the displayed atoms indicate their heights. The red color represents the Cu substrate with dark red indicating the second Cu atom layer. Blue color shows the adsorbed molecular species. DFT calculations by P. Puschnig.

In this way, the degree of bending of the entire iso-kekulene molecule can easily be visualized as well as the height of the two carbon atoms C_1 and C_2 facing the center of the iso-kekulene molecules (see Fig. 5.1**b**, **2**) with respect to the remaining C atoms of the molecule. The color codes of the displayed atoms indicate their heights. The red color represents the Cu substrate with dark red indicating the second Cu atom layer. The blue color shows the adsorbed molecular species. The exact adsorption heights are summarized in Tables 5.1 and 5.2 showing the average height $\bar{h}_C$ of all carbon atoms in Å.

According to DFT predictions, $\bar{h}_C$ is comparably small for all four adsorbate configurations discussed in this section in comparison to that calculated for neutral kekulene on Cu(111) ($\bar{h}_C$ = 3.05 Å) reported in the previous chapter 4. The predicted value of 2.67 Å for iso-kekulene-down in the LB position is very similar as the experimentally derived adsorption height of 2.66 Å for PTCDA on Cu(111) [186], while the adsorption heights of iso-kekulene-up and kekulene on Cu(110) are predicted to be even smaller (2.48 Å and 2.41 Å). Since the adsorption heights are considerably smaller than the sum of van der Waals radii (3.17 Å calculated from carbon in benzene r^{C}_{vdW} = 1.77 Å [187] and copper r^{Cu}_{vdW} = 1.4 Å deduced from organo-metallic compounds (methodologically least reliable) [187]), we can unambiguously describe the interaction between iso-kekulene and kekulene with the Cu(110) substrate as rather strong. This interaction can be described in more detail consulting the electronic properties of the interfaces, which is discussed in the next part of this work.

5.4.2 Electronic structure calculations

Orbitals of free molecules

The electronic properties of free molecules can be described using their orbitals. The real-space representations of, e.g., HOMO and LUMO have characteristic nodal structures which can be accessed experimentally by POT in terms of k maps. The construction of k maps is described in Chapter 2.

The k maps of the molecule's HOMO−1, HOMO, LUMO, LUMO+1, and LUMO+2 orbitals are plotted in Fig. 5.5 for free iso-kekulene and free kekulene in **a**, **b**, respectively. Colored frames denote the particular orbitals HOMO−1 (green), HOMO (blue), LUMO (red), LUMO+1 (black) and LUMO+2 (light blue). [1]

[1] Kinetic energies of 28.5 eV and 30.1 eV were used for occupied and unoccupied states, respectively, in correspondence to experimental POT data recorded at $h\nu$ = 35 eV.

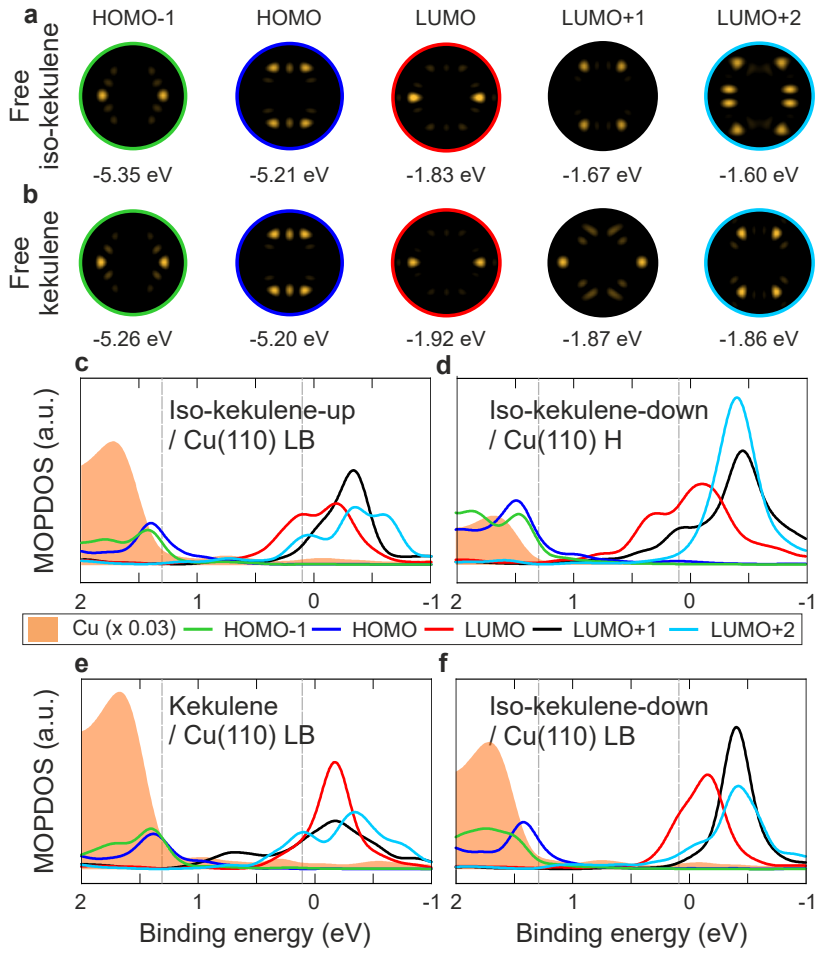

Figure 5.5: Simulated k maps of free molecules and MOPDOS for relaxed iso-kekulene and kekulene on Cu(110)

a, **b** k maps of HOMO−1, HOMO, LUMO, LUMO+1, and LUMO+2 framed in green, blue, red, black, and light blue, respectively, of free iso-kekulene and kekulene, respectively. Calculated energies $E - E_{\mathrm{vac}}$ are given below the corresponding k maps. **c**, **d** Simulated densities of states of the complete molecule/substrate systems projected onto these five molecular orbitals as solid lines and substrate Cu atoms in orange-shaded areas. The calculations are based on the relaxed adsorption species of smallest adsorption energy: **c** Iso-kekulene-up (LB); **d** iso-kekulene-down (H) and **e** kekulene (LB). **f** Iso-kekulene-down in second stable LB site. Gray dashed lines mark binding energies for k maps shown in Fig. 5.6. Calculations by P. Puschnig.

The k maps of HOMO−1 (green), HOMO (blue), and LUMO (red) are barely distinguishable for iso-kekulene and kekulene, which shows that the nodal structure of these orbitals is very similar. In the case of free kekulene, the k maps of LUMO and LUMO+1 (Fig. 5.5**b**, red, black) both have their major emissions along $k_x = 0$ with only a small difference in their k_y position. Although there are weak additional emissions in the LUMO+1 k map, these two orbitals are difficult to discriminate in POT and an overlap of the two would result in an elongated emission lobe along $k_x = 0$.

The k maps of LUMO+1 (black) and LUMO+2 (light blue) of kekulene and iso-kekulene differ more. In general, one might argue that the LUMO+2 is less practical, because it is not occupied in the case of the free molecules and thus does not contribute to the photoemission. Only a substantial CT transfer of more than four electrons would lead to an occupation of this orbital making it accessible in POT. However, in the case of free kekulene, $(E - E_{\mathrm{vac}})$ of LUMO+2 is close to that of the LUMO+1 ($\Delta(E - E_{\mathrm{vac}}) = 0.01$ eV). Therefore, it is worth taking it into account in this discussion. Moreover, since the LUMO+1 and LUMO+2 of kekulene are energetically close, it is not surprising that one of the two k maps (Fig. 5.5**b**, light blue) exhibits the same pattern of four emission lobes as that of the LUMO+1 of iso-kekulene (Fig. 5.5**a**, black). Therefore, it is reasonable to directly compare the LUMO+1 of iso-kekulene (Fig. 5.5**a**, black) to the LUMO+2 of kekulene (Fig. 5.5**b**, light blue) in the following discussion.

Projected density of states and simulated *k* maps

If the molecules are adsorbed on a surface, metal and molecular states may begin to overlap. As a consequence, the real-space distributions of the orbitals may change and therefore also their k maps depending on the influence of the substrate. The interaction between adsorbate and substrate can be approached using the electronic properties of the interface calculated by DFT. Note that although DFT-calculated binding energies are usually shifted due to the lack of an appropriate treatment of exchange-correlation effects, differences in the theoretical MOPDOS are observed for iso-kekulene-up (LB), iso-kekulene-down (H), kekulene (LB), and iso-kekulene-down (LB) on Cu(110). A better agreement between theory and experiment can give rise to the predominant adsorption species.

In this chapter, the electronic properties of the molecule/metal interfaces are accessed via the molecular orbital projected density of states (MOPDOS) calculated by DFT. The results are displayed in Fig. 5.5**c**–**f** in an energy range of −1.0 eV to 2.0 eV for iso-kekulene-up, iso-kekulene-down, and kekulene on Cu(110). The orange-shaded areas display the plane-averaged charge density of all Cu atoms and the colored lines the MOPDOS of the single orbitals (HOMO−1, HOMO,

LUMO, LUMO+1, and LUMO+2 in green, blue, red, black, and light blue). The MOPDOS for the predicted most stable configurations iso-kekulene-up (LB), iso-kekulene-down (H), and kekulene (LB) are plotted in Fig. 5.5**c**, **d**, and **e**, respectively. As mentioned earlier, the H position of iso-kekulene-down turns out to disagree with experimental data later, which is why the MOPDOS of this molecule in the second stable LB site is plotted as well in Fig. 5.5**f**. The dashed gray lines indicate the two binding energies of $E_\mathrm{b} = 0.1$ eV and 1.3 eV for simulated k maps of the molecule/Cu(110) systems shown in Fig. 5.6.

The MOPDOS of HOMO (blue) and HOMO−1 (green) show subtle differences between the four adsorption configurations. Only for iso-kekulene-down (LB) one orbital (HOMO) is stronger than the other, while for the other three adsorption configurations, the course of the MOPDOS of HOMO and HOMO−1 is very similar. Also the contribution of the substrate varies, since the MOPDOS of HOMO and HOMO−1 either overlap with the metal d states partly (for iso-kekulene-down (LB), Fig. 5.5**f**), completely (for iso-kekulene-up (LB) and -down (H), Fig. 5.5**c**, **d**) or are energetically even located within (kekulene (LB), Fig. 5.5**e**) the metal d band.

This is reflected in the k maps simulated at $E_\mathrm{b} = 1.3$ eV and plotted in Fig. 5.6**e**–**h**. In particular, the vicinity to the Cu d band leads to stronger substrate contribution and therefore more complicated emission patterns. Still, the six emission lobes of the molecular orbitals, namely the two along $k_{001} = 0$ Å^{-1} from the HOMO−1 and the remaining four from the HOMO, are clearly visible in the four k maps. In the case of iso-kekulene-up and iso-kekulene-down at the LB sites (Fig. 5.6**e**, **h**), the intensity of the HOMO is more prominent compared to that of HOMO−1, which is why the four emission lobes from the HOMO are more intense. For iso-kekulene-down at the H site (**f**), the emission lobes based on the two orbitals are similarly intense, while in the case of kekulene/Cu(110) (**g**) the two lobes of HOMO−1 prevail. An identification of the adsorption species upon comparison of these k maps close to the metal d band to experimental data is, however, ambiguous due to the strong substrate contribution in the experimental data (see Fig. 5.3**d**).

By definition, the LUMO+2, LUMO+1, and LUMO orbitals of free iso-kekulene and kekulene molecules are not occupied. According to DFT calculations, this changes upon adsorption on Cu(110), as can be seen from the red, black, and light blue MOPDOS curves in Fig. 5.5**c**–**f**. In the case of iso-kekulene on Cu(110), the contribution of the LUMO (red curves) dominates between 0.5 eV and 0 eV. This is reflected in the k maps of the complete molecule/substrate systems at $E_\mathrm{b} \approx 0.1$ eV (see Fig. 5.6**a**, **b**,**d**), in which the two emission lobes along $k_{001} = 0$ Å^{-1} are stronger compared to the others.

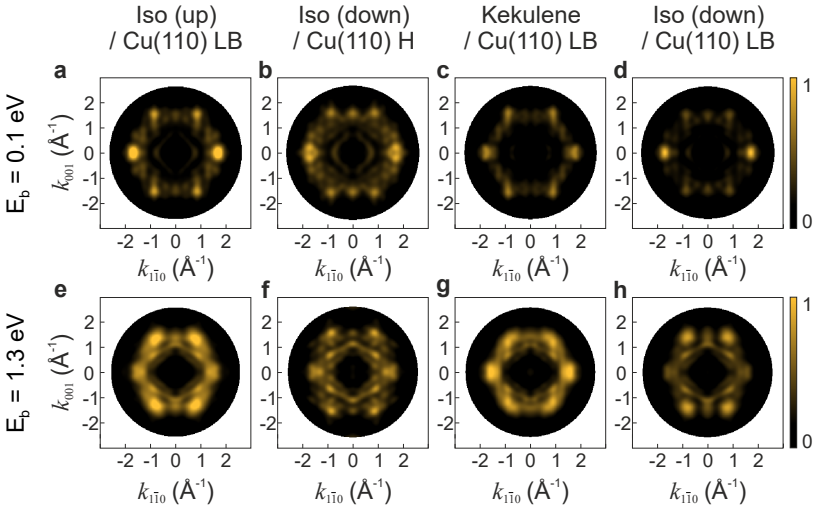

Figure 5.6: Simulated k maps of iso-kekulene and kekulene on Cu(110) Simulated k maps of iso-kekulene-up, iso-kekulene-down, and kekulene at the most favorable long bridge (LB), hollow (H), and LB sites of Cu(110) according to DFT-calculated adsorption energies in first, second, and third columns, respectively. As well as iso-kekulene-down at the second stable LB site in the fourth column. k maps simulated at **a**–**d** $E_\mathrm{b} = 0.1$ eV and **e**–**h** 1.3 eV, respectively, calculated by P. Puschnig.

For kekulene/Cu(110), however, theory predicts roughly equal contributions of the former unoccupied states leading to six similarly intense emission lobes in the k map in Fig. 5.6**c**. Due to this difference in the k maps, one could differentiate whether kekulene or iso-kekulene is the preferred reaction product consulting experimental k maps, e.g., using deconvolution revealing a potential domination of one orbital over the other (see Section 5.5.1).

A differentiation between the iso-kekulene configurations is more difficult. Not only in the data analysis, but also because the ratio between up and down (and kekulene) could change from sample (position) to sample (position). Assuming that the molecules are forced into the LB site according to STM, one could consult the intensity ratio between the emission lobes from the LUMO and LUMO+1, because in the MOPDOS of iso-kekulene-down (LB) (Fig. 5.5**f**) the LUMO clearly dominates resulting in essentially two emission lobes at ($\pm$ 1.7, 0) Å^{-1}. A significant contribution of the molecule's LUMO+1 would thus indicate iso-kekulene-up to be the preferred adsorption product.

5.5 Discussion

In this section, experimental and theoretical POT data are discussed from two different perspectives: either using deconvolution or intensity profile analysis. Moreover, experimental STM images are compared to theoretical ones. The results of POT and STM are combined to evaluate the influence of the substrate's symmetry to the final reaction product of the thermally induced on-surface synthesis.

5.5.1 Deconvolution

In the present chapter, we deconvolute experimental POT data in a binding energy range of 0.5 to −0.2 eV using the theoretical LUMO and LUMO+1 k maps of free iso-kekulene presented in Fig. 5.5**a**. Note that using the k maps of free kekulene (Fig. 5.5**b**) results in the same outcome since the molecule's k maps are very similar. Additionally, because POT is an area-averaging technique and STM already shows that three different species are formed on the Cu(110) surface, it is not possible to identify individual species using the deconvolution. Instead it may be possible to evaluate a preferred reaction product and to get experimental binding energies of the two orbitals.

But, before reviewing the deconvolution result, it is important to take a closer look at the experimental data. An experimental k map recorded at $E_\mathrm{b} = 0.14$ eV is shown in Fig. 5.7**a**. It is important to note the diffuse radial emission intensity in the experimental k map, which indicates some disorder in the molecular layer. This could result from a not full monolayer coverage or that POT was measured at room temperature (note that STM was measured at 100 K). The diffuse background intensity cannot be captured in the deconvolution scheme, where only the very localized emission lobes from the theoretical k maps of LUMO and LUMO+1 are taken into consideration.

The deconvolution result $\sum_i a_i(E_\mathrm{b}) \cdot I_i(\boldsymbol{k}_\parallel)$ is presented in Fig. 5.7**b** in comparison to the experimental k map in **a** at the same E_b. The experimental MOPDOS of LUMO in red and LUMO+1 in black are shown in panel **c**.

The direct comparison of experimental and fitted k maps shows that the the deconvolution procedure exaggerates the contribution of the LUMO+1 since its four emission lobes at (± 0.98, ± 1.52) Å^{-1} are too bright in the deconvolution result (**b**). Nevertheless, the deconvolution still suggests a weaker contribution of LUMO+1 in comparison to the LUMO, which is in general in agreement with the theoretical MOPDOS of iso-kekulene (Fig. 5.5). In contrast, for kekulene/Cu(110) an equal contribution of LUMO and LUMO+1 is expected (Fig. 5.5**e**). The de-

convolution thus gives additional evidence that iso-kekulene is the major reaction product. Interestingly, the experimental MOPDOS from the deconvolution suggest that the LUMO+1 peaks at a smaller binding energy than the LUMO, which is in contrast to the theoretical predictions. That the used exchange-correlation functional does not sufficiently describe the energy alignment and/or the ratio of the MOPDOS of single orbitals is known and has already been described for bisanthene/Cu(110) in Section 3.2.3.

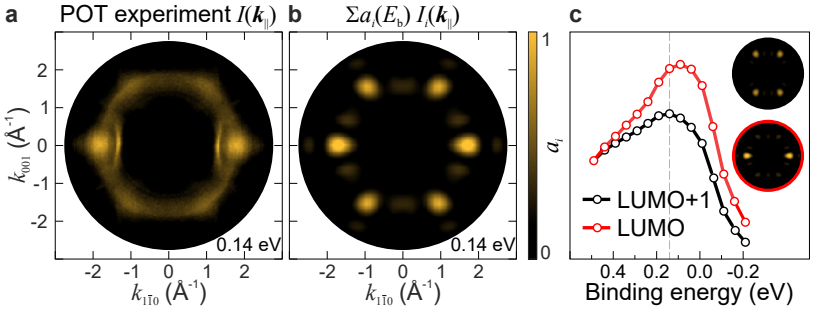

Figure 5.7: Experimental k maps and MOPDOS
a Experimental k map $I(E_b = 0.14$ eV). **b** Theoretical k map $\sum_i a_i(E_b) \cdot I_i(k_\parallel)$ from the deconvolution using the LUMO+1 (black) and LUMO (red) k maps $I_i(k_\parallel)$ of free iso-kekulene (insets of **c**). **c** Fitting parameters $a_i(E_b)$ (experimental MOPDOS) resulting from the deconvolution. Dashed gray line indicates the E_b from the k map in **b**.

5.5.2 Intensity profile analysis

The experimental k map shown in Fig. 5.3**c** is compared to the theoretical k maps simulated for different adsorption configurations of iso-kekulene and kekulene on Cu(110) (Fig. 5.6**a** – **d**) using intensity profiles in Fig. 5.8. The used k maps are replicated for convenience in Fig. 5.8**a** – **e** with their intensity profiles plotted in **f** and **g**. For the intensity analysis, a ring with an inner radius of 1.4 Å^{-1} and fixed width of 0.6 Å^{-1} is defined within the k maps as indicated partly by the white lines in Fig. 5.8**a**–**e**. The intensity along the ring is averaged radially and plotted vs. its azimuthal angle in **f** and **g**. Since the k maps are twofold symmetric, only a defined azimuthal angle range is plotted with $\varphi = 0°$ located at the major lobe at $(k_{1\bar{1}0}, k_{001}) = (1.8$ Å^{-1}, 0.0 Å$^{-1})$. The minor lobes are correspondingly found at $\varphi = \pm 60°$.

At first, we focus on the strongest peak at $\varphi = 0°$ visible in the experimental intensity profile (Fig. 5.8**f**) and in three theoretical ones (Fig. 5.8**g**), namely iso-kekulene-up (LB, white circles), kekulene (LB, blue circles), and iso-kekulene-down (LB, black circles). In the k map of iso-kekulene-down at the H site (green squares), this emission lobe is split in its k map (Fig. 5.8**c**) leading to two maxima in the profile of iso-kekulene-down at the H site (green squares). In contrast, the intensity profile extracted from the experimental k map (Fig. 5.8**f**) shows one clear peak at $\varphi = 0°$ which is neither broadened nor split into two peaks.

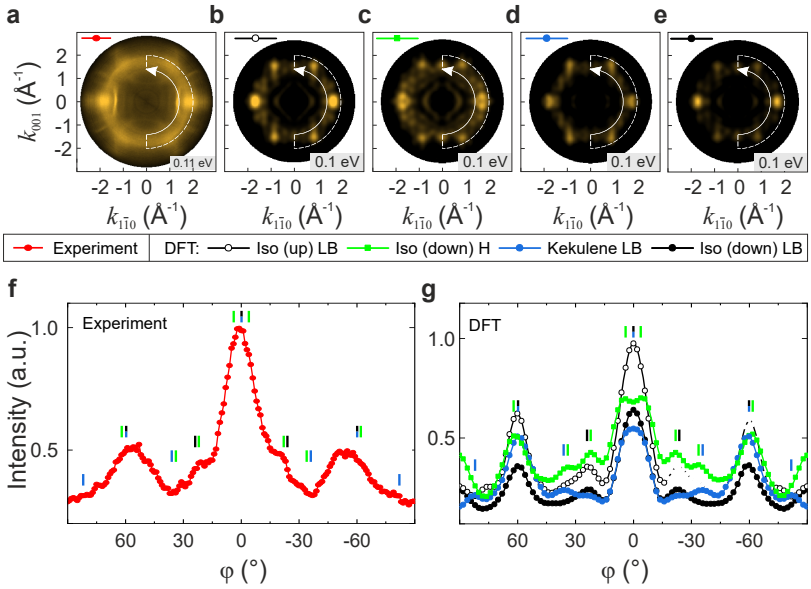

Figure 5.8: Intensity profiles in experimental and theoretical k maps
a Experimental k map. Simulated k maps including the substrate for the favored adsorption sites of **b** iso-kekulene-up at the LB site, **c** iso-kekulene-down at the H site and **d** kekulene (LB). **e** Iso-kekulene-down (LB). The white lines in the k maps display the areas used for intensity averaging. Azimuthal intensity profiles based on the experimental data extracted from the corresponding k maps from **f** experiment (red) and **g** DFT profiles of iso-kekulene-up (white circles), iso-kekulene-down (H) (green rectangles), kekulene (blue circles) and iso-kekulene-down (LB) (black circles).

Consequently, although DFT predicts the H site has energetically favored, POT analysis shows that the corresponding theoretical k map does not match the experimental one. Instead, the k maps calculated for the LB site agree better with the experimental – for iso-kekulene-down, iso-kekulene-up and kekulene on Cu(110) considering the emission from the LUMO orbital ($\varphi = 0°$) in accordance with the preferred adsorption sites of iso-kekulene-up and kekulene (both LB, see Tabs. 5.1 and 5.2).

In a next step, we look at the complete angular range in Fig. 5.8**g**. The blue curve representing the intensity profile of the k map of kekulene has three strong peaks of similar intensity: one at $\varphi = 0°$ and two symmetric at $\varphi = \pm 60°$. In the experiment, the intensity of the major peak at $\varphi = 0°$ is ,however, considerably larger compared to that of the peaks at $\varphi = \pm 60°$ (Fig. 5.8**f**). Moreover, the theoretical profile of kekulene (blue circles) does not show shoulders close the major peak at $\varphi = \pm 23°$, which is visible in the experimental profile (**f**). Consequently, we rule out kekulene as a major reaction product in agreement with STM measurements, DFT, and the deconvolution result.

The remaining profiles to be discussed are those of iso-kekulene-up and -down, both in the LB site, plotted in white and black circles in Fig. 5.8**g**. In both profiles, the major peak has only one maximum and is considerably larger than the peaks of the minor lobes at $\varphi = \pm 60°$. Moreover, shoulders at $\varphi = \pm 23°$ are present in both cases. Qualitatively these profiles thus agree with the experimental profile, which corroborates that iso-kekulene-down is not adsorbed in the H site as predicted initially by DFT. Evaluating whether the theoretical k map of iso-kekulene-up or -down agrees better with the experiment would not be conclusive, because the ratio of the two molecules (and kekulene) could change from sample to sample and the position on the sample.

5.5.3 DFT-simulated STM-contrast

Based on the geometry relaxations in Section 5.4.1 and the results from POT experiments, STM contrast is simulated for the three reaction products at the LB site of the Cu(110) surface. For convenience, the experimental STM image at monolayer coverage is replicated in Fig. 5.9**a**.

The simulated STM contrast of the two iso-kekulene species and kekulene on Cu(110) is presented in Fig. 5.9**b**, **c**, respectively. It is obvious that the contrast of iso-kekulene-up in STM (Fig. 5.9**a**: experimentally, white dashed frame and **b** top: theoretically) is dominated by one bright protrusion, which can therefore easily be identified. The difference between iso-kekulene-down (Fig. 5.9**b**, bottom) and kekulene (**c**) on Cu(110) is more subtle, because the contrast of both

species is predicted to be relatively homogeneous. However, the hexagonal shape of the kekulene molecule contrasts with a rather pentagonal shape for iso-kekulene-down visible in the DFT predictions and also in the experimental STM images. The three configurations on Cu(110) are consequently unambiguously identifiable in STM measurements.

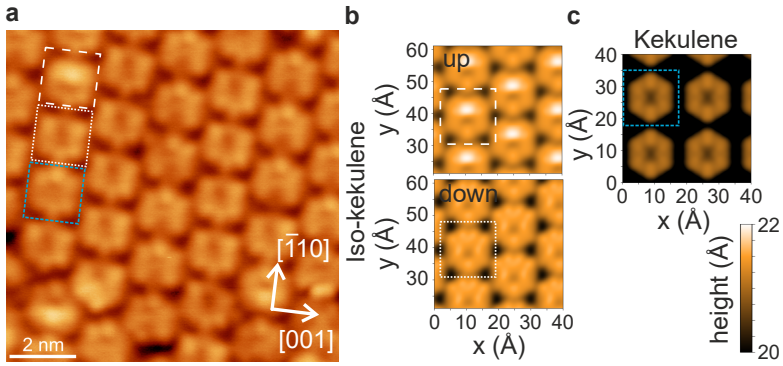

Figure 5.9: Experimental and theoretical STM
a Experimental STM micrograph of kekulene and conformers of iso-kekulene on Cu(110) (U = −1.0 V, I = 0.21 nA). **b** Simulated STM images (U = −1.0 V) for iso-kekulene-up, iso-kekulene-down, and **c** kekulene at the LB sites of Cu(110) in correspondence to the white (dashed and dotted) and blue frames in the experimental STM image, respectively. Experimental STM image by Q. Fan. Calculations by P. Puschnig.

5.5.4 Relation between substrate symmetry and reaction products

In the introduction of this chapter, we focused on the influence of the substrate's surface orientations on the reaction product of an on-surface synthesis. In combination with the previous chapter 4, we are able to identify the reaction products of the thermal reaction of the precursor molecule on Cu(111) and Cu(110).

In the previous chapter 4, we find that the thermal reaction of the precursor on the three-fold symmetric Cu(111) surface results in primarily kekulene molecules that are also three-fold symmetric, if the small alternating out-of-plane bending of the inner hydrogen atoms is taken into account (otherwise D_{6h} symmetry group). In this chapter, the combined analysis of experimental POT and STM data as well

as DFT calculations reveal that changing the underlying substrate to the two-fold symmetric Cu(110) alters the final reaction products.

At monolayer coverage, the three methods state that the leading reaction product is iso-kekulene, while kekulene is formed as a side product. According to STM statistics by Q. Fan, the ratio of these reaction products is 92% : 8% based on an image size of 30×30 nm^2 (showing in total 266 molecules). Although this method only samples a small area of the Cu crystal, POT confirms this outcome with photoemission from a surface area of 2 mm $\times$ 0.5 mm [2]. The two-fold symmetric iso-kekulene is thus identified as the main product on the two-fold Cu(110) surface.

We speculate that the reason for the preference of iso-kekulene on the surface has its origins early in the on-surface synthesis protocol, namely in the stability of the as-deposited precursor on Cu(110). Two aspects may play a role here, which are discussed one after another. First, the rotation of the phenanthrene units and their bulkiness. Second, the overall size of the precursor conformers C1 and C2.

As depicted in Fig. 5.2**b**, the precursor adsorbs with two phenanthrene units flat on the surface. The third unit rotates around the two adjacent single bonds either away or towards the molecule's center resulting in conformers C1 and C2. In the case of C2, the armchair edge of the phenanthrene unit forms the outer edge of the molecule, while in C1 all phenanthrene units have their zigzag-edges at the periphery of the molecule. Note that the zigzag-edge of the phenanthrene unit requires more space than the armchair edge. Due to the attached hydrogen atoms, particularly those in the molecule's center, the part of the phenanthrene unit facing the center is rotated away from the underlying substrate to gain space. In the case of C2, the zigzag-edge is thus pointing towards the vacuum side and the armchair edge towards the substrate. This is reversed for C1, which means that the more bulky part of the phenanthrene unit points towards the underlying substrate. As a consequence, the two flat-lying phenanthrene units are presumably pushed further away from the metal in the case of conformer C1, which decreases the interaction strength between molecule and metal.

In addition to the bulkiness of the two conformers, their actual sizes may play a decisive role in the further reaction pathway and the final reaction product. Accordingly, conformer C2, which is of rather pentagonal shape, requires less space on the surface compared to the hexagonal C1. At monolayer coverage, more C2 molecules can therefore be present on the surface which reduces the total energy of the system. Since C2 transforms into iso-kekulene after dehydrogenation, iso-kekulene is the main product on the surface. This argument is, however, independent of the underlying Cu orientation.

[2] Personal communication with H. Kirschner, 20.09.2022.

After all, most of these aspects do not include any properties of the underlying substrate. We therefore turn to the actual reaction product, iso-kekulene (and kekulene) on Cu(110) and their interplay with the Cu surface. DFT, POT, and STM reveal that iso-kekulene molecules align with their armchair-edge parallel to the $[1\bar{1}0]$ direction, which means perpendicular to the Cu rows of Cu(110).

According to DFT, the preferred adsorption site is the LB site for kekulene and iso-kekulene-up and the H site for iso-kekulene-down. In both adsorption sites, the carbon atoms C_1 and C_2 of the inwards rotated phenanthrene unit are then predicted to be between two Cu rows (see Fig. 5.4**a**, **d**). In the down conformation of iso-kekulene, the two carbon atoms can thus come closer to the surface and "attach" to the Cu(110), which increases the interaction strength, i.e., the hybridization of the metal and molecular states and facilitates charge transfer from the surface to the molecule. In fact, this interpretation only applies to iso-kekulene-down, which turns out to be the preferred reaction product according to STM (see page 127).

Coming back to the actual adsorption sites, DFT predicts iso-kekulene-up and kekulene at the LB site, while the total energy E_{tot} of iso-kekulene-down is significantly smaller (0.52 eV, see Tab. 5.2) at the H site compared to the LB site. The difference in E_{tot} is presumably due to a larger occupation of former unoccupied orbitals upon adsorption at the H site (compare MOPDOS of iso-kekulene-down replicated in Fig. 5.10**b**, **d**). However, taking a closer look at the simulated adsorption configurations in the top view (replicated in Fig. 5.10**a**, **c**) shows that the lateral distance between the carbon atoms C_1 and C_2 and the top substrate layer is smaller, if iso-kekulene-down is adsorbed at the H site (panel **c**) in contrast to the LB site in **a** (considering the Cu atoms in the red–yellow color code, not the dark red atoms which refer to the Cu layer beneath). Accordingly, the C atoms C_1 and C_2 of iso-kekulene-down encounter more space at the LB site. Note that the theoretical results based on the LB site agree with experimental STM and POT data.

5.6 Conclusion

In this chapter, the thermally-induced reaction of specially designed precursor molecules on Cu(110) is investigated using experimental STM measurements, DFT calculations, and the combined theoretical and experimental technique POT.

In contrast to a nearly exclusive formation of kekulene on Cu(111), we find that three different species are formed on the Cu(110) surface. Therein, the ratio of the three species occurs to be coverage dependent. At sub-monolayer coverage,

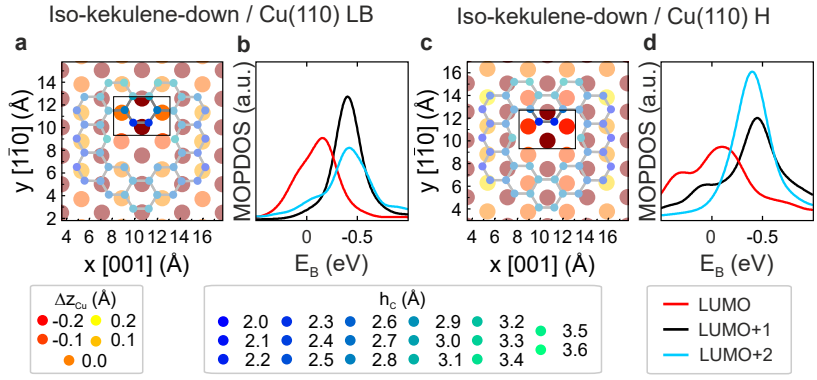

Figure 5.10: Iso-kekulene-down H vs. LB on Cu(110)
Top views and MOPDOS of the relaxed adsorption geometries of Iso-kekulene-down at the **a, b** long bridge (LB) site and **c, d** hollow (H) site. For the top view sketches, the color codes of the displayed atoms indicate their heights. The red color represents the Cu substrate with dark red indicating the second Cu atom layer. The blue color shows the adsorbed molecular species. In the MOPDOS, the colors refer to the former unoccupied molecular orbitals LUMO (red), LUMO+1 (black), and LUMO+2 (blue). DFT calculations by P. Puschnig.

the proportion of three-fold kekulene molecules is doubled in comparison to monolayer coverage, where only 8% of the surface are occupied by kekulene molecules. The formation of two-fold symmetric iso-kekulene is thus preferred on the Cu(110) surface. From STM measurements, we observe that the molecules arrange in a close-packed manner oriented in the same direction. According to theory, however, the obtained unit cell dimensions from LEED experiments only match the size of the iso-kekulene molecules, while for the calculation of kekulene/Cu(110) a larger unit cell is required. In combination with the observations from STM, this suggests that the as-deposited precursor molecules (in both configurations C1 and C2) already arrange in a closed-packed manner at ML coverage. Upon annealing, six hydrogen atoms are relieved. Dependent on the initial adsorption configuration of the precursor molecule, either kekulene or iso-kekulene is formed. Since the adsorption of the precursor configuration C2 (resulting in iso-kekulene upon thermal treatment) is favored due to its overall smaller size, the arrangement of these molecules proclaim the final unit cell dimension in which the kekulene molecules are forced.

In this chapter, we have demonstrated that it is possible to differentiate planar molecules from their nonplanar isomers with POT although this technique was

originally thought to be limited to planar organic molecules. Nevertheless, it was shown that POT can be successfully used to determine the adsorption geometry of nonplanar molecules [211] as well as identifying nonplanar adsorption geometries of planar molecules [AH10, 212]. In the present case, however, we are specifically able to distinguish, which of the species is dominantly formed on the metal surface.

6 | Incidence-Angle-Dependent POT to Approach Spherical Wave Approximation

This chapter discusses a specific geometry used in POT experiments, in which the polarization vector of the incident photon beam $\boldsymbol{\epsilon}$ and the wave vector of the emitted photoelectrons in the final state $\boldsymbol{k}_f$ are parallel. This case is referred to as $\boldsymbol{A} \parallel \boldsymbol{k}$ condition in the literature, or equivalently $\boldsymbol{\epsilon} \parallel \boldsymbol{k}_f$ condition. In this case, the PW final state approximation is mathematically equivalent to the more correct independent atomic center approximations [41, 42]. Following a suggestion by Bradshaw and Woodruff (2015 *New J. Phys.* **17** 013033), we produce k maps in which the $\boldsymbol{\epsilon} \parallel \boldsymbol{k}_f$ condition is fulfilled in each k position, exemplary for three systems, namely benzene (C_6H_6)/Pd(110), bisanthene ($C_{28}H_{14}$)/Cu(110), and graphene/SiC(0001), in order to investigate the accuracy of the plane-wave approximation.

A dedicated journal article is currently in preparation.

The careful planning, acquisition, and analysis of the experimental POT data have been my part in this project. POT experiments were conducted together with colleagues from Karl-Franzens-Universität in Graz, Forschungszentrum Jülich, and Physikalisch Technische Bundesanstalt Berlin.

6.1 Introduction

In POT, the final state of the photoemitted electron is approximated by a simple plane wave. This approximation has been viewed very critically in the PES community [13, 84–88] and abandoned in the 1980s [7, 41, 67, 78, 80, 81, 213–217]. The POT approach was specifically questioned again in 2015 by Bradshaw and Woodruff [42]. In particular, the authors elaborate in which conditions POT is likely to fail. At the same time, the authors suggest specific experiments in order to verify the technique's limits of applicability. One of these suggestions deals with the description of the final state by a simple plane wave, because the excited photoelectron would be better described by a spherical wave [7, 80, 213–215]. Fortunately, there is one specific experimental geometry for each direction of photoemitted electrons (namely the direction of the polarization of the incoming photon beam) in which the plane wave and independent atomic center approximations give exactly the same result. Namely, if the polarization vector of the exciting electromagnetic wave $\boldsymbol{\epsilon}$ is parallel to the momentum $\boldsymbol{k}_f$ of the emitted photoelectron in the final state. Mathematically this means that $\boldsymbol{\epsilon} \cdot \boldsymbol{k}_f = 0$ or expressed differently $|\boldsymbol{\epsilon} \cdot \boldsymbol{k}_f| = |\boldsymbol{\epsilon}| \cdot |\boldsymbol{k}_f|$. This condition is referred to as $\boldsymbol{\epsilon} \parallel \boldsymbol{k}_f$ condition in this work.

Such an experiment has been suggested by Bradshaw and Woodruff [42] in order to verify the foundations of POT. Naturally, it is unfeasible to design an experiment in which at one sample geometry the $\boldsymbol{\epsilon} \parallel \boldsymbol{k}_f$ condition would be fulfilled in the complete k map. Instead, a synthetic k map has to be constructed, each k point of which represents the photoemission intensity measured under the $\boldsymbol{\epsilon} \parallel \boldsymbol{k}_f$ condition. Such a k map is further called $I_{\boldsymbol{\epsilon}\parallel\boldsymbol{k}_f}(k_x, k_y)$ map. Its construction requires the measurement of multiple k maps recorded at different incidence angles α denoted as $I_\alpha(k_x, k_y)$ maps in this chapter. The mathematical description behind and the construction of the $I_{\boldsymbol{\epsilon}\parallel\boldsymbol{k}_f}(k_x, k_y)$ map is described in detail in Section 6.3.

In this work, we carried out incidence-angle-dependent POT experiments for three different well-known systems, namely benzene/Pd(110) and bisanthene/Cu(110) exemplary for molecular systems and the 2D material epitaxial monolayer graphene (EMLG) on SiC(0001). Using well-studied systems in this analysis is advantageous, because their preparation is established and their electronic structure can be checked using data from the literature. Therefore, it is possible to concentrate on the resulting $I_{\boldsymbol{\epsilon}\parallel\boldsymbol{k}_f}(k_x, k_y)$ maps. Basic information about the electronic structure of the investigated samples is given in the following. All POT measurements shown in this chapter were recorded with the toroidal electron analyzer (TEA) (see Section 2.4.4).

6.2 Investigated systems

6.2.1 Benzene/Pd(110)

Benzene has been studied extensively for over 150 years. Adsorbed on various metallic surfaces, the molecule's electronic structure, orientation, adsorption heights, and adsorption sites were investigated experimentally [218–225], and theoretically [226–233]. Benzene is particularly interesting as a model system for small hydrocarbons, e.g., for their adsorption and electronic properties on metal surfaces. The poor quasi-periodicity of benzene's orbital distribution becomes apparent looking at its frontier orbitals having only one nodal plane perpendicular to the molecular plane. Therefore, the emission from its orbitals leads to a greater spread in k space and broader emission features which are difficult to pinpoint. In a collaboration of scientists from Graz, Berlin, and Jülich, ARUPS experiments of benzene/Pd(110) were presented in 2019 [34]. We reproduce their molecular layer in this work using the same sample preparation protocol and the same experimental setup. Consulting their k maps, we prove a successful preparation of benzene/Pd(110). In particular, the Pd(110) crystal was cleaned in multiple sputtering and annealing cycles before it was exposed to a background dose of benzene at a base pressure of $5 \cdot 10^{-8}$ mbar for 5 min at RT. For details about the molecular arrangement on the surface and its electronic structure, see Egger et al. [34].

Band maps

To verify a successful preparation of the molecular layer, we record band maps in the two high-symmetry directions $[1\bar{1}0]$ and [001] of Pd shown in Fig. 6.1**a**, **b**, respectively. The energies are defined as $E - E_{\mathrm{vac}} = h\nu - E_{\mathrm{kin}}$ referenced against the vacuum level as energy zero ($E_{\mathrm{vac}} = 0$), as also in Ref. [34]. The band maps are dominated by the emission from the metal d states between E_{F} at $E - E_{\mathrm{vac}} = 4.0$ eV and approximately 8 eV in agreement with the results by Egger et al. [34]. A comparison to the clean substrate (see EDC of clean Pd in the $[1\bar{1}0]$ direction in Fig. 6.1**c**, black curve) reveals that any photoemission intensity observed at energies larger than 8 eV does not originate from the substrate, but has to stem from the molecular layer. The prominent emissions at approximately 9 eV are therefore assigned to the molecular states of lowest energy.

According to DFT, these states are predicted to be the degenerate π_1 and π_2 orbitals belonging to the irreducible representation $e_{1\mathrm{g}}$ of free benzene simulated in the $D_{6\mathrm{h}}$ symmetry. Both real-space orbitals only have one nodal plane which results in a similar pattern of two emission lobes in each of their k maps (Fig. 6.1**f**). The only difference between their k maps is their orientation in k space.

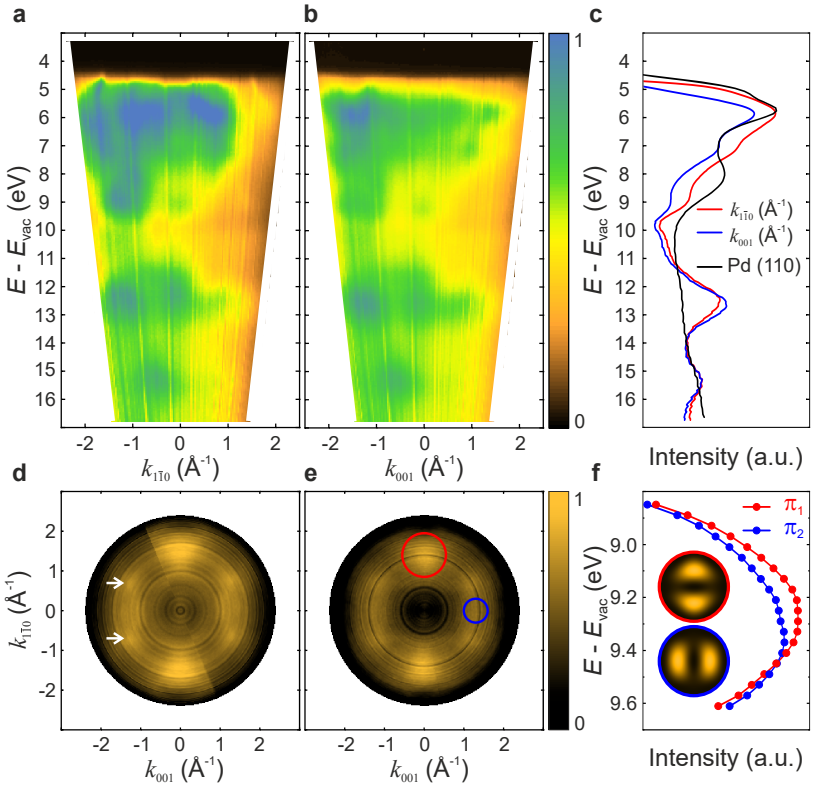

Figure 6.1: Band maps and k maps of benzene/Pd(110)
Band maps recorded along the substrate's high symmetry directions **a** [1$\bar{1}$0] and **b** [001] (both recorded with $h\nu = 25$ eV). **c** Averaged photoemission intensity for benzene/Pd(110) in a $k_{\parallel}$ range of $\pm$ 2Å^{-1} resulting the energy distributions curves (EDC) along [1$\bar{1}$0] and [001] in red and blue, respectively. EDC of clean Pd(110) recorded at $h\nu = 25$ eV in [1$\bar{1}$0] direction averaged in same $k_{\parallel}$ range in black. **d** Reference k map reproduced from the original data of Ref. [34] and **e** own k map of benzene/Pd(110), both recorded at $E - E_{\mathrm{vac}} = 9.25$ eV, $h\nu = 31$ eV, $\alpha = 40°$, and integrated in energy windows of 0.2 and 0.18 eV, respectively. Colored rings in **e** mark regions of interest (ROI) representing the orbitals π_1 and π_2 in red and blue, respectively. Additional emission features are marked with white arrows. **f** Averaged photoemission intensity of ROI plotted as a function of $E - E_{\mathrm{vac}}$. k maps of π_1 and π_2 of free benzene in red and blue, respectively.

Accordingly, the two emission lobes of π_1 are along the $[1\bar{1}0]$ direction of the substrate if adsorbed on Pd(110), where no emission from π_2 is found. In contrast, the emission from π_2 can be discerned in the [001] direction, where no emission from π_1 is expected. Egger et al. [34] observed an energetic splitting of 0.3 eV between these two states experimentally in agreement with a theoretical value of 0.2 eV for the molecule/substrate system, but in contrast to the degeneracy theoretically predicted for free benzene.

To inspect the degeneracy lifting reported by Egger et al. [34] in our experimental data, the photoemission intensities of the two band maps in Fig. 6.1**a**, **b** are integrated in $k_\parallel$ ranges of $\pm$ 2 Å^{-1} around the Γ point ($k_\parallel$ = 0 Å^{-1}). The resulting EDCs from the $[1\bar{1}0]$ and [001] directions are displayed as red and blue lines in Fig. 6.1**c**, respectively. The shoulders visible at $E - E_{\mathrm{vac}} \approx 9$ eV represent the emission from the two π orbitals. To evaluate their exact energetic positions, we subtract a non-linear baseline and fit the residual curves with Gaussian functions (not shown). As a result, the energies $E - E_{\mathrm{vac}}$ are evaluated as 9.24 eV and 9.35 eV for π_1 and π_2, respectively. The degeneracy lifting of the two π orbitals is thus confirmed, however, with a reduced energetic splitting of 0.11 eV in contrast to 0.3 eV (experiment) and 0.2 eV (theory) reported in literature [34].

k maps

An additional indication for a successful preparation of benzene/Pd(110) in accordance with the experiment in Ref. [34] is given by k maps. Fig. 6.1**d**, **e** displays k maps measured at the same $E - E_{\mathrm{vac}}$ = 9.25 eV recorded at $h\nu$ =31 eV, one reproduced from the original data of Ref. [34] (**d**) and another produced in this work (**e**). The emission from the π_1 orbital is visible as two large, dominating lobes along the $[1\bar{1}0]$ direction of the substrate. In the k map reproduced from Ref. [34] in Fig. 6.1**d**, these features appear broader compared to those in Fig. 6.1**e**, however, this impression may be influenced by the more intense background in the former one. The weak features along the [001] direction originate from the π_2 orbital. Their weak intensities again suggest that the two orbitals are not degenerate, i.e., the maxima of the corresponding intensities are shifted in energy.

The energetic splitting of the two orbitals is tested again using the k map displayed in Fig. 6.1**e**. In this measurement, k maps are recorded in an energy window of $E - E_{\mathrm{vac}}$ = 8.85 eV to 9.65 eV. Integrating the intensity over a particular k region and plotting it against $E - E_{\mathrm{vac}}$ produces EDCs comparable to the MOPDOS obtained from the theoretical calculation. To this end, we choose two circular regions of interest (ROIs) capturing the photoemission intensities of either the π_1 or π_2 orbital in the k maps as illustrated by the red and blue circles in Fig. 6.1**e**, respectively.

The experimentally obtained MOPDOS are displayed in Fig. 6.1**f** as red and blue curves for π_1 and π_2, respectively. The two orbitals peak at very similar $E - E_{\mathrm{vac}}$ with an energetic shift of 0.08 eV. This is similar to the evaluated shift from the EDCs (0.11 eV, panel **c**) but still contrary to the previously stated energy difference of 0.3 eV in Ref. [34].

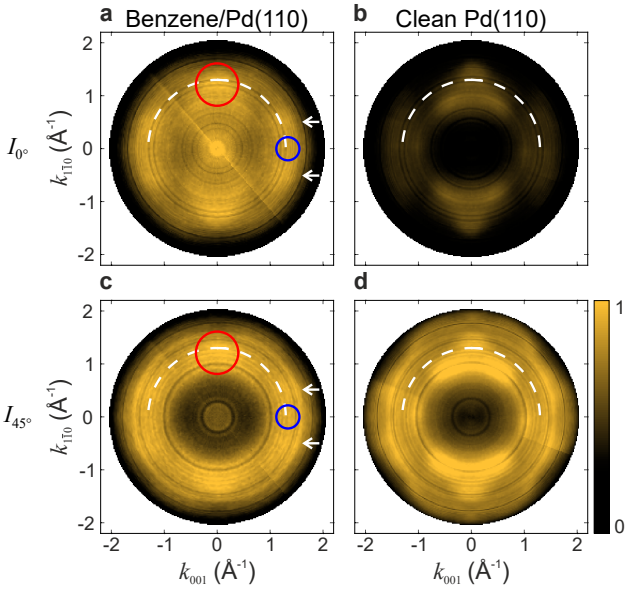

Figure 6.2: k maps of benzene/Pd(110) and clean Pd(110)
k maps recorded at $E - E_{\mathrm{vac}} = 9.25$ eV with $h\nu = 25$ eV for benzene/Pd(110) and clean Pd(110) in sample geometries of **a**, **b** $\alpha = 0°$ and **c**, **d** $\alpha = 45°$. k maps of benzene are plotted with individual color scales, while the maps of clean Pd(110) have the same intensity scaling. Red and blue circles denote emission features originating from the π_1 or π_2 orbitals, respectively. The white arrows mark the dispersion of the π_2 orbital. The white, dashed lines indicate where there is emission intensity for benzene/Pd(110) in **a**, **c**, yet no intensity for clean Pd(110) in **b**, **d** along a circle with radius 1.3 Å^{-1}.

Apart from the emission features of the π_1 and π_2 orbitals in the k maps shown in Fig. 6.1**d**, **e**, two additional intensities can be discerned along the [001] direction at $k_{001} \approx 1.4$ Å^{-1}. These intensities do not resemble the characteristic patterns of either π_1 or π_2, which both constitute of only two large emission lobes each (insets in Fig. 6.1**f**). No other orbital is predicted at this energy. Egger et al. [34] ascribe these additional intensities to the π_2 orbital which strongly interacts with two adjacent Pd atoms of the close-packed Pd-rows. However, at first glance, it cannot be excluded that these features originate from the underlying substrate. Note that a comparison to the clean substrate was not presented in Ref. [34].

Figure 6.2 shows k maps of benzene/Pd(110) and clean Pd(110) recorded in two different experimental geometries, namely incidence angles of $\alpha = 0°$ and $\alpha = 45°$, at $h\nu = 25$ eV and the same $E - E_{\text{vac}} = 9.25$ eV as in Fig. 6.1. The k maps of clean Pd are plotted according to the same color scale to show that the substrate-related emission intensity highly increases in grazing incidence geometry. The red and blue circles in panels **a** and **b** indicate the emission lobes of the molecular π_1 and π_2 orbitals located at a radius of $k_{\parallel} \approx 1.3$ Å^{-1}. This radius is indicated by the dashed, white lines. In the k maps of clean Pd(110) (panels **b**, **d**), there is a clear attenuation in intensity along this $k_{\parallel}$ radius. Since the additional intensities (marked with white arrows in Fig. 6.2**a**, **c**) likewise appear at this radius, we can clearly assign them to molecular features and exclude that these intensities originate from the substrate. Instead, it appears reasonable to assign the origin of these additional intensities to the dispersion of the π_2 orbital as a consequence of its strong interaction with the substrate as suggested by Egger et al. [34].

6.2.2 Bisanthene/Cu(110)

The successful on-surface synthesis of bisanthene from DBBA was demonstrated by Simonov et al. [148]. Frontier π orbitals of bisanthene on Cu(110) were studied by Yang et al. using the POT technique in 2019 [35], while the molecule's molecular orbitals below the Cu d band are subject of this work's chapter 3 published in 2022 [AH9]. Bisanthene/Cu(110) is thus well-studied using POT and it is reasonable to choose it in this chapter discussing the $\boldsymbol{\epsilon} \parallel \boldsymbol{k}_f$ condition as well. Additionally, the system is particularly suitable, because it's preparation is well-known and the k maps of LUMO and HOMO show characteristic and clear features (Fig. 3.4). In contrast to the k maps presented for benzene/Pd(110) in Figs. 6.1, 6.2, the interaction of bisanthene with Cu(110) is rather small. As a consequence, the k maps of the molecule's frontier orbitals do not differ substantially from those calculated for the free molecule. A comparison between experimental k maps and calculated ones based on the PW final state approximation therefore seems straightforward, which is an advantage in this chapter.

6.2.3 Epitaxial monolayer graphene

Graphene is the most classic example of 2D materials studied extensively from varying points of view. A controlled formation of high quality epitaxial graphene is achieved on the Si-terminated 6H-SiC surface. The initial carbon layer prepared by thermal decomposition of the SiC(0001) surface is, however, still covalently bonded to the Si atoms of the SiC crystal. This so-called zero-layer graphene (ZLG) is composed of sp^2 and sp^3 hybridized C atoms and therefore does not show the typical linear dispersion of the π and π^* bands at the $\overline{\mathrm{K}}$ point of the hexagonal Brillouin zone (BZ) of graphene.

Upon further annealing, another carbon layer disengages from the SiC bulk. As a consequence, the initial ZLG is lifted up and turns into a physically decoupled graphene layer usually referred to as EMLG. A sketch of this construction of layers is depicted in Fig. 6.3**a** with EMLG and ZLG marked with "G" and "Z", respectively, and the first two SiC layers indicated by "1" and "2". Because of no direct chemical interaction with the underlying ZLG, the electronic structure of EMLG develops Dirac cones. This originates from the crossing of the π and π^* bands at the $\overline{\mathrm{K}}$ point which marks E_F in neutral graphene. This point in the band structure is called the Dirac point. Note that due to the vicinity of ZLG and SiC bulk, EMLG is doped resulting in partial occupation of the bands above the Dirac point. In ARPES, this is seen as a shift of the band crossing point below E_F.

Band maps of EMLG measured along the $\overline{\Gamma}$–$\overline{\mathrm{K}}$ and $\overline{\Gamma}$–$\overline{\mathrm{M}}$ directions are shown in Fig. 6.3**b** on the right and left sides, respectively. These band maps are recorded at $h\nu = 87$ eV to enlarge the visible k space beyond the 1$^{\mathrm{st}}$ BZ. The energy axis in Fig. 6.3**b** is given both, as $E - E_\mathrm{vac}$ relative to the vacuum level and as binding energy E_b relative to E_F. The two directions in the BZ are illustrated in the bottom left of Fig. 6.3**b** with red and blue arrows. In the band maps, many bands of π and σ character are visible. For the construction of $I_{\boldsymbol{\epsilon}\|\boldsymbol{k}_f}(k_x, k_y)$ maps, we choose two different energies of approximately $E - E_\mathrm{vac} = 7.81$ eV and 8.88 eV indicated by the dashed and dotted, white lines in Fig. 6.3**b**.

The k maps recorded at these energies referred to as map A and map B correspondingly both contain features of π bands. The one at higher binding energy (map B) additionally includes emission intensity of bands with σ character. Representative k maps for map A and map B, both recorded at $h\nu = 87$ eV, are shown in Fig. 6.3**c** in the top and bottom, respectively. In both maps, the majority of intensity originates from π bands. The only emission intensity of the σ band in map B is marked by a white circle. For the construction of $I_{\boldsymbol{\epsilon}\|\boldsymbol{k}_f}(k_x, k_y)$ maps in this chapter, incidence-angle-dependent data sets are recorded at $h\nu = 23$ eV, 40 eV, 60 eV, and 85 eV for map A and $h\nu = 60$ eV, and 85 eV for map B.

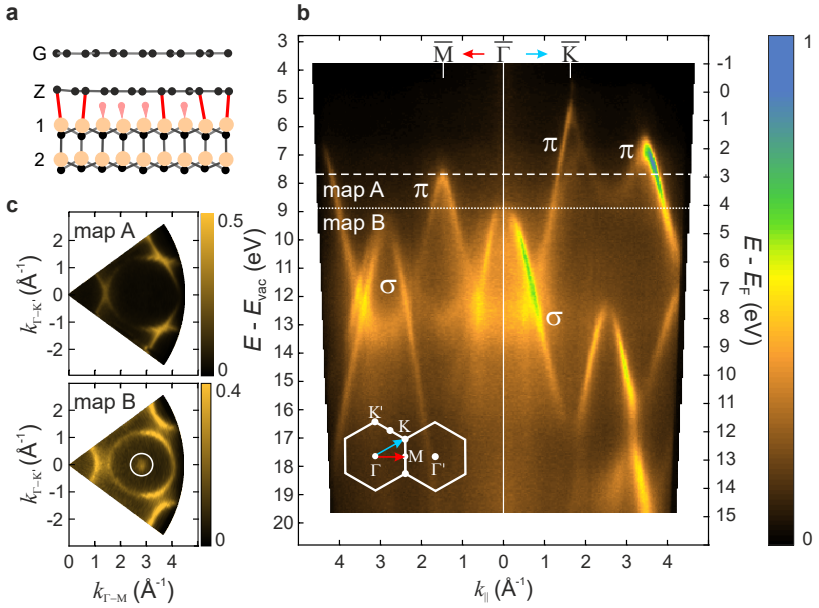

Figure 6.3: Band map and k maps of EMLG
a Side view model of epitaxial monolayer graphene (EMLG). Covalent bonds within the graphene sheets and the SiC bulk are indicated in gray. "G" denotes the EMLG layer and "Z" zero-layer graphene (ZLG). The numbers mark the first and second Si-C bilayers of 6H-SiC(0001). Adapted from Ref. [234]. **b** Band maps of EMLG recorded at $h\nu = 87$ eV in two directions $\overline{\Gamma}$–$\overline{K}$ and $\overline{\Gamma}$–$\overline{M}$ on the right and left side of the figure. Directions are indicated in the sketch of the Brillouin zone (BZ) in the bottom left in blue and red, respectively. The energy axis in (eV) is given as $E - E_{vac}$ (left) and binding energy $E_b = E_{kin} - E_F$ (right). The white dashed and dotted lines mark the used energies for the k maps referred to as map A and map B, respectively. **c** k maps of map A and map B recorded at $E - E_{vac}$ of approximately 7.81 eV and 8.88 eV, respectively, $h\nu = 87$ eV, and $\alpha = 3°$. The white circle in map B encircles emission intensity of a σ band. The remaining intensity stems from π bands.

6.3 Data analysis procedure

To construct synthetic $I_{\boldsymbol{\epsilon}\parallel\boldsymbol{k}_f}(k_x, k_y)$ maps automatically from individual $I_\alpha(k_x, k_y)$ maps measured at different incidence angles, a dedicated python script was written. For the $I_\alpha(k_x, k_y)$ maps, the script calculates the positions in k space for which the $\boldsymbol{\epsilon} \parallel \boldsymbol{k}_f$ condition is fulfilled and extracts the photoemission intensity at these positions. Note that the experimental $I_\alpha(k_x, k_y)$ maps in this work are measured by the TEA, where for each incidence angle the sample is rotated azimuthally along its normal to create a $I_\alpha(k_x, k_y)$ map. Therefore, the region of the $I_\alpha(k_x, k_y)$ map where the $\boldsymbol{\epsilon} \parallel \boldsymbol{k}_f$ condition is fulfilled, corresponds to a ring with a constant radius $k_{\boldsymbol{\epsilon}\parallel\boldsymbol{k}_f}(\alpha)$ depending on the chosen α and E_{kin}. Merging these rings from different $I_\alpha(k_x, k_y)$ maps at one photon energy results in the final complete $I_{\boldsymbol{\epsilon}\parallel\boldsymbol{k}_f}(k_x, k_y)$ map. This procedure is explained in detail in the following, using an example of the HOMO of bisanthene/Cu(110).

To fulfill the $\boldsymbol{\epsilon} \parallel \boldsymbol{k}_f$ condition, the polarization vector $\boldsymbol{\epsilon}$ of the exciting electromagnetic wave has to be parallel to the wave vector $\boldsymbol{k}_f$ (i.e., emission direction) of the emitted photoelectron. This implies for the experimental geometry that the direction of the incoming beam should be perpendicular to the direction of the emission, while the polarization of the electric field is in the same plane. For the TEA, the former requirement is automatically fulfilled if p polarized light is used, because the analyzer accepts electrons emitted exclusively in the plane of incidence (the one containing the photon beam and the sample normal) of the photoelectrons. This geometry is exemplary shown in Fig. 6.4 for $\alpha \approx 60°$.

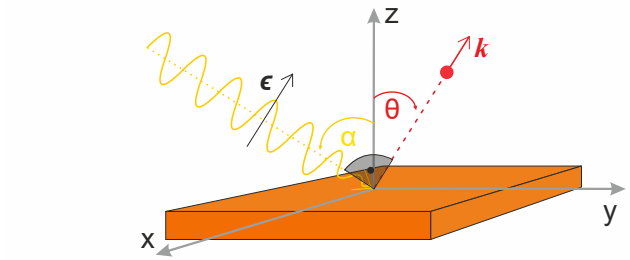

Figure 6.4: Experimental $\boldsymbol{\epsilon} \parallel \boldsymbol{k}_f$ geometry
Illustration of experimental geometry exemplary for an incoming photon beam (yellow line) with incidence angle $\alpha \approx 60°$. Electrons are emitted in all directions, but only those with momenta $\boldsymbol{k}_f$ parallel to the polarization vector of the exciting electromagnetic wave $\boldsymbol{\epsilon}$ fulfill the $\boldsymbol{\epsilon} \parallel \boldsymbol{k}_f$ condition (red line). In this case, the incidence and polar angles α and θ give a right angle.

In general, the photoelectrons are characterized by the direction of emission, i.e., the polar (θ) and azimuthal (ϕ) emission angles, and the kinetic energy E_{kin}. The distribution of photoemission as a function of these is converted into k space to create $I_\alpha(k_x, k_y)$ maps displaying the photoemission intensity at a constant energy vs. k_x and k_y.

In the $I_\alpha(k_x, k_y)$ maps, each (k_x, k_y) point corresponds to a specific $k_\parallel$ ($k_\parallel = \sqrt{k_x^2 + k_y^2}$), which can also be expressed in terms of E_{kin} and θ using

$$k_\parallel = \frac{\sqrt{2m_{\mathrm{e}}E_{\mathrm{kin}}}}{\hbar} \cdot \sin\theta. \tag{6.1}$$

The $\boldsymbol{\epsilon} \parallel \boldsymbol{k}_f$ condition implies that $\alpha + \theta = \frac{\pi}{2}$. Hence, Eq. 6.1 can be rewritten as

$$k_\parallel(\alpha) = \frac{\sqrt{2m_{\mathrm{e}}E_{\mathrm{kin}}}}{\hbar} \cdot \sin(\frac{\pi}{2} - \alpha). \tag{6.2}$$

Since α and E_{kin} do not change while measuring one $I_\alpha(k_x, k_y)$ map corresponding to the chosen incidence geometry, there is only one specific $|k_\parallel|$ per $I_\alpha(k_x, k_y)$ map to fulfill the $\boldsymbol{\epsilon} \parallel \boldsymbol{k}_f$ condition. This $k_\parallel$ corresponds accordingly to a circle in the $I_\alpha(k_x, k_y)$ map around the Γ point which is further referred to as $k_{\boldsymbol{\epsilon}\parallel\boldsymbol{k}_f}(\alpha)$ radius. In other words, the k points in each k map, for which the $\boldsymbol{\epsilon} \parallel \boldsymbol{k}_f$ condition is fulfilled, are located on a circle around the center of the k map with a radius of $k_{\boldsymbol{\epsilon}\parallel\boldsymbol{k}_f}$. For different E_{kin} and α, the circle will vary because of different $k_\parallel$ to fulfill $\boldsymbol{\epsilon} \parallel \boldsymbol{k}_f$. The chosen E_{kin} is fixed by the binding energy E_{b} or $E-E_{\mathrm{vac}}$ of the spectral feature under examination for every used photon energy $h\nu$ ($E_{\mathrm{kin}} = h\nu - E_{\mathrm{b}}$). The influence of the incidence angle α thus remains to be investigated.

Due to technical reasons in the experimental setup of the TEA, the incidence angle in our experiments is varied from zero to at most 69°. As a consequence, the constructed $I_{\boldsymbol{\epsilon}\parallel\boldsymbol{k}_f}(k_x, k_y)$ map is restricted to a certain $k_\parallel$ range. The exact range again depends on the used E_{kin}. Its inner (outer) edges correspond to the $k_\parallel$ calculated for the largest (smallest) measured α. In a real measurement series, it is crucial that the emission features of the orbital under investigation is located between the inner and outer borders. In Fig. 6.6, this is illustrated using the example of bisanthene HOMO recorded at $E_{\mathrm{b}} = 1.12$ eV.

Figure 6.5 illustrates the basic idea behind the construction of a $I_{\boldsymbol{\epsilon}\parallel\boldsymbol{k}_f}(k_x, k_y)$ map schematically from individual $I_\alpha(k_x, k_y)$ maps recorded at five different incidence angles α. From each $I_\alpha(k_x, k_y)$ map, a ring of defined radius and width marked in green will be cut out, which represents the emission intensity where the $\boldsymbol{\epsilon} \parallel \boldsymbol{k}_f$ condition is fulfilled for this individual α. These rings are further referred to as

$i_\alpha^{\boldsymbol{\epsilon}\|\boldsymbol{k}_f}(k_x, k_y)$ rings. How the radii and widths of the $i_\alpha^{\boldsymbol{\epsilon}\|\boldsymbol{k}_f}(k_x, k_y)$ rings come about is explained later in this section using the example of bisanthene HOMO. These rings colored in green in Fig. 6.5 are cut out from each $I_\alpha(k_x, k_y)$ map, and finally merged to form the $I_{\boldsymbol{\epsilon}\|\boldsymbol{k}_f}(k_x, k_y)$ map. The yellow areas indicate the remaining parts of $I_\alpha(k_x, k_y)$ maps that will not contribute to the final $I_{\boldsymbol{\epsilon}\|\boldsymbol{k}_f}(k_x, k_y)$ map.

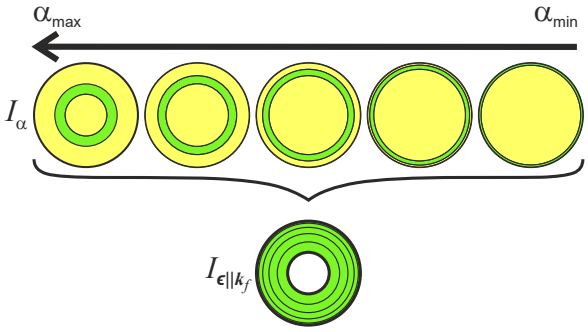

Figure 6.5: Construction of $I_{\boldsymbol{\epsilon}\|\boldsymbol{k}_f}(\boldsymbol{k_x}, \boldsymbol{k_y})$ map
Sketch describing the construction of a $I_{\boldsymbol{\epsilon}\|\boldsymbol{k}_f}(k_x, k_y)$ map from k maps recorded at different incidence angles ($I_\alpha(k_x, k_y)$ maps). Areas, where the $\boldsymbol{\epsilon} \parallel \boldsymbol{k}_f$ condition is fulfilled are marked in green, while others are colored in yellow.

Figure 6.6**a**, **b** shows a $I_\alpha(k_x, k_y)$ map of bisanthene's HOMO recorded at $\alpha = 40°$ ($I_{40°}(k_x, k_y)$). The colored circles in panel **a** denote the $k_{\boldsymbol{\epsilon}\|\boldsymbol{k}_f}(\alpha)$ radii for which the $\boldsymbol{\epsilon} \parallel \boldsymbol{k}_f$ condition is fulfilled exemplary for $\alpha = 0°$, 31°, 49°, and 61° in green, yellow, blue, and red, respectively. In our experiment, α was varied in 3° steps (starting from 1°). To construct the $I_{\boldsymbol{\epsilon}\|\boldsymbol{k}_f}(k_x, k_y)$ map, we cut out rings at these radii from each $I_\alpha(k_x, k_y)$ map as marked by dashed colored lines in Fig. 6.6**b**. The width of these $i_\alpha^{\boldsymbol{\epsilon}\|\boldsymbol{k}_f}(k_x, k_y)$ rings $\Delta k_{\boldsymbol{\epsilon}\|\boldsymbol{k}_f}(\alpha)$ depends on the adjacent $k_{\boldsymbol{\epsilon}\|\boldsymbol{k}_f}(\alpha)$ radii and can be described mathematically using $\frac{\partial k_\parallel(\alpha)}{\partial \alpha}$ and the incidence angle step $\Delta\alpha$:

$$\Delta k_{\boldsymbol{\epsilon}\|\boldsymbol{k}}(\alpha) = \frac{\partial k_\parallel(\alpha)}{\partial \alpha} \cdot \Delta\alpha = \frac{\sqrt{2 m_e E_{\text{kin}}}}{\hbar} \cdot \cos(\frac{\pi}{2} - \alpha) \cdot \Delta\alpha \tag{6.3}$$

The maximum deviations from the $\boldsymbol{\epsilon} \parallel \boldsymbol{k}_f$ condition in each $I_{\boldsymbol{\epsilon}\|\boldsymbol{k}_f}(k_x, k_y)$ map is then given by the largest $i_\alpha^{\boldsymbol{\epsilon}\|\boldsymbol{k}_f}(k_x, k_y)$ ring width $\Delta k_{\boldsymbol{\epsilon}\|\boldsymbol{k}}$ ($\alpha_{\max}$) divided by a factor of two. $\Delta k_{\boldsymbol{\epsilon}\|\boldsymbol{k}}$ ($\alpha_{\max}$)/2 and will be provided for each $I_{\boldsymbol{\epsilon}\|\boldsymbol{k}_f}(k_x, k_y)$ map.

Note that the largest ring width and thus the largest deviation between $I_\alpha(k_x, k_y)$ and $I_{\boldsymbol{\epsilon}\parallel\boldsymbol{k}_f}(k_x, k_y)$ maps occurs for the largest incidence angle, i.e., the inner border of the $I_{\boldsymbol{\epsilon}\parallel\boldsymbol{k}_f}(k_x, k_y)$ map. Conversely we observe the smallest deviation from the $\boldsymbol{\epsilon} \parallel \boldsymbol{k}_f$ condition at the outer border of the $I_{\boldsymbol{\epsilon}\parallel\boldsymbol{k}_f}(k_x, k_y)$ map.

In an alternative approach providing an equidistant slicing of the $I_\alpha(k_x, k_y)$ maps into rings of the same widths would require a non-equidistant variation of α. This would, however, make the experimental procedure less feasible and less reproducible.

Another important technical remark in the context of the $\boldsymbol{\epsilon} \parallel \boldsymbol{k}_f$ experiment is that the intensity of the photon beam used for the first $I_\alpha(k_x, k_y)$ map in the experimental measurement series is larger compared to that of the last $I_\alpha(k_x, k_y)$ map due to the decay operation mode of the storage ring, i.e., the decrease of the electron current in the storage ring and a corresponding decrease of the photon beam intensity. The entire photoemission intensity of each $I_\alpha(k_x, k_y)$ map measured at a particular incidence geometry therefore has to be normalized to the photon flux. This is performed by dividing the intensity in the $i_\alpha^{\boldsymbol{\epsilon}\parallel\boldsymbol{k}_f}(k_x, k_y)$ rings by the drain current $i_m(t)$ recorded during the measurement (see Section 2.4.6 for details).

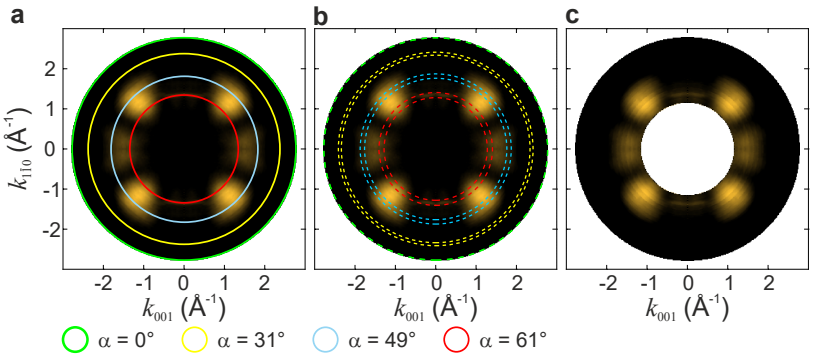

Figure 6.6: Data analysis procedure for HOMO of bisanthene/Cu(110) Exemplary data analysis procedure in three intermediate stages. First two steps show colored lines superimposed with the $I_{40°}(k_x, k_y)$ map to display **a** $k_{\boldsymbol{\epsilon}\parallel\boldsymbol{k}_f}(\alpha)$ radii for which the $\boldsymbol{\epsilon} \parallel \boldsymbol{k}_f$ condition is fulfilled for varying α and **b** $i_\alpha^{\boldsymbol{\epsilon}\parallel\boldsymbol{k}_f}(k_x, k_y)$ rings, which are cut out in the final step to construct the $I_{\boldsymbol{\epsilon}\parallel\boldsymbol{k}_f}(k_x, k_y)$ map. Colors correspond to incidence angles of 0°: green, 31°: yellow, 49°: blue, and 61°: red. **c** $I_{\boldsymbol{\epsilon}\parallel\boldsymbol{k}_f}(k_x, k_y)$ map of bisanthene HOMO.

The exemplary $I_{\boldsymbol{\epsilon}\parallel\boldsymbol{k}_f}(k_x, k_y)$ map of bisanthene HOMO constructed from individual $I_\alpha(k_x, k_y)$ maps measured at $h\nu$ =35 eV and incidence angles from 0° to 64° is shown in Fig. 6.6**c**. The $I_{\boldsymbol{\epsilon}\parallel\boldsymbol{k}_f}(k_x, k_y)$ map shows that at this photon energy, the chosen incidence angle range is sufficient to include all major molecular emission features. If a smaller photon energy was used, these limiting smallest and largest $k_{\boldsymbol{\epsilon}\parallel\boldsymbol{k}_f}(\alpha)$ radii would have moved closer to the center of the $I_{\boldsymbol{\epsilon}\parallel\boldsymbol{k}_f}(k_x, k_y)$ map. At higher photon energies, a reversed trend would occur such as the emission lobes of the orbital would be cut at small $k_{\boldsymbol{\epsilon}\parallel\boldsymbol{k}_f}(\alpha)$ radii and important information would be lost. It follows that the construction of $I_{\boldsymbol{\epsilon}\parallel\boldsymbol{k}_f}(k_x, k_y)$ maps requires careful planning, especially considering the used photon energy and incidence angle range.

In general, the $I_{\boldsymbol{\epsilon}\parallel\boldsymbol{k}_f}(k_x, k_y)$ map would be best-suited to reconstruct the real-space orbital by an inverse Fourier transform. This would lead to an experimentally-derived periodicity of a particular orbital which could be comparable to theory. For a three-dimensional reconstruction, however, multiple $I_{\boldsymbol{\epsilon}\parallel\boldsymbol{k}_f}(k_x, k_y)$ maps recorded at varying photon energies would be required in order to map the z-direction. At the same time, the used photon energy can not be chosen freely as discussed previously, because the experimentally limited incidence angle range and the photon energy define the limiting smallest and largest $k_{\boldsymbol{\epsilon}\parallel\boldsymbol{k}_f}(\alpha)$ radii where molecular emissions are expected in the photoemission maps.

Additionally it is crucial to note that in other usual experimental setups than the TEA, the incidence angle is fixed. The possibility to change the incidence angle from zero to at most 69° in the experimental setup used in this work is rather unique. The results obtained in this chapter using the TEA can thus be used to benchmark those experimental setups, where the incidence angle is fixed.

Combining the two previous paragraphs leads to the objective of this chapter. Namely, to estimate the ideal incidence angle for which a $I_\alpha(k_x, k_y)$ map agrees best with the corresponding $I_{\boldsymbol{\epsilon}\parallel\boldsymbol{k}_f}(k_x, k_y)$ map. To this end a series of analysis steps is performed schematically illustrated in Fig. 6.7. In this analysis scheme, various k maps, individual rings within those k maps or parameters are introduced, which are briefly explained in Tab. 6.1.

For the analysis of $I_{\boldsymbol{\epsilon}\parallel\boldsymbol{k}_f}(k_x, k_y)$ maps, we first subtract the intensity of single $I_\alpha(k_x, k_y)$ maps from the intensity of the $I_{\boldsymbol{\epsilon}\parallel\boldsymbol{k}_f}(k_x, k_y)$ map resulting in residual $\Delta I_\alpha(k_x, k_y)$ maps. This is shown in Fig. 6.7**a**, in which $i_\alpha^{\boldsymbol{\epsilon}\parallel\boldsymbol{k}_f}(k_x, k_y)$ rings are again indicated by green color in the I_α and $I_{\boldsymbol{\epsilon}\parallel\boldsymbol{k}_f}$ maps. The remaining areas in the $I_\alpha(k_x, k_y)$ map are again colored in yellow. The bold lines denote the inner and outer borders from the $I_{\boldsymbol{\epsilon}\parallel\boldsymbol{k}_f}(k_x, k_y)$ map, since a comparison only makes sense within these limits.

Term	Explanation
$\Delta\alpha$	Incidence angle step.
$I_\alpha\ (k_x, k_y)$	I_α map: Typical k map recorded at one incidence angle α, equivalent to k maps in the other chapters of this work.
$k_{\boldsymbol{\epsilon}\parallel\boldsymbol{k}_f}\ (\alpha)$	k radius where the $\boldsymbol{\epsilon} \parallel \boldsymbol{k}_f$ condition is fulfilled after Eq. 6.2.
$\Delta k_{\boldsymbol{\epsilon}\parallel\boldsymbol{k}_f}\ (\alpha)$	The maps are split into rings, where the width $\Delta k_{\boldsymbol{\epsilon}\parallel\boldsymbol{k}_f}$ is defined by adjacent $k_{\boldsymbol{\epsilon}\parallel\boldsymbol{k}_f}(\alpha)$ radii according to $\frac{\partial k_\parallel(\alpha)}{\partial\alpha} \cdot \Delta\alpha$ using Eq. 6.3.
$i_\alpha^{\boldsymbol{\epsilon}\parallel\boldsymbol{k}_f}\ (k_x, k_y)$	If the I_α maps are only cut into one ring, where the $\boldsymbol{\epsilon} \parallel \boldsymbol{k}_f$ condition is fulfilled, single $\boldsymbol{\epsilon} \parallel \boldsymbol{k}_f$ rings are obtained. Mathematically, this constraint is achieved by the delta function where $k = \sqrt{k_x^2 + k_y^2}$: $i_\alpha^{\boldsymbol{\epsilon}\parallel\boldsymbol{k}_f}\ (k_x, k_y) = I_\alpha\ (k_x, k_y) \cdot \delta_{\Delta\alpha}(k - k_{\boldsymbol{\epsilon}\parallel\boldsymbol{k}_f})\ (\alpha)$. These rings are called $\boldsymbol{\epsilon} \parallel \boldsymbol{k}_f$ rings in the text.
$i_\alpha(k_x, k_y)$	If the I_α map is split into rings of identical dimensions as the $i_\alpha^{\boldsymbol{\epsilon}\parallel\boldsymbol{k}_f}\ (k_x, k_y)$ rings with mean radius $k_{\boldsymbol{\epsilon}\parallel\boldsymbol{k}_f}\ (\alpha)$ and width $\Delta k_{\boldsymbol{\epsilon}\parallel\boldsymbol{k}_f}\ (\alpha)$, the single rings are denoted as $i_\alpha(k_x, k_y)$ rings.
$I_{\boldsymbol{\epsilon}\parallel\boldsymbol{k}_f}\ (k_x, k_y)$	Synthetic k map in which the $\boldsymbol{\epsilon} \parallel \boldsymbol{k}_f$ condition is fulfilled at each k point. It is composed of all $i_\alpha^{\boldsymbol{\epsilon}\parallel\boldsymbol{k}_f}\ (k_x, k_y)$ rings.
$\Delta I_\alpha\ (k_x, k_y)$	Residual map where the intensity of one I_α map is subtracted from the $I_{\boldsymbol{\epsilon}\parallel\boldsymbol{k}_f}$ map, namely $\Delta I_\alpha\ (\alpha) = I_{\boldsymbol{\epsilon}\parallel\boldsymbol{k}_f} - I_\alpha\ (\alpha)$.
$\Delta i_\alpha(k_x, k_y)$	If the ΔI_α map is split into rings of identical dimensions as the $i_\alpha^{\boldsymbol{\epsilon}\parallel\boldsymbol{k}_f}\ (k_x, k_y)$ and $i_\alpha(k_x, k_y)$ rings with mean radius $k_{\boldsymbol{\epsilon}\parallel\boldsymbol{k}_f}\ (\alpha)$ and width $\Delta k_{\boldsymbol{\epsilon}\parallel\boldsymbol{k}_f}\ (\alpha)$, the single rings are denoted as $\Delta i_\alpha(k_x, k_y)$. This is equivalent to the subtracted of single $i_\alpha^{\boldsymbol{\epsilon}\parallel\boldsymbol{k}_f}\ (k_x, k_y)$ and $i_\alpha(k_x, k_y)$ rings of the same dimensions.
$A\ (\alpha)$	k space area of rings defined by their mean radius $k_{\boldsymbol{\epsilon}\parallel\boldsymbol{k}_f}\ (\alpha)$ and width $\Delta k_{\boldsymbol{\epsilon}\parallel\boldsymbol{k}_f}\ (\alpha)$ according to $A = 2\pi \cdot k_{\boldsymbol{\epsilon}\parallel\boldsymbol{k}_f} \cdot \Delta k_{\boldsymbol{\epsilon}\parallel\boldsymbol{k}_f}$
$\omega\ (\alpha)$	Weighting factor accounts for the effective contribution of individual $i_\alpha^{\boldsymbol{\epsilon}\parallel\boldsymbol{k}_f}\ (k_x, k_y)$ rings in the $I_{\boldsymbol{\epsilon}\parallel\boldsymbol{k}_f}\ (k_x, k_y)$ maps following Eq. 6.5.
$\Delta i_\alpha^n\ (k_x, k_y)$	Normalized $\Delta i_\alpha(k_x, k_y)$ rings using A and ω (Eq. 6.6).
α_{best}	Incidence angle corresponding to the smallest integrated intensity of $\Delta I_\alpha\ (k_x, k_y)$ maps denoting the best agreement between $I_\alpha\ (k_x, k_y)$ and $I_{\boldsymbol{\epsilon}\parallel\boldsymbol{k}_f}\ (k_x, k_y)$ maps.

Table 6.1: Definitions for data analysis
Explanation of terms used in the analysis of POT data fulfilling the $\boldsymbol{\epsilon} \parallel \boldsymbol{k}_f$ condition.

In the residual $\Delta I_\alpha(k_x, k_y)$ maps in Fig. 6.7**b**, there will be rings of zero and non-zero intensity marked by white or blue color, respectively. Note that a non-zero intensity in the $\Delta I_\alpha(k_x, k_y)$ maps reveals a deviation between $I_\alpha(k_x, k_y)$ and $I_{\boldsymbol{\epsilon}\parallel\boldsymbol{k}_f}(k_x, k_y)$ maps.

The $\Delta I_\alpha(k_x, k_y)$ maps calculated like this exemplary from five different $I_\alpha(k_x, k_y)$ maps are shown in Fig. 6.7**b**. Dependent on the used α, the radius of the ring with zero intensity (white) corresponding to the $\boldsymbol{\epsilon} \parallel \boldsymbol{k}_f$ condition varies. In the next step, the intensity within each complete $\Delta I_\alpha(k_x, k_y)$ map is integrated and plotted against the incidence angle α. An example for the three $\Delta I_\alpha(k_x, k_y)$ maps marked by purple, black, and red frames in Fig. 6.7**b** is shown in panel **d**. Logically, the smallest integrated intensity of the $\Delta I_\alpha(k_x, k_y)$ maps denotes a good resemblance between $I_\alpha(k_x, k_y)$ and $I_{\boldsymbol{\epsilon}\parallel\boldsymbol{k}_f}(k_x, k_y)$ maps. The corresponding α is referred to as α_{best}.

A more detailed analysis of the single $\Delta I_\alpha(k_x, k_y)$ maps is performed for individual rings in the map in the next step presented in Fig. 6.7**c**, **e**. It allows to distinguish to which degree the single rings in the $I_\alpha(k_x, k_y)$ maps contribute to the agreement between $I_\alpha(k_x, k_y)$ and $I_{\boldsymbol{\epsilon}\parallel\boldsymbol{k}_f}(k_x, k_y)$ maps. For this, each $\Delta I_\alpha(k_x, k_y)$ map is decomposed into single $\Delta i_\alpha(k_x, k_y)$ rings. The radii and widths of these rings is chosen to be the same as those of the $i_\alpha^{\boldsymbol{\epsilon}\parallel\boldsymbol{k}_f}(k_x, k_y)$ rings to be directly comparable to the $I_{\boldsymbol{\epsilon}\parallel\boldsymbol{k}_f}(k_x, k_y)$ map.

$$\Delta I_\alpha(k_x, k_y) = \sum_\alpha \Delta i_\alpha(k_x, k_y) \tag{6.4}$$

The intensity of single $\Delta i_\alpha(k_x, k_y)$ rings where $\boldsymbol{\epsilon} \parallel \boldsymbol{k}_f$ is consequently zero. Other $\Delta i_\alpha(k_x, k_y)$ rings will have certain intensities indicated in blue in Fig. 6.7**a**, **b**, **c**.

To compare the integrated intensities of these $\Delta i_\alpha(k_x, k_y)$ rings within one $\Delta I_\alpha(k_x, k_y)$ map, they are normalized by two parameters, namely their k space area $A(\alpha)$ and a weighting factor $\omega(\alpha)$. The latter is calculated using the $I_{\boldsymbol{\epsilon}\parallel\boldsymbol{k}_f}(k_x, k_y)$ map and accounts for the effective contribution of individual $i_\alpha^{\boldsymbol{\epsilon}\parallel\boldsymbol{k}_f}(k_x, k_y)$ rings therein:

$$\omega = \frac{i_\alpha^{\boldsymbol{\epsilon}\parallel\boldsymbol{k}_f}(k_x, k_y)}{I_{\boldsymbol{\epsilon}\parallel\boldsymbol{k}_f}(k_x, k_y)}. \tag{6.5}$$

Rings containing meaningful spectral emission caused by an orbital or band features correspondingly have a higher ω in contrast to rings containing mainly featureless intensity due to the background.

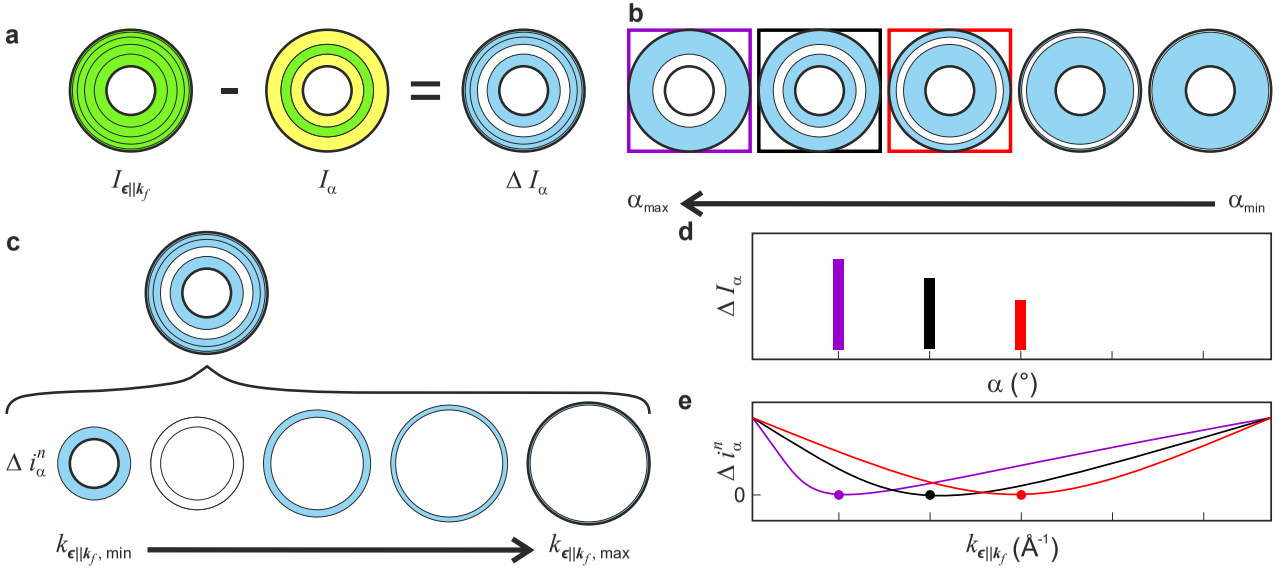

Figure 6.7: Fixed-geometry k map with best agreement to $I_{\epsilon\|k_f}(k_x, k_y)$ map
a Subtraction of $I_\alpha(k_x, k_y)$ map recorded at fixed geometry from $I_{\epsilon\|k_f}(k_x, k_y)$ map resulting in residual $\Delta I_\alpha(k_x, k_y)$ map. **b** Exemplary $\Delta I_\alpha(k_x, k_y)$ maps for five different α. **c** Integrated intensities of $\Delta I_\alpha(k_x, k_y)$ maps plotted against α for the three different $\Delta I_\alpha(k_x, k_y)$ maps marked by blue, black, and red frames in **b**. **c** Exemplary for one $\Delta I_\alpha(k_x, k_y)$ map: Each $\Delta I_\alpha(k_x, k_y)$ map can be decomposed into single $\Delta i^n_\alpha(k_x, k_y)$ rings with radii and width equivalent to the $i^{\epsilon\|k_f}_\alpha(k_x, k_y)$ rings. The intensities within these $\Delta i^n_\alpha(k_x, k_y)$ rings are $\neq 0$ (blue colored rings). Except for the one where the $\epsilon \parallel k_f$ condition is fulfilled for this α. In that case, the intensity within this ring is zero (white color). **e** Integrated and normalized $\Delta i^n_\alpha(k_x, k_y)$ rings are plotted for each $\Delta I_\alpha(k_x, k_y)$ map against their $k_{\epsilon\|k_f}(\alpha)$ radii exemplary for those maps marked by colored frames in **b**. See text for details.

The intensities of the individual $\Delta i_\alpha(k_x, k_y)$ rings within the $\Delta I_\alpha(k_x, k_y)$ maps are finally normalized according to

$$\Delta i^n_\alpha(k_x, k_y) = \frac{\Delta i_\alpha(k_x, k_y) \cdot \omega}{A} \tag{6.6}$$

resulting in normalized $\Delta i^n_\alpha(k_x, k_y)$ rings.

The integrated and normalized intensities of the individual $\Delta i^n_\alpha(k_x, k_y)$ rings within the $\Delta I_\alpha(k_x, k_y)$ maps are plotted against their $k_{\boldsymbol{\epsilon}\parallel\boldsymbol{k}_f}(\alpha)$ radii as exemplary shown in Fig. 6.7**e** for the three $\Delta I_\alpha(k_x, k_y)$ maps in panel **b**. Logically, these plots based on k maps recorded at fixed α must show integrated intensities of zero at those $k_{\boldsymbol{\epsilon}\parallel\boldsymbol{k}_f}(\alpha)$ radii, where the $\boldsymbol{\epsilon} \parallel \boldsymbol{k}_f$ condition is fulfilled. This allows to check whether the calculations were performed correctly.

In Section 6.4, the above-described analysis procedure is applied to the $I_{\boldsymbol{\epsilon}\parallel\boldsymbol{k}_f}(k_x, k_y)$ maps of the three studied systems. The analysis of the individual $\Delta i^n_\alpha(k_x, k_y)$ ring intensities and the integrated residual intensities ($\Delta I_\alpha(k_x, k_y)$) are always described side by side in this work. Later, this procedure is referred to as *residual* $k_{\boldsymbol{\epsilon}\parallel\boldsymbol{k}_f}$ *ring analysis*.

6.4 Results

6.4.1 Benzene/Pd(110)

POT of benzene on Pd(110) introduced in Section 6.2.1 reveals two π states at $E - E_{\text{vac}} = 9.24$ eV and 9.35 eV with their broad emissions located between about (k_{001}, $k_{1\bar{1}0}$)=(0.0, 1.2 – 1.3) Å^{-1} for π_1 (in $I_{40^\circ}(k_x, k_y)$), while that of π_2 is positioned in the perpendicular direction. To capture the complete features in the $I_{\boldsymbol{\epsilon}\parallel\boldsymbol{k}_f}(k_x, k_y)$ map, a photon energy between 20 eV and 31 eV needs to be used in this experimental measurement series.

Using a photon energy of 25 eV seems advantageous, because it provides a reasonable $k_\parallel$ range and photon flux. Moreover, this energy has been routinely used for different POT experiments. In the incidence-angle-dependent measurement series, α is varied from 15–60° in $\Delta\alpha = 3^\circ$ steps resulting in 17 individual $I_\alpha(k_x, k_y)$ maps. The $I_\alpha(k_x, k_y)$ maps are recorded in the full azimuthal range of 360° to ensure the two-fold symmetry of the spectral features already shown in Fig. 6.1.

Measuring $I_\alpha(k_x, k_y)$ maps close to normal incidence experimental geometries (small α), we observe a strong parasitic emission in particular azimuthal orientations of the sample caused by UV light reflected by the sample back to

the analyzer slits. This is exemplary shown in Fig. 6.8**a**, **c**, for $I_{6^\circ}(k_x, k_y)$ and $I_{40^\circ}(k_x, k_y)$. Therefore, it is not possible to use the complete $I_\alpha(k_x, k_y)$ maps for the construction of the $I_{\boldsymbol{\epsilon}\parallel\boldsymbol{k}_f}(k_x, k_y)$ map. Instead, only the upper halves of the $I_\alpha(k_x, k_y)$ maps (positive $k_{1\bar{1}0}$) is used in the following analysis shown in Fig. 6.8**b**, **d**.

Note that only $I_{\alpha>39^\circ}(k_x, k_y)$ maps, where the parasitic emission is less prominent, contain intensity in the $k_\parallel$ range of (0.9 – 1.6) Å^{-1}, where orbital emissions are present. Accordingly, $I_{\alpha<39^\circ}(k_x, k_y)$ maps have only minor contribution to the $I_{\boldsymbol{\epsilon}\parallel\boldsymbol{k}_f}(k_x, k_y)$ maps due to the ω weighting factor from Eq. 6.5. Yet by mischance, $I_\alpha(k_x, k_y)$ maps recorded at large α contributing more to the $I_{\boldsymbol{\epsilon}\parallel\boldsymbol{k}_f}(k_x, k_y)$ maps are more diffuse as visible comparing Fig. 6.8**b**, **d**. The emission intensity in the final $I_{\boldsymbol{\epsilon}\parallel\boldsymbol{k}_f}(k_x, k_y)$ maps is thus more blurred than in, e.g., the $I_{6^\circ}(k_x, k_y)$ map (Fig. 6.8**b**).

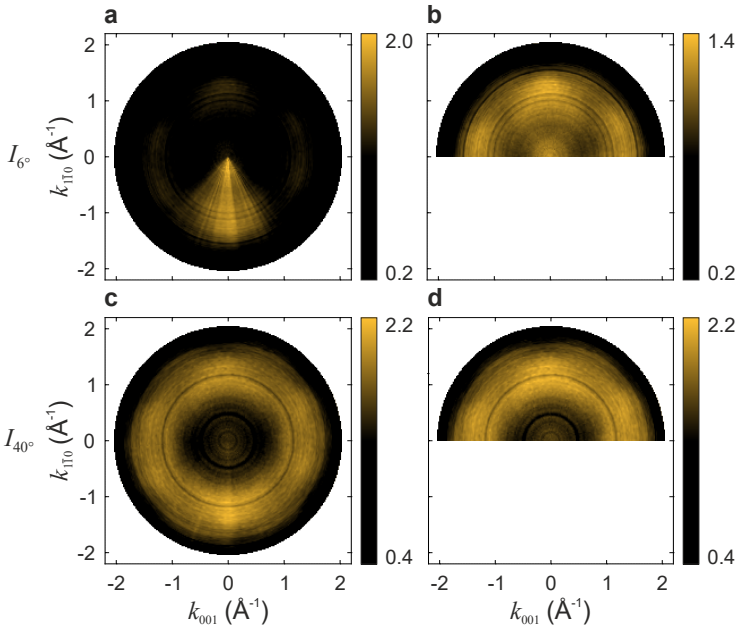

Figure 6.8: Challenges in analysis of benzene/Pd(110)
Experimental $I_{6^\circ}(k_x, k_y)$ and $I_{40^\circ}(k_x, k_y)$ maps in top and bottom row, respectively. **a**, **c** Complete $I_\alpha(k_x, k_y)$ maps. **b**, **d** Upper halves of $I_\alpha(k_x, k_y)$ maps from **a**, **c** plotted with individual color scales. $h\nu = 25$ eV, $E - E_{\text{vac}} = 9.25$ eV.

Fig. 6.9**a**–**c** shows three $I_{\boldsymbol{\epsilon}\|\boldsymbol{k}_f}(k_x, k_y)$ maps constructed for $E - E_{\text{vac}} = 8.97$ eV, 9.25 eV, and 9.54 eV. The map at $E - E_{\text{vac}} = 9.25$ eV corresponds to the maximum intensity of the π_1 state of benzene on Pd(110) (see band map in Fig. 6.1**a**, **b**) and therefore appears with maximal intensity. The $I_{\boldsymbol{\epsilon}\|\boldsymbol{k}_f}(k_x, k_y)$ maps at 8.97 eV and 9.54 eV (Fig. 6.9**a**, **c**) are off the maximum of the π_1 orbital emission and accordingly have lower total intensities. In all $I_{\boldsymbol{\epsilon}\|\boldsymbol{k}_f}(k_x, k_y)$ maps the intensity of the outer edge (large $k_\parallel$) is basically negligibly small. A discernible intensity develops only with $k_\parallel$ radii smaller than ≈ 1.56 Å^{-1} corresponding to $I_{\alpha>40°}(k_x, k_y)$.

The radial intensity artifacts at the junctions between individual $i_\alpha^{\boldsymbol{\epsilon}\|\boldsymbol{k}_f}$ rings to some extent disturb the pattern of orbital emissions making the analysis challenging. It is therefore difficult to get a clear picture of the $I_{\boldsymbol{\epsilon}\|\boldsymbol{k}_f}(k_x, k_y)$ maps. To ease the comparison of the three $I_{\boldsymbol{\epsilon}\|\boldsymbol{k}_f}(k_x, k_y)$ maps, radial profile scans are performed.

To this end, the intensity is azimuthally integrated in the $k_\parallel$ range of $(1.0 - 1.6)$ Å^{-1} and plotted as a function of φ in a range of $\varphi = \pm 130°$ (see replicated $I_{\boldsymbol{\epsilon}\|\boldsymbol{k}_f}(k_x, k_y)$ maps from Fig. 6.9**a**–**c** superimposed with colored lines used for intensity integration in **d**–**f**).

Fig. 6.9**g** shows that the $I_{\boldsymbol{\epsilon}\|\boldsymbol{k}_f}(k_x, k_y)$ maps constructed at varying energies have slightly different radial profiles. Note that the emission from π_1 is expected at $\varphi = \pm 90°$, while that of π_2 is to be seen at $\varphi = 0°$. In agreement with the experimental band maps presented in Fig. 6.1**a**, **b** and the ROI analysis shown in panel **f**, in the intensity profile in Fig. 6.9 the emission of π_1 ($\varphi = \pm 90°$) appears stronger in comparison to the minor lobes at smaller $E - E_{\text{vac}}$ (red and magenta curves). The profile at higher $E - E_{\text{vac}}$ of 9.54 eV (blue curve) has an enhanced contribution of π_2 again (no clear intensity attenuation at $\varphi = 0°$) in agreement with the extracted binding energies of π_1 and π_2 (Section 6.2.1). Thus, the final $I_{\boldsymbol{\epsilon}\|\boldsymbol{k}_f}(k_x, k_y)$ maps indeed reveal emission from both orbitals, π_1 and π_2.

The residual $k_{\boldsymbol{\epsilon}\|\boldsymbol{k}_f}$ ring analysis of benzene/Pd(110) is presented in Fig. 6.10**a** and the integrated $\Delta I_\alpha(k_x, k_y)$ maps in **b**. Looking at Fig. 6.10**a**, it appears that the integrated intensities of $\Delta i_\alpha^n(k_x, k_y)$ rings from all residual $\Delta I_\alpha(k_x, k_y)$ maps reveal that the $\Delta I_\alpha(k_x, k_y)$ maps based on $I_\alpha(k_x, k_y)$ maps of small α deviate more from the $I_{\boldsymbol{\epsilon}\|\boldsymbol{k}_f}(k_x, k_y)$ map compared to those recorded at larger α. This is seen in Fig. 6.10**a** as an increase of $\Delta i_\alpha^n(k_x, k_y)$ of dark colored lines (small α). Note that their intensity is increased for small $k_{\boldsymbol{\epsilon}\|\boldsymbol{k}_f}$ values of $\lesssim 1.4$ Å^{-1} where we observed molecular emissions in the $I_\alpha(k_x, k_y)$ maps. The enhanced disagreement is likewise reflected in the $\Delta I_\alpha(k_x, k_y)$ maps with highest residual intensity at small α (dark colored bars in panel **b**).

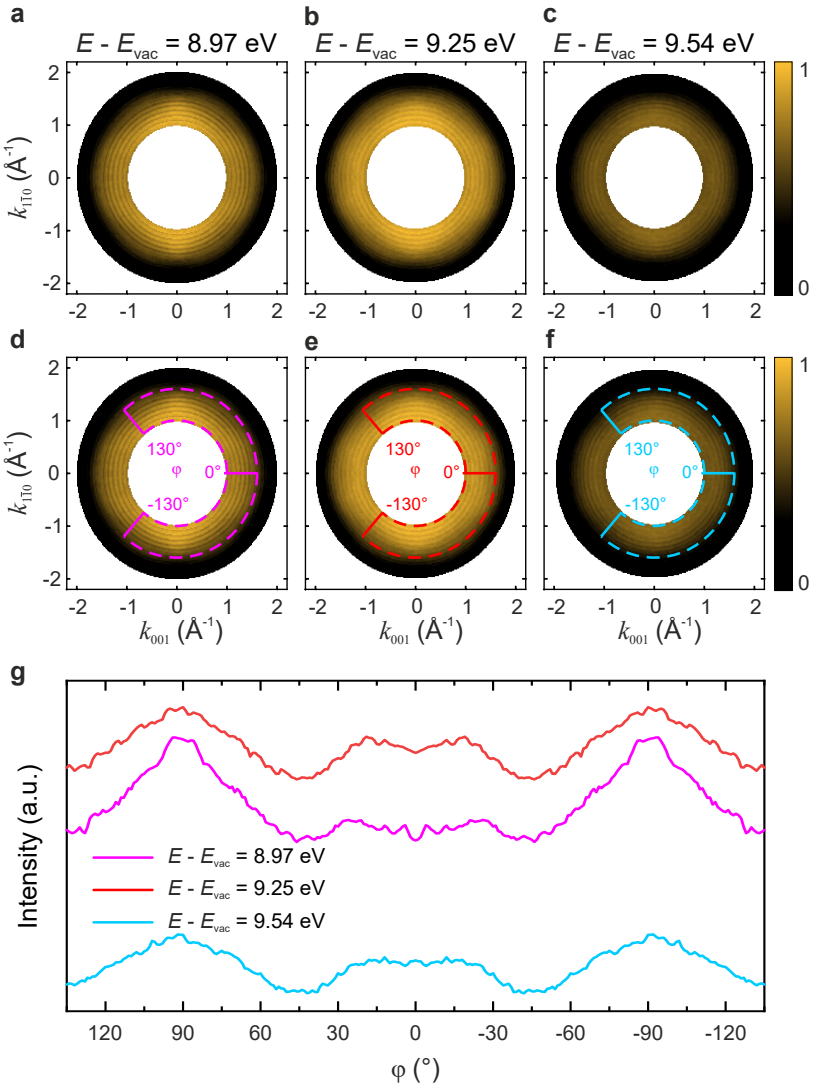

Figure 6.9: $I_{\epsilon\|k_f}(k_x, k_y)$ maps and intensity profiles of benzene/Pd(110) $I_{\epsilon\|k_f}(k_x, k_y)$ maps of benzene/Pd(110) for energies $E - E_{\text{vac}}$ **a** 8.97 eV, **b** 9.25 eV, and **c** 9.54 eV using the $I_\alpha(k_x, k_y)$ maps of $\alpha > 15°$. Same $I_{\epsilon\|k_f}(k_x, k_y)$ maps from **a**–**c** superimposed with **d** magenta, **e** red, and **f** blue lines for azimuthal intensity integration resulting in **g** intensity profiles.

The best agreement between $I_\alpha(k_x, k_y)$ and $I_{\boldsymbol{\epsilon}\parallel\boldsymbol{k}_f}(k_x, k_y)$ maps is quantified by the $\Delta I_\alpha(k_x, k_y)$ maps of smallest residual intensity determined at α_{best} =48° marked with a black arrow in Fig. 6.10**b**. Importantly, the $\Delta i^n_\alpha(k_x, k_y)$ rings of this $\Delta I_{\alpha=48°}(k_x, k_y)$ map (orange curve in panel **a**) show a small residual intensity in the $k_\parallel$ range where the π_1 and π_2 states are observed between (1.2 – 1.3) Å^{-1}. The maximum deviation from the $\boldsymbol{\epsilon} \parallel \boldsymbol{k}_f$ condition in the $I_{\boldsymbol{\epsilon}\parallel\boldsymbol{k}_f}(k_x, k_y)$ is given by $\Delta k_{\boldsymbol{\epsilon}\parallel\boldsymbol{k}_f}$ $(\alpha_{\text{max}})/2$ following Eq. 6.3 yielding 0.045 Å^{-1}.

This analysis of the $I_{\boldsymbol{\epsilon}\parallel\boldsymbol{k}_f}(k_x, k_y)$ maps of benzene/Pd(110) shows that a proper planning of the experiment is vital. Moreover, we learn that an incidence geometry close to 48° provides an optimal condition close to the ideal $I_{\boldsymbol{\epsilon}\parallel\boldsymbol{k}_f}(k_x, k_y)$ map for benzene/Pd(110). Taking into account the integrated residual intensities $\Delta I_\alpha(k_x, k_y)$, only the $I_\alpha(k_x, k_y)$ maps recorded at α =45°, 51°, and 54° in this work deviate from the ideal α = 48° map by $\leqq$ 10%. The $I_\alpha(k_x, k_y)$ map presented by Egger at al. [34] was recorded at α = 40°. In this work, the $I_{40°}$ map deviates roughly 59% from the $I_{48°}$ map. This is also reflected in the $\Delta i^n_\alpha(k_\parallel)$ plot in panel **a** looking at the red curves that reveal a considerable deviation between $I_\alpha(k_x, k_y)$ and $I_{\boldsymbol{\epsilon}\parallel\boldsymbol{k}_f}(k_x, k_y)$ maps in the significant $k_\parallel$ range between (1.2 – 1.3) Å^{-1}, where emission from the π_1 and π_2 states are observed.

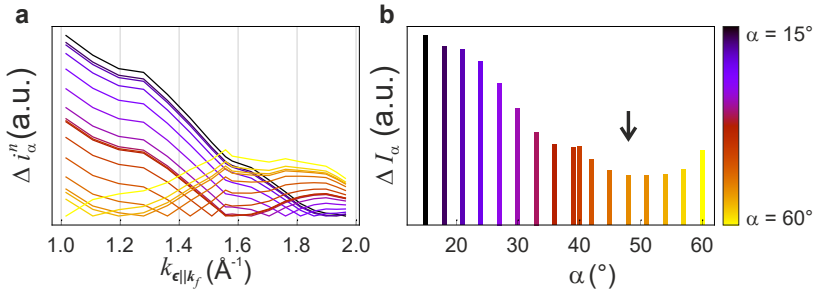

Figure 6.10: Residual $k_{\boldsymbol{\epsilon}\parallel\boldsymbol{k}_f}$ ring analysis of benzene/Pd(110)
a $\Delta i^n_\alpha(k_x, k_y)$ rings from all $\Delta I_\alpha(k_x, k_y)$ maps. **b** Integrated intensities of $\Delta I_\alpha(k_x, k_y)$ maps. Colors correspond to the incidence angles α = 15–60° from dark blue to yellow. α_{best} (48°) is indicated by a black arrow.

6.4.2 Bisanthene/Cu(110)

The on-surface synthesis of bisanthene on Cu(110) from DBBA is introduced in Section 6.2.2. Experimental k maps are recorded for the two frontier orbitals LUMO and HOMO at $E_\mathrm{b} = 0.42$ eV and 1.12 eV at incidence angles of $\alpha = 1$–$60°$ and $\alpha = 0$–$64°$, respectively, to construct their $I_{\boldsymbol{\epsilon}\parallel\boldsymbol{k}_f}(k_x, k_y)$ maps.

Symmetrized $I_{\boldsymbol{\epsilon}\parallel\boldsymbol{k}_f}(k_x, k_y)$ maps of both orbitals are presented in Fig. 6.11**a**, **c**. The gap in the $I_{\boldsymbol{\epsilon}\parallel\boldsymbol{k}_f}(k_x, k_y)$ map of the LUMO (**a**) is due to measuring a too small azimuthal angle range. Note that the single k maps of bisanthene's LUMO were recorded in smaller incidence angle steps ($\alpha = 2°$,3°,5°,6°,8°,9°,11°...) compared to those of the HOMO ($\Delta\alpha = 3°$). This results in a smoother LUMO $I_{\boldsymbol{\epsilon}\parallel\boldsymbol{k}_f}(k_x, k_y)$ map (Fig. 6.11**a**), while borders between the $i_\alpha^{\boldsymbol{\epsilon}\parallel\boldsymbol{k}_f}$ rings are easily visible in the HOMO $I_{\boldsymbol{\epsilon}\parallel\boldsymbol{k}_f}(k_x, k_y)$ map (Fig. 6.11**c**).

The positions of emission intensities in k maps give rise to the real-space periodicity of a particular orbital. In the k maps of bisanthene's LUMO and HOMO, the main emission lobes are clearly defined in comparison to, e.g., large and rather diffuse emission lobes in the k maps of benzene (see Sec. 6.4.1). To evaluate the k space positions of the main lobes for the two bisanthene orbitals, we choose two different approaches presented in Fig. 6.11. I_α and $I_{\boldsymbol{\epsilon}\parallel\boldsymbol{k}_f}(k_x, k_y)$ maps are shown in Fig. 6.11**a**–**d**, results of the first and second approach in panels **e**, **g** and **f**, **h**, respectively.

First, the exact peak positions of the main emission lobes are extracted by varying the intensity contrast in the k maps such that only those pixels with highest intensity remain. Their k positions are plotted in Fig. 6.11**e**, **g** for LUMO and HOMO, respectively. Therein the blue crosses indicate the positions of the maximum intensity in the respective $I_{\boldsymbol{\epsilon}\parallel\boldsymbol{k}_f}(k_x, k_y)$ maps. The positions of the crosses in the green–black–red color code are extracted from $I_\alpha(k_x, k_y)$ maps recorded from highest (green) to smallest (red) incidence angle. For both orbitals, we observe that the position of the intensity maximum is located at higher k values for $I_\alpha(k_x, k_y)$ maps recorded at small α, while it shifts to smaller k values for larger α. The difference in $k_\parallel$ position found for the smallest and highest α is estimated to ≈ 0.12 Å^{-1} for the LUMO and ≈ 0.18 Å^{-1} for the HOMO. The blue crosses indicating the emission lobe position of the $I_{\boldsymbol{\epsilon}\parallel\boldsymbol{k}_f}(k_x, k_y)$ maps are clearly located at even smaller k positions, namely at $k_\parallel = 1.53$ Å^{-1} for bisanthene's LUMO and $k_\parallel = 1.54$ Å^{-1} for the HOMO.

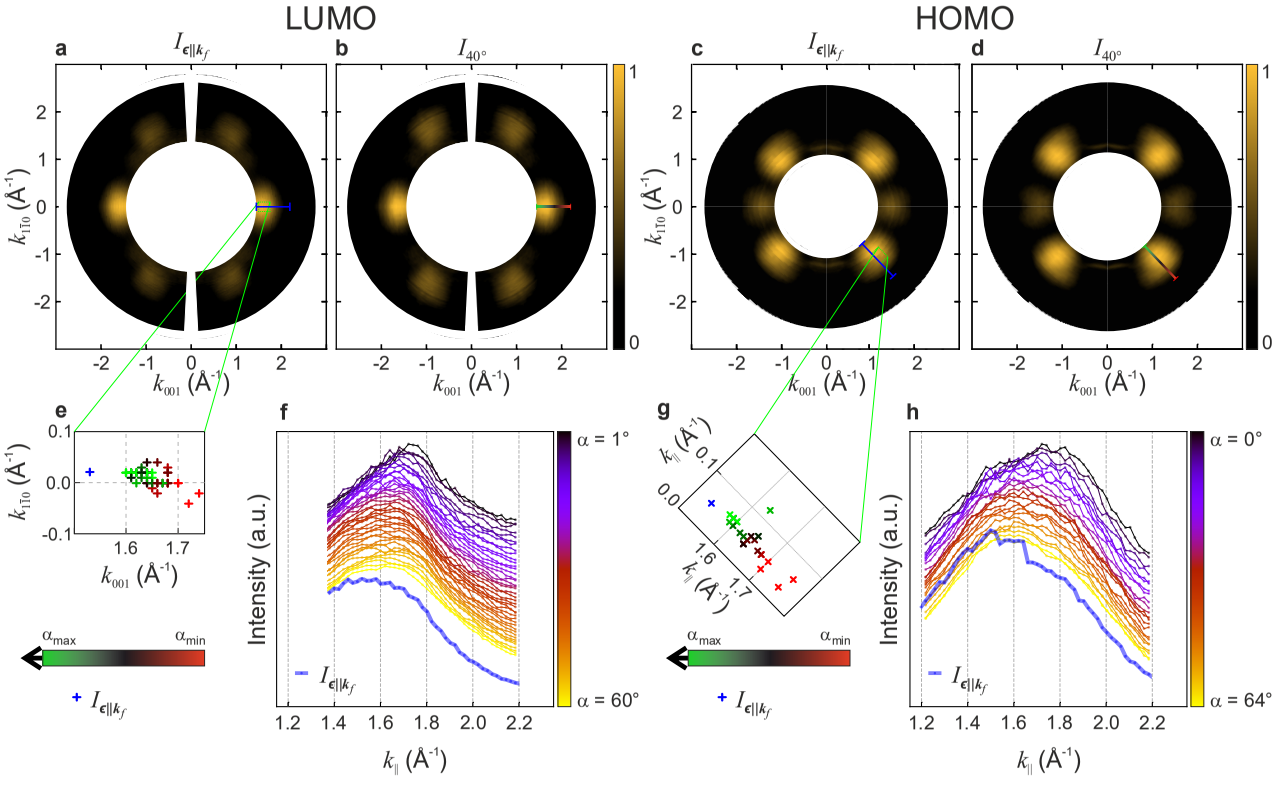

Figure 6.11: Analysis of bisanthene I_α vs. $I_{\epsilon\|k_f}(k_x, k_y)$ maps
Results of bisanthene's LUMO and HOMO on the left and right, respectively. $I_{\epsilon\|k_f}(k_x, k_y)$ maps based on experimental I_α maps recorded at $h\nu$ =35 eV of the **a** LUMO and **c** HOMO. **b** $I_{40°}$ map of the LUMO and at **d** $I_{43°}$ map of the HOMO. Colored crosses in**e** (LUMO) and **g** (HOMO) present the (k_x, k_y) positions of the maximum intensities of those emissions extracted from the $I_{\epsilon\|k_f}(k_x, k_y)$ maps in blue and from the $I_\alpha(k_x, k_y)$ maps recorded at different α in the red-green color code. Intensity profiles extracted along the colored lines drawn in the k maps in **a**–**d** for **f** LUMO and **h** HOMO.

In the second approach, we extract intensity profiles along the lines crossing the main emission lobes in Fig. 6.11**a**–**d** for the I_α and $I_{\boldsymbol{\epsilon}\parallel\boldsymbol{k}_f}(k_x, k_y)$ maps which additionally gives rise to the line shape of the main intensity lobes of LUMO and HOMO. The profiles extracted from the $I_{\boldsymbol{\epsilon}\parallel\boldsymbol{k}_f}(k_x, k_y)$ maps of LUMO and HOMO are plotted as thick, blue lines in Fig. 6.11**f**, **h**, respectively. Those extracted from the $I_\alpha(k_x, k_y)$ maps are displayed as colored lines. Note that the LUMO intensity profiles (**f**) of the $I_\alpha(k_x, k_y)$ maps recorded at large α (yellow curves) have a broader peak in contrast to those at small α (dark curves). This difference in peak width is not observed for bisanthene HOMO (**h**).

Considering the peak positions, the darker curves originating from k maps of small α peak at larger k values, while profiles from $I_\alpha(k_x, k_y)$ maps of larger α (yellow curves) peak at smaller k values for both orbitals. This agrees with the evaluated positions of the intensity maxima in the emission lobes in Fig. 6.11**e**, **g** (large $\alpha \rightarrow$ peak at smaller $k_\parallel$). And again, the peak position of the $I_{\boldsymbol{\epsilon}\parallel\boldsymbol{k}_f}(k_x, k_y)$ map is observed at even smaller k values.

From both approaches, we learn that the main emission lobe is located at substantially smaller $k_\parallel$ positions in the $I_{\boldsymbol{\epsilon}\parallel\boldsymbol{k}_f}(k_x, k_y)$ maps in contrast to the $I_\alpha(k_x, k_y)$ maps. Considering that in the $I_{\boldsymbol{\epsilon}\parallel\boldsymbol{k}_f}(k_x, k_y)$ maps, the $\boldsymbol{\epsilon} \parallel \boldsymbol{k}_f$ condition is fulfilled in the complete available k space, they are the most precise experimental evidence for the orbital's real-space periodicity. As a consequence the Fourier transform of $I_{\boldsymbol{\epsilon}\parallel\boldsymbol{k}_f}(k_x, k_y)$ maps is supposed to result in an adequate experimentally-derived real-space orbital. Although the latter is beyond the scope of this work, the k positions of the main lobes extracted from the $I_{\boldsymbol{\epsilon}\parallel\boldsymbol{k}_f}(k_x, k_y)$ maps can be compared to those of k maps simulated for the free molecule. Accordingly, we find experimental values of $k_\parallel = 1.53$ Å^{-1} for bisanthene's LUMO and $k_\parallel = 1.54$ Å^{-1} for the HOMO. For the free bisanthene molecule calculated with the B3LYP functional, values of $k_\parallel = 1.57$ Å^{-1} and $k_\parallel = 1.64$ Å^{-1} are obtained for LUMO and HOMO, respectively. As a preliminary result we thus conclude that the experimentally-obtained real-space expansion of the frontier orbitals under the $\boldsymbol{\epsilon} \parallel \boldsymbol{k}_f$ condition is larger compared to that obtained for typical experiments recorded at one α and the calculations. A more detailed comparison to theory is, however, beyond the scope of this work.

As mentioned earlier, the construction of $I_{\boldsymbol{\epsilon}\parallel\boldsymbol{k}_f}(k_x, k_y)$ maps requires to measure single k maps at multiple incidence angles. This is, however, not feasible in some experimental setups, since the incidence angle is often fixed. Therefore, it is of interest to on the one hand find out which incidence angle is needed for a particular system to measure a k map which comes closest to the ideal $I_{\boldsymbol{\epsilon}\parallel\boldsymbol{k}_f}(k_x, k_y)$ map. Or on the other hand, how much a k map measured with a particular incidence angle deviates from the $I_{\boldsymbol{\epsilon}\parallel\boldsymbol{k}_f}(k_x, k_y)$ map.

From the analysis presented in Fig. 6.11, we conclude that if the ideal position of the main emission lobe according to the $I_{\boldsymbol{\epsilon}\parallel\boldsymbol{k}_f}(k_x, k_y)$ map is prioritized, a k map measured at a large α matches the $I_{\boldsymbol{\epsilon}\parallel\boldsymbol{k}_f}(k_x, k_y)$ map best (green crosses in Fig. 6.11**e**, **g** and yellow curves in **f**, **h**). However, there would still be a considerable deviation of the position of the main lobe and hence the real-space periodicity.

An alternative approach to evaluate which $I_\alpha(k_x, k_y)$ map comes closest to the $I_{\boldsymbol{\epsilon}\parallel\boldsymbol{k}_f}(k_x, k_y)$ map is the residual $k_{\boldsymbol{\epsilon}\parallel\boldsymbol{k}_f}$ ring analysis introduced in Section 6.3. The analysis is presented in Fig. 6.12 for bisanthene LUMO in **a**, **c** and HOMO in **b**, **d**, respectively.

Fig. 6.12**a** shows the integrated intensity of individual $\Delta i^n_\alpha(k_x, k_y)$ rings from all residual ΔI_α maps for bisanthene LUMO revealing that the disagreement between I_α and $I_{\boldsymbol{\epsilon}\parallel\boldsymbol{k}_f}$ maps is more pronounced at $\Delta i^n_\alpha(k_x, k_y)$ rings closer to the center of the maps. The highest total residual intensity ΔI_α is calculated for $\alpha = 18°$ as shown in Fig. 6.12**c** demonstrating a strong deviation from the $I_{\boldsymbol{\epsilon}\parallel\boldsymbol{k}_f}(k_x, k_y)$ map at this incidence geometry. The ΔI_α map of smallest residual intensity is determined at $\alpha_{\text{best}} = 51°$ for bisanthene's LUMO revealing the best agreement to the $I_{\boldsymbol{\epsilon}\parallel\boldsymbol{k}_f}(k_x, k_y)$ map. The maximum deviation from the $\boldsymbol{\epsilon} \parallel \boldsymbol{k}_f$ condition in the $I_{\boldsymbol{\epsilon}\parallel\boldsymbol{k}_f}(k_x, k_y)$ is given by $\Delta k_{\boldsymbol{\epsilon}\parallel\boldsymbol{k}_f}\ (\alpha_{\text{max}})/2$ following Eq. 6.3 yielding 0.042 Å^{-1}.

In the case of the molecule's HOMO, the analysis is corrupted due to experimental reasons. The I_α maps were recorded starting at $\alpha = 40°$ and reducing α in steps of 3°. After measuring $I_{0°}$, α was set to 43° and increased further until reaching $\alpha = 64°$. It seems that the correction of the photon flux by the mirror current did not succeed in this case. This can be seen in the jump of ΔI_α from $\alpha = 40°$ to $\alpha = 43°$ in Fig. 6.12**d**. Nonetheless, looking at the measurements corresponding to $\alpha > 43°$, we again see a local minimum in Fig. 6.11**d** at $\alpha_{\text{best}} = 52°$ showing the best agreement of individual measurements performed at this incidence geometry with the ideal $I_{\boldsymbol{\epsilon}\parallel\boldsymbol{k}_f}(k_x, k_y)$ map.

The maximum deviation from the $\boldsymbol{\epsilon} \parallel \boldsymbol{k}_f$ condition in the $I_{\boldsymbol{\epsilon}\parallel\boldsymbol{k}_f}(k_x, k_y)$ is given by $\Delta k_{\boldsymbol{\epsilon}\parallel\boldsymbol{k}_f}\ (\alpha_{\text{max}})/2$ following Eq. 6.3 yielding 0.064 Å^{-1}. The larger deviation compared to the LUMO is due to the slightly larger incidence angle step of 3° (HOMO) compared to 1° and 2° (LUMO).

Summing up for bisanthene/Cu(110), we find that $I_\alpha(k_x, k_y)$ maps of the molecule's LUMO and HOMO come closest to the $I_{\boldsymbol{\epsilon}\parallel\boldsymbol{k}_f}(k_x, k_y)$ maps if incidence angles of α_{best} 51° and 52° are used, respectively. Considering the total residual intensities ΔI_α in Fig. 6.11**c**, **d**, a deviation of less than 10% from the ideal map is considered as an appropriate map. In the case of bisanthene LUMO, this applies to incidence geometries of $\alpha = 50°$ and 53°, while for the HOMO the appropriate angular range is slightly larger from $\alpha = 46$–58°.

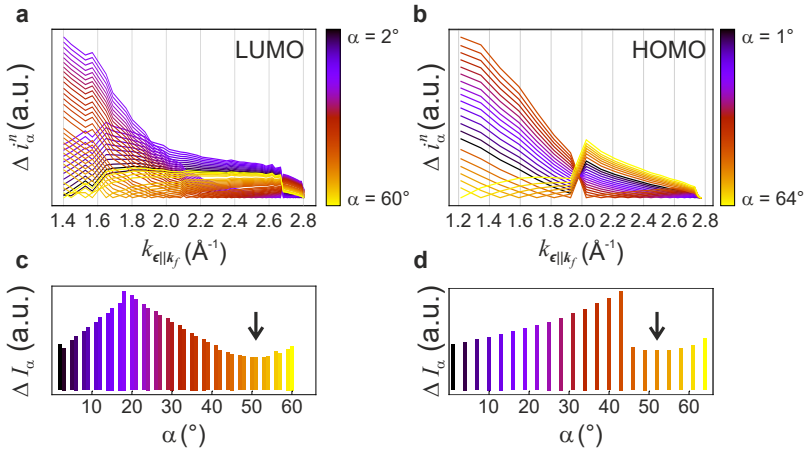

Figure 6.12: Residual $k_{\epsilon\|k_f}$ ring analysis of bisanthene/Cu(110)
a, **b** Integrated intensity of individual $\Delta i^n_\alpha(k_x, k_y)$ rings from all residual ΔI_α maps for bisanthene LUMO and HOMO, respectively. **c**, **d** Integrated total intensities of ΔI_α maps for bisanthene LUMO and HOMO, respectively. Colors correspond to the incidence angles $\alpha = 1 - 64°$ from dark blue to yellow. α_{best} is indicated by black arrows.

In literature, POT studies on bisanthene/Cu(110) presented k maps recorded at α =40° [AH9, 35]. Since this geometry is not within the appropriate angular range found in this work, those measurements were consequently further away from the ideal $I_{\boldsymbol{\epsilon}\|\boldsymbol{k}_f}(k_x, k_y)$ maps.

Nevertheless, this deviation mainly concerns the position of the emission lobes which shifts by at most ≈0.12 Å^{-1} for the LUMO and ≈0.18 Å^{-1} for the HOMO considering the I_α maps recorded at smallest and highest α. The overall symmetry yet remains, which allows qualitative analyses. Note that this analysis was performed for the frontier π orbitals of bisanthene/Cu(110).

The results of bisanthene/Cu(110) presented in this section can also serve as reference for other systems including molecules of similar size. POT studies based on experimental measurements using the TEA were typically recorded at α =40°. Other ARPES-based studies producing experimental k maps were recorded using a NanoESCA PEEM that is operated at grazing incidence geometry with α =65° [25, 33, 235, 236]. These α used in literature are not within the appropriate angle range found in this chapter and are therefore considered to deviate from the ideal $I_{\boldsymbol{\epsilon}\|\boldsymbol{k}_f}(k_x, k_y)$ map and hence also from the ideal spherical wave approximation.

6.4.3 Epitaxial monolayer graphene

Basic information about EMLG is introduced in Section 6.2.3. Unlike molecular systems discussed in this chapter so far, the electronic structure of the 2D material graphene consists of bands dispersing in reciprocal space and energy. Therefore, the $I_\alpha(k_x, k_y)$ maps of graphene (see Fig. 6.3) do not comprise localized emission lobes at distinct $k_\parallel$ positions, but show sharp band-like emission features in the complete k space. Experimental $I_\alpha(k_x, k_y)$ maps of EMLG were recorded for two different energies $E - E_{\text{vac}}$ of approximately 7.81 eV and 8.88 eV that we refer to as maps A and B, respectively. In the $I_\alpha(k_x, k_y)$ maps, we observe emission from π bands or π and σ bands , respectively. Measuring at these varying $E - E_{\text{vac}}$, it is possible to evaluate how the contribution of different bands changes with photon energy.

For map A, photon energy dependent POT data of EMLG are recorded at $h\nu = 23$ eV, 40 eV, 60 eV, and 85 eV at $E - E_{\text{vac}}$ of 7.69 eV, 7.87 eV, 7.86 eV, and 7.82 eV. The $I_\alpha(k_x, k_y)$ maps of individual photon energies shown in Fig. 6.13**a**, **b** are created by integrating the intensities in energy windows of 0.18 eV ($h\nu = 23$ eV), 0.37 eV ($h\nu = 40$ eV and 60 eV), and 0.45 eV ($h\nu = 85$ eV). The slightly different $E - E_{\text{vac}}$ cause varying intensity distributions at the π band crossing at the $\overline{\text{M}}$ point at $k_x \approx 1.5$ Å^{-1} indicated by the blue arrows in Fig. 6.13. For example at $h\nu = 23$ eV, there is one broad emission at this k position (Fig. 6.13, left column), while for $h\nu = 60$ eV an intensity depletion is observed indicated by the white lines (Fig. 6.13**b**, third column). The final $I_{\boldsymbol{\epsilon}\parallel\boldsymbol{k}_f}(k_x, k_y)$ maps are displayed in Fig. 6.13**c** and the residual $k_{\boldsymbol{\epsilon}\parallel\boldsymbol{k}_f}$ ring analysis in Fig. 6.14.

For map B, data sets are recorded at $h\nu = 60$ eV and 85 eV (both at $E - E_{\text{vac}} = 8.88$ eV) with both of their $I_\alpha(k_x, k_y)$ maps constructed from integration in an energy window of 0.41 eV. The results of map B are shown in Figs. 6.15 and 6.16.

Map A

I_{3° and I_{39° maps of map A are displayed in Fig. 6.13**a**, **b** for $h\nu = 23$ eV, 40 eV, 60 eV, and 85 eV from left to right. The most prominent differences between two $I_\alpha(k_x, k_y)$ maps recorded at the same photon energy but different α is the intensity of the π bands (note the individual color scales). Similar to the results of benzene/Pd(110) in Section 6.4.1, the data recorded at small α (**a**) have a weaker π band intensity compared to those I_α maps of grazing incidence (**b**). Since these $I_\alpha(k_x, k_y)$ maps are used for the construction of $I_{\boldsymbol{\epsilon}\parallel\boldsymbol{k}_f}(k_x, k_y)$ maps, one would expect that this intensity difference has an impact on the final $I_{\boldsymbol{\epsilon}\parallel\boldsymbol{k}_f}$ maps.

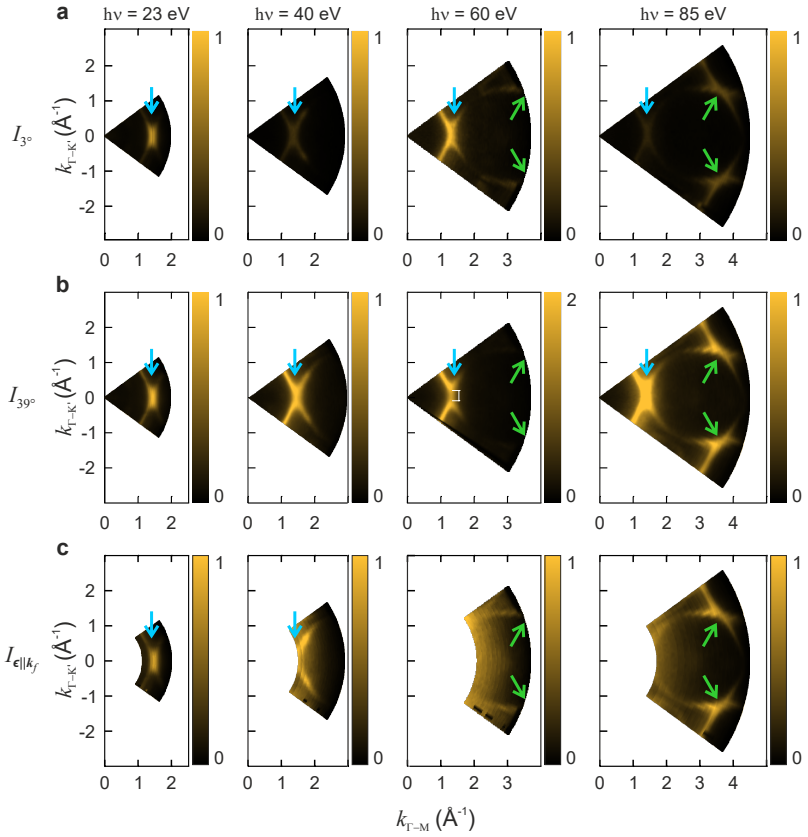

Figure 6.13: Map A: I_α and $I_{\epsilon\|k_f}$ maps
a $I_{3°}$, **b** $I_{39°}$, and **c** $I_{\epsilon\|k_f}$ maps. The k maps are recorded at varying photon energies of 23 eV, 40 eV, 60 eV, and 85 eV displayed in the five columns from left to right with $E - E_{\text{vac}} = 7.69$ eV, 7.87 eV, 7.86 eV, and 7.82 eV. The color scales of the k maps recorded at the same photon energy are adjusted. Correspondingly the color scales of those recorded at 23 eV, 40 eV, and 85 eV are the same and hence directly comparable. The total intensity scale of the $I_{39°}$ map at $h\nu = 60$ eV is twice the intensity scale of the other two I_α maps of the same photon energy.

Considering that $i_\alpha^{\boldsymbol{\epsilon}\parallel\boldsymbol{k}_f}(k_x,k_y)$ rings of large (small) radius originate from $I_\alpha(k_x,k_y)$ maps recorded at small (large) α and the observation that $I_{3^\circ} < I_{39^\circ}$, we expect that the intensity within the $I_{\boldsymbol{\epsilon}\parallel\boldsymbol{k}_f}(k_x,k_y)$ maps diminishes at larger k values.

The $I_{\boldsymbol{\epsilon}\parallel\boldsymbol{k}_f}(k_x,k_y)$ maps of EMLG map A are shown in Fig. 6.13**c** for the photon energies 23 eV, 40 eV, 60 eV, and 85 eV from left to right. The maximum deviation from the $\boldsymbol{\epsilon} \parallel \boldsymbol{k}_f$ condition in the $I_{\boldsymbol{\epsilon}\parallel\boldsymbol{k}_f}(k_x,k_y)$ is given by $\Delta k_{\boldsymbol{\epsilon}\parallel\boldsymbol{k}_f}\,(\alpha_{\max})/2$ following Eq. 6.3 yielding 0.042 Å^{-1}, 0.063 Å^{-1}, 0.077 Å^{-1}, and 0.106 Å^{-1} for $h\nu = 23$ eV, 40 eV, 60 eV, and 85 eV, respectively. Against the previously mentioned expectation, the photoemission intensity does not diminish at large $k_\parallel$. Instead, the emission from the π bands is visible in the complete available k space.

Note that the individual photon energies limit the available k space. As a consequence, regions in k space where the $\boldsymbol{\epsilon} \parallel \boldsymbol{k}_f$ condition is fulfilled are linked to certain photon energies. In our exemplary used photon energies, the π band crossing at the $\overline{\mathrm{M}}$ point at $k_x \approx 1.5$ Å^{-1} (blue arrows in Fig. 6.13) is thus only mapped according to the $\boldsymbol{\epsilon} \parallel \boldsymbol{k}_f$ condition using $h\nu = 23$ eV. The crossing of these bands in the second BZ indicated by green arrows in Fig. 6.13 is, however, only accessed at larger photon energies – 85 eV in our example. To get a full picture regarding the $\boldsymbol{\epsilon} \parallel \boldsymbol{k}_f$ condition, it is therefore necessary to record data and construct $I_{\boldsymbol{\epsilon}\parallel\boldsymbol{k}_f}$ maps from experimental POT series at different photon energies. This also means that the evaluation of α_{best} for EMLG map A is done at the four used photon energies.

The residual $k_{\boldsymbol{\epsilon}\parallel\boldsymbol{k}_f}$ ring analysis for map A of EMLG is presented in Fig. 6.14**a**, **b**, **e**, and **f** and the integrated total intensities of ΔI_α maps in **c**, **d**, **g**, and **h** for the data recorded at $h\nu = 23$ eV, 40 eV, 60 eV, and 85 eV, respectively. We observe that the $\Delta i_\alpha^n(k_x,k_y)$ rings of the $I_\alpha(k_x,k_y)$ maps closer to the center deviate more from the $I_{\boldsymbol{\epsilon}\parallel\boldsymbol{k}_f}(k_x,k_y)$ maps similar to the results of benzene/Pd(110) and bisanthene/Cu(110) (Sections 6.4.1 and 6.4.2). This can be seen by the large $\Delta i_\alpha^n(k_x,k_y)$ values at smaller $k_{\boldsymbol{\epsilon}\parallel\boldsymbol{k}_f}$ particularly for $I_\alpha(k_x,k_y)$ maps recorded at small α (dark curves) as exemplary indicated by the black brackets in Fig. 6.14**b**. This effect is observed for all four data sets.

The best agreement between I_α and $I_{\boldsymbol{\epsilon}\parallel\boldsymbol{k}_f}$ maps is judged by the integrated ΔI_α maps presented in Fig. 6.14 **c**, **d**, **g**, and **h**. The smallest ΔI_α represents the ideal α where the I_α maps come closest to the $I_{\boldsymbol{\epsilon}\parallel\boldsymbol{k}_f}$ maps. This is indicated by black arrows resulting in $\alpha_{\mathrm{best}} = 42^\circ$, 51°, 45°, and 51° for $h\nu = 23$ eV, 40 eV, 60 eV, and 85 eV, respectively. The evaluated variation of α_{best} is particularly interesting, because the same kind of band was investigated in all four incidence-angle-dependent POT measurements. The only differences were the photon energies and the consequential limited $k_{\boldsymbol{\epsilon}\parallel\boldsymbol{k}_f}$ ranges where the $\boldsymbol{\epsilon} \parallel \boldsymbol{k}_f$ condition is fulfilled. However, no trend is observed in the evaluated α_{best} with photon energy or $k_{\boldsymbol{\epsilon}\parallel\boldsymbol{k}_f}$ ranges.

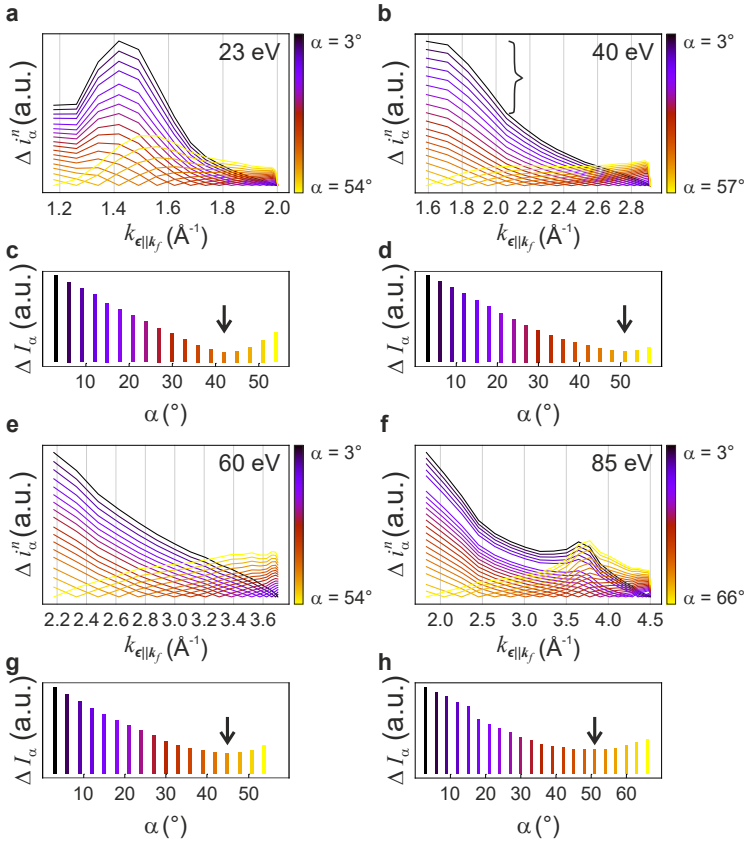

Figure 6.14: Map A: Residual $k_{\epsilon\|k_f}$ ring analysis
Integrated intensity of individual $\Delta i^n_\alpha(k_x, k_y)$ rings from all ΔI_α maps for map A of EMLG at photon energies of **a** 23 eV, **e** 40 eV, **f** 60 eV, and **i** 85 eV. Total intensities of ΔI_α maps at photon energies of **c** 23 eV, **g** 40 eV, **h** 60 eV, and **j** 85 eV. Colors correspond to the incidence angles $\alpha = 3$–$54°$ for $h\nu = 23$ eV, and 60 eV, $\alpha = 3$–$57°$ for $h\nu = 40$ eV, and $\alpha = 3$–$66°$ for $h\nu = 85$ eV from dark blue to yellow. α_{best} is indicated with black arrows.

Map B

The results of the I_α maps recorded at $E - E_{\text{vac}} = 8.88$ eV intersecting π bands and the top of the σ band at the $\overline{\Gamma'}$ point of EMLG's electronic band structure are presented in Figs. 6.15 and 6.16. I_{3° and I_{39° maps are shown in Fig. 6.15**a**, **b**, and **c**, **d**, respectively, recorded at photon energies of $h\nu = 60$ eV and 85 eV in the left and right columns.

Another I_{3° map recorded at $h\nu = 87$ eV was already briefly described in Section 6.2.3 taking the band maps into consideration. In short, the round emission intensity in the center of the I_α maps (marked exemplary with a white circle in I_α maps recorded at $h\nu = 60$ eV in Fig. 6.15**a**, **c**) stems from a σ band, which is further referred to as σ *band emission*. The remaining visible intensities in the I_α maps is of π character. To refer to particular π band emissions, ellipses are drawn into the k maps recorded at $h\nu = 85$ eV in Fig. 6.15**b**, **d**, which are specified in the following.

It is noticeable from the varying intensity scaling of the I_α maps in Fig. 6.15**a**–**d** (0–1 *vs.* 0–0.25 for $h\nu = 60$ eV and 0–1 *vs.* 0–0.4 for $h\nu = 85$ eV) that again the total intensity of the POT data recorded at smaller α is weaker. This is observed for π and σ band emission intensities.

However, not only the total photoemission intensity of the π bands changes but also their intensity distribution within the I_α maps. To address particular features in the maps, red, white, and blue ellipses with different line shapes are drawn into Fig. 6.15**b**, **d**. The dotted ellipses denote π band emission intensity at the border between the first and second BZ in red and white, respectively. The dashed ellipses mark the symmetry equivalent π band emission intensities at the border between the second and third BZ in white and blue, respectively. Interestingly, the π band emission intensity in the second BZ (white ellipses) are throughout weaker compared to their neighboring features (red or blue ellipses) for I_{3° and I_{39° maps in **b**, **d**. Yet, comparing the π band emission intensities in the first (red ellipse) and third (blue ellipses) BZ, the intensity ratio varies with α. In the I_{3° map (**b**), π band emission intensity in the third BZ is more intense than that in the first BZ, while in the I_{39° map (**d**), this is vice versa (compare intensities in the red and blue ellipses).

The final $I_{\boldsymbol{\epsilon}\parallel\boldsymbol{k}_f}(k_x, k_y)$ maps of map B created from the POT series recorded at $h\nu = 60$ eV and 85 eV are presented in Fig. 6.15**e**, **f**, respectively. Due to the limited $k_{\boldsymbol{\epsilon}\parallel\boldsymbol{k}_f}$ ranges in the $I_{\boldsymbol{\epsilon}\parallel\boldsymbol{k}_f}(k_x, k_y)$ maps given by the smallest and largest α, some features visible in the $I_\alpha(k_x, k_y)$ maps are not captured anymore according to the $\boldsymbol{\epsilon} \parallel \boldsymbol{k}_f$ condition.

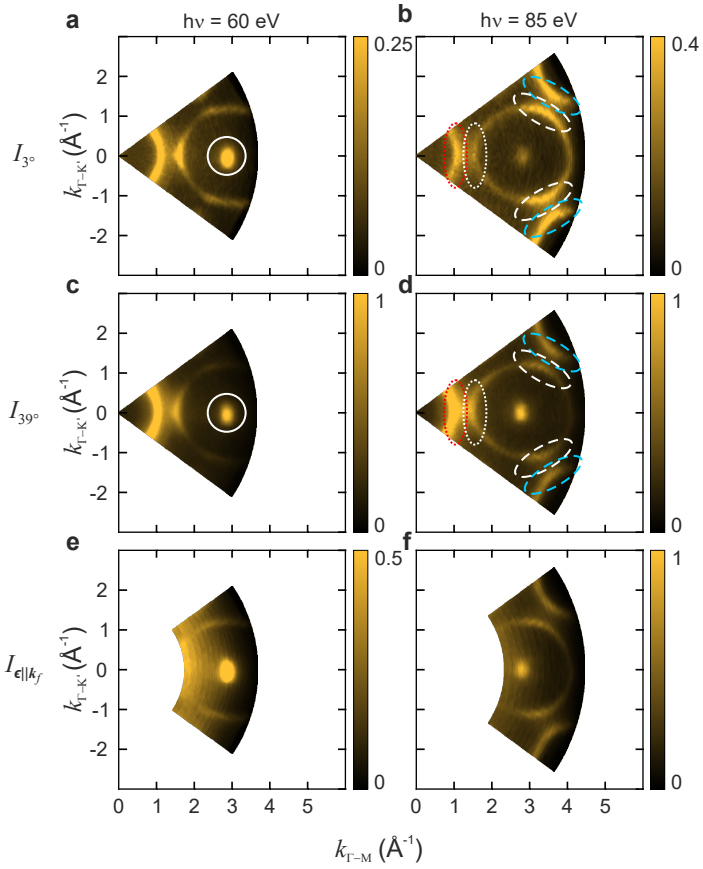

Figure 6.15: Map B: I_α and $I_{\epsilon\|k_f}$ maps
a $I_{3°}$ and **b** $I_{39°}$ maps. The k maps are recorded at different photon energies of 60 eV and 85 eV displayed in the left and right columns, respectively. $E - E_{\text{vac}} = 8.88$ eV for all measurements of map B. The individual color scales are indicated in the figure. Solid white circles mark emission from the σ band, dotted and dashed ellipses emission from the π bands in the first, second, and third BZ in red, white, and blue. **c** $I_{\epsilon\|k_f}(k_x, k_y)$ maps.

This concerns the π band emission intensity at the border between the first and second BZ for the maps recorded at both photon energies marked exemplary in red and white in Fig. 6.15**b**, **d**, which is absent in both shown $I_{\boldsymbol{\epsilon}\parallel\boldsymbol{k}_f}(k_x, k_y)$ maps (**e**, **f**). The other π band emission intensities at the border between the second and third BZ (white and blue ellipses) are again only visible in the $I_{\boldsymbol{\epsilon}\parallel\boldsymbol{k}_f}(k_x, k_y)$ map recorded at 85 eV. Since only the intensity ratio between the emissions marked with the red and blue ellipses varied in the $I_\alpha(k_x, k_y)$ maps, a bare-eye distinction which $I_\alpha(k_x, k_y)$ map agrees best with the $I_{\boldsymbol{\epsilon}\parallel\boldsymbol{k}_f}(k_x, k_y)$ map is not possible.

The evaluation of α_{best} is thus again only achievable with the residual $k_{\boldsymbol{\epsilon}\parallel\boldsymbol{k}_f}$ ring analysis shown in Fig. 6.16**a**, **b** and the integration of total intensities of ΔI_α maps in **c**, **d** for the data recorded at $h\nu = 60$ eV and 85 eV, respectively. Again, the $k_{\boldsymbol{\epsilon}\parallel\boldsymbol{k}_f}$ rings of the I_α maps closer to the center deviate more from the $I_{\boldsymbol{\epsilon}\parallel\boldsymbol{k}_f}$ maps as already observed for map A. In the case of map B, this deviation is, however, more pronounced, because the individual curves in the $k_{\boldsymbol{\epsilon}\parallel\boldsymbol{k}_f}$ vs. $\Delta i^n_\alpha(k_x, k_y)$ plots decay less steep. This means that the deviation between I_α and $I_{\boldsymbol{\epsilon}\parallel\boldsymbol{k}_f}$ maps persists in a larger $k_{\boldsymbol{\epsilon}\parallel\boldsymbol{k}_f}$ range.

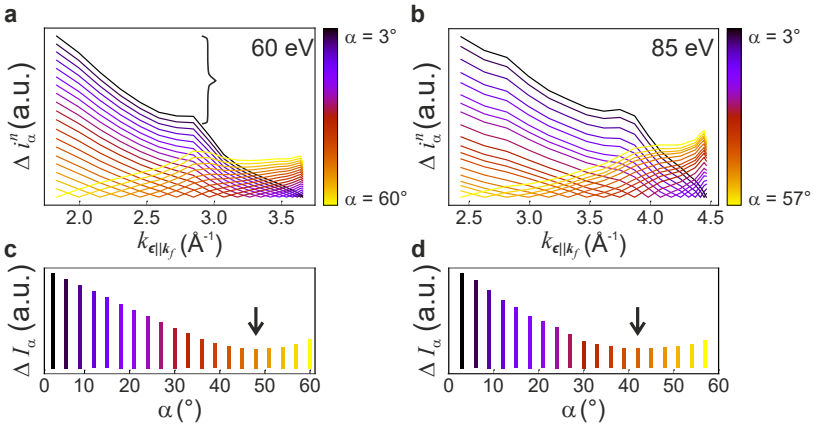

Figure 6.16: Map B: Residual $k_{\boldsymbol{\epsilon}\parallel\boldsymbol{k}_f}$ ring analysis
a, **b** Integrated intensity of individual $\Delta i^n_\alpha(k_x, k_y)$ rings from all residual ΔI_α maps for map B of EMLG with I_α maps recorded at $h\nu = 60$ eV and 85 eV, respectively. **c**, **d** Total intensities of ΔI_α maps for $h\nu = 60$ eV and 85 eV, respectively. Colors correspond to the incidence angles $\alpha = 3$–$60°$ and $\alpha = 3$–$57°$ for $h\nu = 60$ eV and 85 eV from dark blue to yellow. α_{best} is indicated with black arrows.

The best agreement between I_α and $I_{\boldsymbol{\epsilon}\parallel\boldsymbol{k}_f}$ maps is again judged by the total intensities of the residual ΔI_α maps presented in Fig. 6.16**c**, **d**). The smallest ΔI_α represents the ideal α where the I_α maps come closest to the $I_{\boldsymbol{\epsilon}\parallel\boldsymbol{k}_f}$ maps. This is indicated in the corresponding Fig. 6.16**c**, **d** by black arrows resulting in $\alpha_{\text{best}} = 48°$ and 42° for $h\nu = 60$ eV and 85 eV, respectively. The maximum deviation from the $\boldsymbol{\epsilon} \parallel \boldsymbol{k}_f$ condition in the $I_{\boldsymbol{\epsilon}\parallel\boldsymbol{k}_f}(k_x, k_y)$ is given by $\Delta k_{\boldsymbol{\epsilon}\parallel\boldsymbol{k}_f}\ (\alpha_{\text{max}})/2$ following Eq. 6.3 yielding 0.079 Å^{-1}, and 0.096 Å^{-1} for $h\nu = 60$ eV and 85 eV, respectively.

6.5 Conclusion and outlook

The resulting α_{best} and the estimated maximal deviation from the $\boldsymbol{\epsilon} \parallel \boldsymbol{k}_f$ condition $\Delta k_{\boldsymbol{\epsilon}\parallel\boldsymbol{k}_f}\ (\alpha_{\text{max}})/2$ of all investigated systems are summarized in Tab. 6.2. Note that the data set of bisanthene/Cu(110) HOMO (marked with * in Tab. 6.2) suffers from technical artifacts, but still provides valuable information giving a clear minimum in the α-ΔI_α-plot.

In total, three data sets for molecular systems (benzene/Pd(110) and bisanthene/Cu(110) LUMO and HOMO) and six data sets for graphene provide valuable results concerning the $\boldsymbol{\epsilon} \parallel \boldsymbol{k}_f$ condition and the desired incidence geometry at which the typically recorded k maps come closest to the ideal $I_{\boldsymbol{\epsilon}\parallel\boldsymbol{k}_f}$ maps. As a result, the average $\overline{\alpha_{\text{best}}}$ yields 50° for the three data set of molecular systems with a standard variation of 1.5°. For the EMLG data sets, the average $\overline{\alpha_{\text{best}}}$ is calculated to 47° with a standard variation of 3.7°. We finally conclude that k maps recorded at $\alpha = 49° \pm 3$ ° resemble their corresponding $I_{\boldsymbol{\epsilon}\parallel\boldsymbol{k}_f}(k_x, k_y)$ map, in which each position in k space fulfills the $\boldsymbol{\epsilon} \parallel \boldsymbol{k}_f$ condition, best. The estimated error is predominantly <0.1 Å^{-1} and increased with the used photon energy.

Note that for benzene/Pd(110) and all EMLG data sets, the $i_\alpha(k_x, k_y)$ rings of the I_α maps closer to the center (large α) deviate more from the $I_{\boldsymbol{\epsilon}\parallel\boldsymbol{k}_f}(k_x, k_y)$ maps those rings with larger radius (small α). In the case of the molecular system, this trend may arise from the generally higher total intensity of k maps recorded at grazing incidence or due to the fact that the molecular feature only comes into play at a certain $k_\parallel$ radius closer to Γ. Nevertheless, this observation is likewise recognized for data sets recorded at two different $E - E_{\text{vac}}$ of EMLG measured at six photon energies, with photoemission intensity unconfined in the complete available k space. The latter aspect given for the molecular system, namely that there is a better agreement between I_α and $I_{\boldsymbol{\epsilon}\parallel\boldsymbol{k}_f}$ maps when the $i_\alpha^{\boldsymbol{\epsilon}\parallel\boldsymbol{k}_f}$ rings cut the decisive emission feature, is therefore disproved.

	Benzene/	Bisanthene		EMLG					
	Pd(110)	LUMO	HOMO	Map A				Map B	
$h\nu$	25	35	35	23	40	60	85	60	85
α_{best} (°)	48	51	52*	42	51	45	51	48	42
$\frac{\Delta k_{\epsilon\parallel k_f}}{2}$ (Å^{-1})	0.045	0.042	0.064	0.042	0.063	0.077	0.106	0.079	0.096

Table 6.2: Results of incidence-angle-dependent POT
Investigated systems (benzene/Pd(110), bisanthene/Cu(110), and EMLG/SiC(0001)) and used photon energies in eV. Incidence angles α_{best} of I_α maps determined with best agreement to the $I_{\boldsymbol{\epsilon}\parallel\boldsymbol{k}_f}(k_x, k_y)$ maps. Data sets marked with * had technical artifacts (see Section 6.4.2). Maximum deviation from $\boldsymbol{\epsilon} \parallel \boldsymbol{k}_f$ condition evaluated by $\Delta k_{\boldsymbol{\epsilon}\parallel\boldsymbol{k}}\ (\alpha_{\max})/2$ (Eq. 6.3) given in Å^{-1}.

The evaluated, α_{best} of α =49° ± 3 ° allows to draw two important conclusions concerning already measured POT data. In ARUPS measurements using conventional systems, such as the Scienta SES-200 analyzer, the takeoff angle of the photoemitted electrons can only be changed by rotation of the sample. In normal emission, the direction of the incoming light beam is then fixed to 47°, e.g., at the machine located at University of Graz [237, 238], which matches our estimated α_{best}. Retrospectively, k maps measured by these systems and reported in the literature come close to the ideal $I_{\boldsymbol{\epsilon}\parallel\boldsymbol{k}_f}(k_x, k_y)$ maps.

This statement also applies to POT data measured with the TEA to some extent, because the typical incidence angle was set to α = 40° [AH3, AH6, 32, 34, 35, 238]. Although this value is not within the estimated range of $\alpha = 49° \pm 3°$, it is still reasonably close. We therefore infer that the already published data, which were up to date always compared to predictions using the PW final state, remain valid. Moreover, it should be considered in the future of upcoming ARUPS and POT measurements to use $\alpha \approx 49°$, if possible.

The results accomplished in this chapter focused on the acquisition and processing of experimental incidence-angle-dependent POT data to obtain $I_{\boldsymbol{\epsilon}\parallel\boldsymbol{k}_f}(k_x, k_y)$ maps. In a next step, these ideal experimental maps are to be compared to the Fourier transform of the molecule-substrate-system calculated by DFT[1]. This can be done in k space but could also lead to valuable information about the real-space periodicity of particular orbitals. In fact, the most intriguing question will be whether the $I_{\boldsymbol{\epsilon}\parallel\boldsymbol{k}_f}(k_x, k_y)$ map will yield a "better" wave function in contrast to sophisticated mathematical models.

[1] This task is currently subject of a Master's thesis prepared in the group of P. Puschnig (University of Graz).

7 | Final State Descriptions for Photon-Energy-Dependent POT

In this chapter, the POT technique is applied to two different graphene samples, which are – in comparison to typical samples investigated with POT– not molecular but two-dimensional systems. POT data are recorded in a large photon energy range employing a synchrotron beamline with absolute photon flux calibration, which allows to draw conclusions regarding the nature of the final state.

Parts of the experimental data of one sample (QFMLG) are discussed in the following journal article: C. S. Kern, **A. Haags**, X. Yang, H. Kirschner, A. Gottwald, M. Richter, U. De Giovannini, A. Rubio, M. G. Ramsey, F. C. Bocquet, S. Soubatch, F. S. Tautz, P. Puschnig, S. Moser, "Simple extension of the plane-wave final state in photoemission: Bringing understanding to the photon-energy dependence of two-dimensional materials", Phys. Rev. Research **5**, 033075 (2023) [AH12] with a strong focus on the theoretical approaches to approximate the experimental data.

My contribution to this work was the measurement of photon-energy-dependent POT data, their normalization according to Section 2.4.7, and preparation for further data processing steps that were performed by S. Moser (Julius-Maximilians-Universität, Würzburg). POT experiments were conducted together with colleagues from Karl-Franzens-Universität in Graz, Forschungszentrum Jülich, and Physikalisch Technische Bundesanstalt Berlin. Theoretical contribution of the PWA was provided by P. Puschnig (Karl-Franzens-Universität, Graz, Austria), TDDFT data by C. S. Kern (Karl-Franzens-Universität, Graz, Austria), and SWA calculations by S. Moser (Julius-Maximilians-Universität, Würzburg). The samples were prepared by S. Wolff from the group of T. Seyller (Technische Universität Chemnitz).

7.1 Introduction

In literature, POT has so far mainly been utilized to study the orbitals of molecules on metal surfaces, in particular revealing details of molecule-substrate interfaces. To only name a few applications, the hybridization of molecular states with the substrate [239, 240], intermolecular band dispersion assisted by interaction with the substrate [241–243], the geometry and orientation of molecules on the surface [AH10, 236, 244], or the identification of reaction products [AH3, AH9, 35] were explored with POT. The investigations of 2D k maps were highly successful to date and could even be expanded into the third dimension in reciprocal space [11, 18, 19, 22, 245]. In these cases, the interaction among the adsorbed molecules and with the substrate was relatively weak so that the electronic properties of the entire layer could be adequately approximated by a single molecule. That the plane-wave final state in general reproduces the k_x-k_y distribution of extended 2D materials such as graphene sufficiently well has been predicted in a theoretical study [246].

In 2015, Weiss et al. [22] measured the photoemission from PTCDA LUMO and HOMO orbitals with photon energies varied from 14 eV to 55 eV using a carefully calibrated photon source. With these data they succeeded to reconstruct the distribution of the corresponding wave functions in 3D – in reciprocal and real space. Comparing their results to PWA-based calculations, they found that the normalized photoemission intensities of the main lobes of LUMO and HOMO in the k maps are overall well-captured. However, in the experimental data they observed additional intensity resonances at $k_z \approx$ 1.30 Å^{-1} and 2.30 Å^{-1}, exposing a clear deviation to simulated results obtained on the basis of the plane-wave final state. They assigned these resonances to photoelectron diffraction, final state resonance (so-called shape resonance) effects or a correlation to the adsorption height of the molecule [22]. Employing advanced theoretical models which correctly describe these modulations would aid to understand their physical origins.

In order to get an in-depth understanding of photon-energy-dependent final-state interference effects, we minimize the impact of aspects mentioned, e.g., interaction between substrate and adsorbate or degree of scattering in the adsorbate layer, and facilitate the collaborative work between experiment and theory by investigating different graphene samples in this work.

Graphene is a well-studied system from an experimental and theoretical point of view for many years [247]. It is built from a honeycomb carbon lattice that can be described by only two atoms, i.e., containing two p_z orbitals in two sublattices. As a consequence, possible effects in the photoemission process can be reduced to the emission from a single p_z orbital, scattering at the neighboring carbon atoms and sublattices. Since no heavy scatterers are present, a homogeneous emission

is ensured. Additionally, in the case of quasifreestanding monolayer graphene (QFMLG), we choose a freestanding and incommensurate organic layer. As a consequence, scattering from the substrate does not add up coherently.

Due to these changes in the system in comparison to PTCDA on Ag(110) studied by Weiss et al. [22], it seems within reach to create an alternative theoretical model to the PWA that properly reproduces the experimentally-observed effects for graphene. POT data of three kinds of graphene grown on a 6*H*-SiC(0001) surface were measured in this work. However, the results of only two of them are discussed in this chapter due to no clear characterization of the third sample, quasifreestanding twisted bilayer graphene (QFtBLG). A selection of experimental band maps and k maps of QFtBLG is provided in Appendix D.

In this chapter, POT results of epitaxial monolayer graphene (EMLG) and QFMLG are presented. Side view models of both samples are pictured in Fig. 7.1. The EMLG sample is composed of a monolayer graphene on top of a graphene-like honeycomb structure of carbon atoms still covalently bonded to the Si atoms of the SiC crystal. This electronically inactive [234] so-called zero-layer graphene (ZLG) or "buffer layer" in literature is composed of sp^2 and sp^3 hybridized C atoms and indicated by "Z" in Fig. 7.1**a**. Noteworthy, the EMLG layer lies 5.76 Å above the top atomic layer of SiC bulk (and 3.40 Å above ZLG) [248, 249], however, it is not electronically decoupled from the underlying substrate [247].

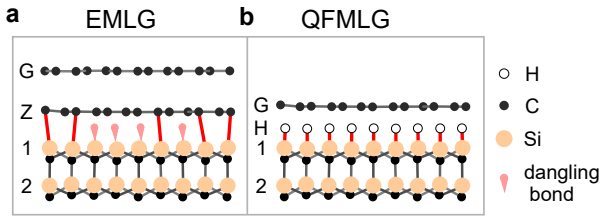

Figure 7.1: Side view models of EMLG and QFMLG
Side view models of **a** epitaxial monolayer graphene (EMLG) and **b** quasifreestanding monolayer graphene (QFMLG). Covalent bonds within the graphene sheets and the SiC bulk are indicated in gray. "G" denotes graphene layers, "Z" the zero-layer graphene (ZLG), and "H" hydrogen atoms from the intercalation. The numbers mark the first and second Si-C bilayers of 6*H*-SiC(0001). Adapted from Ref. [234].

To achieve a decoupling of the graphene layer and to reduced the impact of the SiC substrate onto its electronic structure as well as on the scattering of the photoelectrons by the substrate, one can intercalate the EMLG sample with hydrogen. The distance between the so-obtained freestanding monolayer graphene and the uppermost Si atoms then yields (4.22 ± 0.06) Å according to NIXSW measurements [249]. In combination with DFT calculations, the interaction between QFMLG and the underlying SiC substrate is finally identified as solely of van der Waals type [249]. The incommensurability of the graphene layer is particularly important to minimize the effect of the scattering by the substrate on the photoemission signal from the graphene.

Using graphene instead of a molecular PTCDA film (Weiss et al. [22]) has one major advantages considering the prevention of possible deviations from the PW final state distribution. Namely, any contribution of the substrate due to chemical interactions with the adsorbed layer to the photoemission signal is avoided by decoupling the top graphene layer in QFMLG. This concerns especially potential scattering effects of the photoemitted electrons at the substrate. Thus, one can, on the one hand, simplify the theoretical model and, on the other hand, use higher level theoretical approaches such as TDDFT of a freestanding (graphene) layer as a realistic model for the system. TDDFT can thus provide an independent verification of experimental and theoretical results although being more costly.

This chapter is structured in the following way. First, the sample preparation of EMLG and QFMLG is explained in Section 7.2 followed by the experimental band maps of both samples (Section 7.3). Section 7.4 gives an overview of all measured photon-energy-dependent POT data sets. Experimental photon-energy-dependent POT data of EMLG and QFMLG recorded at two energies are shown and compared in Section 7.5. This is followed by the experimental and theoretical data of QFMLG recorded at a third energy published in Ref. [AH12] (Section 7.6).

7.2 Sample preparation

The preparation of EMLG and QFMLG is well-documented in literature [249–252]. The samples used in this work have been prepared by S. Wolff from the group of T. Seyller at Technische Universität Chemnitz.

Both graphene samples are prepared on a Si-terminated 6*H*-SiC(0001) surface. First, the SiC surface is thermally decomposed. The remaining C atoms arrange in a honeycomb-structure, which is commonly called zero-layer graphene (ZLG or Z) or bufferlayer [250, 251]. Since some of its atoms are sp^3 hybridized and bond covalently to Si atoms of SiC, there is no typical linear dispersion of its π bands

at E_F that would typically manifest a true graphene layer.

Upon further annealing, the next SiC bilayer beneath ZLG decomposes. Si atoms evaporate, while the residual C atoms form a honeycomb-structure beneath the initial ZLG. This new ZLG thus splits off the initial ZLG further up from the bulk SiC. The bonds in the top ZLG restructure resulting in sp^2 hybridized C atoms. The layer facing the vacuum is called EMLG, having typical properties of graphene. The second layer between EMLG and the top SiC layer is again a ZLG with dangling bonds to SiC as depicted in Fig. 7.1**a**.

The preparation of QFMLG again starts with the initial ZLG/SiC sample, which is annealed up to 550°C in hydrogen atmosphere (880 mbar). As a consequence, ZLG is intercalated with hydrogen atoms. The latter break the residual covalent bonds between ZLG and the Si atoms in the topmost SiC bilayer as indicated in Fig. 7.1**b**. The previously sp^3 hybridized C atoms from the former ZLG rehybridize and are now referred to as QFMLG. NIXSW studies showed that the QFMLG layer very weakly interacts with the underlying substrate, but remains slightly p doped [234, 253]. Such a prepared graphene sheet is closest to an ideal freestanding graphene layer and therefore best-suited for comparison with model simulations of a freestanding graphene layer.

After the preparation of the two samples, they were transported in air from the preparation apparatus into an analysis chamber in order to characterize the sample properties. The sample quality, i.e., the chemical structure and electronic characteristics, was verified by LEED and XPS by S. Wolff. For the POT experiments, the samples were again transferred through air to the synchrotron-based facility at MLS in Berlin. Prior to the measurements, the samples were outgased in ultra-high vacuum ($\approx 10^{-10}$ mbar) at ≈ 350°C for 30 min.

7.3 Band maps

Figure 7.2 depicts the experimental band maps of EMLG and QFMLG measured at the MLS in Berlin. The measurements are performed using photon energies of $h\nu = 35$ eV and 87 eV for EMLG shown in Fig. 7.2**a** and **b**, respectively, and $h\nu = 45$ eV for QFMLG in **c**. Fig. 7.2**d** presents a sketch of the first and second Brillouin zones (BZ) of the graphene lattice to illustrate the $\overline{\Gamma}$–$\overline{\mathrm{M}}$ (red) and $\overline{\Gamma}$–$\overline{\mathrm{K}}$ (blue) directions in which the band maps were measured. In the band maps, the Fermi level E_F is indicated by solid white lines, while the dashed white lines correspond to the energies at which photon-energy-dependent k map sets were recorded.

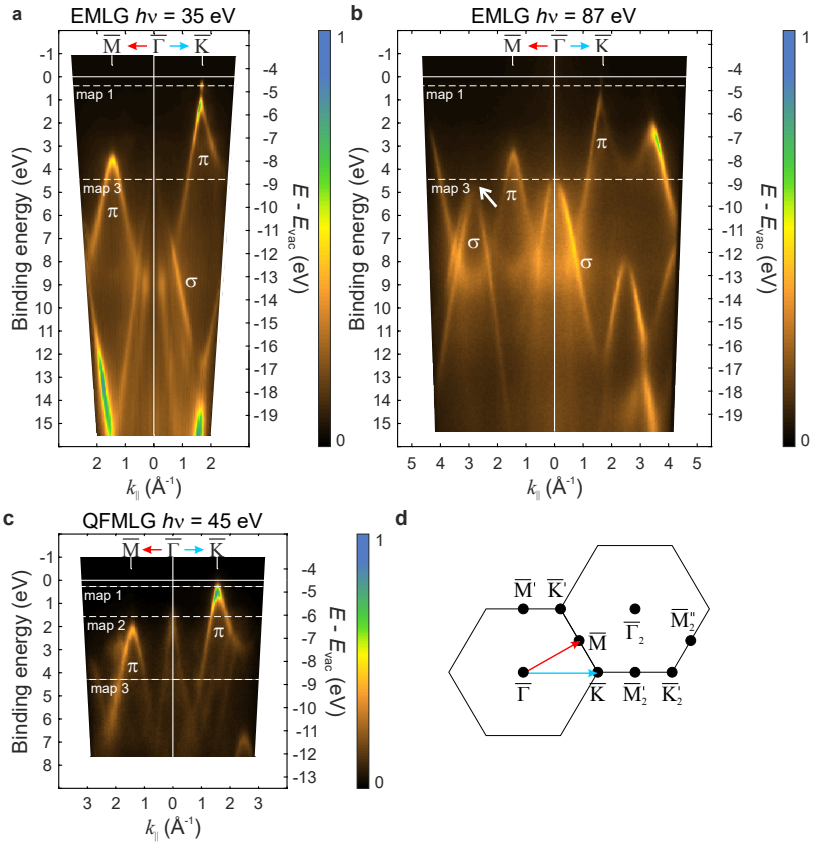

Figure 7.2: Band maps of EMLG and QFMLG
Band maps of **a** EMLG, $h\nu = 35$ eV, **b** EMLG, $h\nu = 87$ eV, and **c** QFMLG, $h\nu = 45$ eV. The y-scale shows the binding energies $E_\mathrm{b} = E_\mathrm{F} - E_\mathrm{kin}$ on the left and $E - E_\mathrm{vac} = h\nu - E_\mathrm{kin}$ on the right side. The left (right) sides of the band maps show the band map along the $\overline{\Gamma}$–$\overline{\mathrm{M}}$ ($\overline{\Gamma}$–$\overline{\mathrm{K}}$) directions recorded in backward emission ($\theta < 0°$). The white solid lines denote the Fermi edge E_F and the white dashed lines the energies where photon-energy-dependent POT series of maps 1–3 have been measured. **d** Sketch of the first and second Brillouin zones (BZ) of the graphene lattice. $\overline{\Gamma}$–$\overline{\mathrm{M}}$ and $\overline{\Gamma}$–$\overline{\mathrm{K}}$ directions of the band maps are indicated by red and blue arrows, respectively.

In our setup, however, the calibration of E_F is difficult for both samples. We therefore set E_F at the abrupt intensity depletion at the $\overline{K}$ point, where consequently $E_b = 0$ eV. Nevertheless, the sample's interaction with SiC [234] gives rise to the electronic structure depending on whether the π band crossing is above, at, or below E_F.

In the case of EMLG, E_F is located about 420 meV [234] (400 meV [253]) above the Dirac point. According to literature, this n doping is caused by the influence of ZLG located between EMLG and SiC [234]. In our measurements (Fig. 7.2**a**, **b**), E_F is located above E_D proving that we indeed measure EMLG.

After hydrogen intercalation, we still see the linearly dispersing π bands of graphene in the band map (Fig. 7.2**c**), but the energetic position of E_D has changed in comparison to EMLG. Thus, we conclude that hydrogen intercalation leads to a strong change in the energy level alignment of the sample and the graphene layer is found to be p doped. This is in accordance with literature, meaning that E_F is now shifted below E_D by about 100 meV [234]/ 240 meV [253]. This indicates that the previously covalently bound carbon layer is now decoupled from the substrate.

7.4 Overview of measurements

The measured photon energy ranges for POT data recorded at different energies $E - E_{vac} = h\nu - E_{kin}$ for both samples are summarized in Tab. 7.1. Three different $E - E_{vac}$ are measured referred to as map 1, 2, and 3 according to increasing energies. All k maps shown in this chapter are produced by integrating the photoemission intensity in an energy range of (0.30 $\pm$ 0.02) eV with the averaged $E - E_{vac}$ noted in Tab. 7.1.

Photon-energy-dependent POT of EMLG is measured in normal incidence (NI) geometry at two different energies, namely $E - E_{vac} = 4.74$ eV (map 1) in a photon energy range of 15 eV to 107 eV and 8.89 eV (map 3) in a range of 45 eV to 111 eV. The data are shown and discussed in Section 7.5. Additionally, a photon-energy-dependent POT series is recorded at $E - E_{vac} = 7.90$ eV. At this energy, the k maps show a fairly complicated pattern which is difficult to analyze. The normalized experimental k maps are shown in 5 eV photon energy steps in Appendix D.

For QFMLG, photon-energy-dependent POT is measured at three different energies. The data of map 1 are recorded at $E - E_{vac} = 4.76$ eV in a photon energy range of 20 eV to 111 eV. The data of map 3 are measured at $E - E_{vac} = 8.53$ eV in a range of 25 eV to 111 eV. The data sets of both energies measured in NI geometry are shown and discussed in Section 7.5 in direct comparison to the data

of EMLG. The data set of map 2 is taken at $E - E_{\mathrm{vac}} = 6.06$ eV in a photon energy range of 21 eV to 96 eV in two different incidence geometries (NI, $\alpha = 0°$ and oblique incidence (OI), $\alpha = -45°$). The experimental data of map 2 are shown and compared to three different simulations of varying computational complexity in Section 7.6.

	Map 1		**Map 2**		**Map 3**	
	$E - E_{\mathrm{vac}}$ (eV)	$h\nu$ (eV)	$E - E_{\mathrm{vac}}$ (eV)	$h\nu$ (eV)	$E - E_{\mathrm{vac}}$ (eV)	$h\nu$ (eV)
EMLG	4.74	15 – 107	-	-	8.89	45 – 111
QFMLG	4.76	20 – 111	6.06	21 – 96	8.53	25 – 111

Table 7.1: Photon-energy-dependent POT data sets of graphene
Overview of presented photon-energy-dependent POT data sets of EMLG and QFMLG. All data were recorded in normal incidence (NI) ($\alpha = 0°$) geometry. The QFMLG series of map 2 was additionally measured in oblique incidence (OI) geometry ($\alpha = -45°$).

7.5 Experimental $h\nu$-dependent intensity distributions of EMLG and QFMLG

In this section, photon-energy-dependent k maps of EMLG and QFMLG recorded at energies of $E - E_{\mathrm{vac}} \approx 4.75$ eV (map 1) and at ≈ 8.70 eV (map 3) are directly compared to each other. This is done by tracing the intensity of particular emission features in the k maps. The normalization procedure is explained in Section 2.4.7.

The decisive difference between the EMLG and QFMLG samples is the interaction with the SiC substrate. Comparing the intensity distributions extracted for EMLG and QFMLG therefore allows to evaluate, which features may be attributed to considerable interactions between the top graphene layer and the SiC substrate.

Map 1: $E - E_{\mathrm{vac}} \approx 4.75$ eV

Figure 7.3 shows k maps of EMLG and QFMLG in the top and bottom row measured at $E - E_{\mathrm{vac}} = 4.74$ eV and $E - E_{\mathrm{vac}} = 4.76$ eV, respectively. In the k maps of both samples, the bright emission at $(k_{\overline{\Gamma}-\overline{\mathrm{K}}}, k_{\overline{\Gamma}-\overline{\mathrm{M}'}}) = (1.70, 0.00)$ Å^{-1} marked with white ellipses represents the Dirac point.

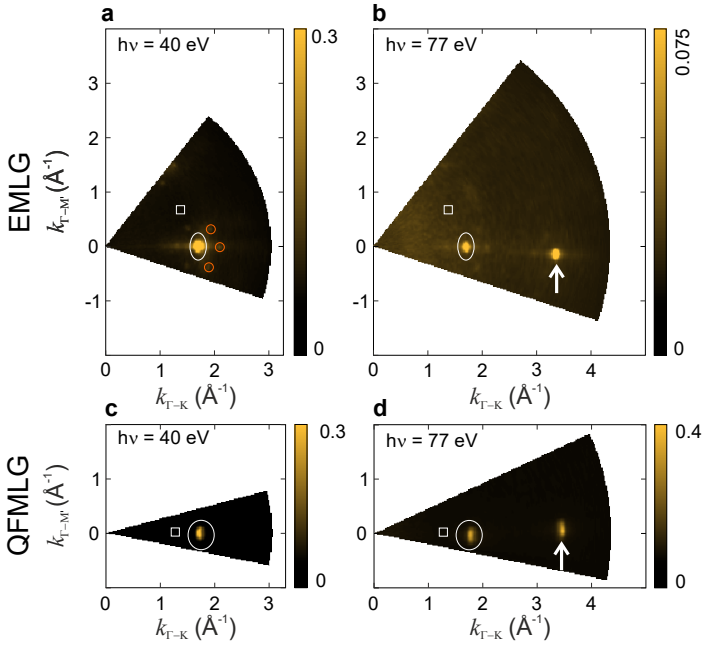

Figure 7.3: EMLG and QFMLG k maps measured at $E - E_{\mathrm{vac}} \approx 4.75$ eV Normalized k maps of **a**, **b** EMLG and **c**, **d** QFMLG recorded at the Dirac point $E - E_{\mathrm{vac}} = 4.74$ eV and $E - E_{\mathrm{vac}} = 4.76$ eV. The shown k maps are recorded at $h\nu = 40$ eV and 77 eV. The ROIs to trace the photoemission intensity are indicated by white ellipses. The rectangular areas are used to obtain a background intensity for the normalization procedure as explained in Section 2.4.7. The orange circles mark additional emission features originating from the $6\sqrt{3}$ reconstruction in EMLG. The white arrows mark the Dirac points at the $\overline{\mathrm{K}'_2}$ points.

In the case of EMLG (top row), the six weak spots surrounding this emission at the $\overline{\mathrm{K}}$ point originate from the $6\sqrt{3}$ reconstruction [234, 249]. Three of these spots are exemplary marked with orange circles in the k map recorded at $h\nu = 40$ eV. Due to

the hydrogen intercalation, these emission spots vanish for QFMLG [234] being an evidence that QFMLG is indeed decoupled from the substrate in agreement with the band maps (Fig. 7.2). If $h\nu > 49$ eV, the photoemission horizon also captures the emission at the $\overline{\mathrm{K}}_2'$ point in the second BZ marked with white arrows in **b**, **d**. The photoemission intensity from the Dirac points at $\overline{\mathrm{K}}$ and $\overline{\mathrm{K}}_2'$ in the graphene lattice are extracted by integrating and normalizing the intensity within the ROI taking into account the exposure time t, the photon flux F, and the background intensity (white rectangle in Fig. 7.3). The resulting intensity distributions are plotted in Fig. 7.4. To discern details at higher photon energies, some data are multiplied by a factor of three indicated by open symbols.

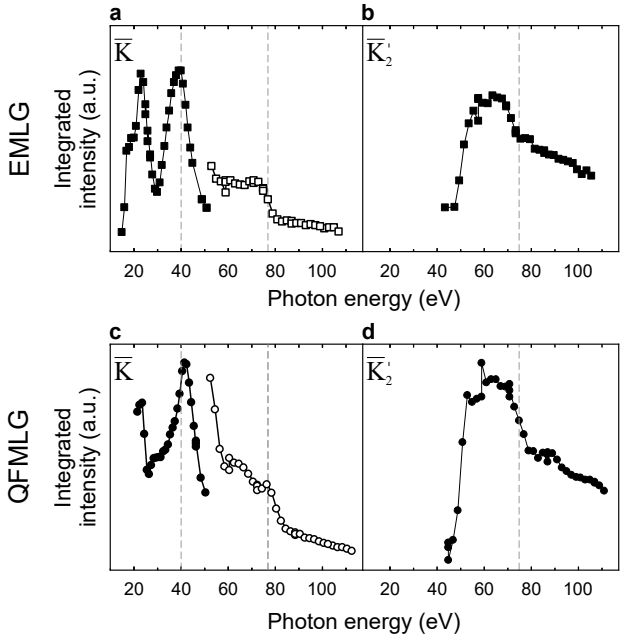

Figure 7.4: Intensity distributions for map 1 of EMLG and QFMLG
Normalized integrated intensities against photon energy extracted from k maps of EMLG and QFMLG measured at $E - E_{\mathrm{vac}}$ of 4.74 eV and 4.76 eV, respectively. Filled symbols are original data and open symbols are data multiplied by a factor of three. Intensity extracted at the $\overline{\mathrm{K}}$ point for **a** EMLG and **c** QFMLG. Intensity extracted at the $\overline{\mathrm{K}}_2'$ point for **b** EMLG and **d** QFMLG. Representative k maps recorded at the photon energies indicated by the gray dashed lines are shown in Fig. 7.3. The normalization of the data is described in Section 2.4.7.

In the case of the Dirac point emission in the first BZ of EMLG (Fig. 7.4**a**), the intensity increases, develops a shoulder at $\approx$ 20 eV before two peaks are observed at 23 eV and $\approx$ 40 eV. For larger photon energies, a monotonic decrease is observed. At $h\nu > 73$ eV, the intensity further reduces and finally stagnates.

For QFMLG, the intensity of the emission at the $\overline{\mathrm{K}}$ point (Fig. 7.4**c**) has a maximum at lowest $h\nu$. With rising photon energy, the intensity increases, establishes a shoulder at about 27 eV and peaks at 40 eV. Then it decreases steeply until reaching a plateau at $h\nu > 59$ eV. At $h\nu > 75$ eV, the intensity further decreases and stagnates for larger photon energies.

The intensity of the emission at the $\overline{\mathrm{K}_2'}$ point develops very similar for EMLG and QFMLG. In the case of EMLG (Fig. 7.4**b**), the intensity rises until it reaches a maximum at $\approx$ 59 eV that remains for about 10 eV. At $h\nu > 69$ eV, the intensity decreases, develops a shoulder at $h\nu \approx 81$ eV and finally weakens slowly. The intensity of the emission in QFMLG in panel **d** steeply rises until $h\nu \approx 53$ eV, stagnates for about 6 eV and rises again peaking at about 61 eV. The intensity drops at $h\nu > 71$ eV and a plateau in the energy range of 70 eV $< h\nu <$ 89 eV develops until it finally decreases again at larger photon energies.

The differences in the intensity distributions extracted at the $\overline{\mathrm{K}}$ points presented in Fig. 7.4 arise at $h\nu < 40$ eV. While in the case of EMLG, a defined peak is observed at $h\nu = 23$ eV with a shoulder at roughly 20 eV, a maximum of intensity is observed for QFMLG at small photon energies of $\approx$ 20 eV. Note that the two peaks observed for EMLG (at $h\nu = 23$ eV and 40 eV) are of similar intensity, while in the case of QFMLG the one at smaller photon energy is weaker compared to that at $h\nu = 40$ eV. Assuming that the observed peaks of EMLG and QFMLG at smaller photon energies have similar physical origins, we observe that if the graphene layer is electronically decoupled from the underlying substrate this peak shifts to slightly smaller photon energies and is reduced in intensity. Additionally, we observe that the peak at $h\nu = 40$ eV becomes broader and develops a shoulder at the low photon energy side.

The intensity distributions at the $\overline{\mathrm{K}}$ point for $h\nu \gtrapprox 60$ eV as well as at the $\overline{\mathrm{K}_2'}$ point shown in Fig. 7.4 are highly similar for both samples. On the one hand, one could agrue that the origin of these peaks cannot be attributed to the interaction between graphene and SiC, because we observe the same intensity distributions for EMLG and QFMLG. On the other hand, these similarities are observed at $h\nu \gtrapprox 60$ eV, where the penetration depth of the photon beam is larger. The contribution of the substrate to the measured photoemission signal could thus cover the photoemission from the graphene layer.

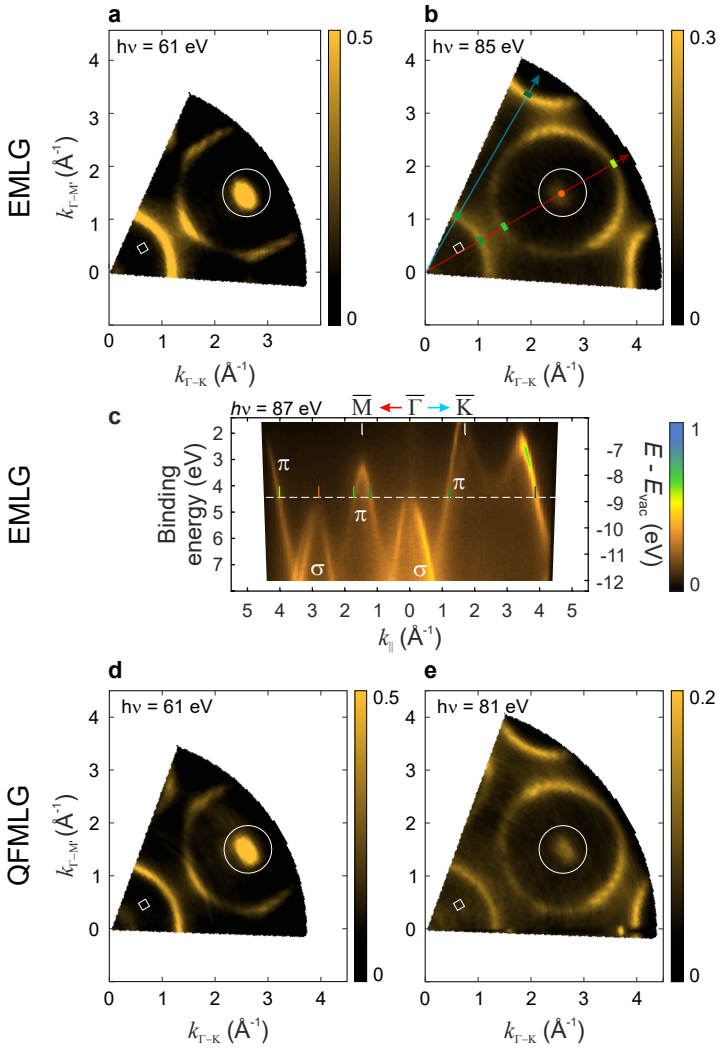

Figure 7.5: EMLG and QFMLG k maps measured at $E - E_{vac} \approx 8.70$ eV Normalized k maps of EMLG and QFMLG recorded at $E - E_{vac} = 8.89$ eV and $E - E_{vac} = 8.53$ eV, respectively. The k maps are recorded at **a** $h\nu = 61$ eV and **b** 85 eV (EMLG) and **d** $h\nu = 61$ eV and **e** 81 eV (QFMLG). The ROIs to trace the photoemission intensity are indicated by white ellipses. The white rectangular areas are used to obtain a background intensity for the normalization procedure. **c** Band map of EMLG replicated from Fig. 7.2**b** recorded at $h\nu = 87$ eV. Colored lines of varying shades of green in **b** and **c** indicate bands of π character. Orange color marks emission from σ bands.

Map 3: $E - E_{\mathrm{vac}} \approx 8.70$ eV

k maps of EMLG and QFMLG recorded at $E - E_{\mathrm{vac}} = 8.89$ eV and $E - E_{\mathrm{vac}} = 8.53$ eV are displayed in Fig. 7.5**a**, **b** and **d**, **e**, respectively. Panel **c** shows the band maps of EMLG in the two high-symmetry directions recorded at $h\nu = 87$ eV (replicated from Fig. 7.2**b**) in order to be able to allocate the emission intensities visible in the complicated k maps to particular bands. Therein different shades of green indicate emission from π bands, while the orange dot in **b** and the orange line in **c** mark emission from the same σ band.

The change of the emission intensity from the π bands with photon energy is fairly complicated. We therefore refuse to trace the emission intensity at this energy quantitatively. Instead, we intend to give a qualitative picture and correlate the emissions visible in the band maps to those in the k maps using the green lines in Fig. 7.5**b** and **c**. The emission intensity visible at smallest $k_{\parallel}$ values in the k maps are marked by dark green lines and visible in both high symmetry directions shown in the band map (panel **c**). The band map recorded in the $\overline{\Gamma}$–$\overline{\mathrm{M}}$ direction shows that this emission (marked in dark green) is the high-intensity branch of the Dirac cone within the first BZ. The other branch of the Dirac cone is less intense, in the second BZ, and marked with a green line in the band map and the k map shown in Fig. 7.5**b** in the case of EMLG. In the k maps of QFMLG (Fig. 7.5**d**, **e**) the intensity ratio between these two branches of the Dirac cone is different, i.e., at $h\nu = 61$ eV (panel **d**) the branches are of approximately the same intensity, while at $h\nu = 81$ eV (panel **e**) the branch at smaller $k_{\parallel}$ is more intense. Following the $\overline{\Gamma}$–$\overline{\mathrm{M}}$ direction in the k maps (red arrow in panel **b**), the subsequent emission intensity visible is the top of the σ band located in the center of the second BZ ($\overline{\Gamma_2}$ point, see sketch in Fig. 7.2**d**). The circular π band emission around this $\overline{\Gamma_2}$ point has a discontinuous intensity distribution, where at smaller photon energies the intensity is enhanced at the $\overline{M}$ point between the first and second BZ while at higher photon energies (e.g., $h\nu > 80$ eV) the emission is more intense at the corresponding $\overline{M}$ points between the second and third BZ, e.g., the $\overline{M_2''}$ point (see Fig. 7.2**d**). Its intensity distribution is shown in more detail using more experimental k maps at different photon energies in Appendix D.

Although the change in the π band emission intensity is highly interesting, it is not easily traceable. In contrast, it is feasible to trace the emission intensity of the top of the σ band (orange dot in Fig. 7.5**b**). This is done by integrating the emission intensity of the k maps within the ROI indicated by the white ellipses in Fig. 7.5. Extracting and normalizing the photoemission intensity from the σ band at this energy results in the distributions shown in Fig. 7.6. The vertical dashed lines mark the energies of the k maps shown in Fig. 7.5. For both samples, only one peak is observed at $h\nu = 61$ eV. This can on the one hand be associated with the

larger photon energies $h\nu \gtrapprox 60$ eV or the large $k_\parallel$ position (note that the emission from the Dirac point at $\overline{\mathrm{K}_2'}$ is very similar for EMLG and QFMLG in Fig. 7.4**b**, **d**). On the other hand, the comparable intensity distributions could mean that their origin is independent from the interaction between the top graphene layers and the underlying ZLG and/or substrate.

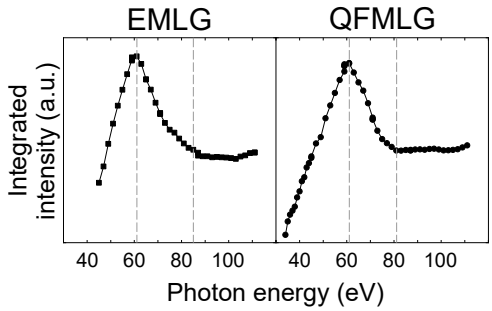

Figure 7.6: Intensity distributions for map 3 of EMLG and QFMLG
Normalized integrated intensities within the ROI indicated by white ellipses in Fig. 7.5 against photon energy extracted from k maps of **a** EMLG and **b** QFMLG measured at $E - E_{\mathrm{vac}}$ of 8.89 eV and 8.53 eV, respectively. The vertical dashed lines mark the energies of the k maps shown in Fig. 7.5.

The direct comparison of photon-energy-dependent experimental POT data of EMLG and QFMLG allows to assign particular features in the intensity distributions to the properties of the two samples. Discrepancies in the intensity distributions can hence be attributed to differences in the sample systems, namely mainly the interaction between the top graphene layer and the SiC substrate. While in QFMLG that top layer is above a decoupling hydrogen layer, the top graphene layer in EMLG is above zero-layer graphene and still electronically influenced by the SiC substrate. According to our experimental intensity distributions, the underlying SiC is thus still influencing the photoemission signal from π bands in the first BZ and accordingly small $k_\parallel$ position for $h\nu \lessapprox 60$ eV. There is, however, no substantial difference observed in the photoemission intensity at higher photon energies, emission from σ bands and/or an emission outside of the first BZ of graphene. Note however that the traceable emission from the σ band in the second BZ at this $E - E_{\mathrm{vac}}$ only arises at $h\nu \gtrapprox 40$ eV. Also it is important to note that at higher photon energies, the penetration depth of the photon beam is increased which reduces the surface sensitivity. Any photoemission intensity recorded at large photon energies is thus dominated by the contribution from deeper lying layers, i.e., the substrate.

7.6 SWA: A simple extension of the plane-wave final state

For QFMLG, two additional photon-energy-dependent data sets were recorded at $E - E_{\mathrm{vac}} = 6.06$ eV, i.e., about 1.35 eV below the Dirac point E_{D} in two different experimental geometries: One in normal incidence (NI, $\alpha = 0°$) and another in oblique incidence (OI, $\alpha = -45°$). While in the previous section 7.5 experimental data are solely presented and integrated intensity distributions of two samples are compared, the experimental k maps recorded at $E - E_{\mathrm{vac}} = 6.06$ eV (map 2) are compared to theory. The results are published in Ref. [AH12].

The used experimental geometries are sketched in Fig. 7.7**a**, **b** for NI and OI, respectively. The direction and polarization of the incoming photon beam is indicated by the yellow lines.

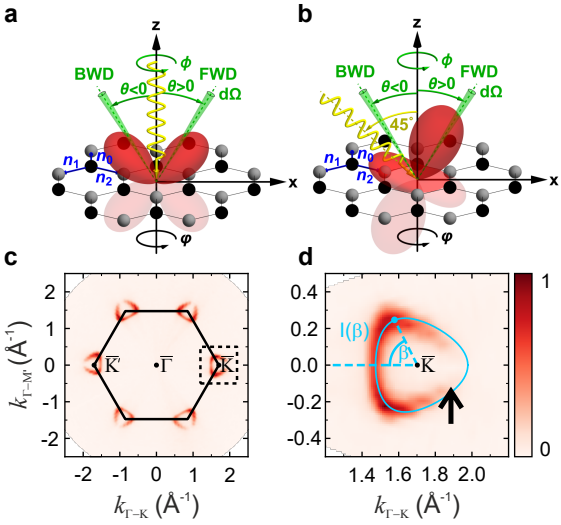

Figure 7.7: Experimental geometries and QFMLG k maps
Experimental geometries of **a** normal incidence (NI, $\alpha = 0°$) and **b** oblique incidence (OI, $\alpha = -45°$). See text for details. **c** Overview and **d** zoom-in experimental k maps of the characteristic horseshoe patterns of QFMLG at $E - E_{\mathrm{vac}} = 6.06$ eV. The black solid line indicates the first BZ of graphene and the dashed black line in **c** denotes the area shown in **d**. The light blue line in **d** indicates the trajectory and angle β (blue) along which the emission intensity is extracted for Fig. 7.9.

Positive and negative emission angles θ are defined as forward (FWD) and backward (BWD) emission directions, respectively, counting from the sample normal and taking the direction towards the light source as negative. The black and gray spheres represent the two sublattices of graphene connected by the vectors $\boldsymbol{n}_j$. Angle-resolved detection in $d\Omega$ around inclination θ and azimuth ϕ is illustrated in green. The red lobes visualize the angular distributions of the pure emission from the d channels, d^2_{NI} and d^2_{OI}, respectively.

In the experiment with the TEA, only photoelectrons emitted into the (x, z) plane, where $\phi = 0$, are detected. To obtain the k maps shown in Fig. 7.7**c**, **d**, the sample is rotated around the z axis varying φ simultaneously measuring in backward emission direction (BWD, $\theta < 0°$) and in forward emission direction (FWD, $\theta > 0°$). θ correspondingly depicts the emission angle as visualized in Fig. 7.7**a**, **b**. Naturally, in NI geometry the BWD and FWD emission directions are symmetric. In OI geometry, the polarization vector $\boldsymbol{\epsilon}$ is still perpendicular to the photon k vector, but the emission direction in respect to the polarization varies between BWD and FWD.

At $E - E_{\mathrm{vac}} = 6.06$ eV, the k maps show a redistribution of spectral weight within graphene's characteristic *horseshoe signatures* centered at the $\overline{\mathrm{K}}$ and $\overline{\mathrm{K}'}$ points as visible in Fig. 7.7**c**, **d**. In the experiment, we observe that the intensity along the light blue trajectory marked in the k map in Fig. 7.7**d** varies with the kinetic energy. This is shown in seven experimental representative k maps measured at varying kinetic energies in NI geometry in Fig. 7.8. The visible inhomogeneous intensity distribution of the horseshoe arises from the structural interference of the initial state Bloch wave that is scattered at the two sublattices of graphene. Therefore, this emission feature is characteristic for a honeycomb lattice.

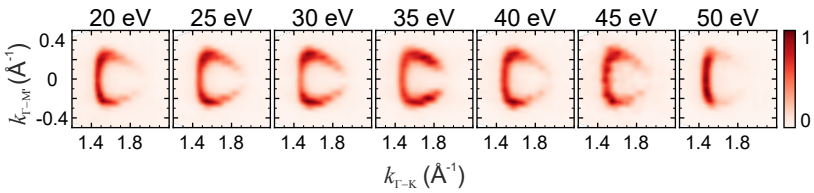

Figure 7.8: k maps of graphene's horseshoe measured at different E_{kin}
Experimental horseshoe patterns recorded at one fixed $E - E_{\mathrm{vac}} = 6.06$ eV. The photon energy is changed leading to k maps measured for different kinetic energies E_{kin} of the emitted photoelectrons.

The intensity suppression around the light blue trajectory indicated by the black arrow in Fig. 7.7**d** is commonly referred to as *dark corridor*. It emerges due to the relative geometric phases $\vartheta_{\boldsymbol{k}} = \arg \sum_{j=0}^{2} e^{i\boldsymbol{n}_j \cdot \boldsymbol{k}}$ at graphene's lattice sites, where $\boldsymbol{n}_j$ connect neighboring carbon atoms, producing a structure factor $(1 + e^{i\vartheta_{\boldsymbol{k}}})$ that suppresses valence band intensity along this direction in k space (see Section 2.4.3).

To trace this intensity variation quantitatively, we extract the photoemission intensity along the trajectory shown in Fig. 7.7**d** as a function of the angle β, which corresponds to the different positions along the horseshoe. This is performed for the k maps measured at different kinetic energies between 15 eV and 80 eV and plotted against E_{kin}. The resulting experimental intensity distributions are shown in the leftmost column of Fig. 7.9**a**–**c** for NI geometry (**a**) and OI geometry in BWD (**b**) and FWD (**c**). For NI (**a**), discernible photoemission intensity only appears below $E_{\text{kin}} \lessapprox 50$ eV. It accumulates in two streaks at $\beta \approx \pm\, \pi/3$, while a homogeneous intensity distribution is observed between these streaks at 20 eV $\lessapprox E_{\text{kin}} \lessapprox$ 44 eV. Between 30 eV and 40 eV, the emission shifts to higher angles $\beta = \pm\, 2\pi/3$, which is attributed to nearest-neighbor final state scattering [AH12]. Both data sets recorded in OI geometry (Fig. 7.9 **b**, **c**) show a more homogeneous intensity distribution that is confined to smaller angles in BWD (**b**). In comparison to NI, the emission intensity now reaches up to $E_{\text{kin}} \approx 60$ eV with a suppression around 44 eV in BWD (**b**).

The experimental data are compared to results of three different theoretical approaches, namely the plane-wave approximation (PWA), time-dependent density functional theory (TDDFT), and the scattered-wave approximation (SWA), shown in the other three columns of Fig. 7.9. Details about the methods can be found in Section 2.4 and Ref. [AH12].

The results based on the PWA are shown in the second column of Fig. 7.9. It predicts a monotonous decay of intensity with no intensity redistribution around the horseshoe with increasing E_{kin}. The rich experimental structure is thus not reproduced. Importantly, the polarization factor $|\boldsymbol{\epsilon} \cdot \boldsymbol{k}_f|^2$ of the PWA incorrectly forecasts an absent photoemission intensity in the OI-BWD geometry (**b**), where the photoemission occurs (nearly) perpendicular to the polarization vector of light.

In contrast, the simulations of TDDFT (third column of Fig. 7.9) are in striking agreement with the experimental observations apart from an overall ≈ 3 eV kinetic energy shift with respect to the experiment. In the simulations, no substrate was considered but solely a perfectly flat, freestanding graphene layer. Detailed information about the settings in the TDDFT approach are described in the SI of Ref. [AH12].

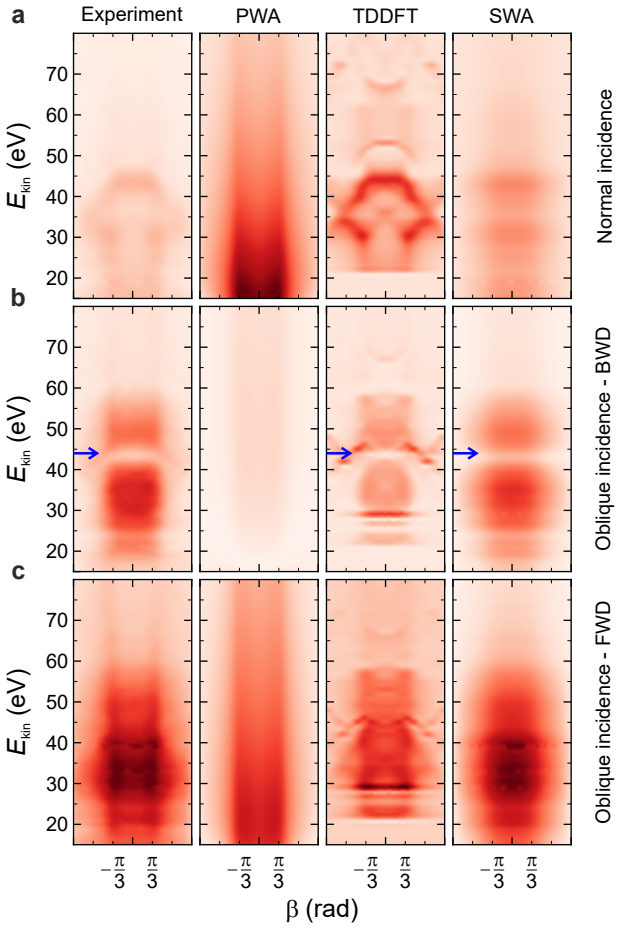

Figure 7.9: E_{kin} dependent emission intensity around the horseshoe Intensity profiles of horseshoe extracted along the light blue line in Fig. 7.7**b** and plotted vs. β for kinetic energies between 15 eV and 80 eV from experimental data (1st column) in comparison to theoretical data from PWA (2nd column), TDDFT (3rd column, shifted by 3 eV), and SWA (4th column) calculations without nearest-neighbor scattering. **a** NI, **b** OI-BWD, and **c** OI-FWD. The relative intensity of each column is printed to scale, while the scaling between the columns is arbitrary. The arrows in **b** mark the prominent intensity depletion at $E_{\mathrm{kin}} = 44$ eV.

The experimentally observed structures in the the photoemission intensity distribution can therefore not be explained by, e.g., hybridization with the substrate, photoelectron scattering from the underlying substrate atoms, or buckling of the graphene layer. As TDDFT, however, accurately models graphene's surface potential, it also fully accounts for scattering of the outgoing photoelectron in the graphene lattice itself. The overall offset of the surface potential calculated with TDDFT is due to the absent SiC substrate and explains the 3 eV shift in E_{kin} in comparison to the experiment.

Yet, it is not possible to understand the physical origin of the simulated photoemission intensity from the TDDFT simulation due to its computational complexity. It would be, however, particularly informative if a simple and intuitive connection between the intensity distribution and the initial state would be accessible.

7.6.1 Scattered-wave approximation

The desired simple and intuitive connection between the intensity distribution and the initial state is achieved in our recently developed SWA model (see Section 2.4.3), which provides an improved model for the final state. Therein, scattering effects are included via angular-momentum-dependent and kinetic-energy-dependent phase shifts between partial waves of the outgoing Coulomb wave [94]. This allows to model kinetic-energy-dependent interference effects in the final state between the two dipole-allowed $l \pm 1$ partial wave channels. Similar ideas were already used to simulate the photoemission from gas phase molecules [41, 84, 85, 93], but were formally extended to periodic systems for the first time in our publication [AH12] to simulate the photoemission data of the horseshoe of graphene observed experimentally (Fig. 7.9 first column). To this end, we employ the Bloch nature of the initial state as well as, in a second step, additionally nearest-neighbor Coulomb scattering of the outgoing photoelectron.

As a result, we can describe the photoemission intensity from the C $2p_z$-derived valence band of graphene by

$$\begin{aligned} I(k_f, \Omega; h\nu, \boldsymbol{\epsilon}) &\propto |M_{\boldsymbol{k}_f,\boldsymbol{k}}|^2 \\ &= \delta_{\boldsymbol{k},\boldsymbol{k}_{f\parallel}} \left| \boldsymbol{\epsilon} \cdot \boldsymbol{M}_{210}(\boldsymbol{k}_f)(1 + e^{i\vartheta_{\boldsymbol{k}}}) \right|^2, \end{aligned} \tag{7.1}$$

where $\delta_{\boldsymbol{k},\boldsymbol{k}_{f\parallel}}$ describes momentum conservation modulo reciprocal lattice translations, and $(1 + e^{i\vartheta_{\boldsymbol{k}}})$ is the initial-state structure factor. Note that the $\boldsymbol{\epsilon} \cdot \boldsymbol{k}_f \times \mathcal{F}[\phi_{nlm}(\boldsymbol{r})](\boldsymbol{k}_f)$ term of the PWA used previously is now replaced by $\boldsymbol{\epsilon} \cdot \boldsymbol{M}_{nml}(\boldsymbol{k}_f)$.

Considering a C $2p_z$ orbital with quantum numbers $\{nlm\} = \{210\}$, the matrix element is then given by

$$\boldsymbol{M}_{210}(\boldsymbol{k}_f) \;=\; \underbrace{\widetilde{g}(k_f)\;\boldsymbol{Y}_{1,0,0}(\theta,\phi)}_{s\,\text{channel}} - \underbrace{\widetilde{f}(k_f)\;\boldsymbol{Y}_{1,2,0}(\theta,\phi).}_{d\,\text{channel}} \tag{7.2}$$

It includes the dipole selection rule as well as the corresponding angular distribution in the differential cross section for photoemission from C $2p_z$ orbitals. As indicated in Eq. 7.2, the complex-valued quantities $\widetilde{g}(k_f)$ and $\widetilde{f}(k_f)$ contain the k_f-dependent amplitude and phase of the s and d photoemission partial waves. They are determined by the effective on-site scattering potential. The vector spherical harmonics $\boldsymbol{Y}_{l,l\mp1,m}$ in Eq. 7.2 describe the photoemission angular distribution in these two channels, whose entries can be individually addressed by the principal components of the light polarization $\boldsymbol{\epsilon}$ [101].

In the next step, we take advantage of the two different experimental geometries used to measure the photoemission intensity. With this, Eq. 7.1 becomes

$$I_{\text{NI}} \;\propto\; |\widetilde{f}(k_f)|^2 d_{\text{NI}}(\theta,\phi)^2 |1 + e^{i\vartheta_{\boldsymbol{k}_{f,\parallel}}}|^2 \tag{7.3}$$

$$\begin{aligned} I_{\text{OI}} \;&\propto\; \big[|\widetilde{f}(k_f)|^2 d_{\text{OI}}(\theta,\phi)^2 + 8|\widetilde{g}(k_f)|^2 \\ &+\; 4\sqrt{2}|\widetilde{f}(k_f)||\widetilde{g}(k_f)| d_{\text{OI}}(\theta,\phi)\cos\Delta\sigma\big] |1 + e^{i\vartheta_{\boldsymbol{k}_{f,\parallel}}}|^2, \end{aligned} \tag{7.4}$$

Therein, the angular intensity distributions of the pure d channel is described as $d_{\text{NI}}(\theta,\phi) = \sin 2\theta\cos\phi$ and $d_{\text{OI}}(\theta,\phi) = 3\sin 2\theta\cos\phi + 3\cos 2\theta + 1$ for NI and OI geometry data. $\Delta\sigma = \arg(\widetilde{f}/\widetilde{g})$ denotes the relative phase between s and d partial waves.

In Eq. 7.3, we see no dependence of the photoemission intensity on $\widetilde{g}(k_f)$. The s channel is thus suppressed in the symmetric NI geometry data with the entire emission from the d channel symmetric in θ. In OI data, in contrast, the emission intensity emanates from the interference between the isotropic s and the anisotropic d channels.

Coming back to the comparison of experimental and SWA results, we can already now draw important conclusions from these equations without simulated any intensity distribution to be compared to the experiment. Namely, in our experimental measurements, only photoelectrons emitted into the (x,z) plane, where $\phi = 0$,

are detected as indicated in Fig. 7.7**a**, **b**. Inserting $\phi = 0$ in our definition for d_{OI}, we get that $d_{\mathrm{OI}}(\phi = 0, \theta)^2$ vanishes at $\theta_0^- \approx -29.3°$. The minus sign denotes BWD ($\theta < 0°$). Since the horseshoe is centered at the $\overline{\mathrm{K}}$ point of graphene, where $k_\parallel \approx 1.7$ Å^{-1}, we can calculate the corresponding E_{kin} for the estimated θ_0^- using $k_f = \sqrt{2mE_{\mathrm{kin}}}$ and $k_f = k_\parallel / \sin\theta_0^-$. We yield a kinetic energy E_{kin} of ≈ 44 eV. Looking at the experimental data in the first column of Fig. 7.9**b**, we indeed observe an intensity depletion at this E_{kin} marked by the blue arrow. It is assigned to a node in the d channel. This already proves the improved applicability of the SWA in contrast to the simple PWA. Note that the second root of $d_{\mathrm{OI}}(\phi = 0, \theta)^2$ appears in forward direction at $\theta_0^+ \approx 74.3°$, which corresponds to $E_{\mathrm{kin}} = 11.4$ eV. This is, however, outside of our measurement range and therefore cannot be verified experimentally.

To be able to calculate the expected intensity distributions in any geometry, we need to reconstruct the functions $|\widetilde{g}(k_f)|$ and $|\widetilde{f}(k_f)|$. This can be done using Eqs. 7.3 and 7.4. $|\widetilde{f}(k_f)|$ - the amplitude of the d channel - is obtained by dividing the experimental NI data from Fig. 7.9**a** at a fixed angle $\beta = 0$ by $\sin^2 2\theta$. The result is shown as blue curve in Fig. 7.10**a**.

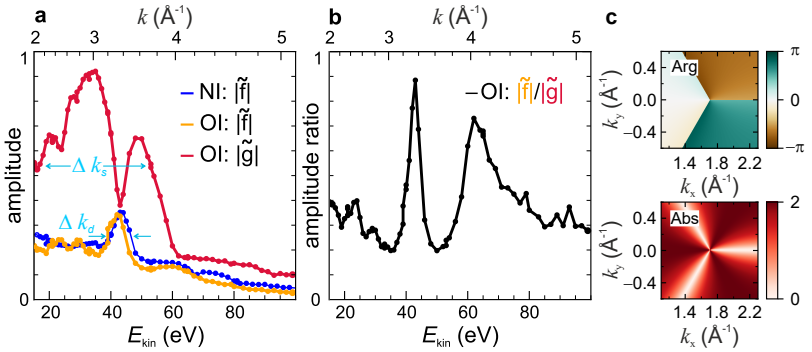

Figure 7.10: Photoemission into s and d channels as a function of E_{kin}
a Amplitudes $|\widetilde{g}|$ and $|\widetilde{f}|$ of the s and d channels and **b** their ratio in OI geometry plotted against the final-state E_{kin}. The curves were extracted from the experimental NI and OI data at $\beta = 0$, using the SWA without NN scattering. Positive real values were only obtained for in-phase photoemission in s and d channels, i.e., $\Delta\sigma = 0$. The width of the curves Δk_{s} and Δk_{d} indicated in blue in **a** give rise to the corresponding real-space distributions of the Coulomb partial waves. **c** Amplitude and phase of the nearest-neighbor scattering factor $(e^{-i\vartheta_{\boldsymbol{k}_{f\parallel}}} + e^{i2\vartheta_{\boldsymbol{k}_{f\parallel}}})$ that gives rise to the intensity redistribution around the horseshoe.

Doing the same for the two OI geometries BWD and FWD leads to two linearly independent equations for $I_{\mathrm{OI}}(k_f)$. We find positive real values for $|\widetilde{g}(k_f)|$ and $|\widetilde{f}(k_f)|$ (red and orange curves in Fig. 7.10**a**) for an in-phase emission of the two emission channels ($\Delta\sigma = 0$).

It is important to note here that $|\widetilde{f}(k_f)|$ obtained from the OI geometry data is in remarkably absolute agreement with that from the NI geometry (compare blue and orange curves in Fig. 7.10**a**). Without any scaling correction, this highlights the excellent photon flux calibration provided by the MLS in Berlin [53]. Fig. 7.10 **b** shows the ratio $|\widetilde{f}|/|\widetilde{g}|$. Accordingly, the s channel ($|\tilde{g}|$) is consistently predominant, except for E_{kin} of 43 eV and 63 eV, where the s and d channels are of the same order (or the d channel is larger).

These so-obtained radial cross sections $|\tilde{g}|$ and $|\tilde{f}|$ as well as the phase shift $\Delta\sigma = 0$ are inserted back into Eq. 7.1 to predict the horseshoe intensity distribution for any experimental configuration. The results are shown in the third column of Fig. 7.9 with those of OI geometry in solid agreement with the experimental data. The NI results based on the SWA model in this form deviate from the experimental data, particularly in the kinetic-energy-dependent modulation along β. This is overcome by including nearest-neighbor (NN) scattering in the final state taking into consideration the scattering of photoelectrons emitted from sublattice A into the Coulomb wave centered at one of the neighboring B sites. Eq. 7.1 then reads:

$$\begin{aligned} I(k_f, \Omega_{\boldsymbol{k}_f}; h\nu, \boldsymbol{\epsilon}) \;&\propto\; \Big|\boldsymbol{\epsilon}\cdot\boldsymbol{M}_{210}(\boldsymbol{k}_f)\times\big[1+e^{i\vartheta_{\boldsymbol{k}}} \\ &+\; \big(e^{-i\vartheta_{\boldsymbol{k}_{f\parallel}}}+e^{i\vartheta_{\boldsymbol{k}}}e^{i\vartheta_{\boldsymbol{k}_{f\parallel}}}\big)u(\boldsymbol{k}_f)\big]\Big|^2\delta_{\boldsymbol{k},\boldsymbol{k}_{f\parallel}}. \end{aligned} \tag{7.5}$$

Therein, an additional NN scattering factor $(e^{-i\vartheta_{\boldsymbol{k}_{f\parallel}}}+e^{i\vartheta_{\boldsymbol{k}}}e^{i\vartheta_{\boldsymbol{k}_{f\parallel}}})u(\boldsymbol{k}_f)$ emerges, which originates from the structural interference between initial *and* final state, both of which are scattered at the two graphene sublattices. Due to momentum conservation, this scattering factor reduces to $(e^{-i\vartheta_{\boldsymbol{k}_{f\parallel}}}+e^{i2\vartheta_{\boldsymbol{k}_{f\parallel}}})u(\boldsymbol{k}_f)$ which rapidly varies in β as depicted in Fig. 7.10**c**. On the photoemission hemisphere $\Omega_{\boldsymbol{k}_f}$, $u(\boldsymbol{k}_f)$ only varies slowly. At a given k_f, $u(\boldsymbol{k}_f)$ can therefore be approximated as a merely kinetic-energy-dependent fit parameter that is not momentum-vector-dependent. In this case, it is constant around the horseshoe, i.e., $u(\boldsymbol{k}_f) \approx |u(k_f)|e^{i\arg\, u(k_f)}$, while the suppressed valence band intensity along dark corridors in momentum space is a consequence of the scattering factor.

Fitting Eq. 7.5 under this assumption to our experimental data (Fig. 7.9**a**), we obtain the intensity distribution presented in Fig. 7.11**c** and the corresponding $u(\boldsymbol{k}_f)$ in Fig. 7.11**d**. The result displayed in Fig. 7.11**c** is very satisfactory

agreement with the experiment (**a**) and the TDDFT results (**b**). Importantly, the SWA with NN scattering reproduces the shift of the intensity to $\beta \approx \pm 2\pi/3$ in the kinetic energy range between 30 eV and 40 eV and also below 20 eV. Additionally, the concurrent depletion of the intensity in the interval $[-\pi/3, +\pi/3]$ is captured. These redistributions are a direct consequence of the minima and maxima of $|(e^{-i\vartheta_{\mathbf{k}_{f\parallel}}} + e^{i2\vartheta_{\mathbf{k}_{f\parallel}}})|$ at $\beta = \pm\pi/3$ and $\beta = \pm 2\pi/3$, respectively, as well as the maxima of $|u(k_f)|$ in these kinetic energy ranges. This proves that the essence of the observed intensity distribution, in both kinetic energy and k space, is well-reproduced, if the SWA and nearest-neighbor final-state scattering are combined ($\mathrm{SWA}^{\mathrm{NN}}$).

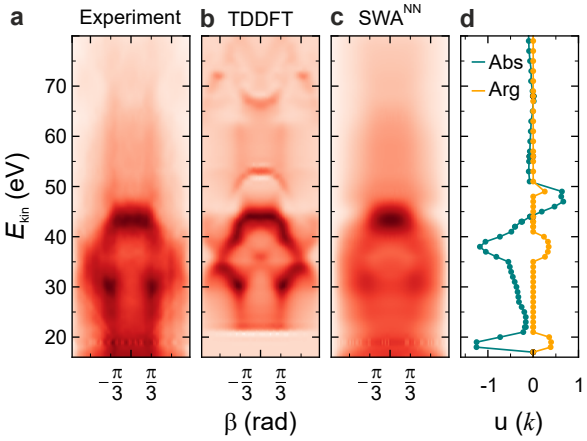

Figure 7.11: SWA with nearest-neighbor scattering
Photoemission intensity in the NI geometry replicated from Fig. 7.9**a** for **a** the experiment with a different contrast scaling and **b** TDDFT. **c** SWA prediction including nearest-neighbor (NN) final-state scattering. (d) k_f-dependent scattering amplitude and phase of $u(k_f)$ that fits the data in **a** best. For a compact display we have plotted Abs $\equiv |u| \times \mathrm{sgn}(\arg u)$ and Arg $\equiv \mod(\arg u, \pi)$.

Comparing the overall intensity distribution in β calculated with $\mathrm{SWA}^{\mathrm{NN}}$ (Fig. 7.11**c**) with those of the three experimental geometries in Fig. 7.9**a**–**c** shows that nearest-neighbor final-state scattering is most prevalent in the NI geometry. To a much lesser extent it is also present in the OI-FWD geometry, but in OI-BWD, where the intensity is mostly confined in the interval $[-\pi/3, +\pi/3]$, it is essentially absent. The geometry with dominant s channel (OI-BWD) consequently does not show NN scattering, while experimental geometries that

have significant d channel contributions [NI, OI-FWD, cf. Eqs. 7.3 and 7.4] do. This can be rationalized by the k_f dependences of the individual emission channels using Heisenberg's uncertainty principle $\Delta k \Delta r \geq \hbar/2$ and the estimated d and s wave resonances from Fig. 7.10 **a**. Using width of 0.3 Å^{-1} and 1.5 Å^{-1} results in real-space distributions of the corresponding Coulomb partial waves of the order $\Delta r_d \approx 1.7$ Å and $\Delta r_s \approx 0.3$ Å around the carbon nucleus. Considering a carbon-carbon distance of 1.42 Å, a significant overlap between partial waves emanating from nearest neighbors is thus only expected for the d channel.

7.7 Conclusion

In summary, we measured photon-energy-dependent POT data of EMLG and QFMLG at different binding energies as well as varying sample geometries using a well-calibrated photon flux calibration.

Comparing the photon-energy-dependent intensity distributions of the two samples directly shows no substantial difference at higher photon energies ($\gtrapprox 60$ eV), emission from σ bands and/or an emission outside of the first BZ of graphene. For fixed initial states of π character within the first BZ of graphene (Dirac point), however, the photoemission signal varies. This is attributed to the different properties of the two samples. While in QFMLG that top layer is above a decoupling hydrogen layer, the top graphene layer in EMLG is above zero-layer graphene and still electronically influenced by the SiC substrate.

The resonances observed in the intensity distribution for π states go beyond the prediction of the plane-wave final state approximation, which is also observed for the complex intensity distribution around the horseshoe at $E - E_{\mathrm{vac}} = 6.06$ eV. Instead, the surface-flux method within the framework of TDDFT reproduces the angle-resolved photoemission intensities of the horseshoe of QFMLG. In order to receive an intuitive physical picture behind the calculations, we used the SWA for the photoemission final state allowing for the interference of the dipole-allowed s and d photoemission channels. To simulate the photoemission from the C $2p_z$ derived valence band of graphene, we formally extended the SWA to a periodic system including the Bloch nature of the initial state and nearest-neighbor scattering of the outgoing photoelectron. Due to the excellent agreement of kinetic-energy-dependent photoemission intensities around the horseshoe of SWA and two experimental geometries (NI and OI), we were able to extract the amplitudes and phases of both s and d partial waves and show that their overlap between nearest neighbors is only expected for the d channel.

Since both computationally advanced methods, namely SWA^{NN} and TDDFT, to describe the intensity distribution along the horseshoe throughout consider a free-standing graphene layer, we can conclude that the observed modulations can not be explained by any hybridization of the graphene layer with the substrate, photoelectron scattering from the underlying substrate atoms, or buckling of the graphene layer. Looking back to the band map of QFMLG, it is important to notice that the horseshoe emission basically belongs to the same band as the Dirac point, only cut at another energy. Considering the findings from the SWA^{NN} calculations, we can therefore specify which sample properties lead to the varying intensity distributions observed for the Dirac points of EMLG and QFMLG. The resonances observed for the Dirac point of QFMLG can thus be attributed to nearest-neighbor scattering within the graphene layer in accordance with the SWA^{NN} calculations of the horseshoe. The shift of the resonances to smaller photon energies observed for EMLG can consequently be attributed to the interaction between the graphene layer and the underlying substrate, i.e., hybridization of the graphene layer with the substrate, photoelectron scattering from the underlying substrate atoms, or buckling of the graphene layer.

7.8 Outlook

The extracted kinetic-energy-dependent amplitudes and phases of the two partial waves s and d present a benchmark for *ab initio* theories that focus on a more sophisticated description of the photoemission process. This could especially aid to understand dichroism. Using the provided material in Ref. [AH12] along with Eqs. 7.1 and 7.2, one could also easily calculate the horseshoe intensities with arbitrary polarized light. These calculations could thus be used to absolutely calibrate the photon flux purely based on the photoemission response of the robust 2D material QFMLG in any photoemission measurement with variable photon energy and geometry. Or differently, complex kinetic-energy-dependent intensity modulations of other sample systems, such as layers of π conjugated organic molecules or (quasi-) 2D quantum materials could be understood with our SWA model providing an intuitive physical picture of the photoemission process.

8 | Summary and Conclusion

The main objective of this thesis was to verify the limits of POT and extend the technique's applicabilities. In particular, the following questions were formulated in the introduction: (1) Is POT applicable to a broader range of electronic states, particularly σ orbitals and bent π systems? (2) Using this extended possibilities, can POT shed light on details about the chemical state of molecules or (3) identify adsorbed molecules such as the reaction products of on-surface syntheses? (4) Is it possible to obtain experimental k maps fulfilling the ideal $\boldsymbol{\epsilon} \parallel \boldsymbol{k}_f$ condition and how strongly does the resulting ideal k map deviate from typically recorded ones? (5) Which theoretical model can appropriately reproduce experimental photon-energy-dependent POT and shed light on the nature of the observed resonances?

In order to be able to interpret the results, information about the used experimental and theoretical methods is provided in Chapter 2.

Chapter 3 deals with the first question and thereby tests one precondition in the original formulation of POT, namely that only molecular orbitals that consist of atomic orbitals with the "same chemical and orbital character" [41] can be correctly described using the PWA in POT. As a consequence of this assumption, previous POT studies focused on valence π orbitals composed of p_z orbitals. In Chapter 3, the accessible orbital range is extended to π orbitals at higher binding energies as well as σ orbitals which allows to provide an experimentally-derived energy level alignment of σ and π orbitals in a binding energy range of $\approx$ 0 eV – 10 eV. The experimental results serve as a benchmark for the performance of electronic structure calculations and reveal that among four widely used functionals, the range-separated hybrid functional HSE agrees best with the experimental energies. The detailed analysis of two particular σ orbitals allows to differentiate between a metalated, fully or partly hydrogenated reaction product of the thermal reaction of DBBA on Cu(110). We identify the fully hydrogenated bisanthene as final reaction product which would not have been possible considering only π orbitals.

In Chapter 4, we study the thermal reaction of a specially designed precursor molecule on Cu(111) and identify its reaction product as kekulene. We particularly focus on the description of the molecule's aromatic stabilization that was debated in literature for many years. For the first time, our POT results provide experimental evidence on kekulene's aromatic state focusing on electronic properties rather than geometric ones. Consulting two hypothetical theoretical models

with varying geometric and electronic characteristics of Clar and superaromatic type, we reveal that the former aromatic state is favored for kekulene.

Chapter 5 discusses the geometric and electronic properties of the three observed molecular species after thermal reaction of the same precursor used in Chapter 4 on Cu(110). STM images of full monolayer coverage show that planar kekulene molecules are formed besides nonplanar iso-kekulene molecules that appear in two different geometric configurations with the inwards rotated phenanthrene moity tilted out of the molecular plane pointing either away from the substrate ("up") or towards it ("down"). Molecule/metal calculations reveal that there are differences in the MOPDOS of the three species on Cu(110), which affects the intensity distribution of individual emission lobes in the k maps. Comparing experimental and theoretical k maps for varying species on the Cu(110) surface, we find that iso-kekulene is the major reaction product on the surface in agreement with a statistical evaluation of large-scale STM images. This proves that POT is able to differentiate isomeric reaction products and reveal charge transfer from the metal to the molecule due to experimentally identified k maps of LUMO and LUMO+1 of iso-kekulene. Chapters 4 and 5 thus respond to questions (2) and (3) proving that POT is able to identify reaction products on the one hand and on the other hand can shed light on the aromatic state of particular molecules.

The fourth question is tackled in Chapter 6, where we construct synthetic k maps fulfilling the $\boldsymbol{\epsilon} \parallel \boldsymbol{k}_f$ condition using incidence-angle-dependent POT data. This is done for three different sample systems, namely benzene/Pd(110), bisanthene/Cu(110), and EMLG. Although we observe clear deviations between the ideal $I_{\boldsymbol{\epsilon}\parallel\boldsymbol{k}_f}(k_x, k_y)$ maps in comparison to those recorded at single incidence angles, the best agreement between ideal and usually recorded k maps is found using $\alpha = 49° \pm 3$ °.

In Chapter 7, we learn that the PWA used in POT can be successfully used to qualitatively describe the results of two-dimensional material graphene. This proves that the technique is not limited to molecular systems and thus opens the field for a new set of materials. However, the experimental photon-energy-dependent POT results cannot be reproduced quantitatively using the PWA. The origin of some features can, however, be understood by comparison of EMLG and QFMLG results, because the interaction strength between the top graphene layer and the underlying SiC substrate varies in the two graphene samples. The majority of peaks in the intensity vs. photon energy distributions is observed for both samples, for which we accordingly rule out the influence of the underlying substrate. To be able to understand physical origins behind the experimentally-observed resonances in correlation to the actual photoemission process, we consult two advanced theoretical approaches. The results of TDDFT fully agree with the experiment but

an intuitive picture is not allowed in its complex computational description. The recently developed SWA, however, allows a more detailed analysis of the photon-energy-dependent data set of QFMLG recorded in normal and grazing incidence geometry. In the study, we are able to extract the momentum-dependent amplitude and phase of the dipole-allowed s and d photoemission channels.

Summing up, the results of this thesis prove that POT is not limited to (i) π orbitals from (ii) large, (iii) planar (iv) molecules, and (v) a particular experimental geometry as initially postulated by Puschnig et al. [11]. In particular, we show that POT provides valuable information to identify exact reaction products of on-surface syntheses using π (kekulene and iso-kekulene, Chapters 4 and 5) and σ orbitals (bisanthene vs. metalated bisanthene, Chapter 3). Additionally, POT can be applied to small molecules (benzene, Chapter 6) as well as two-dimensional systems (graphene, Chapters 6 and 7), and is able to pinpoint the long-disputed aromatic stabilization in kekulene (Chapter 4). The investigation of experimental k maps fulfilling the $\boldsymbol{\epsilon} \parallel \boldsymbol{k}_f$ condition further supports to perform future POT experiments using incidence angles close to 49°. Thereby, the experimental k maps come as close as possible to the more exact IAC approximation without performing time-consuming incidence-angle-dependent POT measurements. Additionally, we learned that if photon-energy-dependent POT studies are performed for two different graphene samples, resonances that can be correlated to an influence of the underlying substrate are only observed at $h\nu <$ 60 eV. In general the intensity distribution cannot be reproduced using the simple PW final state. In this work, the more adequate final state descriptions in TDDFT and the SWA are consulted. Both methods agree with the experimental data, but only the SWA allows to draw conclusions about the physical origins of the observed resonances.

Finally, my work shows that POT can be utilized to study a variety of adsorbate/metal systems and provides valuable information beyond the original ideas postulated in 2009. As a consequence, novel application possibilities in the future of POT are established that will give rise to exact electronic descriptions of adsorbate layers on the orbital-level.

A | Data Analysis Software

The analysis of POT measurements was performed with the python-based software `MOZI` developed by X. Yang during his PhD thesis based on a previous IGOR Pro-based software. It allows to import, process, and plot POT data recorded with the TEA. Some functionalities concerning the calibration, presentation as well as in- and export of POT data series where either the photon energy or the incidence angle were varied have been expanded during the course of this PhD thesis. Options to be set by the user are presented in the screenshot of the program in Fig. A.1**a** explained in more detail in the following using the numbers 0–15 corresponding to the colored spheres in the figure. The red spheres correspond to features concerning data import, presentation, and exportation. The purple spheres concern plotting photoemission intensities vs. photon energy or incidence angle. The blue spheres can only apply to photon energy dependent data series.

Prior to importing POT data recorded at constant kinetic energy, the data type needs to be defined in (0) to either **Energy-dependent** or **Angle-dependent**. The data are imported using **Choose Data Files** (1). Energy dependent data can be presented in three different variants exemplary plotted in figure A.1**b–d**, namely as raw data $I(\theta, \phi)$, $I(k_{\parallel}, \phi)$, or k map $I(k_{\mathrm{x}}, k_{\mathrm{y}})$ by defining the **Options** in (2). Angle-dependent data can only be shown as k maps $I(k_{\mathrm{x}}, k_{\mathrm{y}})$. In option (3), the user can choose whether raw or normalized data shall be plotted. The latter option is thus only selectable if normalization options have been chosen that will be discussed later in this section (15). For all plot options, the user can choose how many energy slices shall be averaged (**Slice Min** and **Slice Max**, (4)). Additionally, for k maps parameters like the arcshift or the polarshift can be defined. These parameters shall be calibrated using the main `MOZI` program not further discussed in this work. The data can be plotted by pressing **Show** (5). Single k maps may be exported in matplotlib (e.g. as *.png or *.jpg) using **Open map in Matplotlib** (6), while the complete data set can be exported as an *.hdf5 file using **Export 3D data set to HDF** (7).

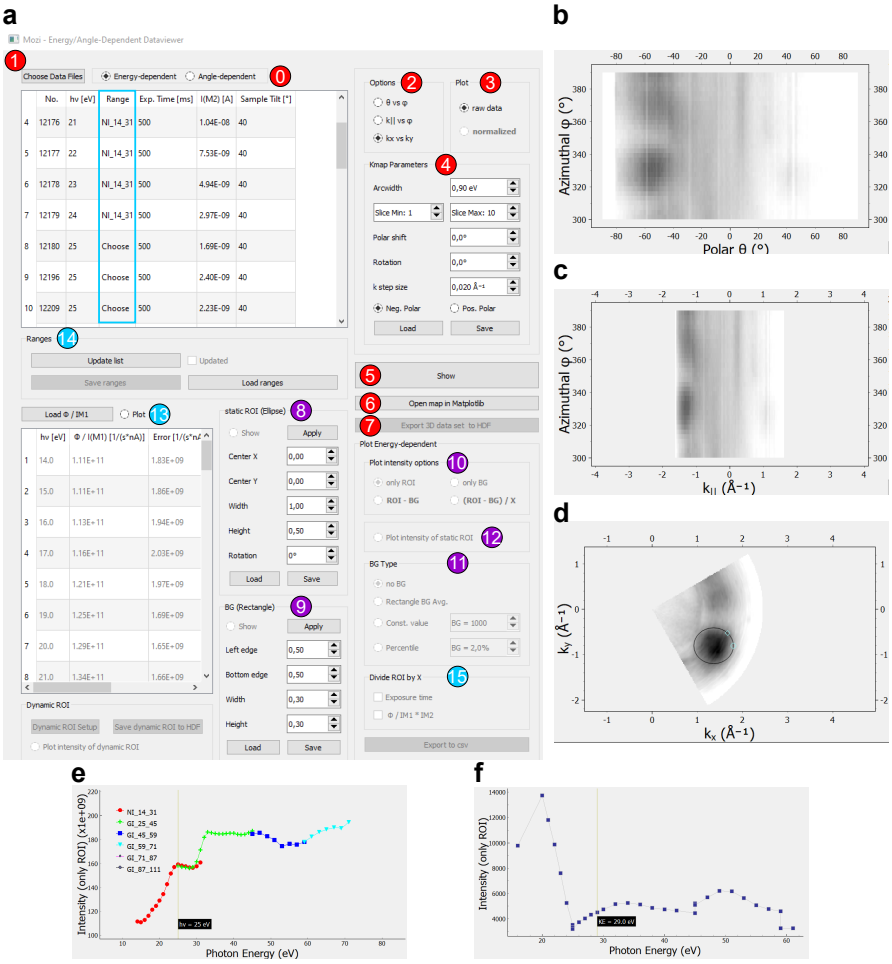

Figure A.1: Screenshot of `MOZI` for analysis of POT data series
a Updated functionalities of `MOZI` to analyze POT data series. Individual features are marked with colored spheres and numbers. The red spheres correspond to data import, presentation, and exportation. The purple spheres concern plotting photoemission intensities vs. photon energy or incidence angle. The blue spheres correspond to the normalization of photon energy dependent data series. Data can be presented in three different ways, namely **b** $I(\theta, \phi)$, **c** $I(k_{\parallel}, \phi)$, or **d** k map $I(k_{\mathrm{x}}, k_{\mathrm{y}})$. **e** Photon yield or **f** photoemission intensity vs. photon energy plots.

To trace the photoemission intensity of specific features vs. photon energy or incidence angle, one can define an elliptical as well as a rectangular region of interest denoting the ROI and BG, respectively, in (8) and (9). Their sizes and positions can be saved and loaded for later use. The integrated photoemission intensity in these areas can be plotted by pressing **Plot intensity options** (10). There are four plot options, namely **only ROI**, **only BG**, **ROI-BG**, and **(ROI-BG)/X**. If one options is selected, the intensity is plotting by checking the **Plot intensity of static ROI** (12) as exemplary shown in Fig. A.1**f** using the ROI defined in **d**.

The BG can be chosen differently in the **BG Type** section (11). If a rectangular BG has been defined, choose **Rectangle BG Avg.**. Note that the default is set to **no BG**, which means that the user has to choose another **BG Type** if a plot option is selected that uses the BG.

The "X" in the last plot option defines to which quantity the photoemission intensity is normalized. This can be either the **Exposure time** and/or the photon flux **Φ / IM1 * IM2** in (15). The exposure time and the mirror current IM2 (i_m in Section 2.4.6) are saved during data acquisition and therefore automatically imported. Φ/IM1 ($\eta(h\nu)$ in Section 2.4.6), however, needs to be loaded separately using the button **Load Φ / IM1** (13). The loaded data are presented in the list below including the photon energy "$h\nu$", the photon yield Φ/IM1, its error, and the beamline configuration. The photon yield can be plotted by the **Plot** option (13) as exemplary shown in Fig. A.1**e**. The colors represent the beamline configurations already mentioned in Section 2.4.6. The following abbreviations were used: 15 eV to 31 eV, NI, 3rd harmonic, no filter: "NI_14_31"; 25 eV to 45 eV, GI, 3rd harmonic, Mg filter: "GI_25_45"; 45 eV to 59 eV, GI, 6th harmonic, Al filter: "GI_45_59"; 59 eV to 71 eV, GI, 10th harmonic, Al filter: "GI_59_71"; 71 eV to 87 eV, GI, 10th harmonic, Be filter: "GI_71_87"; and 87 eV to 111 eV, GI, wiggler mode, Be filter: "GI_87_111". Note that for some photon energies, two different beamline configurations could be used. To normalize the recorded POT data with the photon flux, it is therefore ambiguous for some photon energies, which configuration has been used during the experiment. Especially because this information is not saved during data acquisition but only noted in the labbook. It is therefore necessary that the user assigns the correct beamline configuration to the required imported POT data which are labeled by **Choose** in the data list marked by the lightblue frame. To change the **Choose** to the desired beamline configuration, doubleclick on the word and type in the correct abbreviation. To check whether the assignment was done correctly for all POT data, click on **Update list** (14). If **Updated** is checked, your assignment was successful. This information can be

saved in a separate file by pressing **Save ranges** and loaded again using **Load ranges** (14). Now, the data can be normalized to the photon flux, which means that **Φ / IM1 * IM2** in (15) is selectable.

The intensity integrated in the area of ROI and BG and plotted vs. the photon energy can now be normalized to **Exposure time** and/or the photon flux **Φ / IM1 * IM2** by defining "X" in (15). Selecting **(ROI-BG)/X** in (10) then also allows to plot this normalized intensity in (12). The k maps can also be normalized in this way. The normalized k maps can be plotted choosing **normalized** in (3) and again pressing **Show** (5). If the k maps have been normalized, the normalized and raw data are saved in the *.hdf5 file pressing (7).

The option **Dynamic ROI** in the bottom left corner of Fig. A.1**a** was not used for data analysis in this work and is therefore not discussed further.

B | MOPDOS Obtained with Approach 2

The deconvolution analysis using approach 2 is applied to the π orbitals above the Cu d band and to σ orbitals down to a binding energy of about 10 eV. In the this approach, the only initial input is the experimental data cube and all individual k maps of the orbitals of the free molecule bisanthene. In a first step, a data cube $I(E_\mathrm{b}, k_x, k_y)$ is fitted with a single theoretical k map $I_i(k_x, k_y)$, where the index i labels the orbitals. This is repeated for all orbitals (e.g., $i = 1, \ldots 27$ for σ orbitals see Tab. 3.6). These initial fits with single k maps result in broad peaks that allow to narrow down the binding energy range in which the respective orbital is to be expected. In a second step, each data cube is deconvolved using its so-obtained set of contributing orbitals. In these curves, however, the contribution of some orbitals is negligibly small or unstructured in particular energy ranges or the features in the theoretical k maps obviously do not match the experimental one. In such cases, the orbitals are excluded in the next analysis step. Single case-to-case judgments can be found in the SI of Ref. [AH13]. After finding an appropriate fitting model for each energy range, there are multiple deconvolution results $a_i(E_\mathrm{b})$ for each orbital from neighboring energy ranges. These results of all ranges for one orbitals are always shown in one plot, e.g., in the left column of Fig. B.5 for the π orbitals or Figs. B.1, B.3.

For the same reasons as in approach 1, the obtained MOPDOS from varying measurements (energy ranges) can not be directly related. To overcome this incompatibility in between energy ranges, we interpolate the deconvolution results in neighboring energy ranges (and in some cases of different fitting models in one energy range) for each orbital individually in approach 2. This is exemplary shown in Fig. 3.10 with the original deconvolution results as gray curves and the final MOPDOS in red. The results of all orbitals are shown in the right column of Fig. B.5 for the π orbitals or Figs. B.2, B.4. Each of these plots contains four k maps. The one next to the orbital's label is calculated for this orbital of the free molecule. In the set of three k maps with the same binding energies, the top k map is an experimental one $I(E_\mathrm{b}, \boldsymbol{k}_\parallel)$, the middle is the deconvolution result $\sum_i a_i(E_\mathrm{b}) \cdot I_i(\boldsymbol{k}_\parallel)$ using the k maps $I_i(\boldsymbol{k}_\parallel)$ of free bisanthene and the fitting parameters $a_i(E_\mathrm{b})$. The bottom k map is the residual residual $I(E_\mathrm{b}, \boldsymbol{k}_\parallel) - \sum_i a_i(E_\mathrm{b}) \cdot I_i(\boldsymbol{k}_\parallel)$.

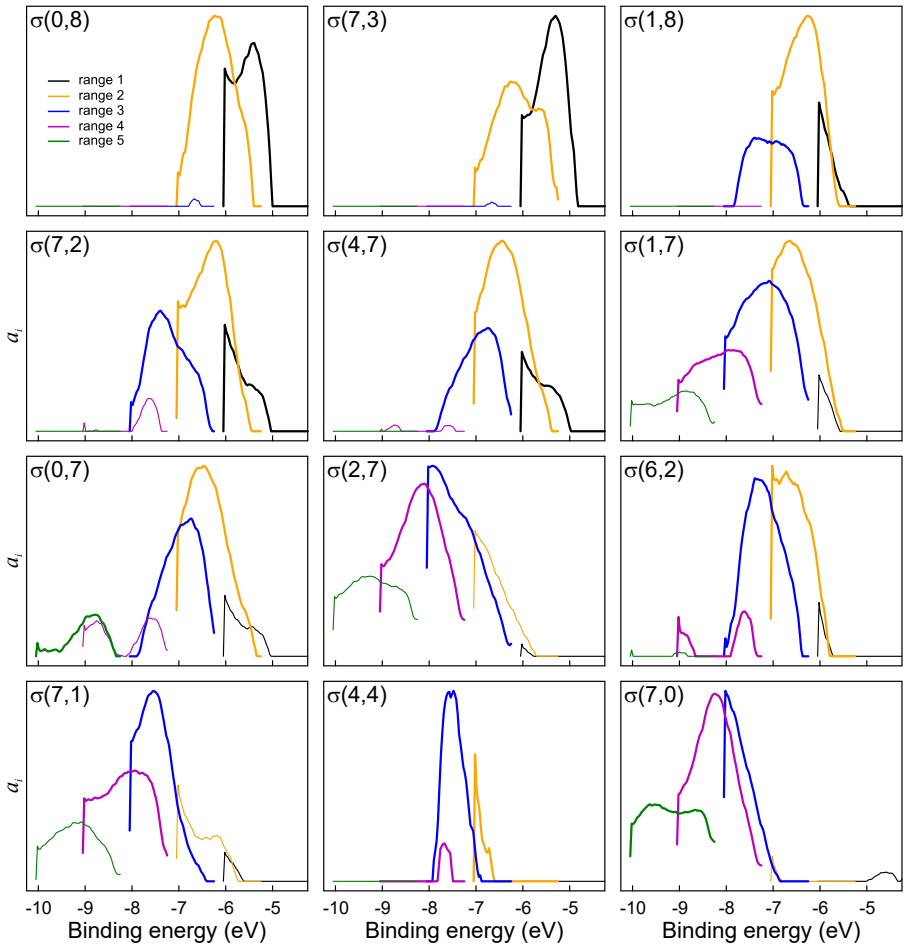

Figure B.1: σ orbital deconvolution results of approach 2
Deconvolution results of single σ orbitals using approach 2. Therein, each experimental data cube is fitted with only one orbital. The results of one orbital fitted in all five ranges in plotted as a function of binding energy.

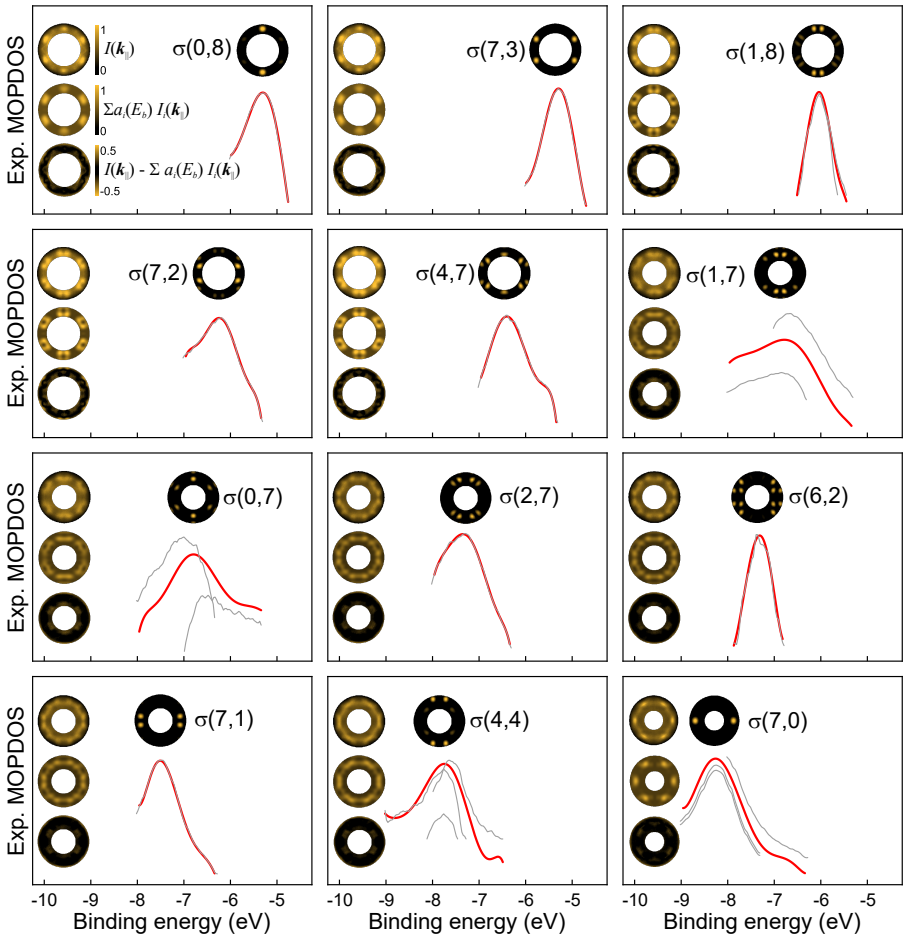

Figure B.2: σ orbital deconvolution results of approach 2
Considering the results of Fig. B.1, the obtained fit results of some orbitals are sometimes negligibly small or unstructured in particular energy ranges. Those curves are ignored, while the remaining curves drawn in gray in this plot, are interpolated resulting in the red curves further referred to as experimental MOPDOS of one single orbital. The k map shown next to the orbital's label is calculated for this orbital of the free molecule. In the set of three k maps with the same binding energies, the top k map is an experimental one $I(E_\mathrm{b}, \boldsymbol{k}_\parallel)$, the middle is the deconvolution result $\sum_i a_i(E_\mathrm{b}) \cdot I_i(\boldsymbol{k}_\parallel)$ using the k maps $I_i(\boldsymbol{k}_\parallel)$ of free bisanthene and the fitting parameters $a_i(E_\mathrm{b})$. The bottom k map is the residual residual $I(E_\mathrm{b}, \boldsymbol{k}_\parallel) - \sum_i a_i(E_\mathrm{b}) \cdot I_i(\boldsymbol{k}_\parallel)$.

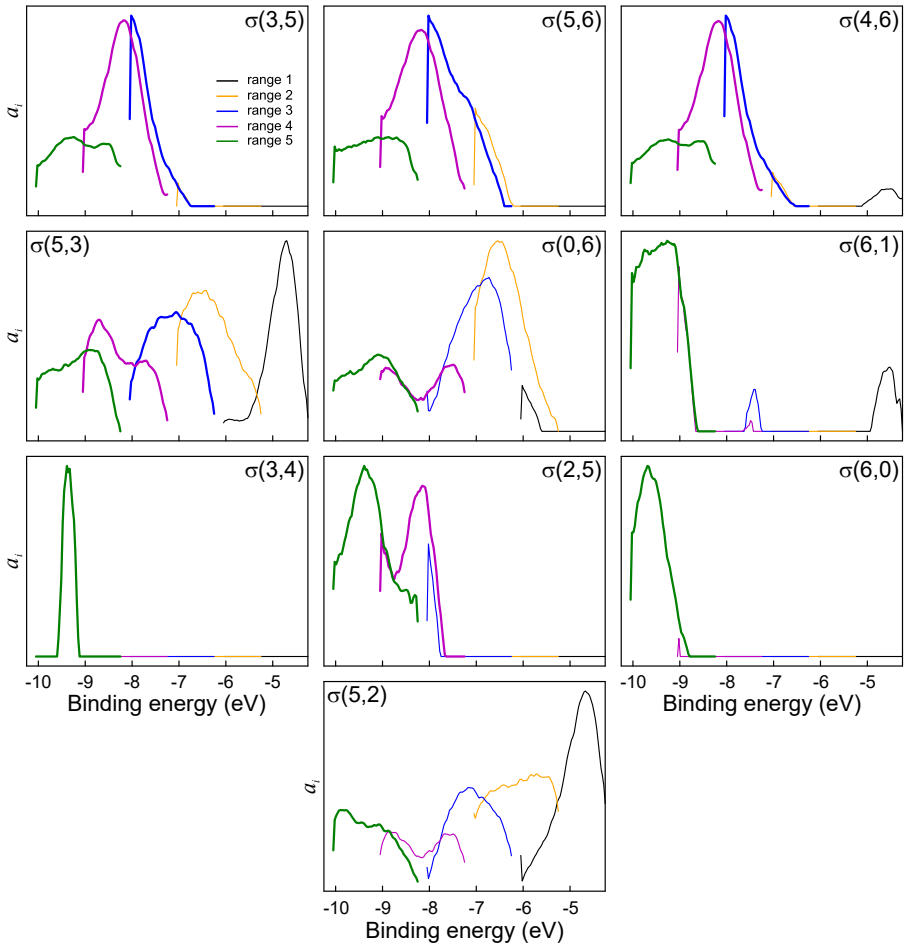

Figure B.3: σ orbital deconvolution results of approach 2
Deconvolution results of single σ orbitals using approach 2. Therein, each experimental data cube is fitted with only one orbital. The results of one orbital fitted in all five ranges in plotted as a function of binding energy.

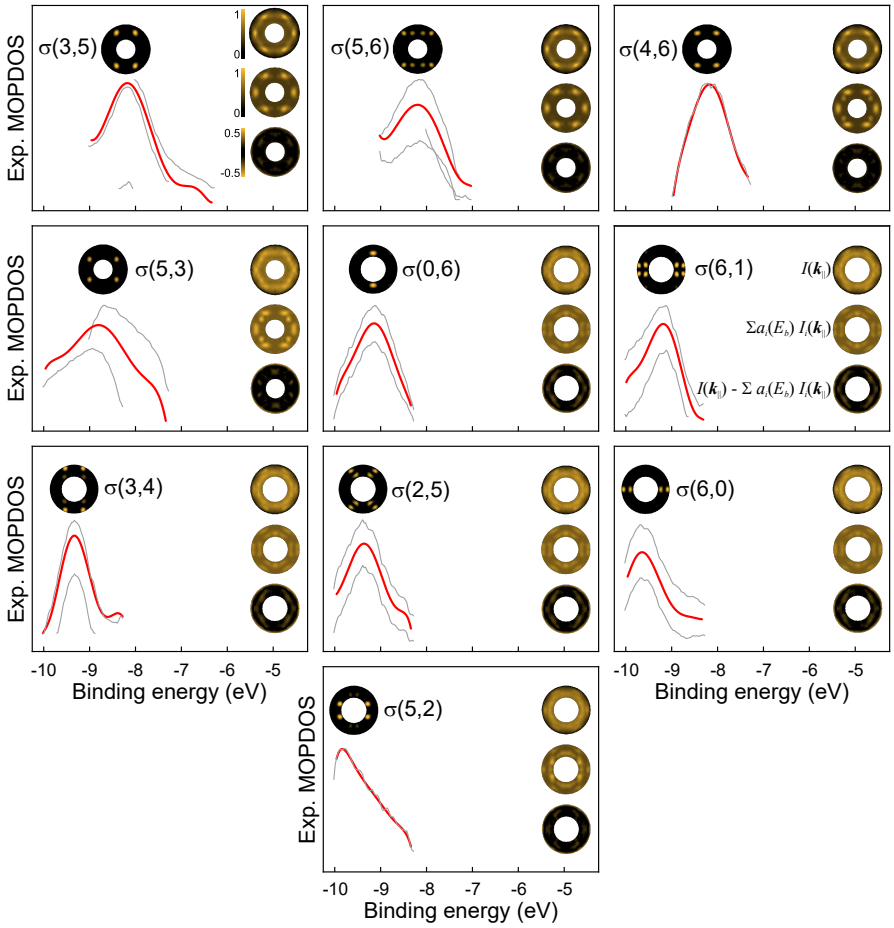

Figure B.4: σ orbital deconvolution results of approach 2
Considering the results of Fig. B.1, the obtained fit results of some orbitals are sometimes negligibly small or unstructured in particular energy ranges. Those curves are ignored, while the remaining curves drawn in gray in this plot, are interpolated resulting in the red curves further referred to as experimental MOPDOS of one single orbital. The k map shown next to the orbital's label is calculated for this orbital of the free molecule. In the set of three k maps with the same binding energies, the top k map is an experimental one $I(E_\mathrm{b}, \boldsymbol{k}_\parallel)$, the middle is the deconvolution result $\sum_i a_i(E_\mathrm{b}) \cdot I_i(\boldsymbol{k}_\parallel)$ using the k maps $I_i(\boldsymbol{k}_\parallel)$ of free bisanthene and the fitting parameters $a_i(E_\mathrm{b})$. The bottom k map is the residual residual $I(E_\mathrm{b}, \boldsymbol{k}_\parallel) - \sum_i a_i(E_\mathrm{b}) \cdot\ I_i(\boldsymbol{k}_\parallel)$.

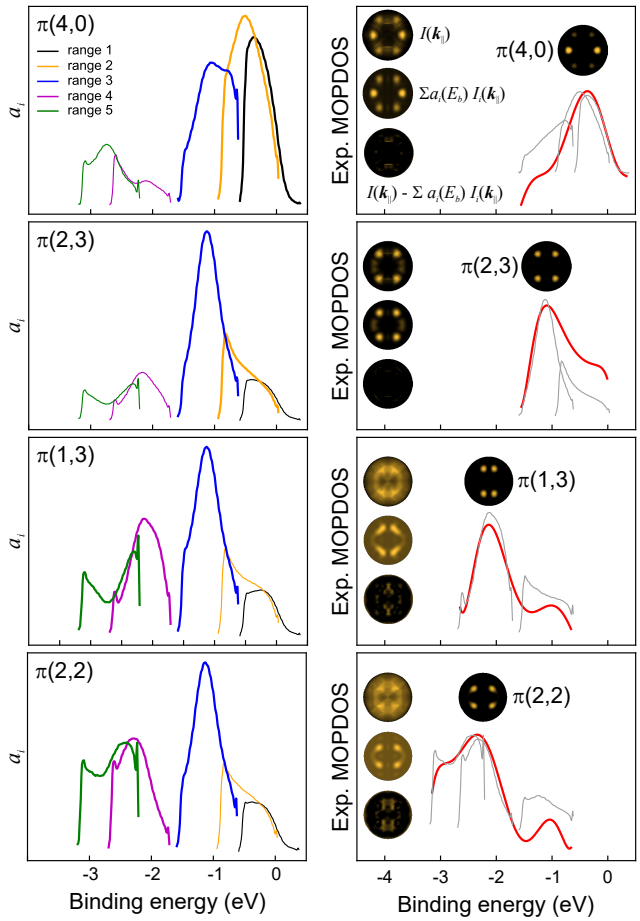

Figure B.5: π orbitals approach 2
Left column: Deconvolution results of single σ orbitals using approach 2. Therein, each experimental data cube is fitted with only one orbital. The results of one orbital fitted in all five ranges in plotted as a function of binding energy. Right column: Interpolated fit curves of each orbital in red further referred to as experimental MOPDOS of one single orbital. The k map shown next to the orbital's label is calculated for this orbital of the free molecule. In the set of three k maps with the same binding energies, the top k map is an experimental one $I(E_\mathrm{b}, \boldsymbol{k}_\parallel)$, the middle is the deconvolution result $\sum_i a_i(E_\mathrm{b}) \cdot I_i(\boldsymbol{k}_\parallel)$ using the k maps $I_i(\boldsymbol{k}_\parallel)$ of free bisanthene and the fitting parameters $a_i(E_\mathrm{b})$. The bottom k map is the residual residual $I(E_\mathrm{b}, \boldsymbol{k}_\parallel) - \sum_i a_i(E_\mathrm{b}) \cdot I_i(\boldsymbol{k}_\parallel)$.

C | LEED of Iso-kekulene/Cu(110)

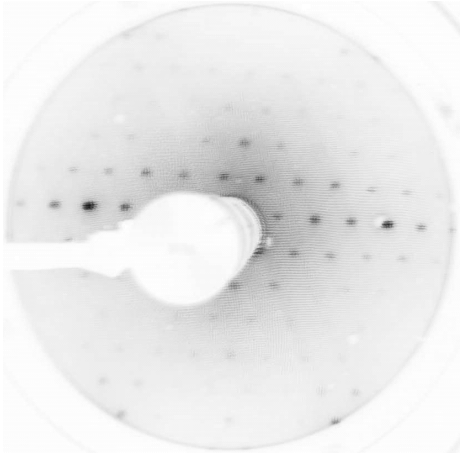

Figure C.1: LEED of iso-kekulene/Cu(110)
LEED image of a monolayer of annealed precursor molecules on Cu(110) measured with an electron energy of 45 eV.

D | Photon-Energy-Dependent POT of Graphene

QFtBLG

We additionally measured photon energy dependent POT for a third sample that we refer to as quasifreestanding twisted bilayer graphene (QFtBLG). It is supposed to be similar to QFMLG, yet extended by one graphene layer on top. The two topmost graphene layers are rotated to each other by 30°. In respect to the substrate, the topmost layer is then in the same orientation as the substrate, while the second graphene layer is rotated by 30°. Therefore, the first and second layers are called 0° and 30° rotated graphene, respectively.

Unfortunately, the investigated sample showed ambiguous results in other surface science techniques such as NIXSW and LEED. We are therefore not sure, whether we measured POT of the desired QFtBLG sample [1]. Nevertheless, we show the measured band map in Fig. D.1 and k maps in Figs. D.2 and D.4.

In the band map of QFtBLG, dispersing π bands are visible in Fig. D.1 originate from the 30°-rotated top-layer graphene in the $\bar{\Gamma} - \bar{K}$ direction, while in $\bar{\Gamma} - \bar{M}$ the linear dispersion of the π bands from the second, 0°-rotated graphene layer are discernible. The crossing of the π bands are at the same energy, which means that the first and second graphene layers have the same electronic properties. Again, the absent gap in the π bands indicates a decoupling of the graphene sheets to the SiC similar to QFMLG.

In the band map, two dashed white line are indicated which mark the energies where photon-energy-dependent POT series of have been measured. The used energies correspond to those already discussed in Chapter 7 that were referred to as maps 1 and 3 recorded at $E - E_{\mathrm{vac}} \approx 4.75$ eV and ≈ 8.9 eV. For QFtBLG, we recorded comparable photon-energy-dependent POT data at $E - E_{\mathrm{vac}} = 4.74$ eV and $E - E_{\mathrm{vac}} = 8.67$ eV, respectively.

[1] Personal communication with F. Bocquet.

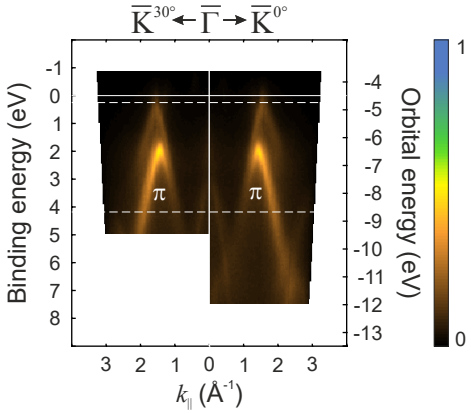

Figure D.1: Band maps of QFtBLG
Band maps of QFtBLG recorded at $h\nu = 45$ eV in two high symmetry directions. Assuming that we actually have a QFtBLG sample, one direction is along the $\overline{\Gamma}$–$\overline{K^{0°}}$ and another along the $\overline{\Gamma}$–$\overline{K^{30°}}$ direction where $\overline{K^{0°}}$ and $\overline{K^{30°}}$ denote the $\overline{K}$ points of the two graphene layers rotated towards each other by 30°. The y-scale shows the binding energies $E_b = E_F - E_{kin}$ on the left and $E - E_{vac} = h\nu - E_{kin}$ on the right side. The white solid line denotes the Fermi edge and the white dashed lines the energies where photon-energy-dependent POT series of have been measured.

Map 1 - Dirac point

In the case of QFtBLG, two ROIs are defined to trace the intensity of the Dirac point emissions from the k maps recorded at $E - E_{\mathrm{vac}} = 4.74$ eV. The ROI drawn with a solid line (ROI1) in Fig. D.2 accounts for the top 0°-rotated and that with a dotted line (ROI2) for the second 30°-rotated graphene sheets. The integrated intensity at the first BZ is plotted vs. the photon energy in Fig. D.3**a**–**c**. To discern details at higher photon energies and for ROI2 of QFtBLG, the data points are multiplied by a factor of three indicated by open symbols. The intensities plotted in **d**–**f** are extracted from the emission at the second BZ. Fig. D.3 additionally includes the corresponding intensity distributions that were extracted from k maps of EMLG and QFMLG at similar $E - E_{\mathrm{vac}}$ presented and discussed in Section 7.5.

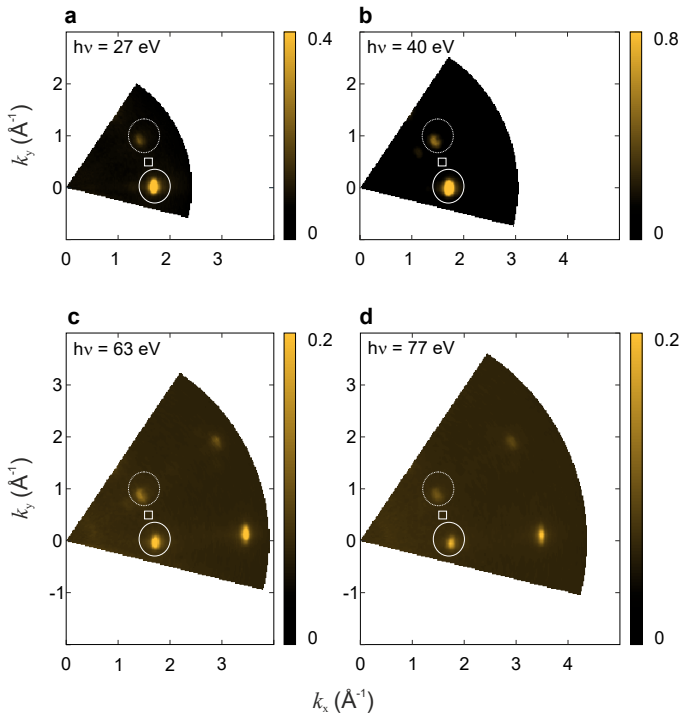

Figure D.2: k maps of QFtBLG at $E - E_{\mathrm{vac}} = 4.74$ eV (map 1)
k maps of QFtBLG at $E - E_{\mathrm{vac}} = 4.74$ eV in a photon energy range of 15 eV to 111 eV. ROI1 and ROI2 for intensity integration are indicated by solid and dotted white ellipses and the BG with a white rectangle.

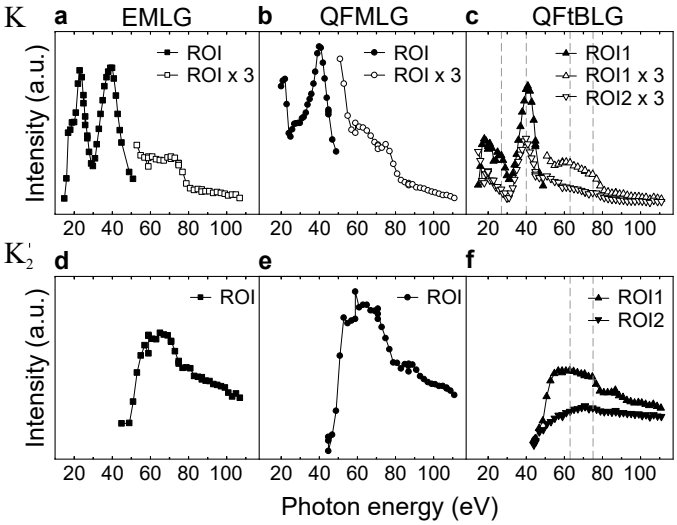

Figure D.3: Intensity distributions from QFtBLG at $E - E_{\mathrm{vac}} = 4.74$ eV
Normalized integrated intensities I_{ROI} against photon energy extracted from k maps of QFtBG measured at $E - E_{\mathrm{vac}} = 4.74$ eV (map 1). The data are compared to the results of EMLG and QFMLG recorded at $E - E_{\mathrm{vac}} = 4.74$ eV and 4.76 eV, respectively, presented in Fig. 7.4. Intensity extracted at the $\overline{\mathrm{K}}$ point (solid white ellipses in Fig. D.2) for **a** EMLG, **b** QFMLG, and **c** QFtBLG. Intensity extracted at the $\overline{\mathrm{K}_2'}$ point (dotted white ellipses in Fig. D.2) for **c** EMLG, **d** QFMLG, and **e** QFtBLG. The corresponding k maps are shown in Figs. 7.3 (EMLG and QFMLG), and D.2 (QFtBLG). The normalization of the data is described in Section 2.4.7.

Map 3 - graphene's σ and π band emissions

Similar to the results presented in Section 7.5 for EMLG and QFMLG, we likewise recorded photon-energy-dependent k maps of QFtBLG at $E - E_{\mathrm{vac}} = 8.67$ eV. In the k maps presented in Fig. D.4**a**–**e**, we see emission from the σ band at the $\overline{\Gamma'}$ point in the second BZ as an elliptical spot. The inhomogeneous circle around and the additional lines at the corners of the k maps stem from π bands. The emission intensity from the σ band is extracted using the ROI marked in Fig. D.4**a**–**e**. The resulting intensity distribution plotted against the photon energy is shown in **f** in comparison to the corresponding results of EMLG and QFMLG already discussed in Section 7.5. Again, we observe only one peak at $h\nu = 61$ eV just as for the other two samples.

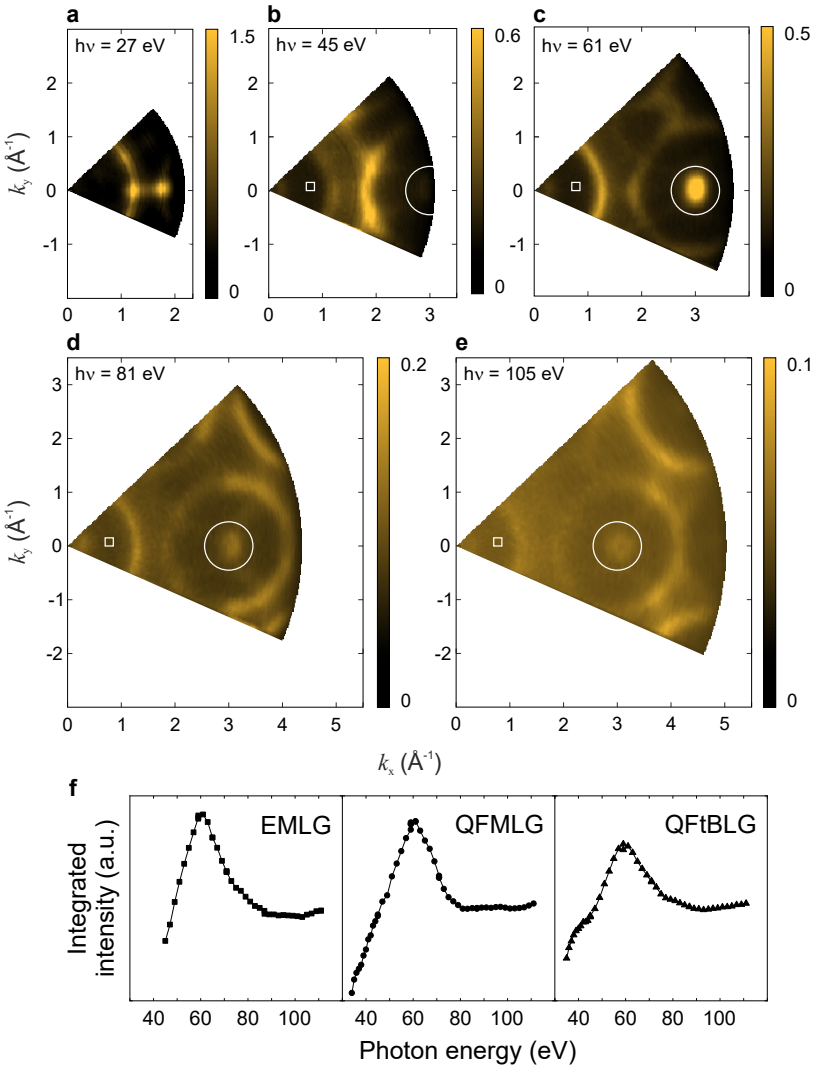

Figure D.4: QFtBLG at $E - E_{\mathrm{vac}} = 8.67$ eV (map 3)
a–e k maps of QFtBLG at $E - E_{\mathrm{vac}} = 8.67$ eV in a $h\nu$ range of 19 eV to 111 eV. The ROI for intensity integration and the BG are indicated by white ellipses and rectangles, respectively. **f** Normalized integrated intensities I_{ROI} against $h\nu$. The data are compared to the results of EMLG and QFMLG recorded at $E - E_{\mathrm{vac}} = 8.89$ eV and 8.53 eV, respectively (Fig. **??**). The corresponding k maps are shown in Figs. 7.5 (EMLG and QFMLG). The normalization of the data is described in Section 2.4.7.

EMLG: $E - E_{\mathrm{vac}} = 7.90$ eV

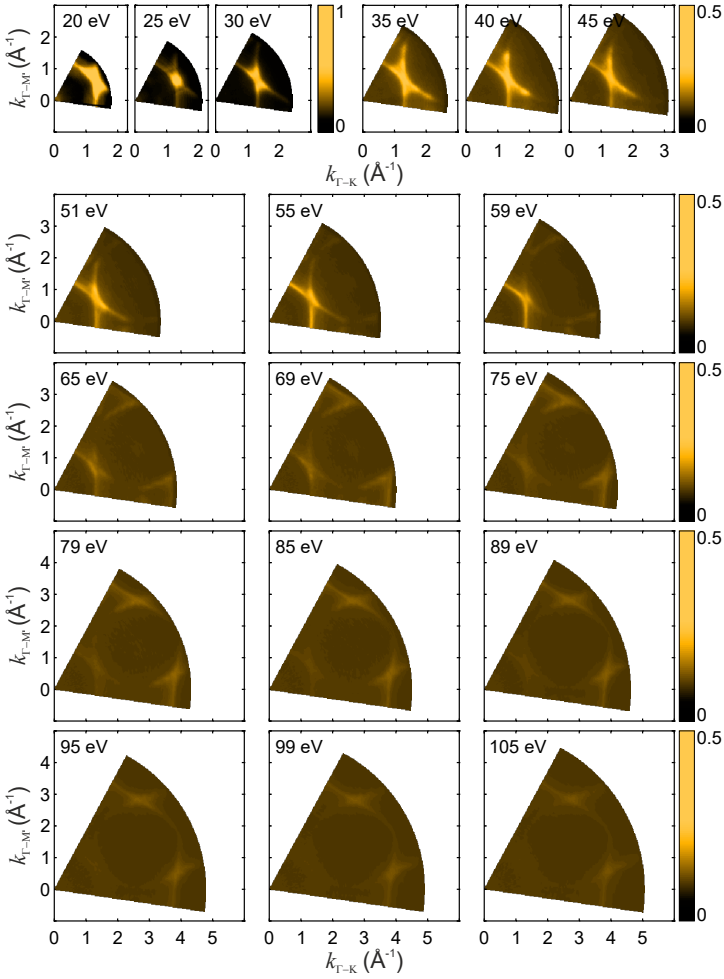

Figure D.5: EMLG k maps at $E - E_{\mathrm{vac}} = 7.90$ eV
Normalized k maps of EMLG recorded at $E - E_{\mathrm{vac}} = 7.90$ eV integrated in an energy window of 0.24 eV in a photon energy range from 20 eV to 105 eV. The k maps show a fairly complicated pattern. Therefore, it is not reasonable to place a ROI in the k map to trace the intensity vs. photon energy.

Map 3: $E - E_{\mathrm{vac}} = 8.70$ eV

The discontinuous intensity distribution of the circular π band emission around the $\overline{\Gamma_2}$ point is illustrated with the help of more experimental k maps than shown in Fig. 7.5 is presented in Figs. D.6 and D.7 for EMLG and QFMLG, respectively. Arrows and lines are drawn into the k maps of QFMLG to be able to address particular emission intensities.

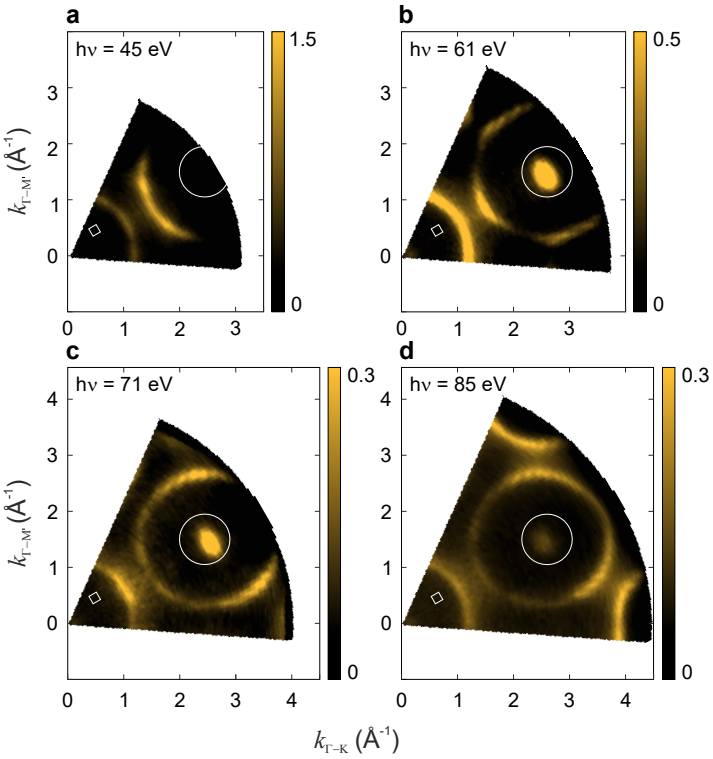

Figure D.6: EMLG k maps measured at $E - E_{\mathrm{vac}} \approx 8.70$ eV
Normalized k maps of EMLG recorded at $E - E_{\mathrm{vac}} \approx 8.89$ eV. The k maps are recorded at **a** $h\nu = 45$ eV, **b** 61 eV, **c** 71 eV, and **d** 85 eV. The ROIs to trace the photoemission intensity (Fig. 7.6) are indicated by white ellipses. The white rectangular areas are used to obtain a background intensity for the normalization procedure.

While a weak, rather homogeneous intensity along the circle (dashed line in Fig. D.7**c**) remains in the k maps of both samples at all photon energies, the intensity along the ring is enhanced in the $\overline{\Gamma}$–$\overline{\mathrm{M}}$ direction at small photon energies (white arrow in k map of QFMLG recorded at $h\nu = 27$ eV in Fig. D.7**a**). With increasing $h\nu$, this "spot" splits up into two separate emission intensities that move symmetrically along the circle to higher $k_{\parallel}$ values indicated by white arrows in Fig. D.7**b**). The enhanced intensity moves along the circle until approximately $h\nu = 87$ eV. In the k maps recorded at $h\nu \geq 80$ eV, these emission intensities are located at the border to the π band emission ring of the next BZ. This is indicated by white arrows in Fig. D.7**d**.

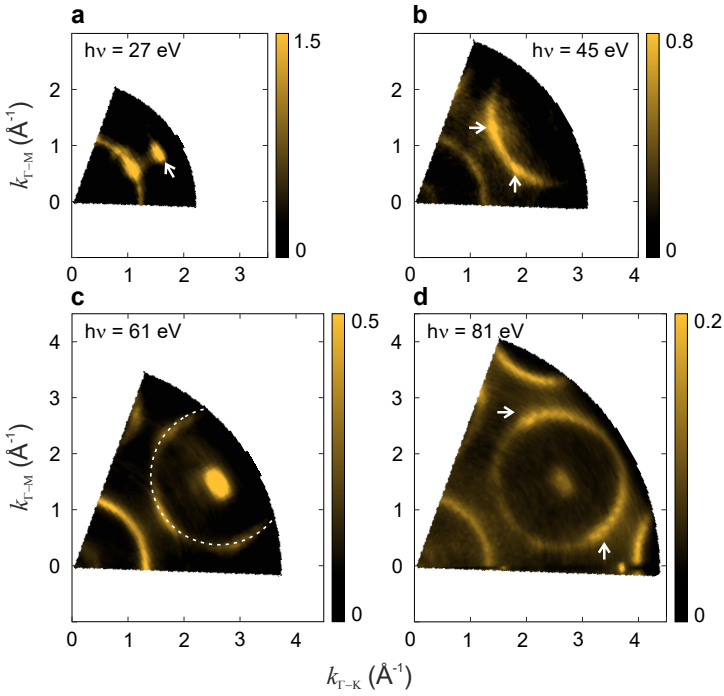

Figure D.7: QFMLG k maps measured at $E - E_{\mathrm{vac}} \approx 8.53$ eV
Normalized k maps of QFMLG recorded at $E - E_{\mathrm{vac}} \approx 8.53$ eV. The k maps are recorded at **a** $h\nu = 27$ eV, **b** 45 eV, **c** 61 eV, and **d** 81 eV. The ROIs to trace the photoemission intensity (Fig. 7.6)are indicated by white ellipses. The white rectangular areas are used to obtain a background intensity for the normalization procedure.

Bibliography

[AH1] P. J. Blowey, A. Haags, L. A. Rochford, J. Felter, D. A. Warr, D. A. Duncan, T.-L. Lee, G. Costantini, C. Kumpf, and D. P. Woodruff, "Characterization of growth and structure of TCNQ phases on Ag (111)", Phys. Rev. Mater. **3**, 116001 (2019).

[AH2] A. Haags, L. A. Rochford, J. Felter, P. J. Blowey, D. Duncan, D. P. Woodruff, and C. Kumpf, "Growth and Evolution of TCNQ and K Coadsorption Phases on Ag(11)", New J. Phys. **10**, 22408 (2020).

[AH3] A. Haags, A. Reichmann, Q. Fan, L. Egger, H. Kirschner, T. Naumann, S. Werner, T. Vollgraff, J. Sundermeyer, L. Eschmann, X. Yang, D. Brandstetter, F. C. Bocquet, G. Koller, A. Gottwald, M. Richter, M. G. Ramsey, M. Rohlfing, P. Puschnig, J. M. Gottfried, S. Soubatch, and F. S. Tautz, "Kekulene: On-surface synthesis, orbital structure, and aromatic stabilization", ACS Nano **14**, 15766 (2020).

[AH4] P. Hurdax, M. Hollerer, L. Egger, G. Koller, X. Yang, A. Haags, S. Soubatch, F. S. Tautz, M. Richter, A. Gottwald, P. Puschnig, M. Sterrer, and M. G. Ramsey, "Controlling the electronic and physical coupling on dielectric thin films", Beilstein J. Nanotechnol. **11**, 1492 (2020).

[AH5] L. Egger, M. Hollerer, C. S. Kern, H. Herrmann, P. Hurdax, A. Haags, X. Yang, A. Gottwald, M. Richter, S. Soubatch, F. S. Tautz, G. Koller, P. Puschnig, M. G. Ramsey, and M. Sterrer, "Charge-promoted self-metalation of porphyrins on an oxide surface", Angew. Chem. Int. Ed. **60**, 5078 (2021).

[AH6] M. S. Sättele, A. Windischbacher, L. Egger, A. Haags, P. Hurdax, H. Kirschner, A. Gottwald, M. Richter, F. C. Bocquet, S. Soubatch, F. S. Tautz, H. F. Bettinger, H. Peisert, T. Chassé, M. G. Ramsey, P. Puschnig, and G. Koller, "Going beyond pentacene: Photoemission tomography of a heptacene monolayer on Ag(110)", J. Phys. Chem. C **125**, 2918 (2021).

[AH7] M. Raths, C. Schott, J. Knippertz, M. Franke, Y. R. Lin, A. Haags, M. Aeschlimann, C. Kumpf, and B. Stadtmüller, "Growth, domain structure, and atomic adsorption sites of hBN on the Ni(111) surface", Phys. Rev. Mater. **5**, 094001 (2021).

[AH8] M. S. Sättele, A. Windischbacher, K. Greulich, L. Egger, A. Haags, H. Kirschner, R. Ovsyannikov, E. Giangrisostomi, A. Gottwald, M. Richter, S. Soubatch, F. S. Tautz, M. G. Ramsey, P. Puschnig, G. Koller, H. F. Bettinger, T. Chassé, and H. Peisert, "Hexacene on Cu(110) and Ag(110): Influence of the Substrate on Molecular Orientation and Interfacial Charge Transfer", J. Phys. Chem. C **126**, 5036 (2022).

[AH9] A. Haags, X. Yang, L. Egger, D. Brandstetter, H. Kirschner, F. C. Bocquet, G. Koller, A. Gottwald, M. Richter, J. M. Gottfried, M. G. Ramsey, P. Puschnig, S. Soubatch, and F. S. Tautz, "Momentum space imaging of σ orbitals for chemical analysis", Sci. Adv. **8**, 819 (2022).

[AH10] P. Hurdax, C. S. Kern, T. G. Boné, A. Haags, M. Hollerer, L. Egger, X. Yang, H. Kirschner, A. Gottwald, M. Richter, F. C. Bocquet, S. Soubatch, G. Koller, F. S. Tautz, M. Sterrer, P. Puschnig, and M. G. Ramsey, "Large distortion of fused aromatics on dielectric interlayers quantified by photoemission orbital tomography", ACS Nano (2022).

[AH11] P. Schädlich, C. Ghosal, M. Stettner, B. Matta, S. Wolff, F. Schölzel, P. Richter, M. Hutter, A. Haags, S. Wenzel, Z. Mamiyev, J. Koch, S. Soubatch, P. Rosenzweig, C. Polley, F. S. Tautz, C. Kumpf, K. Küster, U. Starke, T. Seyller, F. C. Bocquet, and C. Tegenkamp, "Domain Boundary Formation Within an Intercalated Pb Monolayer Featuring Charge-Neutral Epitaxial Graphene", Adv. Mater. Interfaces, 2300471 (2023).

[AH12] C. S. Kern, A. Haags, X. Yang, H. Kirschner, A. Gottwald, M. Richter, U. D. Giovannini, A. Rubio, M. G. Ramsey, F. Bocquet, S. Soubatch, F. S. Tautz, P. Puschnig, and S. Moser, "Simple extension of the plane-wave final state in photoemission: Bringing understanding to the photon-energy dependence of two-dimensional materials", Phys. Rev. Research **5** (2023).

[1] E. Schrödinger, "Die Erfassung der Quantengesetze durch kontinuierliche Funktionen", Naturwissenschaften **17**, 486 (1929).

[2] P. Dirac, "Über die Quantenmechanik der Stoßvorgänge", Zeitschrift für Physik **44**, 585 (1927).

[3] N. Bohr, "Das Quantenpostulat und die neuere Entwicklung der Atomistik", Naturwissenschaften **16**, 245 (1928).

[4] J. W. Gadzuk, "Surface Molecules and Chemisorption. II. Photoemission Angular Distributions", Phys. Rev. B **10**, 5030 (1974).

[5] A. Liebsch, "Theory of angular resolved photoemission from adsorbates", Phys. Rev. Lett. **32**, 1203 (1974).

[6] N. V. Smith, M. M. Traum, J. A. Knapp, J. Anderson, and G. J. Lapeyre, "Polarization effects in angle-resolved photoemission using synchrotron radiation", Phys. Rev. B **13**, 4462 (1976).

[7] J. W. Davenport, "Ultraviolet photoionization cross sections for N_2 and CO", Phys. Rev. Lett. **36**, 945 (1976).

[8] N. V. Smith, "Angular Dependent Photoemission", in *Photoemission in Solids I* (Springer Berlin, Heidelberg, 1978).

[9] F. Pauty, G. Matula, and P. J. Vernier, "An electron spectrometer for measuring both angular and energy distributions of photoemitted electrons", Rev. Sci. Instrum. **45**, 1203 (1974).

[10] T. Permien, R. Engelhardt, and E. E. Koch, "Angle-resolved photoemission from oriented films of lead phthalocyanine on a Cu(100) surface", Chem. Phys. Lett. **98** (1983).

[11] P. Puschnig, S. Berkebile, A. J. Fleming, G. Koller, K. Emtsev, T. Seyller, J. D. Riley, C. Ambrosch-Draxl, F. P. Netzer, and M. G. Ramsey, "Reconstruction of molecular orbital densities from photoemission data", Science **326**, 702 (2009).

[12] X. Yang, M. Jugovac, G. Zamborlini, V. Feyer, G. Koller, P. Puschnig, S. Soubatch, M. G. Ramsey, and F. S. Tautz, "Momentum-selective orbital hybridisation", Nat. Commun. **13** (2022).

[13] S. Kera, S. Tanaka, H. Yamane, D Yoshimura, K. K. Okudaira, K. Seki, and N. Ueno, "Quantitative analysis of photoelectron angular distribution of single-domain organic monolayer film: NTCDA on GeS(001)", Chem. Phys. **325**, 113 (2006).

[14] E. L. Shirley, L. J. Terminello, A. Santoni, and F. J. Himpsel, "Brillouin-zone-selection effects in graphite photoelectron angular distributions", Phys. Rev. B **51**, 13614 (1995).

[15] M. Dauth, T. Körzdörfer, S. Kümmel, F. Reinert, J. Ziroff, M. Wiessner, A. Schöll, M. Arita, and K. Shimada, "Orbital density reconstruction for molecules", Phys. Rev. Lett. **107**, 193002 (2011).

[16] P. Puschnig, E. M. Reinisch, T. Ules, G. Koller, S. Soubatch, M. Ostler, L. Romaner, F. S. Tautz, C. Ambrosch-Draxl, and M. G. Ramsey, "Orbital tomography: Deconvoluting photoemission spectra of organic molecules", Phys. Rev. B **84**, 235427 (2011).

[17] M. Willenbockel, B. Stadtmüller, K. Schönauer, F. C. Bocquet, D. Lüftner, E. M. Reinisch, T. Ules, G. Koller, C. Kumpf, S. Soubatch, P. Puschnig, M. G. Ramsey, and F. S. Tautz, "Energy offsets within a molecular monolayer : the influence of the molecular environment", New J. Phys. **15**, 033017 (2013).

[18] D. Lüftner, T. Ules, E. M. Reinisch, G. Koller, S. Soubatch, F. S. Tautz, M. G. Ramsey, and P. Puschnig, "Imaging the wave functions of adsorbed molecules", Proc. Natl. Acad. Sci. U. S. A. **111**, 605 (2014).

[19] M. Wießner, D. Hauschild, C. Sauer, V. Feyer, A. Schöll, and F. Reinert, "Complete determination of molecular orbitals by measurement of phase symmetry and electron density", Nat. Commun. **5**, 4156 (2014).

[20] M. Willenbockel, D. Lüftner, B. Stadtmüller, G. Koller, C. Kumpf, S. Soubatch, P. Puschnig, M. G. Ramsey, and F. S. Tautz, "The interplay between interface structure, energy level alignment and chemical bonding strength at organic–metal interfaces", Phys. Chem. Chem. Phys. **17**, 1530 (2015).

[21] B. Stadtmüller, M. Willenbockel, S. Schröder, C. Kleimann, E. M. Reinisch, T. Ules, S. Soubatch, M. G. Ramsey, F. S. Tautz, and C. Kumpf, "Modification of the PTCDA-Ag bond by forming a heteromolecular bilayer film", Phys. Rev. B **91**, 155433 (2015).

[22] S. Weiß, D. Lüftner, T. Ules, E. M. Reinisch, H. Kaser, A. Gottwald, M. Richter, S. Soubatch, G. Koller, M. G. Ramsey, F. S. Tautz, and P. Puschnig, "Exploring three-dimensional orbital imaging with energy-dependent photoemission tomography", Nat. Commun. **6**, 8287 (2015).

[23] N. L. Nguyen, G. Borghi, A. Ferretti, I. Dabo, and N. Marzari, "First-principles photoemission spectroscopy and orbital tomography in molecules from Koopmans-compliant functionals", Phys. Rev. Lett. **114**, 166405 (2015).

[24] M. Graus, M. Grimm, C. Metzger, M. Dauth, C. Tusche, J. Kirschner, S. Kümmel, A. Schöll, and F. Reinert, "Electron-vibration coupling in molecular materials: Assignment of vibronic modes from photoelectron momentum mapping", Phys. Rev. Lett. **116**, 147601 (2016).

[25] K. Schönauer, S. Weiss, V. Feyer, D. Lüftner, B. Stadtmüller, D. Schwarz, T. Sueyoshi, C. Kumpf, P. Puschnig, M. G. Ramsey, F. S. Tautz, and S. Soubatch, "Charge transfer and symmetry reduction at the CuPc/Ag(110) interface studied by photoemission tomography", Phys. Rev. B **94**, 205144 (2016).

[26] P. Puschnig, A. D. Boese, M. Willenbockel, M. Meyer, D. Lüftner, E. M. Reinisch, T. Ules, G. Koller, S. Soubatch, M. G. Ramsey, and F. S. Tautz, "Energy ordering of molecular orbitals", J. Phys. Chem. Lett. **8**, 208 (2017).

[27] M. Hollerer, D. Lüftner, P. Hurdax, T. Ules, S. Soubatch, F. S. Tautz, G. Koller, P. Puschnig, M. Sterrer, and M. G. Ramsey, "Charge Transfer and Orbital Level Alignment at Inorganic/Organic Interfaces: The Role of Dielectric Interlayers", ACS Nano **11**, 6252 (2017).

[28] D. Lüftner, S. Weiß, X. Yang, P. Hurdax, V. Feyer, A. Gottwald, G. Koller, S. Soubatch, P. Puschnig, M. G. Ramsey, and F. S. Tautz, "Understanding the photoemission distribution of strongly interacting two-dimensional overlayers", Phys. Rev. B **96**, 125402 (2017).

[29] G. Zamborlini, D. Lüftner, Z. Feng, B. Kollmann, P. Puschnig, C. Dri, M. Panighel, G. D. Santo, A. Goldoni, G. Comelli, M. Jugovac, V. Feyer, and C. M. Schneider, "Multi-orbital charge transfer at highly oriented organic/metal interfaces", Nat. Commun. **8**, 335 (2017).

[30] S. Moser, "An experimentalist′s guide to the matrix element in angle resolved photoemission", J. Electron Spectrosc. Relat. Phenom. **214**, 29 (2017).

[31] P. Puschnig and M. G. Ramsey, "Photoemission tomography: valence band photoemission as a quantitative method for investigrating molecular films", in *Encyclopedia of interfacial chemistry: Surface science and electrochemistry*, edited by K. Wandelt (Elsevier Science, 2018), pp. 380–391.

[32] X. Yang, I. Krieger, D. Lüftner, S. Weiß, T. Heepenstrick, M. Hollerer, P. Hurdax, G. Koller, M. Sokolowski, P. Puschnig, M. G. Ramsey, F. S. Tautz, and S. Soubatch, "On the decoupling of molecules at metal surfaces", Chem comm. **54**, 9039 (2018).

[33] P. Kliuiev, G. Zamborlini, M. Jugovac, Y. Gurdal, K. V. Arx, K. Waltar, S. Schnidrig, R. Alberto, M. Iannuzzi, V. Feyer, M. Hengsberger, J. Osterwalder, and L. Castiglioni, "Combined orbital tomography study of multi-configurational molecular adsorbate systems", Nat. Commun. **10**, 5255 (2019).

[34] L. Egger, B. Kollmann, P. Hurdax, D. Lüftner, X. Yang, S. Weiss, A. Gottwald, M. Richter, G. Koller, S. Soubatch, F. S. Tautz, P. Puschnig, and M. G. Ramsey, "Can photoemission tomography be useful for small, strongly-interacting adsorbate systems?", New J. Phys. **21**, 043003 (2019).

[35] X. Yang, L. Egger, P. Hurdax, H. Kaser, D. Lüftner, F. C. Bocquet, G. Koller, A. Gottwald, P. Tegeder, M. Richter, M. G. Ramsey, P. Puschnig, S. Soubatch, and F. S. Tautz, "Identifying surface reaction intermediates with photoemission tomography", Nat. Commun. **10**, 3189 (2019).

[36] R. Wallauer, M. Raths, K. Stallberg, L. Münster, D. Brandstetter, X. Yang, J. Güdde, P. Puschnig, S. Soubatch, C. Kumpf, F. C. Bocquet, F. S. Tautz, and U. Höfer, "Tracing orbital images on ultrafast time scales", Science **371**, 1056 (2021).

[37] D. Brandstetter, X. Yang, D. Lüftner, F. S. Tautz, and P. Puschnig, "kMap.py: A Python program for simulation and data analysis in photoemission tomography", Comput. Phys. Commun. **263**, 107905 (2021).

[38] A. Adamkiewicz, M. Raths, M. Stettner, M. Theilen, L. Münster, S. Wenzel, M. Hutter, S. Soubatch, C. Kumpf, F. C. Bocquet, R. Wallauer, F. S. Tautz, and U. Höfer, "Coherent and Incoherent Excitation Pathways in Time-Resolved Photoemission Orbital Tomography of CuPc/Cu(001)-2O", J. Phys. Chem. C **127**, 20411 (2023).

[39] L. Egger, "Photoemission tomography of oriented molecular films", (2020), Ph. D. thesis, Karl-Franzens-Universität Graz.

[40] C. Metzger, M. Graus, M. Grimm, G. Zamborlini, V. Feyer, M. Schwendt, D. Lüftner, P. Puschnig, A. Schöll, and F. Reinert, "Plane-wave final state for photoemission from nonplanar molecules at a metal-organic interface", Phys. Rev. B **101**, 165421 (2020).

[41] W. D. Grobman, "Angle-resolved photoemission from molecules in the independent-atomic-center approximation", Phys. Rev. B **17**, 4573 (1978).

[42] A. M. Bradshaw and D. P. Woodruff, "Molecular orbital tomography for adsorbed molecules: is a correct description of the final state really unimportant?", New J. Phys. **17**, 013033 (2015).

[43] I. Pozo, Z. Majzik, N. Pavliček, M. Melle-Franco, E. Guitián, D. Peña, L. Gross, and D. Pérez, "Revisiting kekulene: Synthesis and single-molecule imaging", J. Am. Chem. Soc. **141**, 15488 (2019).

[44] P. Krüger, F. D. Pieve, and J. Osterwalder, "Real-space multiple scattering method for angle-resolved photoemission and valence-band photoelectron diffraction and its application to Cu(111)", Phys. Rev. B **83**, 115437 (2011).

[45] S. Thevuthasan, G. S. Herman, A. P. Kaduwela, R. S. Saiki, Y. J. Kim, W. Niemczura, M. Burger, and C. S. Fadley, "Electron emission holography at keV energies: Estimates of accuracy and limitations", Phys. Rev. Lett. **67**, 469 (1991).

[46] H. Hertz, "Über den Einfluss des ultravioletten Lichtes auf die elektrische Entladung", Ann. Phys. (Berlin) **31**, 983 (1887).
[47] A. Einstein, "On a heuristic point of view toward the emission and transformation of light", Ann. Phys. **17** (1905).
[48] S. Hüfner, *Photoelectron spectroscopy: Principles and applications*, in (Springer-Verlag Berlin Heidelberg GmbH, 2003), p. 41.
[49] F. C. Bocquet, G. Mercurio, M. Franke, G. V. Straaten, S. Weiß, S. Soubatch, C. Kumpf, and F. S. Tautz, "Torricelli: a software to determine atomic spatial distributions from normal incidence x-ray standing wave data", Comput. Phys. Commun. **235**, 502 (2019).
[50] D. P. Woodruff, in *Modern techniques of surface science*, 3rd (Cambridge University Press, 2016).
[51] D. P. Woodruff, "Surface structure determination using x-ray standing waves", Rep. Prog. Phys. **68**, 743 (2005).
[52] J. Zegenhagen and A. Kazimirov, *The X-Ray Standing Wave Technique*, in , Vol. 7 (WORLD SCIENTIFIC, Apr. 2013).
[53] A. Gottwald, H. Kaser, and M. Kolbe, "The U125 insertion device beamline at the Metrology Light Source", J. Synchrotron Rad. **26**, 535 (2019).
[54] K. Wandelt, "The local work function: Concept and implications", Appl. Surf. Sci. **111**, 1 (1997).
[55] D. Cahen and A. Kahn, "Electron energetics at surfaces and interfaces: Concepts and experiments", Adv. Mater. **15**, 271 (2003).
[56] R. Schlaf, "Calibration of photoemission spectra and work function determination", Tutorial notes, University of South Florida.
[57] A. Damascelli, "Probing the electronic structure of complex systems by ARPES", Physica Scripta **T109**, 61 (2004).
[58] SPECS: Hemispherical Energy Analyzer - PHOIBOS 150 NAP MCD, Accessed: 03.02.2023.
[59] SCIENTA OMICRON: ARPES Lab, Accessed: 03.02.2023.
[60] SCIENTA OMICRON: EW4000, Accessed: 03.02.2023.
[61] SPECS: ARPES analyzer - ASTRAIOS 190 2D-CMOS, Accessed: 03.02.2023.
[62] L. Broekman, A. Tadich, E. Huwald, J. Riley, R. Leckey, T. Seyller, K. Emtsev, and L. Ley, "First results from a second generation toroidal electron spectrometer", J. Electron Spectrosc. Relat. Phenom. **144-147**, 1001 (2005).
[63] SPECS: Electron Momentum Spectrometer for Small Spot ARPES and Momentum Microscopy - KREIOS 150, Accessed: 03.02.2023.
[64] SPECS: TOF Analyzer for Momentum Microscopy - METIS 1000, Accessed: 03.02.2023.
[65] SCIENTA OMICRON: NanoESCA, Accessed: 03.02.2023.
[66] G. D. Mahan, "Theory of photoemission in simple metals", Phys. Rev. B **2**, 4334 (1970).
[67] A. Liebsch, "Theory of photoemission from localized adsorbate levels", Phys. Rev. B **13**, 544 (1976).
[68] P. J. Feibelman and D. E. Eastman, "Photoemission spectroscopy — Correspondence between quantum theory and experimental phenomenology", Phys. Rev. B **10**, 4932 (1974).
[69] J. B. Pendry, "Theory of photoemission", Surf. Sci. **57**, 679 (1976).
[70] H. Y. Fan, "Theory of photoelectric emission from metals", Phys. Rev. **68**, 43 (1945).
[71] C. N. Berglund and W. E. Spicer, "Photoemission Studies of Copper and Silver: Theory", Phys. Rev. **136**, A1030 (1964).
[72] G. D. Mahan, "Angular dependence of photoemission in metals", Phys. Rev. Lett. **24**, 1068 (1970).

[73] U. Gerhardt and E. Dietz, "Angular distribution of photoelectrons emitted from copper single crystals", Phys. Rev. Lett. **26**, 1477 (1971).

[74] R. Y. Koyama and L. R. Hughey, "Angular anisotropies in the photoemission from polycrystalline gold", Phys. Rev. Lett. **29**, 1518 (1972).

[75] N. V. Smith and M. M. Traum, "Angular Dependence of Photoemission from the (110) Face of GaAs", Phys. Rev. Lett. **31**, 1247 (1973).

[76] J. W. Gadzuk, "Angle resolved photoemission from chemisorbed layers: Further theoretical considerations", Surf. Sci. **53**, 132 (1975).

[77] N. V. Smith, J. Anderson, and G. J. Lapeyre, "Adsorbate orientation using angle-resolved polarization-dependent photoemission", Phys. Rev. Lett. **37**, 1081 (1976).

[78] S. M. Goldberg, C. S. Fadley, and S. Kono, "Photoelectric cross-sections for fixed-orientation atomic orbitals: Relationship to the plane-wave final state approximation and angle-resolved photoemission", Solid State Commun. **28**, 459 (1978).

[79] J. W. Rabalais, T. P. Debies, J. L. Berkosky, J.-T. J. Huang, and F. O. Ellison, "Calculated photoionization cross sections and relative experimental photoionization intensities for a selection of small molecules", J. Chem. Phys. **61**, 516 (1974).

[80] J. W. Davenport, "Determination of adsorbate bond geometry using photoemission", J. Vac. Sci. Technol. **15**, 433 (1978).

[81] N. V. Richardson, "Comments on angle-resolved photoemission from oriented films of lead phthalocyanine on a Cu(100) surface", Chem. Phys. Lett. **102**, 390 (1983).

[82] G. L. Nyberg and N. V. Richardson, "Symmetry analysis of angle-resolved photoemission: polyrization dependence and lateral interactions in chemisorbed benzene", Surf. Sci. **85**, 335 (1979).

[83] B. J. Bandy, D. R. Lloyd, and N. V. Richardson, "Selection rules in photoemission from adsorbates: pyridine adsorbed on copper", Surf. Sci. **89**, 344 (1979).

[84] N. Ueno, K. Suzuki, S. Hasegawa, K. Kamiya, K. Seki, and H. Inokuchi, "Angle-resolved photoemission spectroscopy of ultrathin films of H_2 - phthalocyanine on MoS_2 surfaces", J. Chem. Phys. **99**, 7169–7174 (1993).

[85] N. Ueno, A. Kitamura, K. K. Okudaira, T. Miyamae, Y. Harada, H. Sinji, H. Ishii, H. Inokuchi, T. Fujikawa, T. Miyazaki, and K. Seki, "Angle-resolved ultraviolet photoelectron spectroscopy of thin films of bis (1,2 ,5-thiadiazolo)-*p*-quinobis (1,3-dithiole) on the MoS_2 surface", J. Chem. Phys. **107**, 2079 (1997).

[86] Y. Liu, D. Ikeda, S. Nagamatsu, T. Nishii, N. Ueno, and S. Kera, "Impact of molecular orbital distribution on photoelectron intensity for picene film", J. Electron Spectrosc. Relat. Phenom. **195**, 287 (2014).

[87] M. Dauth, M. Graus, I. Schelter, M. Wießner, A. Schöll, F. Reinert, and S. Kümmel, "Perpendicular emission, dichroism, and energy dependence in angle-resolved photoemission: The importance of the final state", Phys. Rev. Lett. **117**, 183001 (2016).

[88] N. Komiya, K. Hatada, F. Ota, P. Krüger, T. Fujikawa, and K. Niki, "Multiple scattering approach to photoemission from the highest occupied molecular orbital of pentacene", J. Electron Spectrosc. Relat. Phenom. **220**, 21 (2017).

[89] S. Hasegawa, H. Inokuchi, K. Sekib, and N. Ueno, "Angle-resolved photoemission from oriented thin films of naphthacene: comparison with theoretical spectra", J. Electron Spectrosc. Relat. Phenom. **78**, 391 (1996).

[90] S. Narioka, H. Ishii, K. Edamatsu, K. Kamiya, S. Hasegawa, T. Ohta, N. Ueno, and K. Seki, "Angle-resolved photoelectron spectroscopic study of oriented *p*-sexiphenyl: Wavenumber conservation and blurring in a short model compound of poly(*p*-phenylene)", Phys. Rev. B **52**, 2362 (1995).

[91] N. Ueno, "Angle-resolved ups of ultrathin films of functional organic molecules with synchrotron radiation: determination of molecular orientation by quantitative analysis of photoelectron angular distribution", J. Electron Spectrosc. Relat. Phenom. **78**, 345 (1996).
[92] S. Hasegawa, S. Tanaka, Y. Yamashita, H. Inokuchi, H. Fujimoto, K. Kamiya, K. Seki, and N. Ueno, "Molecular orientation in thin films of bis(1,2,5-thiadiazolo)-*p*-quinobis(1, 3-dithiole) on graphite studied by angle-resolved photoelectron spectroscopy", Phys. Rev. B **48**, 2596 (1993).
[93] G. Schönhense, "Circular Dichroism and Spin Polarization in Photoemission from Adsorbates and Non-Magnetic Solids", Phys. Scr. **T31**, 255 (1990).
[94] S. Moser, "A toy model for dichroism in angle resolved photoemission", J. Electron Spectrosc. Relat. Phenom. **262**, 147278 (2023).
[95] N. Mukunda, "Completeness of the Coulomb wave functions in quantum mechanics", Am. J. Phys. **46**, 910 (1978).
[96] L. Landau and E. Lifshitz, in *Quantum mechanics* (Elsevier, 1977), pp. 50–81.
[97] M. Abramowitz, I. A. Stegun, and R. H. Romer, "Handbook of Mathematical Functions with Formulas, Graphs, and Mathematical Tables", Am. J. Phys. **56**, 958 (1988).
[98] J. Avery and J. Avery, "Generalized Sturmians and Atomic Spectra", in *Generalized sturmians and atomic spectra* (WORLD SCIENTIFIC, 2006).
[99] A. Messiah, "Quantum Mechanics", in *Quantum mechanics* (North-Holland Publishing, Amsterdam, 1961).
[100] J. Humblet, "Analytical structure and properties of Coulomb wave functions for real and complex energies", Ann. Phys. (Berlin) **155**, 461 (1984).
[101] G. B. Arfken, H. J. Weber, and F. E. Harris, "Mathematical Methods for Physicists", in *Mathematical methods for physicists*, 7th (Elsevier Academic Press, 2013).
[102] V. Aquilanti and A. Caligiana, "Sturmian approach to one-electron many-center systems: integrals and iteration schemes", Chem. Phys. Lett. **366**, 157 (2002).
[103] J. Avery, "Many-center Coulomb Sturmians and Shibuya-Wulfman integrals", J. Phys. Chem. **100**, 121 (2004).
[104] C. Bronner and P. Tegeder, "Tracking and removing Br during the on-surface synthesis of a graphene nanoribbon", J. Phys. Chem. C **119**, 486 (2015).
[105] X. Yang, "Investigating the Interaction between π-Conjugated Organic Molecules and Metal Surfaces with Photoemission Tomography", (2019), Ph. D. thesis, RWTH Aachen.
[106] R. C. G. Leckey and J. D. Riley, "A toroidal angle-resolved electron spectrometer for surface studies", Appl. Surf. Sci. **22**, 196 (1985).
[107] K. Fukui, T. Yonezawa, and H. Shingu, "A molecular orbital theory of reactivity in aromatic hydrocarbons", J. Chem. Phys. **20**, 722 (1952).
[108] R. B. Woodward and R. Hoffmann, "The conservation of orbital symmetry", Angew. Chem. internat. Edit. **8**, 781 (1969).
[109] R. Hoffmann, "An extended Hückel theory. I. Hydrocarbons", J. Chem. Phys. **39**, 1397–1412 (1963).
[110] R. Hoffmann, "Interaction of orbitals through space and through bonds", Acc. Chem. Res. **4**, 1 (1971).
[111] R. Hoffmann, "Building bridges between inorganic and organic chemistry (Nobel lecture)", Angew. Chem. internat. Edit. **21**, 711 (1982).
[112] K. Fukui, "The role of frontier orbitals in chemical reactions (Nobel lecture)", Angew. Chem. internat. Edit. **21**, 801 (1981).
[113] F. Garczarek and K. Gerwert, "Functional waters in intraprotein proton transfer monitored by FTIR difference spectroscopy", Nature **439**, 109 (2006).

[114] S. Mastel, A. A. Govyadinov, T. V. D. Oliveira, I. Amenabar, and R. Hillenbrand, "Nanoscale-resolved chemical identification of thin organic films using infrared near-field spectroscopy and standard Fourier transform infrared references", Appl. Phys. Lett. **106**, 023113 (2015).

[115] S. Thussing, S. Flade, K. Eimre, C. A. Pignedoli, R. Fasel, and P. Jakob, "Reaction pathway toward seven-atom-wide armchair graphene nanoribbon formation and identification of intermediate species on Au(111)", J. Phys. Chem. C **124**, 16009 (2020).

[116] L. Mester, A. A. Govyadinov, S. Chen, M. Goikoetxea, and R. Hillenbrand, "Subsurface chemical nanoidentification by nano-FTIR spectroscopy", Nat. Commun. **11**, 3359 (2020).

[117] J. Repp, G. Meyer, S. Paavilainen, F. E. Olsson, and M. Persson, "Imaging bond formation between a gold atom and pentacene on an insulating surface", Science **312**, 1196 (2006).

[118] F. Albrecht, M. Neu, C. Quest, I. Swart, and J. Repp, "Formation and characterization of a molecule-metal-molecule bridge in real space", J. Am. Chem. Soc. **135**, 9200 (2013).

[119] A. Riss, S. Wickenburg, P. Gorman, L. Z. Tan, H. Z. Tsai, D. G. D. Oteyza, Y. C. Chen, A. J. Bradley, M. M. Ugeda, G. Etkin, S. G. Louie, F. R. Fischer, and M. F. Crommie, "Local electronic and chemical structure of oligo-acetylene derivatives formed through radical cyclizations at a surface", Nano Lett. **14**, 2251 (2014).

[120] D. G. de Oteyza, P. Gorman, Y.-C. Chem, S. Wickenburg, A. Riss, D. J. Mowbray, G. Etkin, Z. Peddrarazi, H.-Z. Tsai, A. Rubio, M. F. Crommie, and F. R. Fisher, "Direct imaging of covalent bond structure in single-molecule chemical reactions", Science **340**, 1434 (2013).

[121] F. Mohn, J. Repp, L. Gross, G. Meyer, M. S. Dyer, and M. Persson, "Reversible bond formation in a gold-atom-organic-molecule complex as a molecular switch", Phys. Rev. Lett. **105**, 266102 (2010).

[122] A. Riss, A. P. Paz, S. Wickenburg, H. Z. Tsai, D. G. D. Oteyza, A. J. Bradley, M. M. Ugeda, P. Gorman, H. S. Jung, M. F. Crommie, A. Rubio, and F. R. Fischer, "Imaging single-molecule reaction intermediates stabilized by surface dissipation and entropy", Nat. Chem **8**, 678 (2016).

[123] P. Chen, D. Fan, A. Selloni, E. A. Carter, C. B. Arnold, Y. Zhang, A. S. Gross, R. Chelikowsky James, and N. Yao, "Observation of electron orbital signatures of single atoms within metal-phthalocyanines using atomic force microscopy", Nat. Commun. **14**, 1460 (2023).

[124] Q. Fan, L. Yan, M. W. Tripp, O. Krejčí, S. Dimosthenous, S. R. Kachel, M. Chen, A. S. Foster, U. Koert, P. Liljeroth, and J. M. Gottfried, "Biphenylene network: A nonbenzenoid carbon allotrope", Science **372**, 852 (2021).

[125] Q. Fan, J. N. Luy, M. Liebold, K. Greulich, M. Zugermeier, J. Sundermeyer, R. Tonner, and J. M. Gottfried, "Template-controlled on-surface synthesis of a lanthanide supernaphthalocyanine and its open-chain polycyanine counterpart", Nat. Commun. **10**, 5049 (2019).

[126] Q. Fan, D. Martin-Jimenez, D. Ebeling, C. K. Krug, L. Brechmann, C. Kohlmeyer, G. Hilt, W. Hieringer, A. Schirmeisen, and J. M. Gottfried, "Nanoribbons with nonalternant topology from fusion of polyazulene: Carbon allotropes beyond graphene", J. Am. Chem. Soc. **141**, 17713 (2019).

[127] Q. Fan, D. Martin-Jimenez, S. Werner, D. Ebeling, T. Koehler, T. Vollgraff, J. Sundermeyer, W. Hieringer, A. Schirmeisen, and J. M. Gottfried, "On-surface synthesis and characterization of a cycloarene: C108 graphene ring", J. Am. Chem. Soc. **142**, 894 (2020).

[128] M. Chen, J. Shang, Y. Wang, K. Wu, J. Kuttner, G. Hilt, W. Hieringer, and J. M. Gottfried, "On-surface synthesis and characterization of honeycombene oligophenylene macrocycles", ACS Nano **11**, 134 (2017).

[129] Q. Fan, L. Liu, J. Dai, T. Wang, H. Ju, J. Zhao, J. Kuttner, G. Hilt, J. M. Gottfried, and J. Zhu, "Surface adatom mediated structural transformation in bromoarene monolayers: precursor phases in surface Ullmann reaction", ACS Nano **12**, 2267 (2018).

[130] J. Shang, Y. Wang, M. Chen, J. Dai, X. Zhou, J. Kuttner, G. Hilt, X. Shao, J. M. Gottfried, and K. Wu, "Assembling molecular Sierpiński triangle fractals", Nat. Chem **7**, 389 (2015).

[131] L. Grill, M. Dyer, L. Lafferentz, M. Persson, M. V. Peters, and S. Hecht, "Nano-architectures by covalent assembly of molecular building blocks", Nat. Nanotechnol. **2**, 687 (2007).

[132] J. A. Lipton-Duffin, O. Ivasenko, D. F. Perepichka, and F. Rosei, "Synthesis of polyphenylene molecular wires by surface-confined polymerization", Small **5**, 592 (2009).

[133] M. D. Giovannantonio, X. Yao, K. Eimre, J. I. Urgel, C. A. Pignedoli, K. Müllen, R. Fasel, A. Narita, A Pignedoli, K. Müllen, R. Fasel, and A. Narita, "Large-cavity coronoids with different inner and outer edge structures", J. Am. Chem. Soc. **142**, 12046–12050 (2020).

[134] E. A. Lewis, C. J. Murphy, M. L. Liriano, and E. C. H. Sykes, "Atomic-scale insight into the formation, mobility and reaction of Ullmann coupling intermediates", Chem. Commun. **50**, 1006 (2014).

[135] Q. Fan, C. Wang, L. Liu, Y. Han, J. Zhao, J. Zhu, J. Kuttner, G. Hilt, and J. M. Gottfried, "Covalent, organometallic, and halogen-bonded nanomeshes from tetrabromoterphenyl by surface-assisted synthesis on Cu(111)", J. Phys. Chem. C **118**, 13018 (2014).

[136] J. Eichhorn, T. Strunskus, A. Rastgoo-Lahrood, D. Samanta, M. Schmittel, and M. Lackinger, "On-surface Ullmann polymerization via intermediate organometallic networks on Ag(111)", Chem. comm. **50**, 7680 (2014).

[137] M. Bieri, M. T. Nguyen, O. Gröning, J. Cai, M. Treier, K. Aït-Mansour, P. Ruffieux, C. A. Pignedoli, D. Passerone, M. Kastler, K. Müllen, and R. Fasel, "Two-dimensional polymer formation on surfaces: Insight into the roles of precursor mobility and reactivity", J. Am. Chem. Soc. **132**, 16669 (2010).

[138] R. Gutzler, L. Cardenas, J. Lipton-Duffin, M. El Garah, L. E. Dinca, C. E. Szakacs, C. Fu, M. Gallagher, M. Vondráček, M. Rybachuk, D. F. Perepichka, and F. Rosei, "Ullmann-type coupling of brominated tetrathienoanthracene on copper and silver", Nanoscale **6**, 2660 (2014).

[139] M. Koch, M. Gille, A. Viertel, S. Hecht, and L. Grill, "Substrate-controlled linking of molecular building blocks: Au(111) vs. Cu(111)", Surf. Sci. **627**, 70 (2014).

[140] M. Chen, J. Xiao, H.-P. Steinrück, S. Wang, W. Wang, N. Lin, W. Hieringer, and J. M. Gottfried, "Combined photoemission and scanning tunneling microscopy study of the surface-assisted Ullmann coupling reaction", J. Phys. Chem. C **118**, 6820 (2014).

[141] Q. Fan, J. M. Gottfried, and J. Zhu, "Surface-catalyzed C-C covalent coupling strategies toward the synthesis of low-dimensional carbon-based nanostructures", Acc. Chem. Res. **48**, 2484 (2015).

[142] Q. Fan, T. Wang, L. Liu, J. Zhao, J. Zhu, and J. M. Gottfried, "Tribromobenzene on Cu(111): Temperature-dependent formation of halogenbonded, organometallic, and covalent nanostructures", J. Chem. Phys. **142**, 101906 (2015).

[143] Q. Fan, C. Wang, Y. Han, J. Zhu, W. Hieringer, J. Kuttner, G. Hilt, and J. M. Gottfried, "Surface-assisted organic synthesis of hyperbenzene nanotroughs", Angew. Chem. Int. Ed. **52**, 4668 (2013).

[144] M. D. Giovannantonio, M. E. Garah, J. Lipton-Duffin, V. Meunier, L. Cardenas, Y. F. Revurat, A. Cossaro, A. Verdini, D. F. Perepichka, F. Rosei, and G. Contini, "Insight into organometallic intermediate and its evolution to covalent bonding in surface-confined Ullmann", ACS Nano **7**, 8190 (2013).

[145] W. Wang, X. Shi, S. Wang, M. A. V. Hove, and N. Lin, "Single-molecule resolution of an organometallic intermediate in a surface-supported Ullmann coupling reaction", J. Am. Chem. Soc. **133**, 13264 (2011).

[146] J. Cai, P. Ruffieux, R. Jaafar, M. Bieri, T. Braun, S. Blankenburg, M. Muoth, A. P. Seitsonen, M. Saleh, X. Feng, K. Müllen, and R. Fasel, "Atomically precise bottom-up fabrication of graphene nanoribbons", Nature **466**, 470 (2010).

[147] C. Sánchez-Sánchez, T. Dienel, O. Deniz, P. Ruffieux, R. Berger, X. Feng, K. Müllen, and R. Fasel, "Purely armchair or partially chiral: noncontact atomic force microscopy characterization of dibromo-bianthryl-based graphene nanoribbons grown on Cu(111)", ACS Nano **10**, 8006 (2016).

[148] K. A. Simonov, N. A. Vinogradov, A. S. Vinogradov, A. V. Generalov, E. M. Zagrebina, G. I. Svirskiy, A. A. Cafolla, T. Carpy, J. P. Cunniffe, T. Taketsugu, A. Lyalin, N. Mårtensson, and A. B. Preobrajenski, "From graphene nanoribbons on Cu(111) to nanographene on Cu(110): Critical role of substrate structure in the bottom-up fabrication strategy", ACS Nano **9**, 8997 (2015).

[149] P. Han, K. Akagi, F. F. Canova, R. Shimizu, H. Oguchi, S. Shiraki, P. S. Weiss, N. Asao, and T. Hitosugi, "Self-assembly strategy for fabricating connected graphene nanoribbons", ACS Nano **9**, 12035 (2015).

[150] S. Linden, D. Zhong, A. Timmer, N. Aghdassi, J. H. Franke, H. Zhang, X. Feng, K. Müllen, H. Fuchs, L. Chi, and H. Zacharias, "Electronic structure of spatially aligned graphene nanoribbons on Au(788)", Phys. Rev. Lett. **108**, 23 (2012).

[151] M. Wießner, N. S. R. Lastra, J. Ziroff, F. Forster, P. Puschnig, L. Dössel, K. Müllen, A. Schöll, and F. Reinert, "Different views on the electronic structure of nanoscale graphene: Aromatic molecule versus quantum dot", New J. Phys. **14**, 113008 (2012).

[152] M. P. Seah and W. A. Dench, "Quantitative electron spectroscopy of surfaces: a standard data base for electron inelastic mean free paths in solids", Surf. Interface Anal. **1**, 2 (1979).

[153] D. Lüftner, S. Refaely-Abramson, M. Pachler, R. Resel, M. G. Ramsey, L. Kronik, and P. Puschnig, "Experimental and theoretical electronic structure of quinacridone", Phys. Rev. B **90**, 075204 (2014).

[154] Y. Furukawa, K. Kiuchi, K. ichi Kumagai, Y. Ajiro, Y. Narumi, M. Iwaki, K. Kindo, A. Bianchi, S. Carretta, P. Santini, F. Borsa, G. A. Timco, and R. E. P. Winpenny, "Evidence of spin singlet ground state in the frustrated antiferromagnetic ring Cr_8Ni", Phys. Rev. B **79**, 134416 (2009).

[155] N. Marom, O. Hod, G. E. Scuseria, and L. Kronik, "Electronic structure of copper phthalocyanine: A comparative density functional theory study", J. Chem. Phys. **128**, 164107 (2008).

[156] J. P. Perdew, K. Burke, and M. Ernzerhof, "Generalized gradient approximation made simple", Phys. Rev. Lett. **77**, 3865 (1996).

[157] P. Puschnig, "Organic molecule database: a database for molecular orbitals of conjugated organic molecules based on the atomic simulation environment (ASE) and NWChem as the DFT calculator", (2020).

[158] J. Heyd and G. E. Scuseria, "Efficient hybrid density functional calculations in solids: Assessment of the Heyd-Scuseria-Ernzerhof screened Coulomb hybrid functional", J. Chem. Phys. **121**, 1187 (2004).

[159] J. Heyd, G. E. Scuseria, and M. Ernzerhof, "Erratum: "Hybrid functionals based on a screened coulomb potential" (J. Chem. Phys. (2003) 118 (8207))", J. Chem. Phys. **124**, 219906 (2006).

[AH13] A. Haags, X. Yang, L. Egger, D. Brandstetter, H. Kirschner, A. Gottwald, M. Richter, G. Koller, M. G. Ramsey, F. C. Bocquet, S. Soubatch, F. S. Tautz, and P. Puschnig, "Benchmarking theoretical electronic structure methods with photoemission orbital tomography", submitted.

[160] A. D. Becke, "Density-functional thermochemistry. III. The role of exact exchange", J. Chem. Phys. **98**, 5648 (1993).

[161] J. P. Perdew, M. Ernzerhof, and K. Burke, "Rationale for mixing exact exchange with density functional approximations", J. Chem. Phys. **105**, 9982 (1996).

[162] S. Refaely-Abramson, S. Sharifzadeh, M. Jain, R. Baer, J. B. Neaton, and L. Kronik, "Gap renormalization of molecular crystals from density-functional theory", Phys. Rev. B **88**, 081204 (2013).

[163] L. Kronik and S. Kümmel, "Dielectric screening meets optimally tuned density functionals", Adv. Mater. **30**, 1706560 (2018).

[164] A. T. Balaban, "Is aromaticity outmoded?", Pure Appl. Chem. **52**, 1409 (1980).

[165] M. A. Kekulé, "Sur la constitution des substances aromatique", Bulletin mensuel de la Société chimique de Paris **3**, 98 (1865).

[166] J. i. Aihara, "Is superaromaticity a fact or an artifact? The Kekulene problem", J. Am. Chem. Soc. **114**, 865 (1992).

[167] H. Jiao and P. V. R. Schleyer, "Is kekulene really superaromatic?", Angew. Chem., Int. Ed. Engl. **35**, 2383 (1996).

[168] Z. Zhou, "Are kekulene, coronene, and corannulene tetraanion superaromatic? Theoretical examination using hardness indices", J. Phys. Org. Chem. **8**, 103 (1995).

[169] J. i. Aihara, M. Makino, T. Ishida, and J. R. Dias, "Analytical study of superaromaticity in cycloarenes and related coronoid hydrocarbons", J. Phys. Chem. A **117**, 4688 (2013).

[170] J. i. Aihara, "A simple method for estimating the superaromatic stabilization energy of a super-ring molecule", J. Phys. Chem. A **112**, 4382 (2008).

[171] J. C. Buttrick and B. T. King, "Kekulenes, cycloarenes, and heterocycloarenes: Addressing electronic structure and aromaticity through experiments and calculations", Chem. Soc. Rev. **46**, 7 (2017).

[172] D. Setiawan, E. Kraka, and D. Cremer, "Quantitative assessment of aromaticity and antiaromaticity utilizing vibrational spectroscopy", J. Org. Chem. **81**, 9669 (2016).

[173] P. M. Lathi, "Localization of aromaticity in fused-ring cycloarene systems: Prediction by an effective molecular mechanics model", J. Org. Chem. **53**, 4590 (1988).

[174] F. Diederich and H. A. Staab, "Benzenoid *versus* annulenoid aromaticity: Synthesis and properties of kekulene", Angew. Chem., Int. Ed. Engl. **17**, 372 (1978).

[175] C. Liu, Y. Ni, X. Lu, G. Li, and J. Wu, "Global aromaticity in macrocyclic polyradicaloids: Hückel′s rule or Baird′s rule?", Acc. Chem. Res. **52**, 2309 (2019).

[176] Z. Chen and R. B. King, "Spherical aromaticity: Recent work on fullerenes, polyhedral boranes, and related structures", Chem. Rev. **105**, 3613 (2005).

[177] J. i. Aihara, "On the number of aromatic sextets in a benzenoid hydrocarbon", Bull. Chem. Soc. Jpn. **49**, 1429 (1976).

[178] C. Krieger, F. Diederich, D. Schweitzer, and H. A. Staab, "Molecular structure and spectroscopic properties of kekulene", Angew. Chem., Int. Ed. Engl. **18**, 699 (1979).

[179] H. A. Staab, F. Diederich, C. Krieger, and D. Schweitzer, "Molecular structure and spectroscopic properties of kekulene", Chem. Ber. **116**, 3504 (1983).

[180] H. Tian, J. Shi, S. Dong, D. Yan, L. Wang, Y. Geng, and F. Wang, "Novel highly stable semiconductors based on phenanthrene for organic field-effect transistors", Chem. Commun. **33**, 3498 (2006).

[181] M. A. Majewski, Y. Hong, T. Lis, J. Gregoliński, P. J. Chmielewski, J. Cybińska, D. Kim, and M. Stępień, "Octulene: A hyperbolic molecular belt that binds chloride anions", Angew. Chem., Int. Ed. **55**, 14072 (2016).

[182] A. Reichmann, "Electronic and aromatic structure of kekulene studied by density functional theory", (2021), Master's thesis, Universität Graz.

[183] A. Tkatchenko and M. Scheffler, "Accurate molecular van der Waals interactions from ground-state electron density and free-atom reference data", Phys. Rev. Lett. **102**, 6 (2009).

[184] V. G. Ruiz, W. Liu, E. Zojer, M. Scheffler, and A. Tkatchenko, "Density-functional theory with screened van der Waals interactions for the modeling of hybrid inorganic-organic systems", Phys. Rev. Lett. **108**, 146103 (2012).

[185] M. E. Straumanis and L. S. Yu, "Lattice Parameters , Densities , Expansion Coefficients and Perfection of Structure of Cu and of Cu-In α Phase", Acta Cryst. **25**, 676 (1969).

[186] L. Romaner, D. Nabok, P. Puschnig, E. Zojer, and C. Ambrosch-Draxl, "Theoretical study of PTCDA adsorbed on the coinage metal surfaces, Ag(111), Au(111) and Cu(111)", New J. Phys. **11**, 053010 (2009).

[187] A. Bondi, "Van der Waals volumes and radii", J. Phys. Chem. **68**, 441 (1964).

[188] J. Kruszewski and T. M. Krygowski, "Definition of aromaticity basing on the harmonic oscillator model", Tetrahedron Lett. **13**, 3839 (1972).

[189] T. M. Krygowski, "Crystallographic studies of inter- and intramolecular interactions reflected in aromatic character of π-electron systems", J. Chem. Inf. Model. **33**, 70 (1993).

[190] P. V. R. Schleyer, C. Maerker, A. Dransfeld, H. Jiao, and N. J. V. E. Hommes, "Nucleus-independent chemical shifts: a simple and efficient aromaticity probe", J. Am. Chem. Soc. **118**, 6317 (1996).

[191] J. Poater, X. Fradera, M. Duran, and M. Solà, "The delocalization index as an electronic aromaticity criterion: application to a series of planar polycyclic aromatic hydrocarbons", Chemistry - A European Journal **9**, 400 (2003).

[192] C. L. Firme, S. E. Galembeck, O. A. Antunesa, and P. M. Esteves, "Density, degeneracy, delocalization-based index of aromaticity (D3BIA)", J. Braz. Chem. Soc. **18**, 1397 (2007).

[193] M. D. Harmony, "The equilibrium carbon-carbon single-bond length in ethane", J. Chem. Phys. **93**, 7522 (1990).

[194] N. C. Craig, P. Groner, and D. C. McKean, "Equilibrium structures for butadiene and ethylene: Compelling evidence for Π-electron delocalization in butadiene", J. Phys. Chem. A **110**, 7461 (2006).

[195] D. Setiawan, E. Kraka, and D. Cremer, "Hidden bond anomalies: The peculiar case of the fluorinated amine chalcogenides", J. Phys. Chem. A **119**, 9541 (2015).

[196] Q. Shen, H. Y. Gao, and H. Fuchs, "Frontiers of on-surface synthesis: From principles to applications", Nano Today **13**, 77 (2017).

[197] Q. Fan, S. Werner, J. Tschakert, D. Ebeling, A. Schirmeisen, G. Hilt, W. Hieringer, and J. M. Gottfried, "Precise monoselective aromatic C-H bond activation by chemisorption of meta-aryne on a metal surface", J. Am. Chem. Soc. **140**, 7526 (2018).

[198] S. Song, J. Su, M. Telychko, J. Li, G. Li, Y. Li, C. Su, J. Wu, and J. Lu, "On-surface synthesis of graphene nanostructures with π-magnetism", Chem. Soc. Rev. **50**, 3238 (2021).

[199] S. Mishra, D. Beyer, K. Eimre, S. Kezilebieke, R. Berger, O. Gröning, C. A. Pignedoli, K. Müllen, P. Liljeroth, P. Ruffieux, X. Feng, and R. Fasel, "Topological frustration induces unconventional magnetism in a nanographene", Nat. Nanotechnol. **15**, 22 (2020).

[200] K. Xu, J. I. Urgel, K. Eimre, M. D. Giovannantonio, A. Keerthi, H. Komber, S. Wang, A. Narita, R. Berger, P. Ruffieux, C. a. Pignedoli, J. Liu, K. Müllen, R. Fasel, and X. Feng, "On-surface synthesis of a nonplanar porous nanographene", J. Am. Chem. Soc. **141**, 7726 (2019).

[201] C. Rogers, C. Chen, Z. Pedramrazi, A. A. Omrani, H. Z. Tsai, H. S. Jung, S. Lin, M. F. Crommie, and F. R. Fischer, "Closing the nanographene gap: Surface-assisted synthesis of peripentacene from 6,6′-bipentacene precursors", Angew. Chem. Int. Ed. **54**, 15143 (2015).

[202] Z. Chen, A. Narita, and K. Müllen, "Graphene nanoribbons: On-surface synthesis and integration into electronic devices", Adv. Mater. **32**, 2001893 (2020).

[203] L. Talirz, P. Ruffieux, and R. Fasel, "On-surface synthesis of atomically precise graphene nanoribbons", Adv. Mater. **28**, 6222 (2016).

[204] D. J. Rizzo, G. Veber, T. Cao, C. Bronner, T. Chen, F. Zhao, H. Rodriguez, S. G. Louie, M. F. Crommie, and F. R. Fischer, "Topological band engineering of graphene nanoribbons", Nature **560**, 204 (2018).

[205] O. Gröning, S. Wang, X. Yao, C. A. Pignedoli, G. B. Barin, C. Daniels, A. Cupo, V. Meunier, X. Feng, A. Narita, K. Müllen, P. Ruffieux, and R. Fasel, "Engineering of robust topological quantum phases in graphene nanoribbons", Nature **560**, 209 (2018).

[206] P. Ruffieux, S. Wang, B. Yang, C. Sanchez-Sanchez, J. Liu, T. Dienel, L. Talirz, P. Shinde, C. A. Pignedoli, D. Passerone, T. Dumslaff, X. Feng, K. Müllen, and R. Fasel, "On-surface synthesis of graphene nanoribbons with zigzag edge topology", Nature **531**, 489 (2016).

[207] U. Beser, M. Kastler, A. Maghsoumi, M. Wagner, C. Castiglioni, M. Tommasini, A. Narita, X. Feng, and K. Müllen, "A C216-nanographene molecule with defined cavity as extended coronoid", J. Am. Chem. Soc. **138**, 4322 (2016).

[208] Q. Li, B. Yang, H. Lin, N. Aghdassi, K. Miao, J. Zhang, H. Zhang, Y. Li, S. Duhm, J. Fan, and L. Chi, "Surface-controlled mono/diselective ortho C-H bond activation", J. Am. Chem. Soc. **138**, 2809 (2016).

[209] J. Liu, Q. Chen, L. Xiao, J. Shang, X. Zhou, Y. Zhang, Y. Wang, X. Shao, J. Li, W. Chen, G. Q. Xu, H. Tang, D. Zhao, and K. Wu, "Lattice-directed formation of covalent and organometallic molecular wires by terminal alkynes on Ag surfaces", ACS Nano **9**, 6305 (2015).

[210] Z. F. Liu, Q. P. Wu, A. X. Chen, X. B. Xiao, N. H. Liu, and G. X. Miao, "Helical edge states and edge-state transport in strained armchair graphene nanoribbons", Scientific Reports **7**, 8854 (2017).

[211] N. Haag, D. Lüftner, F. Haag, J. Seidel, L. L. Kelly, G. Zamborlini, M. Jugovac, V. Feyer, M. Aeschlimann, P. Puschnig, M. Cinchetti, and B. Stadtmüller, "Signatures of an atomic crystal in the band structure of a C_{60} thin film", Phys. Rev. B **101**, 165422 (2020).

[212] D. M. Janas, A. Windischbacher, M. S. Arndt, M. Gutnikov, L. Sternemann, D. Gutnikov, T. Willershausen, J. E. Nitschke, K. Schiller, D. Baranowski, V. Feyer, I. Cojocariu, K. Dave, P. Puschnig, M. Stupar, S. Ponzoni, M. Cinchetti, and G. Zamborlini,

"Metalloporphyrins on oxygen-passivated iron: conformation and order beyond the first layer", Inorganica Chimica Acta **557**, 121705 (2023).

[213] A. Liebsch, "Theory of angle-resolved photoemission from ordered overlayers", Phys. Rev. Lett. **38**, 248 (1977).

[214] J. W. Davenport, "Multiple scattering theory of photoemission", Int. J. Quantum Chem. **12**, 89 (1977).

[215] N. J. Shevchik, "Atomic dipole theory of photoemission from molecules adsorbed on surfaces?", J. Phys. C Solid State Phys. **11**, 3521 (1978).

[216] M. Scheffler, K. Kambe, and F. Forstmann, "Angle resolved photoemission from adsorbates: Theoretical considerations of polarization effects and symmetry", Solid State Commun. **25**, 93 (1978).

[217] K. Kambe and M. Scheffler, "Theory of photoexcitation of adsorbates: an analysis of atomic, adlayer, and substrate effects", Surf. Sci. **89**, 262 (1979).

[218] P. Hofmann, K. Horn, and A. M. Bradshaw, "Orientation of adsorbed benzene from angle-resolved photoemission measurements", Surf. Sci. **105**, 260 (1981).

[219] F. P. Netzer, G. Rangelov, G. Rosina, H. B. Saalfeld, M. Neumann, and D. R. Lloyd, "Benzene on Pd(110): The first example of nonparallel adsorption", Phys. Rev. B **37**, 10399(R) (1988).

[220] W. Huber, H. P. Steinrück, T. Pache, and D. Menzel, "The electronic structure and molecular symmetry of pure benzene and benzene coadsorbed with CO on Ni(111)", Surf. Sci. **217**, 103 (1989).

[221] W. Huber, M. Weinelt, P. Zebisch, and H. P. Steinrück, "Azimuthal reorientation of adsorbed molecules induced by lateral interactions: benzene/Ni(110)", Surf. Sci. **253**, 72 (1991).

[222] M. G. Ramsey, D. Steinmüller, F. P. Netzer, T. Schedel, A. Santaniello, and D. R. Lloyd, "Compressed benzene on Ni(110)", Surf. Sci. **251-252**, 979 (1991).

[223] O. Schaff, V. Fernandez, P. Hofmann, K. M. Schindler, A. Theobald, V. Fritzsche, A. M. Bradshaw, R. Davis, and D. P. Woodruff, "Scoverage-dependent changes in the adsorption geometry of benzene on Ni{111}", Surf. Sci. **348**, 89 (1996).

[224] J. H. Kang, R. L. Toomes, J. Robinson, D. P. Woodruff, O. Schaff, R. Terborg, R. Lindsay, P. Baumgärtel, and A. M. Bradshaw, "Local adsorption geometry of benzene on Ni(110) at low coverage", Surf. Sci. **448**, 23 (2000).

[225] M. Doering, H. P. Rust, B. G. Briner, and A. M. Bradshaw, "Imaging benzene on nickel and copper {110} surfaces with low temperature STM: The adsorption site", Surf. Sci. **410**, L736 (1998).

[226] R. Duschek, F. Mittendorfer, R. I. Blyth, F. P. Netzer, J. Hafner, and M. G. Ramsey, "The adsorption of aromatics on sp-metals: Benzene on Al(111)", Chem. Phys. Lett. **318**, 43 (2000).

[227] F. Mittendorfer and J. Hafner, "Density-functional study of the adsorption of benzene on the (111), (100) and (110) surfaces of nickel", Surf. Sci. **472**, 133 (2001).

[228] W. Reckien, M. Eggers, and T. Bredow, "Theoretical study of the adsorption of benzene on coinage metals", Beilstein J. Org. Chem. **10**, 1775 (2014).

[229] G. Canduela-Rodriguez, M. K. Sabbe, M. F. Reyniers, J. F. Joly, and G. B. Marin, "Periodic DFT study of benzene adsorption on Pd(100) and Pd(110) at medium and saturation coverage", J. Phys. Chem. C **118**, 21483 (2014).

[230] W. Liu, F. Maaß, M. Willenbockel, C. Bronner, M. Schulze, S. Soubatch, F. S. Tautz, P. Tegeder, and A. Tkatchenko, "Quantitative prediction of molecular adsorption: Structure and binding of benzene on coinage metals", Phys. Rev. Lett. **115**, 036104 (2015).

[231] F. Maaß, Y. Jiang, W. Liu, A. Tkatchenko, and P. Tegeder, "Binding energies of benzene on coinage metal surfaces: Equal stability on different metals", J. Chem. Phys. **148**, 214703 (2018).

[232] J. B. Neaton, M. S. Hybertsen, and S. G. Louie, "Renormalization of Molecular Electronic Levels at Metal-Molecule Interfaces", Phys. Rev. Lett. **97**, 216405 (2006).

[233] Z. F. Liu, D. A. Egger, S. Refaely-Abramson, L. Kronik, and J. B. Neaton, "Energy level alignment at molecule-metal interfaces from an optimally tuned range-separated hybrid functional", J. Chem. Phys. **146**, 092326 (2017).

[234] C. Riedl, C. Coletti, T. Iwasaki, A. A. Zakharov, and U. Starke, "Quasi-free-standing epitaxial graphene on SiC obtained by hydrogen intercalation", Phys. Rev. Lett. **103**, 246804 (2009).

[235] X. Yang, L. Egger, J. Fuchsberger, M. Unzog, D. Lüftner, F. Hajek, P. Hurdax, M. Jugovac, G. Zamborlini, V. Feyer, G. Koller, P. Puschnig, F. S. Tautz, M. G. Ramsey, and S. Soubatch, "Coexisting charge states in a unary organic monolayer film on a metal", J. Phys. Chem. Lett. **10**, 6438 (2019).

[236] V. Feyer, M. Graus, P. Nigge, M. Wießner, R. G. Acres, C. Wiemann, C. M. Schneider, A. Schöll, and F. Reinert, "Adsorption geometry and electronic structure of iron phthalocyanine on Ag surfaces: A LEED and photoelectron momentum mapping study", Surf. Sci. **621**, 64 (2014).

[237] E. M. Reinisch, "n-Doping of Conjugated Molecules on fcc Metal Surfaces: Investigations employing Photoemission Tomography", (2015), Ph. D. thesis, Karl-Franzens-Universität Graz.

[238] T. Ules, "Orbital tomographic investigations of organic molecular films and their interfaces", (2014), Ph. D. thesis, Karl-Franzens-Universität Graz.

[239] J. Ziroff, F. Forster, A. Schöll, P. Puschnig, and F. Reinert, "Hybridization of organic molecular orbitals with substrate states at interfaces: PTCDA on silver", Phys. Rev. Lett. **104**, 233004 (2010).

[240] S. Berkebile, T. Ules, P. Puschnig, L. Romaner, G. Koller, A. J. Fleming, K. Emtsev, T. Seyller, C. Ambrosch-Draxl, F. P. Netzer, and M. G. Ramsey, "A momentum space view of the surface chemical bond", Phys. Chem. Chem. Phys. **13**, 3604 (2011).

[241] M. Wießner, J. Ziroff, F. Forster, M. Arita, K. Shimada, P. Puschnig, A. Schöll, and F. Reinert, "Substrate-mediated band-dispersion of adsorbate molecular states", Nat. Commun. **4**, 1514 (2013).

[242] M. Wießner, J. Kübert, V. Feyer, P. Puschnig, A. Schöll, and F. Reinert, "Lateral band formation and hybridization in molecular monolayers: NTCDA on Ag(110) and Cu(100)", Phys. Rev. B **88**, 075437 (2013).

[243] T. Ules, D. Lüftner, E. M. Reinisch, G. Koller, P. Puschnig, and M. G. Ramsey, "Orbital tomography of hybridized and dispersing molecular overlayers", Phys. Rev. B **90**, 155430 (2014).

[244] D. Lüftner, M. Milko, S. Huppmann, M. Scholz, N. Ngyuen, M. Wießner, A. Schöll, F. Reinert, and P. Puschnig, "CuPc/Au(110): Determination of the azimuthal alignment by a combination of angle-resolved photoemission and density functional theory", J. Electron Spectrosc. Relat. Phenom. **195**, 293 (2014).

[245] J. Itatani, J. Lavesque, D. Zeidler, H. Niikura, H. Pépin, J. C. Kieffer, P. B. Corkum, and D. M. Villeneuve, "Tomographic imaging of molecular orbitals", Nature **432**, 867 (2004).

[246] P. Puschnig and D. Lüftner, "Simulation of angle-resolved photoemission spectra by approximating the final state by a plane wave: From graphene to polycyclic aromatic hydrocarbon molecules", J. Electron Spectrosc. Relat. Phenom. **200**, 193 (2015).

[247] A. Bostwick, T. Ohta, J. L. McChesney, K. V. Emtsev, T. Seyller, K. Horn, and E. Rotenberg, "Symmetry breaking in few layer graphene films", New J. Phys. **9**, 385 (2007).

[248] L. Nemec, V. Blum, P. Rinke, and M. Scheffler, "Thermodynamic equilibrium conditions of graphene films on SiC", Phys. Rev. Lett. **111**, 065502 (2013).

[249] J. Sforzini, L. Nemec, T. Denig, B. Stadtmüller, T.-L. Lee, C. Kumpf, S. Soubatch, U. Starke, P. Rinke, V. Blum, F. C. Bocquet, and F. S. Tautz, "Approaching truly free-standing graphene: the structure of hydrogen-intercalated graphene on 6H - SiC(0001)", Phys. Rev. Lett. **114**, 106804 (2015).

[250] K. V. Emtsev, F. Speck, T. Seyller, and L. Ley, "Interaction, growth, and ordering of epitaxial graphene on SiC{0001} surfaces: A comparative photoelectron spectroscopy study", Phys. Rev. B **77**, 155303 (2008).

[251] F. Varchon, R. Feng, J. Hass, X. Li, B. N. Nguyen, C. Naud, P. Mallet, J. Veuillen, C. Berger, E. H. Conrad, and L. Magaud, "Electronic structure of epitaxial graphene layers on SiC: Effect of the substrate", Phys. Rev. Lett. **99**, 126805 (2007).

[252] S. Tanabe, Y. Sekine, H. Kageshima, and H. Hibino, "Electrical characterization of bi-layer graphene formed by hydrogen intercalation of monolayer graphene on SiC(0001)", Jpn. J. Appl. Phys. **51**, 02BN02 (2012).

[253] S. Mammadov, J. Ristein, J. Krone, C. Raidel, M. Wanke, V. Wiesmann, F. Speck, and T. Seyller, "Work function of graphene multilayers on SiC(0001)", 2D Mater. **4**, 015043 (2017).

List of Own Publications

- P. J. Blowey, **A. Haags**, L. A. Rochford, J. Felter, D. A. Warr, D. A. Duncan, T.-L. Lee, G. Constantini, C. Kumpf and D. P. Woodruff, "Characterization of growth and structure of TCNQ phases on Ag(111)", Physical Review Materials **3**, 116001 (2019).
- **A. Haags**, L. A. Rochford, J. Felter, P. J. Blowey, D. A. Duncan, D. P. Woodruff and C. Kumpf, "Growth and evolution of tetracyanoquinodimethane and potassium coadsorption phases on Ag(111)", New Journal of Physics, **22**, 063028 (2020).
- **A. Haags**, A. Reichmann, Q. Fan, L. Egger, H. Kirschner, T. Naumann, S. Werner, T. Vollgraff, J. Sundermeyer, L. Eschmann, X. Yang, D. Brandstetter, F. C. Bocquet, G. Koller, A. Gottwald, M. Richter, M. G. Ramsey, M. Rohlfing, P. Puschnig, J. M. Gottfried, S. Soubatch, and F. S. Tautz, "Kekulene: On-Surface Synthesis, Orbital Structure, and Aromatic Stabilization", ACS Nano **14**, 15766 (2020).
- P. Hurdax, M. Hollerer, L. Egger, G. Koller, X. Yang, **A. Haags**, S. Soubatch, F. S. Tautz, M. Richter, A. Gottwald, P. Puschnig, M. Sterrer and M. G. Ramsey, "Controlling the electronic and physical coupling on dielectric thin films", Beilstein Journal of Nanotechnology, **11**, 1492–1503 (2020).
- L. Egger, M. Hollerer, C. S. Kern, H. Herrmann, P. Hurdax, **A. Haags**, X. Yang, A. Gottwald, M. Richter, S. Soubatch, F. S. Tautz, G. Koller, P. Puschnig, M. G. Ramsey and M. Sterrer, "Charge-Promoted Self-Metalation of Porphyrins on an Oxide Surface", Angewandte Chemie International Edition, **60**, 5078–5082 (2021).
- M. S. Sättele, A. Windischbacher, L. Egger, **A. Haags**, P. Hurdax, H. Kirschner, A. Gottwald, M. Richter, F. C. Bocquet, S. Soubatch, F. S. Tautz, H. F. Bettinger, H. Peisert, T. Chassé, M. G. Ramsey, P. Puschnig and G. Koller, "Going beyond Pentacene: Photoemission Tomography of a Heptacene Monolayer on Ag(110)", The Journal of Physical Chemistry C, **125**, 2918–2925, (2021).

- M. Raths, C. Schott, J. Knippertz, M. Franke, Y.-R. Lin, **A. Haags**, M. Aeschlimann, C. Kumpf and B. Stadtmüller, "Growth, domain structure, and atomic adsorption sites of hBN on the Ni(111) surface", Physical Review Materials, **5**, 094001, (2021).
- M. S. Sättele, A. Windischbacher, K. Greulich, L. Egger, **A. Haags**, H. Kirschner, R. Ovsyannikov, E. Giangrisostomi, A. Gottwald, M. Richter, S. Soubatch, F. S. Tautz, M. G. Ramsey, P. Puschnig, G. Koller, H. F. Bettinger, T. Chassé and H. Peisert, "Hexacene on Cu(110) and Ag(110): Influence of the Substrate on Molecular Orientation and Interfacial Charge Transfer", The Journal of Physical Chemistry, **125**, 10, 5036–5045 (2022).
- **A. Haags**, X. Yang, L. Egger, D. Brandstetter, H. Kirschner, F. C. Bocquet, G. Koller, A. Gottwald, M. Richter, J. M. Gottfried, M. G. Ramsey, P. Puschnig, S. Soubatch, and F. S. Tautz, "Momentum-space imaging of σ-orbitals for chemical analysis", Science Advances, **8**, 29, (2022).
- P. Hurdax, C. Kern, T. Bone, **A. Haags**, M. Hollerer, L. Egger, X. Yang, H. Kirschner, A. Gottwald, M. Richter, F. C. Bocquet, S. Soubatch, G. Koller, F. S. Tautz, M. Sterrer, P. Puschnig, M. G. Ramsey, "Large Distortion of Fused Aromatics on Dielectric Interlayers Quantified by Photoemission Orbital Tomography", ACS Nano, **16**, 10, 17435-17443 (2022).
- P. Schädlich, S. Wolff, F. Schölzel, P. Richter, Th Seyller, M. Stettner, M. Hutter, S. Wenzel, **A. Haags**, S. Soubatch, F.C. Bocquet, C. Kumpf, B. Matta, Ph. Rosenzweig, K. Küster, U. Starke, C. Polley, C. Ghosal, Z. Mamiyev, J. Koch, C. Tegenkamp, "Domain boundary formation within an intercalated Pb monolayer featuring charge-neutral epitaxial graphene", Adv. Mater. Interfaces, **10**, 27, 2300471, (2023).
- C. S. Kern, **A. Haags**, X. Yang, H. Kirschner, S. Wolff, T. Seyller, A. Gottwald, M. Richter, U. De Giovannini, A. Rubio, M. G. Ramsey, F. C. Bocquet, S. Soubatch, F. S. Tautz, P. Puschnig and S. Moser, "Simple extension of the plane-wave final state in photoemission: Bringing understanding to the photon-energy dependence of two-dimensional materials", Phys. Rev. Research, **5**, 033075 (2023).

- **A. Haags**, X. Yang, L. Egger, D. Brandstetter, H. Kirschner, A. Gottwald, M. Richter, G. Koller, M. G. Ramsey, F. C. Bocquet, S. Soubatch, F. S. Tautz and P. Puschnig, "Benchmarking theoretical electronic structure methods with photoemission orbital tomography" arXiv:2209.11516
  submitted
- **A. Haags**, H. Kirschner, A. Gottwald, M. Richter, M. G. Ramsey, F. C. Bocquet, P. Puschnig, S. Soubatch, and F. S. Tautz, "Polarization factor and experimental geometry in photoemission orbital tomography"
  in preparation

Acknowledgments

During my PhD time, I had the opportunity to work, discuss, and share knowledge with many people, whom I would like to thank.

First and foremost I am grateful to my PhD advisor, F. Stefan Tautz, for his supervision, invaluable advice, and continuous support during my PhD study.

I thank Michael G. Ramsey for accepting to co-referee my PhD thesis and the opportunity to discover the beauty of POT from one of the technique's pioneers.

I could not have undertaken this journey without Sergey Subach. Thank you for your expertise, your permanent support, many discussions about work and life, uncountable russian sayings, and the most entertaining yet efficient beamtimes at the UVSOR synchrotron facility in Okazaki, Japan, at Diamond Light Source in Oxfordshire, England, and at the Metrology Light Source in Berlin.

Especially, during the writing process of this thesis, Moritz Sokolowski has helped and encouraged me over many months to finalize my work in Jülich. Thank you for many supportive and motivating words. By employing me at the Rheinische Friedrich-Wilhelms-Universität Bonn, you gave me the opportunity to learn more about LEED-IV.

The results presented in this work arise from collaborative projects between Jülich and other groups from Graz, Berlin, Würzburg, Marburg, and Münster. Many thanks to Larissa Egger, Philipp Hurdax, and Georg Koller from Karl-Franzens-Universität Graz, Austria for experimental support at the synchrotron, to Dominik Brandstetter, Christian Kern, Alexander Reichmann, and Peter Puschnig from Karl-Franzens-Universität Graz, Austria for many discussions and for providing comprehensible explanations about the quantum chemical calculations presented in this work. Thanks to Hans Kirschner, Hendrik Kaser, Alexander Gottwald, and Mathias Richter from Metrology Light Source in Berlin, who provided us with a well-calibrated synchrotron beamline, to Simon Moser from Julius-Maximilians-Universität Würzburg for patiently guiding me to the matrix element in angle resolved photoemission and to Qitang Fan and J. Michael Gottfried from Philipps-Universität Marburg for fruitful discussions and providing STM measurements. For friendly assistance during beamtime, I would like to thank Marie-Sophie Sättele and Katharina Greulich from Eberhard Karls Universität Tübingen as well as Susanne Wolff from TU Chemnitz.

For technical support at Diamond Light Source, I would like to thank David Duncan and Tien-Lin Lee. Furthermore, I would also like to acknowledge that I had the pleasure of working with Matthias Meissner, Fumihiko Matsui, and Satoshi Kera at the UVSOR synchrotron facility in Okazaki, Japan.

I am also grateful for the friendly working atmosphere with my colleagues from Peter Grünberg Institute (PGI-3) at Forschungszentrum Jülich. To name a few, who have come along the PhD-journey with me, I thank Xiaosheng Yang, Mark Hutter, Sabine Wenzel, François Posseik, Miriam Raths, and Christian Kumpf.

Finally, special thanks to my parents, family, friends and especially my fiancé Patrick, for your loving support and words of encouragement.

Band / Volume 90
Modeling and Suppressing Unwanted Parasitic Interactions in Superconducting Circuits
X. Xu (2022), 123, XVIII pp
ISBN: 978-3-95806-671

Band / Volume 91
Activating molecular magnetism by controlled on-surface coordinationI. Cojocariu (2022), xi, 169 pp
ISBN: 978-3-95806-674-8

Band / Volume 92
Computational study of structural and optical properties of two-dimensional transition-metal dichalcogenides with implanted defects
S. H. Rost (2023), xviii, 198 pp
ISBN: 978-3-95806-682-3

Band / Volume 93
DC and RF characterization of bulk CMOS and FD-SOI devices at cryogenic temperatures with respect to quantum computing applications
A. Artanov (2023), xv, 80, xvii-liii pp
ISBN: 978-3-95806-687-8

Band / Volume 94
HAXPES study of interface and bulk chemistry of ferroelectric HfO_2 capacitors
T. Szyjka (2023), viii, 120 pp
ISBN: 978-3-95806-692-2

Band / Volume 95
A brain inspired sequence learning algorithm and foundations of a memristive hardware implementation
Y. Bouhadjar (2023), xii, 149 pp
ISBN: 978-3-95806-693-9

Band / Volume 96
Characterization and modeling of primate cortical anatomy and activity
A. Morales-Gregorio (2023), ca. 260 pp.
ISBN: 978-3-95806-698-4

Band / Volume 97
Hafnium oxide based memristive devices as functional elements of neuromorphic circuits
F. J. Cüppers (2023), vi, ii, 214 pp
ISBN: 978-3-95806-702-8

Band / Volume 98
Simulation and theory of large - scale cortical networks
A. van Meegen (2023), ca. 250 pp
ISBN: 978-3-95806-708-0

Band / Volume 99
Structure of two-dimensional multilayers and topological superconductors: surfactant mediated growth, intercalation, and doping
Y.-R. Lin (2023), x, 111 pp
ISBN: 978-3-95806-716-5

Band / Volume 100
Frequency mixing magnetic detection for characterization and multiplex detection of superparamagnetic nanoparticles
A. M. Pourshahidi (2023), X, 149 pp
ISBN: 978-3-95806-727-1

Band / Volume 101
Unveiling the relaxation dynamics of Ag/HfO2 based diffusive memristors for use in neuromorphic computing
S. A. Chekol (2023), x, 185 pp
ISBN: 978-3-95806-729-5

Band / Volume 102
Analysis and quantitative comparison of neural network dynamics on a neuron-wise and population level
R. Gutzen (2024), xii, 252 pp
ISBN: 978-3-95806-738-7

Band / Volume 103
3D Scaffolds with Integrated Electrodes for Neuronal Cell Culture
J. Abu Shihada (2024), vii, 163 pp
ISBN: 978-3-95806-756-1

Band / Volume 104
Advances in Photoemission Orbital Tomography
A. Haags (2024), ix, 254 pp
ISBN: 978-3-95806-766-0

Weitere ***Schriften des Verlags im Forschungszentrum Jülich*** unter
http://wwwzb1.fz-juelich.de/verlagextern1/index.asp

Information
Band / Volume 104
ISBN 978-3-95806-766-0

Mitglied der Helmholtz-Gemeinschaft

JÜLICH
Forschungszentrum